

# NAPHTHALENE DIIMIDE-BASED ACCEPTORS FOR ORGANIC SOLAR CELLS



**Kira Rundel**

B.S. Engineering (Honours)

Department of Materials Science and Engineering  
Monash University

This dissertation is submitted for the degree of  
*Doctor of Philosophy*

March 2019



To my fellow Sisters in Science





## Copyright Notice

© Kira Rundel (2019)

I certify that I have made all reasonable efforts to secure copyright permissions for third-party content included in this thesis and have not knowingly added copyright content to my work without the owner's permission.



## Abstract

Organic solar cells have the potential to dramatically impact the future of the energy industry by offering a light-weight, flexible, partially transparent, and inexpensive alternative to complement silicon solar technology. However, solar conversion efficiency and lifetime limitations, both of which are lower than that of silicon solar cells, has limited the commercial success of organic photovoltaics. In order to realize their full potential, the materials used in the active layer of organic solar cells must be improved in order to increase both device efficiency and lifetime. This thesis focuses on small molecule and polymeric alternatives to costly and degrading fullerene materials, typically used as acceptors in bulk-heterojunction organic solar cells. Though device performance for these alternatives was initially lower than devices employing fullerene acceptors, over the past few years, several advancements have enabled sizable improvements in organic solar cell efficiency, which now approaches 16% for single-junction fullerene-free solar cells. This thesis explores naphthalene diimide (NDI)-based acceptors, which have shown device efficiencies surpassing 11% in polymeric form, with small molecule acceptors lagging behind. Novel small molecule and polymeric material structures are studied, where the effect of substituent and substitutional atoms on the optoelectronic and properties of these molecules is explored. In particular, different substituent atoms attached to the NDI core and the substitution of sulfur atoms for oxygen atoms in the imide unit (thionation) are both investigated as potential strategies for improving solar cell performance. Synchrotron-based techniques are heavily relied upon for characterizing both the thin-film morphology as well as electronic structure. Additionally, this thesis includes an in-depth analysis utilizing density functional theory-based calculations to predict the near-edge X-ray absorption fine structure, in order to better understand the electronic structure of naphthalene diimide, and how it is influenced by substitutional atoms. It is found that both the material structure, as well as substitutional or substituent atoms, influence the optoelectronic and physical properties of the NDI-based acceptors, both of which can drastically influence solar cell efficiency.



# Thesis Including Published Works Declaration

I hereby declare that this thesis contains no material which has been accepted for the award of any other degree or diploma at any university or equivalent institution and that, to the best of my knowledge and belief, this thesis contains no material previously published or written by another person, except where due reference is made in the text of the thesis.

This thesis includes two original papers published in peer reviewed journals. The core theme of the thesis is exploring the relationship between substitutional atoms inserted either into the core or imide positions of naphthalene diimide and the resulting effect these have on the optical and electronic properties of the material. The ideas, development and writing up of all the papers in the thesis were the principal responsibility of myself, the student, working within the Materials Science and Engineering Department under the supervision of Professor Christopher McNeill.

The inclusion of co-authors reflects the fact that the work came from active collaboration between researchers and acknowledges input into team-based research.

In the case of Chapters 5 and 7, my contribution to the work involved the following:

| Thesis Chapter | Publication Title  | Status    | Nature and % of student contribution   | Co-author names, Nature, and % of Co-author's contribution   | Co-authors, Monash student Y/N          |
|----------------|--|-----------|--|--|---|
| 5              | <i>Naphthalene diimide-based small molecule acceptors for organic solar cells</i>  | Published | 70%, concept and collecting most data and writing first manuscript draft                 | 1) Subashani Maniam, material synthesis, input into manuscript 15%<br>2) Kedar Deshmukh, solar cell optimization, input into manuscript 5%<br>3) Eliot Gann, R-SoXS measurement, input into manuscript 5%<br>4) Shyamal K. K. Prasad, PL Quenching measurement, input into manuscript, 5%<br>5) Justin M. Hodgkiss<br>6) Steven J. Langford<br>7) Christopher R. McNeill | No<br>Yes<br>No<br>No<br>No<br>No<br>No |
| 7              | <i>Understanding the effect of thionation on naphthalene diimide using first-principles predictions of near-edge X-ray absorption fine structure spectra</i> | Published | 80%, concept and performing calculations and analysis and writing first manuscript draft | 1) YuFeng Liang, authoring code, input into manuscript 5%<br>2) Adam Welford, experimental NEXAFS measurements, input into manuscript 5%<br>3) David Prendergast, interpretation of results, input into manuscript 10%<br>4) Christopher R. McNeill  | No<br>Yes<br>No<br>No                   |

I have reformatted sections of submitted or published papers in order to generate a consistent presentation within the thesis.

**Student signature:**

**Date:**

The undersigned hereby certify that the above declaration correctly reflects the nature and extent of the student's and co-authors' contributions to this work. In instances where I am not the responsible author I have consulted with the responsible author to agree on the respective contributions of the authors.

**Main Supervisor signature:**

**Date:**

## Acknowledgments

There are several people I would like to acknowledge, without whom this thesis would never have been written.

Throughout the course of my education, there have been two incredibly strong, intelligent and inspiring women, whose belief in me has been paramount to my pursuit of this Doctor of Philosophy. First, I would like to thank Celine Cohn, my long-time mentor from the first time I ever set foot in a research laboratory, as a Senior in High School, at the University of Arizona in Tucson. Celine: you believed in me from the beginning, you encouraged me and you instilled a confidence in my ability as a researcher that I have had to rely on constantly throughout this journey. You opened a door for me that has led me down this incredible path, and I am forever grateful to you, for taking me under your wing and instilling in me a passion for science and the pursuit of furthering humanity's understanding of how things work. I would also like to thank Professor Erin Ratcliff from the University of Arizona. Though you were just starting out as a professor when I approached you in my Senior year as a prospective student, you welcomed me in to your lab, and gave me the freedom to explore my own interests and develop a method for approaching complex problems that I have relied on countless times over the past few years. You once said I reminded you of yourself when you were at the start of your research career, and these words have stayed with me, as a reminder of my capabilities to succeed, and I will always be thankful to you for that.

I would also like to thank the incredible friends who have kept me sane and helped me to take advantage of the amazing city I have been fortunate to call home for the past three and a half years. Through you I have discovered a love for wheel-throwing pottery, world-class gin, that there is more to wine than simply "white" or "red," and the absolutely fantastic Melbourne food scene, among countless other adventures that will forever hold a special place in my heart. Melbourne has been a truly inspirational place for me to undertake this PhD, and although I cannot say the journey was without hardships, I am grateful for the opportunities I have had here to grow in both a professional as well as a personal sense.

My parents will forever be the original inspiration for me to pursue a career in science, and I would not have been able to achieve half of the things that I have without their constant support, love, encouragement, and belief in me. Mom and dad: you inspire me to be a better person every day, to question the *status quo*, and to do my part in making this world a better place. I love you!

I would like to thank Professor Chris McNeill and the members of the McNeill research group that I have had the pleasure of working alongside over the past three and a half years. Chris, you have been a pillar of support for me throughout my PhD, and I never could have achieved so much without you. Your approach in supervision is truly exceptional, and the care and effort with which you mentor each of your students is very much appreciated!

Finally, I would like to thank Dr. David Prendergast from the Molecular Foundry at the Lawrence Berkeley National Laboratory for his support in teaching me the computational methods used in Chapter 7 of this thesis. I am also very grateful to the Materials Science and Engineering department at Monash University, for selecting me to receive the Research Training Program scholarship, without which this work would not have been possible. Edna Tan, your support for the department is extraordinary and I very much appreciate everything you do for all of us!



## Publications during Enrollment

K. Rundel, S. Maniam, K. Deshmukh, E. Gann, S. K. K. Prasad, J. M. Hodgkiss, S. J. Langford, and C. R. McNeill. "Naphthalene diimide-based small molecule acceptors for organic solar cells." *Journal of Materials Chemistry A*, vol. 5, pp. 12266-12277, 2017.

K. Rundel, Y. Shin, A. Chesman, A. Liu, A. Welford, L. Thomsen, M. Sommer, and C. R. McNeill. "Effect of thionation on the performance of PNDIT2-based polymer solar cells." *The Journal of Physical Chemistry C*, vol. 123, pp. 12062-12072, 2019.

K. Rundel, Y. Liang, A. Welford, D. Prendergast, and C. R. McNeill. "Understanding the effect of thionation on naphthalene diimide using first principles predictions of near-edge X-ray absorption fine structure spectra." *Journal of Chemical Physics*, vol. 150, pp. 104302, 2019.

T. Weller, K. Rundel, G. Krauss, C. R. McNeill, and M. Thelakkat. "Highly efficient and balanced charge transport in thieno[3,4-*c*]pyrrole-4,6-dione copolymers: dramatic influence of thieno[3,2-*b*]thiophene comonomer on alignment and charge transport." *Journal of Physical Chemistry C*, vol. 122, pp. 7565-7574, 2018.

T. T. Do, K. Rundel, Q. Gu, E. Gann, S. Manzhos, K. Feron, J. Bell, C. R. McNeill, and P. Sonar. "9-Fluorenone and 9,10-anthraquinone potential fused aromatic building blocks to synthesize electron acceptors for organic solar cells." *New Journal of Chemistry*, vol. 41, pp. 2899-2909, 2017.

H. Xin, C. Ge, X. Jiao, X. Yang, K. Rundel, C. R. McNeill, and X. Gao. "Incorporation of 2,6-connected azulene units into the backbone of conjugated polymers: towards high-performance organic optoelectronic materials." *Angewante Chemie International Edition*, vol. 57, pp. 1322-1326, 2017.

J. Zhang, Q. Gu, T. T. Do, K. Rundel, P. Sonar, R. H. Friend, C. R. McNeill, and A. A. Bakulin. "Control of geminate recombination by the material composition and processing conditions in novel polymer: nonfullerene acceptor photovoltaic devices." *Journal of Physical Chemistry A*, vol. 122, pp. 1253-1260, 2018.

# Contents

|  |             |
|--|-------------|
| <b>Abbreviations</b>   | <b>xiii</b> |
| <b>1 Introduction</b>  | <b>1</b>    |
| 1.1 Motivation for the need for renewable energy . . . . .               | 1           |
| 1.2 Introduction to photovoltaics . . . . .                              | 5           |
| 1.3 Introduction to organic photovoltaics . . . . .                      | 8           |
| 1.4 Overview of the thesis . . . . .                                     | 11          |
| References . . . . .   | 15          |
| <b>2 Literature Review</b>   | <b>23</b>   |
| 2.1 Introduction . . . . .   | 23          |
| 2.2 Organic semiconductors . . . . .                                     | 23          |
| 2.2.1 Working principles . . . . .                                       | 23          |
| 2.2.1.1 Electronic structure of organic semiconductors . . . . .         | 26          |
| 2.2.2 Optoelectronic properties . . . . .                                | 27          |
| 2.2.2.1 Light absorption in organic semiconductors . . . . .             | 27          |
| 2.2.2.2 Introduction to charge transport . . . . .                       | 29          |
| 2.3 Organic solar cells . . . . .  | 31          |
| 2.3.1 OPV Operation . . . . .  | 31          |
| 2.3.1.1 Charge transport . . . . .                                       | 34          |
| 2.3.1.2 Active layer morphology . . . . .                                | 35          |
| 2.3.1.3 Device architecture . . . . .                                    | 40          |
| 2.3.1.3.1 Inverted architecture . . . . .                                | 43          |
| 2.3.2 Characterization . . . . .   | 43          |
| 2.3.3 Materials . . . . .  | 45          |
| 2.3.3.1 Donor materials . . . . .  | 46          |
| 2.3.3.2 Recent progress in acceptor materials . . . . .                  | 48          |
| 2.3.3.3 Overview of NDI-based small molecule acceptors . . . . .         | 52          |
| 2.3.3.3.1 Substituent atoms . . . . .                                    | 55          |
| References . . . . .   | 59          |
| <b>3 Experimental</b>  | <b>75</b>   |
| 3.1 Introduction . . . . .   | 75          |
| 3.2 Materials . . . . .  | 75          |
| 3.2.1 Material Properties . . . . .                                      | 78          |
| 3.2.1.1 Measuring Energy Levels . . . . .                                | 78          |
| 3.2.1.2 UV-visible absorption spectroscopy . . . . .                     | 80          |
| 3.2.1.3 Near edge X-ray absorption fine structure spectroscopy . . . . . | 82          |

|           |   |            |
|-----------|---|------------|
| 3.2.1.3.1 | Experimental . . . . .  | 83         |
| 3.2.1.3.2 | Calculations . . . . .  | 86         |
| 3.3       | Solar cell fabrication and characterization . . . . .                       | 89         |
| 3.3.1     | Device fabrication . . . . .  | 89         |
| 3.3.2     | Device characterization . . . . .   | 90         |
| 3.3.2.1   | $J - V$ measurements . . . . .  | 91         |
| 3.3.2.2   | EQE measurements . . . . .  | 91         |
| 3.3.2.3   | Intensity dependent measurements . . . . .                                  | 91         |
| 3.3.2.4   | Transient photocurrent measurements . . . . .                               | 92         |
| 3.3.3     | Space-charge limited current devices . . . . .                              | 93         |
| 3.4       | Active layer morphology characterization . . . . .                          | 93         |
| 3.4.1     | Surface Profiler . . . . .  | 94         |
| 3.4.2     | Photoluminescence quenching . . . . .                                       | 94         |
| 3.4.3     | Atomic force microscopy . . . . .   | 95         |
| 3.4.4     | Grazing incidence wide-angle X-ray scattering . . . . .                     | 95         |
| 3.4.5     | Transmission electron microscopy . . . . .                                  | 100        |
| 3.4.6     | Resonant soft X-ray scattering . . . . .                                    | 100        |
|           | References . . . . .  | 105        |
| <b>4</b>  | <b>Effect of substituent atoms on the properties of naphthalene diimide</b> | <b>111</b> |
| 4.1       | Introduction . . . . .  | 112        |
| 4.2       | Experimental Details . . . . .  | 113        |
| 4.2.1     | Cyclic Voltammetry . . . . .  | 113        |
| 4.2.2     | Organic Solar Cells . . . . .   | 114        |
| 4.3       | Results and discussion . . . . .  | 114        |
| 4.4       | Conclusions . . . . .   | 119        |
|           | References . . . . .  | 121        |
| <b>5</b>  | <b>Naphthalene diimide-based small molecule acceptors</b>                   | <b>123</b> |
| 5.1       | Context . . . . .   | 124        |
| 5.2       | Article . . . . .   | 126        |
| 5.3       | Updates and Conclusions . . . . .   | 138        |
|           | References . . . . .  | 141        |
| <b>6</b>  | <b>Photovoltaic performance of thionated NDI-based acceptors</b>            | <b>143</b> |
| 6.1       | Introduction and Context . . . . .  | 144        |
| 6.2       | Experimental Details . . . . .  | 146        |
| 6.2.1     | Materials . . . . .   | 146        |
| 6.2.2     | Solar Cell Fabrication . . . . .  | 146        |
| 6.2.3     | Optoelectronic Properties Measurements . . . . .                            | 147        |
| 6.2.4     | Photoluminescence Quenching . . . . .                                       | 147        |
| 6.2.5     | Space-charge limited current devices . . . . .                              | 147        |
| 6.3       | Results and Discussion . . . . .  | 147        |
| 6.3.1     | Thionated NDI-based Small Molecule Acceptors . . . . .                      | 147        |
| 6.3.2     | Effect of Thionation on PNDIT2 . . . . .                                    | 150        |
| 6.4       | Conclusions . . . . .   | 160        |
|           | References . . . . .  | 163        |

---

|          |   |            |
|----------|---|------------|
| <b>7</b> | <b>NEXAFS calculations of thionated naphthalene diimide</b> | <b>167</b> |
| 7.1      | Introduction and Context . . . . .                          | 168        |
| 7.2      | Article . . . . .   | 170        |
| 7.3      | Conclusions . . . . .                                       | 180        |
|          | References . . . . .  | 181        |
| <b>8</b> | <b>Conclusions and outlook</b>                              | <b>183</b> |
| 8.1      | Conclusions . . . . .                                       | 183        |
| 8.2      | Outlook . . . . .   | 185        |
|          | References . . . . .  | 189        |
|          | <b>Appendix A Supplementary material for Chapter 4</b>      | <b>191</b> |
|          | <b>Appendix B Supplementary material for Chapter 5</b>      | <b>195</b> |
|          | <b>Appendix C Supplementary material for Chapter 6</b>      | <b>217</b> |
|          | <b>Appendix D Supplementary material for Chapter 7</b>      | <b>223</b> |



# Abbreviations

|                  |   |
|------------------|---|
| AFM              | Atomic Force Microscopy   |
| BT               | Benzothiadiazole  |
| CB               | Chlorobenzene   |
| CS <sub>2</sub>  | Carbon Disulfide  |
| CT               | Charge Transfer   |
| CV               | Cyclic Voltammetry  |
| DFT              | Density Functional Theory   |
| DIO              | 1,8-diiodooctane  |
| DPP              | Diketopyrrolopyrrole  |
| EQE              | External Quantum Efficiency   |
| FF               | Fill Factor   |
| GIWAXS           | Grazing Incidence Wide Angle X-ray Scattering   |
| GW               | Gigawatt  |
| Hz               | Hertz   |
| ITIC             | 3,9-bis(2-methylene-(3-(1,1-dicyanomethylene)-indanone))-5,5,11,11-tetrakis(4-hexylphenyl)-dithieno[2,3-d:2',3'-d']-s-indaceno[1,2-b:5,6-b']dithiophene |
| ITO              | Indium Tin Oxide  |
| J <sub>SC</sub>  | Short-Circuit Current Density   |
| MoO <sub>x</sub> | Molybdenum Oxide  |
| NDI              | Naphthalene Diimide   |
| NEXAFS           | Near-Edge X-ray Absorption Fine Structure   |
| nm               | Nanometer   |
| NREL             | National Renewable Energy Laboratory  |

|            |  |
|------------|--|
| OPV        | Organic Photovoltaics  |
| OSC        | Organic Semiconductor  |
| P3HT       | Poly(3-hexylthiophene-2,5-diyl)  |
| PBDTTT-EFT | Poly[4,8-bis(5-(2-ethylhexyl)thiophen-2-yl)benzo[1,2-b;4,5-b']<br>dithiophene-2,6-diyl-alt-(4-(2-ethylhexyl)-3-fluorothieno[3,4-b]thi-<br>ophene-)-2-carboxylate-2-6-diyl] |
| PBE        | Perdew-Burke-Ernzerhof   |
| PCBM       | Phenyl-C <sub>61</sub> -butyric acid methyl ester  |
| PCE        | Power Conversion Efficiency  |
| PDPE       | Polytetrafluoroethylene  |
| PDI        | Perylene Diimide   |
| PEIE       | Polyethylenimine Ethoxylated   |
| PESA       | Photoelectron Spectroscopy in Air  |
| PV         | Photovoltaics  |
| RE         | Renewable Energy   |
| RSOXS      | Resonant Soft X-ray Scattering   |
| SAXS       | Small-Angle X-ray Scattering   |
| SCLC       | Space-Charge Limited Current   |
| STC        | Standard Testing Conditions  |
| SVA        | Solvent Vapor Annealing  |
| TCO        | Transparent Conductive Oxide   |
| THF        | Tetrahydrofuran  |
| TP         | Transition Potential   |
| TT         | Thieno[3,2-b]thiophene   |
| $V_{OC}$   | Open-Circuit Voltage   |
| XAS        | X-ray Absorption Spectroscopy  |
| XRD        | X-ray Diffraction  |
| ZnO        | Zinc Oxide   |

# Chapter 1

## Introduction

*I'd put my money on the sun and solar energy. What a source of power! I hope we don't have to wait till oil and coal run out before we tackle that.*

— Thomas Edison, March 1931

*It's electrifying!*

— John Travolta as Danny Zuko in *Grease*, 1978

### 1.1 Motivation for the need for renewable energy

The widespread accessibility to energy, made possible by the Industrial Revolution of the mid-1700s, has shaped Western culture and made possible significant advances in human history. An inexpensive supply of energy is responsible for promoting millions of people out of poverty, adding years to average life expectancy, and granting ubiquitous access to education, sanitation, transportation and many more common, modern commodities. However, in his book about the Industrial Revolution, Robert Allen refers to the Revolution as “the two faces of Dr. Jekyll and Mr. Hyde,”<sup>1</sup> in that the outcomes of the Industrial Revolution are not solely positive. From the mid-1800s, the main source of energy powering Western society has been coal, and other fossil fuels, which are still predominantly burned to produce electricity today - ~80% of the total energy supplied in the United States, see Figure 1.1.<sup>2</sup> Fossil fuels can be defined as fuel formed by natural processes, such as anaerobic decomposition of buried dead organisms, containing energy originating in ancient photosynthesis<sup>3</sup> and there are several disadvantages to burning them for energy, including their finite availability,<sup>4</sup> role in creating political instability<sup>5</sup> and, perhaps most importantly of all, the air pollution and resulting health problems and global climate change caused by releasing large quantities of carbon dioxide into the Earth's atmosphere.<sup>6</sup>

The burning of fossil fuels induces a combustion reaction that causes carbon dioxide,  $\text{CO}_2$ , to be released into the Earth's atmosphere, where approximately 60% is permanently trapped.<sup>7,8</sup> Today,  $\text{CO}_2$  levels average just over 400 ppm globally, which is a 25% increase over 1958 levels, when atmospheric carbon levels began being recorded, and the highest it has been over the last 400,000 years, the furthest that is able to be traced by carbon tracking in glacial ice caps.<sup>8</sup> The dramatic rise



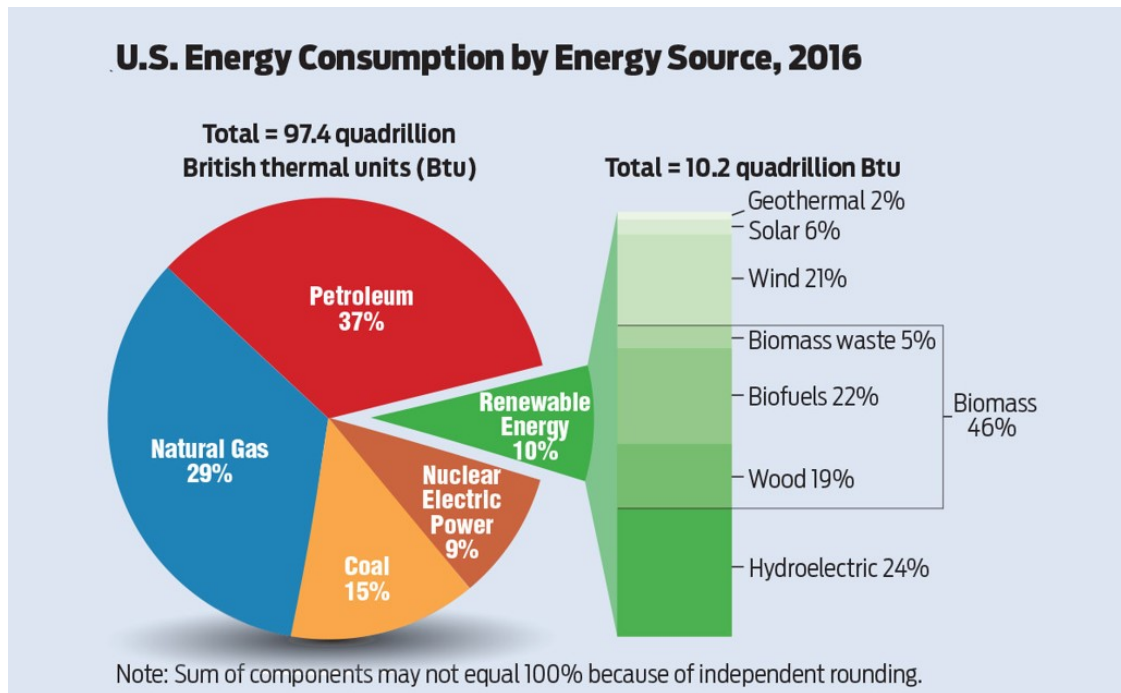


Figure 1.1: Total energy consumption in the United States by energy source in 2016.<sup>2</sup>

in atmospheric carbon levels has been directly correlated to the onset of wide-spread fossil fuel burning beginning around 1850, coinciding with the Industrial Revolution.<sup>9</sup> Such high atmospheric carbon levels have already begun to have wide-spread detrimental consequences,<sup>10</sup> primarily because carbon absorbs heat that would otherwise irradiate away from Earth's surface and into space.<sup>11</sup> This process essentially traps heat close to the earth's surface, resulting in higher temperatures than in the absence of CO<sub>2</sub>.<sup>12</sup> Already, rising global temperatures have been linked to accelerated glacial melting,<sup>13,14</sup> and the resulting rise in sea levels<sup>15</sup> threaten to displace inhabitants of low-lying coastal areas.<sup>16</sup>

At the current rate of fossil fuel consumption, it is predicted that global temperatures will increase by 3-6 °C by the end of the 21<sup>st</sup> century, resulting in a 0.2 - 0.6 m rise in sea levels.<sup>16</sup> This poses a major risk of flooding to low-lying communities world-wide. Apart from rising sea levels, such a dramatic increase in global temperatures would have damaging effects on a majority of the Earth's ecosystems. Coral reefs, which have an estimated global value of 29.8 billion USD,<sup>17</sup> are especially vulnerable to warming ocean waters. An increase of just 1-3 °C is predicted to cause widespread mortality of these fragile organisms.<sup>18</sup> However, aquatic habitats are not the only threatened ecosystems in the world. In fact, roughly 20-30% of global species are threatened with extinction due to rising temperatures.<sup>16</sup> Climate change is also predicted to change global weather patterns, causing desertification in the Americas and Sub-Saharan Africa, which threatens to displace millions of people as a result of decreasing arable land.<sup>16,19</sup> These are just some examples of negative impacts that the unabated use of fossil fuels for energy will have on the planet, causing widespread concern for their continued use.

Despite the negative byproducts of relying so heavily on fossil fuels, the inexpensive consumption of electricity is a commodity that is becoming increasingly impossible to reduce. Around the world, millions of people are still rising out of poverty,<sup>20</sup>

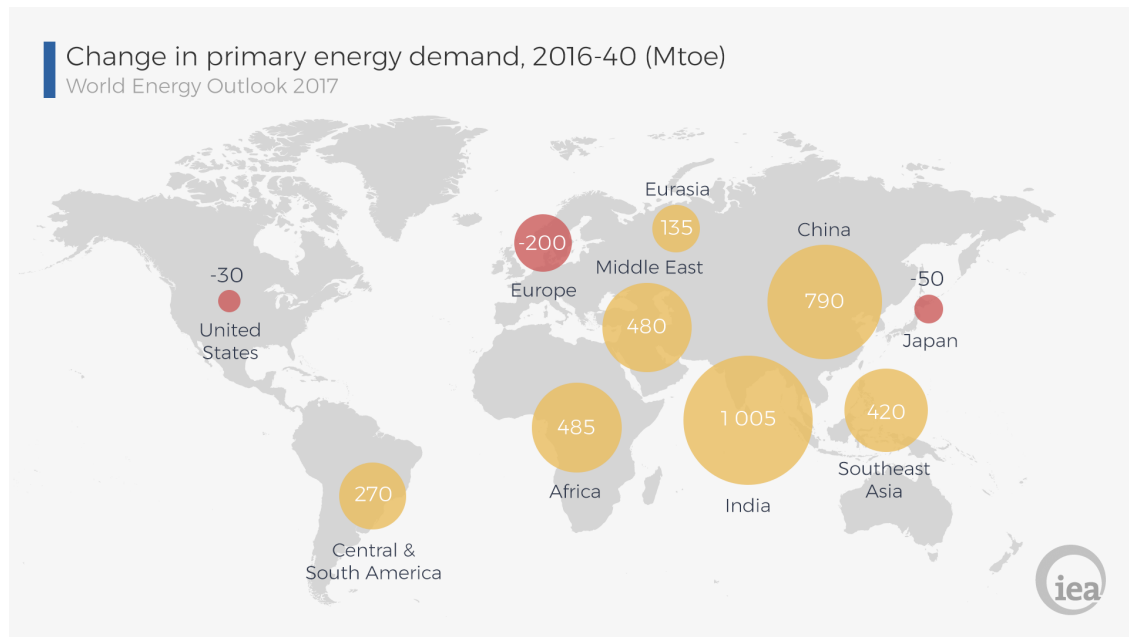


Figure 1.2: Projected changes in the world's energy demands from 2016 - 2040 in million tons of oil equivalent (Mtoe).<sup>2</sup>

meaning more people than ever before are gaining access to energy in their daily lives. As well, the United Nations predicts that the total global population will reach 9.7 billion people by 2050, compared to a population of 7.6 billion people in 2018, meaning the rising demand for access to inexpensive electricity shows no signs of slowing down, and is, in fact, expected to increase by 30% over the next twenty years.<sup>2,21</sup> However, the global centers for energy consumption are changing. Figure 1.2 is reproduced from the 2017 World Energy Outlook Report produced by the International Energy Agency (IEA) and illustrates the shifts in global energy demand from 2016 to 2040.<sup>2</sup> This figure clearly highlights that current large electricity consuming nations, mainly the United States and those in Europe, will actually decrease their energy demand over the next 20 years as populations are predicted to decline, especially in Europe.<sup>21</sup> The largest growth in energy demand is predicted to be in Africa, India and China with increases of 485, 1,005, and 790 million tons of oil equivalent, respectively, compared to 2016 levels. This dramatic increase in energy consumption would be disastrous from an environmental perspective, if fossil fuels remain the dominant energy source in the world's energy mix. However, as was mentioned previously, the emerging centers for energy consumption are primarily located in geographic areas where widespread electricity networks are not commonplace, opening the possibility to utilize environmentally friendly alternatives for a major portion of these necessary energy capacity additions.

The U.S. Energy Information Administration estimates that roughly 5% of the electricity generated in the United States is lost in transmission from where the electricity is initially generated to where it is consumed.<sup>22</sup> Modern technologies have higher energy efficiency and the ability to be located in closer proximity to consumption centers, reducing the overall electricity that must be generated to meet demands. Because a majority of rising electricity consumers are located in areas that are not well equipped to cater for these demands today, new infrastructure will have to be built, which will

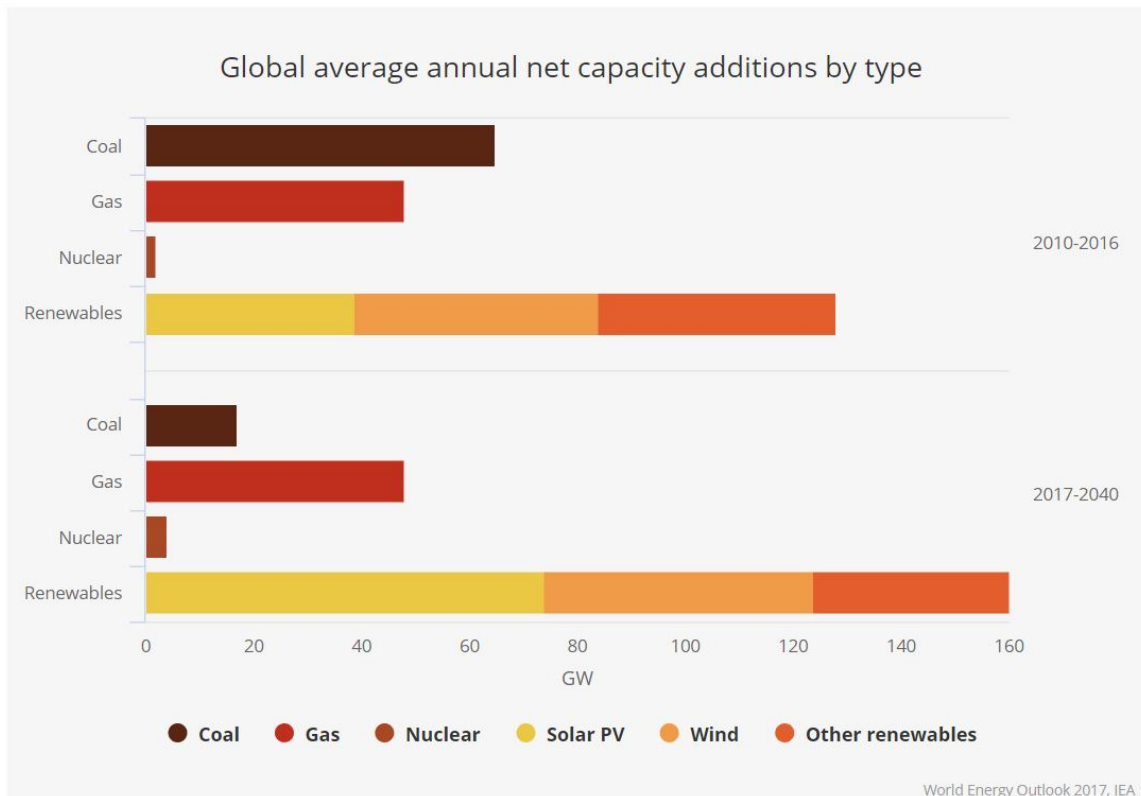


Figure 1.3: Projected global energy capacity additions from 2010-2014 and 2017-2040.<sup>2</sup>

take advantage of modern advances. Additionally, there is already an observed shift away from fossil fuel-based energy production in current energy consumption centers. The migration towards more environmentally responsible forms of energy are reflected in the IEA predictions shown in Figure 1.3, which compares global average annual net energy capacity additions by type from 2010-2016 to projections for 2017-2040. The projections show a strong shift away from coal, with added capacities shrinking considerably in the future. Additionally, they predict a significant increase in added capacity for renewable energy (RE) sources.<sup>2</sup>

The Australian Renewable Energy Agency, ARENA, defines renewable energy as energy that “is produced using natural resources that are constantly replaced and never run out.”<sup>23</sup> This is exactly the type of energy required to minimize fossil fuel usage while enabling the continued rise of global living standards. Figure 1.1 shows that, overall, renewable energy accounted for 10% of the energy consumed in the United States in 2016. There are several different types of RE sources, including hydroelectric, biomass, wind, and solar, which can be subdivided into three categories: solar thermal, solar fuels and photovoltaics. Solar thermal is the utilization of solar energy in the form of heat, where concentrated energy from the sun is used to produce steam to drive a turbine, similarly to how fossil fuels are burned for the same purpose.<sup>24</sup> Solar fuels refer to chemical fuels that are produced directly from solar or thermal energy through photochemical or thermochemical processes.<sup>25</sup> Photovoltaics, on the other hand, enable the direct conversion of solar radiation into electricity. Global trends indicate that energy consumption is electrifying, with increases in electric cooling and heating, vehicles and digitalization being the driving force behind this gradual transition.<sup>2</sup> The direct production of electricity from solar sources makes photovoltaics

particularly attractive for future energy creation, and reference to solar energy in this thesis will pertain to photovoltaics from this point forward. Additionally, solar radiation is an extremely abundant resource, with, famously, “the sunlight striking the earth’s surface in just one hour deliver[ing] enough energy to power the world economy for one year.”<sup>26</sup> The threat of environmental devastation by maintaining the status quo of burning fossil fuels for energy, coupled with an abundant, alternative resource that can be used instead, is a major driving force for the recent progress and implementation of solar energy world-wide.

Referring back to Figure 1.1, solar energy contributed 6% to the total RE consumed, or 0.6% to the overall energy consumption in the United States in 2016. Comparatively, in Europe solar energy comprised 4% of the total energy consumption of 2016.<sup>27</sup> However, although RE sources contribute only slightly to the energy produced in these regions today, there is a noticeable shift towards cleaner energy production beginning to take place world-wide. The Global Trends in Renewable Energy Investment report for 2018, published by the Frankfurt School – UNEP Collaborating Centre for Climate & Sustainable Energy Finance, indicates that, globally, more solar energy was added than any other form of energy technology in 2017: 157 gigawatts (GW) of solar compared to 70 GW of fossil fuel-derived energy additions.<sup>28</sup> In the United States, solar and wind comprised 100% of the large-capacity additions to the electricity grid in January of 2018.<sup>29</sup> However, most notable is the massive shift towards solar energy by China in recent years. Since 2013, China has been the world’s largest installer of solar energy capacity, with an impressive 130 GW of installed solar by the end of 2017 - a 400% increase over the previous year.<sup>30</sup> These trends are in agreement with, and even outperform, the IEA projections discussed earlier (Figure 1.3), highlighting the important role solar energy will play in future energy generation. The following section details the current status of solar energy, including an introduction to present and emerging technologies.

## 1.2 Introduction to photovoltaics

As was mentioned previously, photovoltaics (PV) utilize light to produce energy. More specifically, the word photovoltaic can be broken into two parts: “photo,” meaning light and “voltaic” being derived from the creation of electrical current, as in a battery. Distinctly, a photovoltaic device has the additional ability to sustain a voltage, setting it apart from other light-sensitive devices such as photoelectric cells, which are only capable of sustaining a current. Very generally, a photovoltaic device directly converts solar radiation into usable energy in the form of electricity. This behavior, known as the “photovoltaic effect,” was first reported by Edmund Becquerel in 1839, when he measured a photo-induced voltage between two electrodes after they were submerged in an electrolyte.<sup>31</sup>

Fundamentally, photovoltaic cells must be comprised of a light-absorbing component (a semiconductor to separate charges in energy to produce a photovoltage) and electrodes (metals to extract generated charges to produce a current). While several different types of semiconductor can be used as the light-absorber, there are some ubiquitous characteristics that a semiconductor must exhibit for efficient photovoltaic behavior. First, the absorber should strongly absorb light produced by the sun, which primarily encompasses wavelengths in the visible range between 400 – 650 nm or en-

ergies from 3.1 – 1.9 eV.<sup>32</sup> This means semiconductors with a band gap over 1 eV are appropriate, because they will absorb a large proportion of the visible spectrum, resulting in high densities of free charge carriers. The second requirement for efficient solar cell operation is a large charge carrier diffusion length, which is the average distance a charge carrier moves during its lifetime, encompassing both the lifetime of an excited state as well as the carrier’s mobility through the semiconductor. When a semiconductor absorbs a photon of light, an electron in the valence band is promoted to the conduction band, leaving a positively charged “hole,” in its place. Negatively charged electrons and positively charged holes must be quickly extracted from the solar cell before the electron is able to relax back to the valence band, annihilating the two free carriers. Therefore, charges must have high mobility and a long enough lifetime to reach the electrodes before relaxing to an unexcited state. Finally, a solar cell should have “electronic asymmetry” to induce the migration of holes in one direction, opposite to the direction of electron migration.<sup>33</sup> There are several design strategies that can be implemented to achieve this asymmetry, depending on the semiconductor used as the absorber. For example, in silicon-based solar cells this is achieved via a p-n junction between doped p-type and n-type silicon, while in organic solar cells it is realized by utilizing electrodes of different work functions which create a built-in field in the device, discussed in more detail in Section 2.3.1.

When comparing solar technologies, there are three parameters that are typically used to determine commercialization potential: lifetime, efficiency and cost. The US Department of Energy defines solar cell efficiency as “the percentage of solar energy shining on a PV device that is converted into usable electricity.”<sup>34</sup> Exactly how this is determined is discussed in further detail in Section 2.3.1. The National Renewable Energy Laboratory (NREL) produces an annual chart that shows the efficiency progress for photovoltaics made from different semiconducting materials (see Figure 1.4).<sup>35</sup> The chart shows the evolution in efficiency for over 20 different types of solar cells, divided into five classes: multi-junction, single-junction, crystalline silicon, thin-film and emerging technologies. Within the crystalline silicon category is non-concentrated single-crystal silicon – the most well-studied and dominant commercial PV technology today. Crystalline silicon PV is responsible for the rising solar energy capacity in recent years, discussed in the previous section, making up 93% of the global solar installed capacity,<sup>36</sup> primarily due to the significant reduction in cost for crystalline silicon solar wafers and the improved efficiency of manufactured cells. In fact, in 2017, the average cost (\$/kWh) of electricity generated from PV sources in the US was \$0.10/kWh, compared to \$0.07/kWh for fossil fuel-based sources - a 350% reduction compared to PV-derived electricity prices in 2010, making solar energy a financially competitive form of energy production.<sup>37</sup>

While these are some distinct advantages silicon-based solar cells have over other photovoltaics, the technology is not without its drawbacks. Silicon is a very brittle material, meaning a silicon solar cell requires protective housing that adds significant costs and weight to the device. A recent study<sup>38</sup> found that the module cost of crystalline silicon solar cells could be broken down as follows: 48% silicon wafer, 16% cell and 36% module, which includes components such as the glass and frame that protect the delicate wafer. This means the brittle nature of silicon is responsible for adding over 30% to the final solar cell cost. Additionally, silicon has a very low absorption coefficient, requiring a relatively thick, opaque absorbing layer of hundreds of microns to absorb low-energy wavelengths, adding to the final cost of the module, and limiting

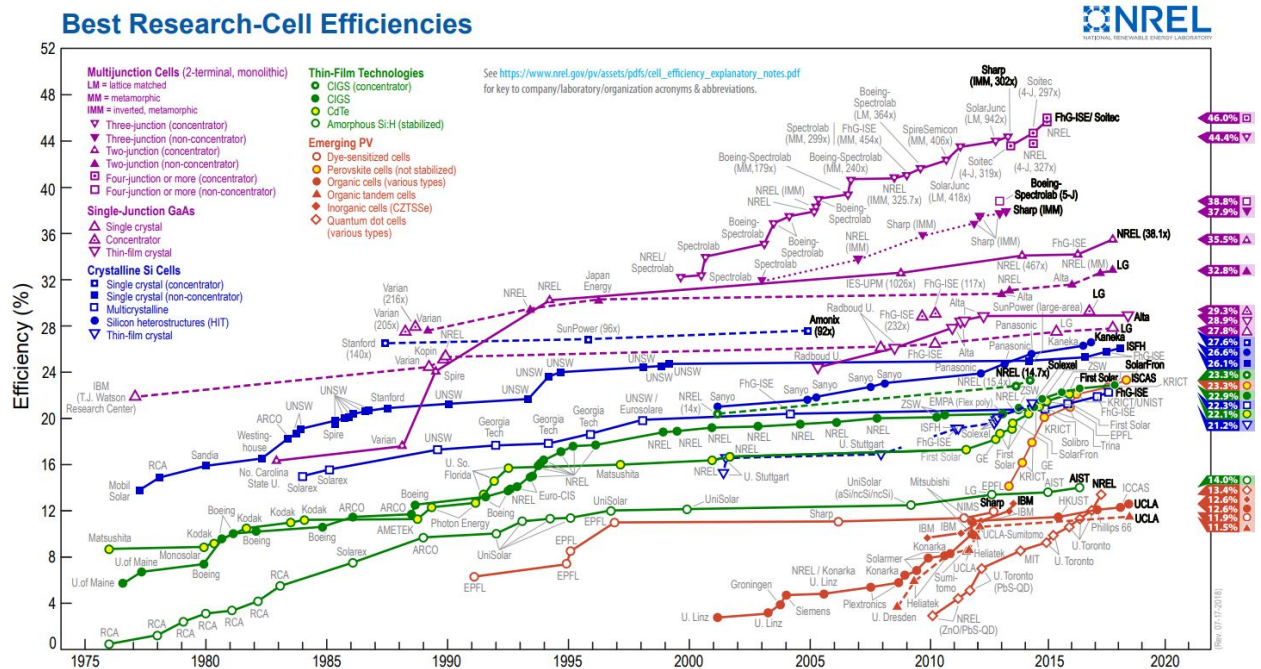


Figure 1.4: Highest confirmed solar cell efficiencies by materials class. Organic solar cells are included under Emerging Photovoltaics.<sup>35</sup>

applications of silicon-based solar cells.<sup>39</sup> Apart from increasing the production cost, the rigidity and weight of a silicon solar module also limit its potential deployment. These cells are primarily installed either on the ground or on a rooftop where the cells perform best when tilted towards the sun, often requiring neighboring modules to be spaced apart, taking up additional space. Finally, the energy pay-back time, or time required for the solar cell to produce as much energy as was required in its manufacture, of silicon solar cells is quite long - 1.5 to 2 years depending on their location.<sup>40</sup> These shortcomings limit the deployment of silicon-based solar cells in niche applications. In order to further increase PV contributions to the international energy mix, technologies that offer mechanically and optically unique properties must be developed. If the semiconducting component of the solar cell were flexible, for example, PV modules could be printed using printing techniques such as roll-to-roll processing, significantly lowering the cost and time required to make the module. If the semiconductor were partially transparent, the solar cell could be retrofitted into windows in high-rise office buildings, generating electricity directly where it is needed most: city centers. Solar cells that are comprised of semiconductors with different colors could be utilized as modern art pieces in urban parks and streets, serving to power street lamps and promote public awareness for the importance of renewable energy. While crystalline silicon photovoltaics will continue to dominate the solar energy market, it is clear that their shortcomings must be made up for by alternative types of solar cells.

Referring back to the NREL efficiency chart, there is a PV technology listed under “emerging technologies” termed organic solar cells. Although the efficiency of organic solar cells has been steadily increasing over the past ten years, it is still well below that of commercial silicon PV modules (15.7% compared to 26.1%). However, organic solar cells have the advantage of being composed of light-weight, flexible and semi-transparent materials, meaning they could be deployed in niche applications similar to



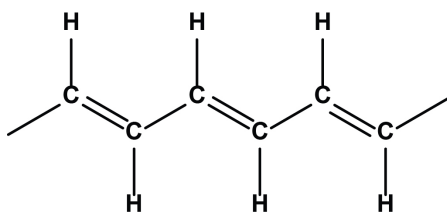


Figure 1.5: Chemical structure of polyacetylene.

those suggested above.<sup>41–43</sup> They have the potential to be incorporated into existing infrastructure, such as coating external windows in large-scale office and high-density living buildings, bringing energy production directly to the consumer, instead of from solar farms or coal-fired plants located up to hundreds of kilometers away. Also, because they are solution-processable, organic solar cells can be printed quickly and using very little energy, compared to the high-temperature extraction of single crystal silicon ingots. This has led to some estimates indicating an energy-payback time of as little as a single day for organic solar cells.<sup>44</sup> Though the potential applications of organic solar cells are vast, the technology suffers from lower stability and efficiency over conventional solar cells, and further improvements must be made in order for large-scale deployment of organic photovoltaics to be possible, which will be addressed further in the following chapters.

### 1.3 Introduction to organic photovoltaics

The term organic refers, generally, to carbon-based materials, however, because there are millions of compounds known, of which upwards of 90% are organic, in this context the term organic will refer to conjugated aromatic hydrocarbons.<sup>45</sup> Unlike conventional semiconductors, like silicon, which exhibit semiconducting properties intrinsically, organic materials must be designed to follow certain rules in order for semiconducting behavior to be realized. The most important of these is the inclusion of conjugated segments consisting of alternating single and double carbon bonds. A detailed explanation of the electronic configuration that is created by such a conjugated structure is further discussed in Section 2.2.1, however, basically, the hybridization of  $s$  and  $p$  orbitals in carbon facilitates  $\pi$ -bonding between adjacent carbon atoms, with alternating single and double bonds giving rise to electron delocalization over segments of molecules or polymers with regions of extended conjugation. This allows free carriers to move from atom to atom in the molecule, giving rise to charge transport behavior.

Although there were numerous demonstrations of electronically active organic materials in the 1950s and 1960s,<sup>46,47</sup> polyacetylene ( $\text{CH}_x$ ) is a simple organic conjugated molecule that revolutionized the field of organic electronics with its demonstration of high electrical conductivity in 1977. Its molecular structure is shown in Figure 1.5.<sup>48</sup> Polyacetylene consists of weakly coupled chains of CH units which form a one-dimensional lattice.  $\sigma$ -bonds between carbon atoms are responsible for a backbone that can exhibit either a helical or planar configuration,<sup>49</sup> while the remaining valence electron has the symmetry of a  $2p_z$  orbital, with its charge density oriented perpendicular to the backbone formed by the hybrid orbitals. The overlap of  $p_z$  orbitals between adjacent carbon atoms facilitates electron delocalization and the formation of  $\pi$ -bonding and  $\pi$ -anti-bonding orbitals, discussed in more detail in Section 2.2.1. The

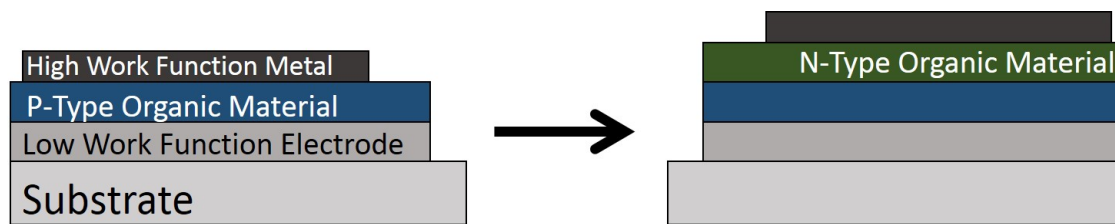


Figure 1.6: Schematic of an organic solar cell with a single layer of organic material (left) and a bilayer heterojunction (right).

discovery of high electrical conductivity in polyacetylene doped with iodine vapor<sup>50</sup> was followed by a rigorous effort to synthesize organic molecules that could be used in various electronic applications such as field effect transistors,<sup>51</sup> light emitting diodes,<sup>52</sup> and photovoltaics.<sup>53</sup> In fact, the discovery of high conductivity in polyacetylene proved to be so significant, that the 2000 Nobel Prize in Chemistry was awarded to Alan J. Heeger, Alan G. MacDiarmid, and Hideki Shirakawa for their contributions to the discovery in the 1970s.<sup>54</sup>

Early efforts to engineer organic photovoltaics (OPV) involved sandwiching a p-type organic semiconductor between low and high work function electrodes, with the low work function electrode typically consisting of a thin, vacuum evaporated aluminum layer that allowed significant portions of the solar spectrum to be transmitted to the light-absorbing organic center.<sup>55</sup> The substrate onto which this sandwich was deposited could be composed of a range of different materials that did not seem to affect the performance of the solar cell, including Pyrex, Mylar and polyester.<sup>53</sup> Largely motivating this research effort was the ability to build photovoltaic devices onto inexpensive and flexible substrates such as Mylar, coupled with the possibility to coat large areas due to the solubility of organic molecules in common solvents. However, although OPV showed great potential to drastically reduce the cost of solar energy, they exhibited significantly lower power conversion efficiencies (PCEs) in the late 1970s, with a maximum of  $\sim 1\%$  compared to  $\sim 17\%$  exhibited by their silicon-based counterparts, at the time.<sup>55,56</sup>

A new era of research in organic solar cells began in 1986, with the introduction of a second, n-type organic material into the sandwich structure (Figure 1.6).<sup>57</sup> This cell, termed the Tang cell after its developer, is responsible for the approach still used today when researching novel OPV materials and device structures. Tang found that the inclusion of a second organic layer, now referred to as a bilayer heterojunction, was responsible for photogenerating charge carriers, where previously the device performance had primarily been determined by the nature of the electrode interfaces. A dramatic increase in fill factor (FF) was observed in the bilayer device, because the generation efficiency of charges was only weakly dependent on the bias field. Additionally, the open-circuit voltage ( $V_{OC}$ ), which represents the maximum voltage output of the cell, was previously limited by the electrode-organic interface, whereas in the new device it was almost exclusively determined by the organic-organic interface, opening the possibility to tune the selection of the organic materials in order to maximize this value. Essentially, the introduction of a second organic layer to the structure allowed for much more control over the intrinsic properties of the solar cell. Additionally, the electrodes sandwiching the two organic materials could be tuned to maximize



efficiency by choosing materials with appropriate work functions depending on whether they serve as the electron or hole extraction electrode. The discovery of the flexibility to choose materials which complement each other, either energetically or physically (but preferably both), has created a field of research that is nearly infinite in scope, as the number of possible organic semiconductors is limited only by the imagination of materials scientists and the practical synthetic ability of chemists, opening the door to modern organic photovoltaics research.

In the early 1990s, the improved performance demonstrated by the bilayer heterojunction was attributed to ultrafast photo-induced electron charge transfer from the p-type (donor) polymeric material, where incident photons are absorbed, to the n-type (acceptor) material. The low dielectric constant of organic semiconductors results in absorbed photons generating bound electron-hole pairs instead of free carriers. Without a driving force to separate these carriers, they quickly relax back to an unexcited state – useless for solar cell operation. However, if this bound electron-hole pair is able to come in contact with a material of different electron affinity than that of the material in which it was absorbed, the charges can be separated, both energetically and physically, leaving the carriers free to diffuse to their respective electrodes.<sup>58,59</sup> Although the Tang cell mentioned previously was comprised of two organic molecular materials, ultrafast photo-induced electron charge transfer was first demonstrated on thin films cast from a 1:1 by weight solution of the polymer poly(2-methoxy-5-(2'-ethyl-hexyloxy)-1,4-phenylene vinylene) (MEH-PPV) with C<sub>60</sub> buckminsterfullerene, which, at the time, was generating strong scientific interest due to its recent discovery and strong electron affinity, being able to accept up to 6 electrons at a time.<sup>60</sup> It was concluded that the charge transfer phenomena could allow the interface between MEH-PPV and C<sub>60</sub> to serve as a photovoltaic junction in an organic solar cell,<sup>59</sup> however its effect would be limited to photons absorbed very close to the interface between the two materials, due to the limited diffusion length of the bound electron-hole pairs mentioned previously (discussed in more detail in Section 2.3.1). In 1995, organic photovoltaic research was again revolutionized when a mixed solution of polymer and fullerene was used to make a single, blended layer, termed a bulk heterojunction.<sup>61</sup> In this new configuration, the photo-induced electron charge transfer was no longer limited to a single interface between layers of donor and acceptor material, and was instead possible throughout the entire bulk of the film, dramatically increasing the number of charge carriers that could be generated by the device, leading to an observed short circuit current that is two orders of magnitude above that of pure MEH-PPV devices. Whereas before, device efficiencies had not surpassed 1%,<sup>62,63</sup> the bulk heterojunction exhibited an efficiency of 2.9%,<sup>61</sup> catapulting the race to develop next-generation materials for even higher power conversion efficiencies.

Poly(3-hexylthiophene) (P3HT) is pictured in Figure 1.7 and is amongst the most highly cited materials in organic solar cell history. In fact, from 2002-2010, over 1000 articles were published featuring bulk heterojunctions made from P3HT and PCBM, a soluble C<sub>60</sub> derivative.<sup>64</sup> Although maximum device efficiencies for this combination averaged approximately 3%,<sup>65-67</sup> and devices with PCEs high enough to consider commercialization were never realized, the broad and systematic study of the P3HT:PCBM blend did shed light onto material and device processing parameters that could be used to greatly influence the performance of organic solar cells. For example, it was shown that the molecular weight of P3HT as well as ratio of P3HT to PCBM in the blend, and even the solvent used to deposit the materials, all play significant roles in the final

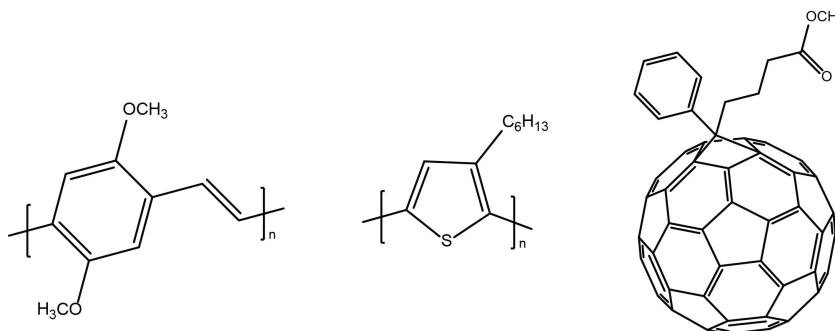


Figure 1.7: Molecular structures of MEH-PPV (left), P3HT (center) and PCBM (right).

performance of the device.<sup>64</sup> These considerations have led to the continued development of novel materials, with devices surpassing 10% PCE in 2014<sup>68</sup> and currently, the highest reported (but not yet certified) efficiency of nearly 16% being achieved by a blend of fullerene-free organic molecules.<sup>69</sup>

Although the progress made in power conversion efficiencies since the mid-1980s is very promising, organic solar cells still suffer from short device lifetimes as a result of their susceptibility to degradation, which is mainly due to two factors: photodegradation of the organic materials and extrinsic degradation that occurs at the electrode/organic interface in the presence of oxygen and water.<sup>70,71</sup> Improving the stability, in addition to attaining the commercialization threshold of 15% PCE, is paramount for realizing organic solar cells as a viable alternative source for future energy generation.

In recent years, there has been a shift away from fullerene acceptors, towards n-type polymers and small molecules, which has been driven by the electronic tunability and improved device stability of non-fullerene acceptors.<sup>72,73</sup> In 2015, when the work presented in this thesis began, these so-called non-fullerene acceptors comprised an emerging class of material that has become evermore wide-spread throughout the time that this research was conducted. In particular, one material that showed potential early on as both an acceptor material for organic solar cells as well as an electron transporting material in high-mobility organic field-effect transistors was a polymer that has been referred to by several names including N2200, PNDIT2, and P(NDI2OD-T2).<sup>74–77</sup> This polymer incorporated a naphthalene diimide moiety (described in more detail in the next section) with a bithiophene linker between mer units, and while it exhibited amongst the highest performance for non-fullerene acceptors, naphthalene diimide-based small molecule acceptors lagged behind.<sup>78–80</sup> However, the well-defined structure of small molecules compared to their polymeric counterparts facilitates their synthesis and purification, and can improve their chemical stability and charge carrier mobility,<sup>81</sup> which motivated the search for high-performing NDI-based small molecule acceptors, explored in more detail in this thesis.

## 1.4 Overview of the thesis

Within the rylene family of organic materials, naphthalene diimide (NDI), Figure 1.8, is the smallest but a versatile aromatic compound that displays tremendous chemical, thermal and photochemical stability.<sup>82–84</sup> As polymeric acceptors, NDI-based mate-

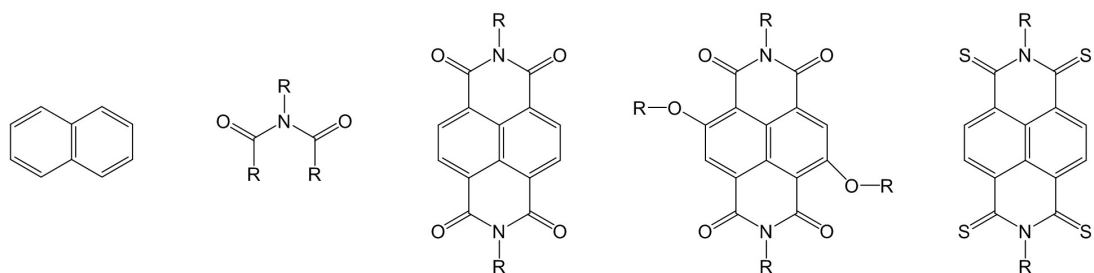


Figure 1.8: Molecular structure of, in order from left to right, naphthalene, imide, naphthalene diimide, core-substituted naphthalene diimide, and fully thionated naphthalene diimide.

rials have shown amongst the highest conversion efficiencies in so-called all-polymer solar cells at nearly 11% PCE,<sup>85</sup> however the performance of solar cells utilizing NDI-based small molecule acceptors has lagged far behind, although recently an efficiency of 7.65% has been reported.<sup>86</sup> This thesis explores the relationship between substituent or substitutional atoms introduced to NDI-based acceptor materials, with an emphasis on molecular acceptors, for fullerene-free organic solar cells. There are two themes in the presented work: the basic quantum chemical properties of NDI acceptors as well as device applications of novel NDI molecules with core substitutions and thionation. The first two results chapters (Chapters 4 and 5) explore the effect of core-substituent oxygen, nitrogen and sulfur atoms, on the optoelectronic and photovoltaic properties of NDI, while the final two results chapters (Chapters 6 and 7) are centered around thionation of the NDI unit.

As an overview: Chapter 2 provides a detailed review of existing literature on organic solar cells, including their working principles, theory and gaps in present knowledge. Experimental details, including theory, are provided in Chapter 3. The first two results chapters (Chapters 4 and 5) demonstrate the drastic change in material properties when either oxygen, sulfur or nitrogen is introduced at lateral positions of the core NDI molecule. Chapter 4 focuses on investigations into this substitution on the NDI molecule itself, with either oxygen, sulfur or nitrogen incorporated into an additional side-chain attached to the NDI core. When compared to the parent, or substituent-free molecule, the substituent atom changes both the physical and electronic properties of the NDI molecule, with nitrogen dramatically reducing and sulfur and oxygen improving the solar cell performance over the parent molecule. Molecules with substituent atoms are also shown to have a reduction in thin-film crystallinity, due to additional side-chains, which disrupt molecular packing, but also the substituent itself changing the packing morphology for the molecule. Although useful in determining the impact of substituent atoms on the behavior of NDI, the molecule itself is not ideal for solar cell operation: it has a high tendency to aggregate, producing acceptor-rich domains that are too large for efficient exciton dissociation to create free charge carriers. Chapter 5 builds on the fundamental knowledge attained in Chapter 4, but changes the molecular geometry of the NDI-based molecules in an attempt to improve device efficiency by disrupting molecular aggregation. Two geometries are proposed: a star-shaped molecule with a triarylamine core and a linear molecule comprised of two NDI moieties linked by a bithiophene bridge. These molecules exhibit greatly improved performance compared to the materials introduced in Chapter 4, demonstrating that both the molecular geometry and substituent atoms can dramatically affect the per-

formance of the solar cell.

The last two results chapters focus on the effect of systematic substitution of oxygen for sulfur in the NDI core - termed thionation. It has been shown that thionating the NDI molecule improves the mobility of electrons in field-effect transistors<sup>87</sup> and the purpose of these two chapters is to determine if thionation can be an effective strategy to boost solar cell performance. Chapter 6 focuses on practical investigations, with solar cell performance measured for a series of devices made from systematically thionated NDI-based polymers and small molecules. In all-polymer solar cells, thionation did not lead to improved photovoltaic performance, however the small molecule acceptors did exhibit improved performance with some degrees of thionation. Systematic changes with thionation, such as reduction in  $V_{OC}$ , were found for both polymeric and small molecule acceptors. Chapter 7 focuses on near-edge X-ray absorption fine structure (NEXAFS) spectroscopy calculations for the systematically thionated NDI molecules investigated in Chapter 6 in order to explain changes observed in the NEXAFS spectra for these molecules, such as a systematic reduction in the absorption on-set energy with increasing thionation.



# References

- [1] R. C. Allen, *The Industrial Revolution: A Very Short Introduction*, vol. 1. Oxford University Press, 2017.
- [2] IEA, “World Energy Outlook 2017,” <https://www.iea.org/weo2017/>.
- [3] M. Sato, “Thermochemistry of the formation of fossil fuels,” *Special Publication - The Geochemical Society*, vol. 2, pp. 271–283, 1990.
- [4] J. J. MacKenzie, “Oil as a finite resource,” *Nonrenewable Resources*, vol. 7, no. 2, pp. 97–100, 1998.
- [5] P. H. Gleick, “Environment and security: The clear connections,” *Bulletin of the Atomic Scientists*, vol. 47, no. 16, 1991.
- [6] A. Sommer, “Burning fossil fuels,” *International Journal of Health Services*, vol. 46, no. 1, pp. 48–52, 2016.
- [7] I. W. Smith, “The combustion rates of coal chars: A review,” *Symposium (International) on Combustion*, vol. 19, no. 1, pp. 1045–1065, 1982.
- [8] NOAA, “Trends in Atmospheric Carbon Dioxide,” <https://www.esrl.noaa.gov/gmd/ccgg/trends/>, 2018.
- [9] D. M. Etheridge, L. P. Steele, R. L. Langenfelds, and R. J. Francey, “Natural and anthropogenic changes in atmospheric carbon dioxide over the last 1000 years from air in Antarctic ice and firn,” *Journal of Geophysical Research*, vol. 101, no. 95, pp. 4115–4128, 1996.
- [10] T. R. Karl and K. E. Trenberth, “Modern global climate change,” *Science*, vol. 302, no. 5651, pp. 1719–23, 2003.
- [11] S. B. Idso, D. Johnson, A. Lacis, S. Lebedeff, P. Lee, D. Rind, and G. Russell, “The climatological significance of a doubling of earth’s atmospheric carbon dioxide concentration,” *Science*, vol. 207, no. 4438, pp. 1462–3, 1980.
- [12] G. S. Callendar, “Can carbon dioxide influence climate?,” *Weather*, vol. 4, no. 10, pp. 310–314, 1949.
- [13] J. H. Zwally, W. Abdalati, T. Herring, K. Larson, J. Saba, and K. Steffen, “Surface melt-induced acceleration of Greenland ice-sheet flow,” *Science*, vol. 297, no. 5579, pp. 218–222, 2002.

- [14] J. L. Chen, C. R. Wilson, and B. D. Tapley, “Satellite gravity measurements confirm accelerated melting of Greenland ice sheet,” *Science*, vol. 313, no. 5795, pp. 1958–60, 2006.
- [15] R. J. Nicholls and A. Cazenave, “Sea-level rise and its impact on coastal zones,” *Science*, vol. 328, no. 5985, pp. 1517–20, 2010.
- [16] M. L. Parry, O. F. Canziani, J. P. Palutikof, P. J. van der Linden, and C. E. Hanson, “Contribution of Working Group II to the Fourth Assessment Report of the Intergovernmental Panel on Climate Change,” tech. rep., Cambridge University Press, Cambridge, 2007.
- [17] H. Cesar, L. Burke, and L. Pet-Soede, *The Economics of Worldwide Coral Reef Degradation*. Zeist: Cesar Environmental Economics Consulting, 2003.
- [18] T. P. Hughes, A. H. Baird, D. R. Bellwood, M. Card, S. R. Connolly, C. Folke, R. Grosberg, O. Hoegh-Guldberg, J. B. C. Jackson, J. Kleypas, J. M. Lough, P. Marshall, M. Nystrom, S. R. Palumbi, J. M. Pandolfi, B. Rosen, and J. Roughgarden, “Climate change, human impacts, and the resilience of coral reefs,” *Science*, vol. 301, no. 5635, pp. 929–933, 2003.
- [19] S. E. Nicholson, “Climatic and environmental change in Africa during the last two centuries,” *Climate Research*, vol. 17, pp. 123–144, 2001.
- [20] S. Dhongde and C. Minoiu, “Global poverty estimates: a sensitivity analysis,” *World Development*, vol. 44, pp. 1–13, 2013.
- [21] “World Population Prospects: the 2017 Revision, Key Findings and Advanced Tables,” *United Nations, Department of Economic and Social Affairs, Population Division*, p. ESA/P/WP/248, 2017.
- [22] EIA, “How much electricity is lost in transmission and distribution in the United States?,” <https://www.eia.gov/tools/faqs/faq.php?id=105&t=3>, 2018.
- [23] ARENA, “What is renewable energy,” <https://arena.gov.au/about/what-is-renewable-energy/>, 2018.
- [24] W. W. S. Charters, T. L. Pryor, and Victorian Solar Energy Council., *Solar energy: theory and design of solar thermal systems*. Australian Syndicators for the Victorian Solar Energy Council, 1982.
- [25] D. Gust, T. A. Moore, and A. L. Moore, “Solar fuels via artificial photosynthesis,” *Accounts of Chemical Research*, vol. 42, no. 12, pp. 1890–1898, 2009.
- [26] L. R. L. R. Brown, J. E. Larsen, J. M. Roney, E. E. Adams, and Earth Policy Institute., *The great transition: shifting from fossil fuels to solar and wind energy*. New York: W.W. Norton & Company, 2015.
- [27] M. Schmela, T. Döring, A. P.-B. Gómez, and A. Roesch, “Solar Power in Europe: Status and Outlook,” in *A Comprehensive Guide to Solar Energy Systems*, pp. 37–52, Elsevier, 2018.

- [28] A. Louw, R. Boyle, D. Strahan, B. Collins, M. Kimmel, E. Giannakopoulou, and L. Becker, “Global Trends in Renewable Energy Investment 2018,” tech. rep., Frankfurt School - UNEP Collaborating Centre for Climate & Sustainable Energy Finance, Frankfurt, 2018.
- [29] “Energy Infrastructure Update,” tech. rep., Federal Energy Regulatory Commission, 2018.
- [30] “2017 National renewable power development monitoring and evaluation report,” tech. rep., National Energy Administration of China, 2018.
- [31] E. Becquerel, “Memoire sur les effets electriques produits sous l’influence des rayons solaires,” *Comptes rendus hebdomadaires des séances de l ’ Académie des sciences, Série B*, pp. 561–567, 1839.
- [32] R. Bird, R. Hulstrom, and L. Lewis, “Terrestrial solar spectral data sets,” *Solar Energy*, vol. 30, no. 6, pp. 563–573, 1983.
- [33] S. Applications and M. A. Green, “Solar cells - operating principles, technology and system applications,” *Solar Energy*, vol. 28, no. 5, p. 447, 1982.
- [34] DOE, “Solar Performance and Efficiency,” <https://www.energy.gov/eere/solar/articles/solar-performance-and-efficiency>, 2013.
- [35] NREL, “Research Cell Efficiency Records,” <https://www.energy.gov/eere/solar/downloads/research-cell-efficiency-records>, 2018.
- [36] K. Melkonyan, “PV Module Materials Report,” tech. rep., IHS Markit Technology, 2017.
- [37] IRENA, “Renewable Power Generation Costs in 2017,” <http://www.irena.org/publications/2018/Jan/Renewable-power-generation-costs-in-2017>, 2018.
- [38] A. Louwen, W. van Sark, R. Schropp, and A. Faaij, “A cost roadmap for silicon heterojunction solar cells,” *Solar Energy Materials and Solar Cells*, vol. 147, pp. 295–314, 2016.
- [39] K. Rajkanan, R. Singh, and J. Shewchun, “Absorption coefficient of silicon for solar cell calculations,” *Solid-State Electronics*, vol. 22, no. 9, pp. 793–795, 1979.
- [40] M. Mariska de Wild-Scholten, “Energy payback time and carbon footprint of commercial photovoltaic systems,” *Solar Energy Materials and Solar Cells*, vol. 119, pp. 296–305, 2013.
- [41] S. Günes, H. Neugebauer, and N. S. Sariciftci, “Conjugated polymer-based organic solar cells,” *Chemical Reviews*, vol. 107, no. 4, pp. 1324–1338, 2007.
- [42] B. C. Thompson and J. M. J. Fréchet, “Polymer-fullerene composite solar cells,” *Angewandte Chemie International Edition*, vol. 47, no. 1, pp. 58–77, 2008.
- [43] R. Søndergaard, M. Hösel, D. Angmo, T. T. Larsen-Olsen, and F. C. Krebs, “Roll-to-roll fabrication of polymer solar cells,” *Materials Today*, vol. 15, no. 1, pp. 36–49, 2012.



- [44] N. Espinosa, M. Hösel, D. Angmo, and F. C. Krebs, “Solar cells with one-day energy payback for the factories of the future,” *Energy & Environmental Science*, vol. 5, no. 1, pp. 5117–5132, 2012.
- [45] M. Pope and C. E. Swenberg, “Optical properties of organic molecules and crystals,” in *Electronic Processes in Organic Crystals and Polymers*, pp. 1–180, New York City: Oxford University Press, 2nd ed., 1999.
- [46] A. Bernanose, “Sur le mécanisme de l’électroluminescence organique,” *Journal de Chimie Physique*, vol. 52, pp. 396–400, 1955.
- [47] H. Kallmann and M. Pope, “Preparation of thin anthracene single crystals,” *Review of Scientific Instruments*, vol. 29, no. 11, pp. 993–994, 1958.
- [48] C. K. Chiang, C. R. Fincher, Y. W. Park, A. J. Heeger, H. Shirakawa, E. J. Louis, S. C. Gau, and A. G. MacDiarmid, “Electrical conductivity in doped polyacetylene,” *Physical Review Letters*, vol. 39, no. 17, pp. 1098–1101, 1977.
- [49] M. L. Elert and C. T. White, “Helical versus planar cis-polyacetylene,” *Physical Review B*, vol. 28, no. 12, pp. 7387–7389, 1983.
- [50] C. K. Chiang, Y. W. Park, A. J. Heeger, H. Shirakawa, E. J. Louis, and A. G. Macdiarmid, “Conducting polymers: Halogen doped polyacetylene,” *The Journal of Chemical Physics*, vol. 691, no. 10, pp. 5098–946, 1978.
- [51] H. Koezuka, A. Tsumura, and T. Ando, “Field-effect transistor with polythiophene thin film,” *Synthetic Metals*, vol. 18, no. 1-3, pp. 699–704, 1987.
- [52] C. W. Tang and S. A. Vanslyke, “Organic electroluminescent diodes,” *Applied Physics Letters*, vol. 51, no. 12, pp. 913–915, 1987.
- [53] G. A. Chamberlain, “Organic solar cells: A review,” *Solar Cells*, vol. 8, no. 1, pp. 47–83, 1983.
- [54] A. Heeger, A. G. MacDiarmid, and H. Shirakawa, “The Nobel Prize in chemistry, 2000: Conductive polymers,” *Stockholm, Sweden: Royal Swedish Academy of Sciences*, pp. 1–16, 2000.
- [55] C. W. Tang, “Multilayer organic photovoltaic elements,” *US Patent*, vol. 4164431, 1979.
- [56] E. S. Rittner and R. A. Arndt, “Comparison of silicon solar cell efficiency for space and terrestrial use,” *Journal of Applied Physics*, vol. 47, no. 7, pp. 2999–3002, 1976.
- [57] C. W. Tang, “Two-layer organic photovoltaic cell,” *Applied Physics Letters*, vol. 48, no. 2, p. 183, 1986.
- [58] N. S. Sariciftci, L. Smilowitz, A. J. Heeger, and F. Wudi, “Photoinduced electron transfer from a conducting polymer to buckminsterfullerene,” *Science*, vol. 258, no. 5087, pp. 1474–1476, 1992.

- [59] N. S. Sariciftci and A. J. Heeger, “Reversible, metastable, ultrafast photoinduced electron-transfer from semiconducting polymers to buckminsterfullerene and in the corresponding donor-acceptor bulk heterojunctions,” *International Journal of Modern Physics B*, vol. 8, pp. 237–274, 1994.
- [60] H. W. Kroto, A. W. Allaf, and S. P. Balm, “C60: buckminsterfullerene,” *Chemical Reviews*, vol. 91, no. 6, pp. 1213–1235, 1991.
- [61] G. Yu, J. Gao, J. C. Hummelen, F. Wudl, and A. J. Heeger, “Polymer photovoltaic cells - enhanced efficiencies via a network of internal donor-acceptor heterojunctions,” *Science*, vol. 270, pp. 1789–1791, 1995.
- [62] M. Hiramoto, H. Fukusumi, and M. Yokoyama, “Organic solar cell based on multistep charge separation system,” *Applied Physics Letters*, vol. 61, no. 21, pp. 2580–2582, 1992.
- [63] N. S. Sariciftci, D. Braun, C. Zhang, V. I. Srdanov, A. J. Heeger, G. Stucky, and F. Wudl, “Semiconducting polymer-buckminsterfullerene heterojunctions: Diodes, photodiodes, and photovoltaic cells,” *Applied Physics Letters*, vol. 62, no. 585, pp. 585–587, 1993.
- [64] M. T. Dang, L. Hirsch, and G. Wantz, “P3HT:PCBM, best seller in polymer photovoltaic research,” *Advanced Materials*, vol. 23, no. 31, pp. 3597–3602, 2011.
- [65] D. Chen, A. Nakahara, D. Wei, D. Nordlund, and T. P. Russell, “P3HT/PCBM bulk heterojunction organic photovoltaics: correlating efficiency and morphology,” *Nano Letters*, vol. 11, no. 2, pp. 561–567, 2011.
- [66] P. Vanlaeke, A. Swinnen, I. Haeldermans, G. Vanhoyland, T. Aernouts, D. Cheyns, C. Deibel, J. D’Haen, P. Heremans, J. Poortmans, and J. Manca, “P3HT/PCBM bulk heterojunction solar cells: Relation between morphology and electro-optical characteristics,” *Solar Energy Materials and Solar Cells*, vol. 90, no. 14, pp. 2150–2158, 2006.
- [67] J. Schafferhans, A. Baumann, A. Wagenpfahl, C. Deibel, and V. Dyakonov, “Oxygen doping of P3HT:PCBM blends: Influence on trap states, charge carrier mobility and solar cell performance,” *Organic Electronics*, vol. 11, no. 10, pp. 1693–1700, 2010.
- [68] S. H. Liao, H. J. Jhuo, P. N. Yeh, Y. S. Cheng, Y. L. Li, Y. H. Lee, S. Sharma, and S. A. Chen, “Single junction inverted polymer solar cell reaching power conversion efficiency 10.31% by employing dual-doped zinc oxide nano-film as cathode interlayer,” *Scientific Reports*, vol. 4, 2014.
- [69] J. Yuan, Y. Zhang, L. Zhou, G. Zhang, H.-L. Yip, T.-K. Lau, X. Lu, C. Zhu, H. Peng, P. A. Johnson, M. Leclerc, Y. Cao, J. Ulanski, Y. Li, and Y. Zou, “Single-Junction Organic Solar Cell with over 15% Efficiency Using Fused-Ring Acceptor with Electron-Deficient Core,” *Joule*, 2019.
- [70] N. Sai, K. Leung, J. Zádor, and G. Henkelman, “First principles study of photo-oxidation degradation mechanisms in P3HT for organic solar cells,” *Physical Chemistry Chemical Physics*, vol. 16, no. 17, pp. 8092–8099, 2014.

- [71] H. Cao, W. He, Y. Mao, X. Lin, K. Ishikawa, J. H. Dickerson, and W. P. Hess, "Recent progress in degradation and stabilization of organic solar cells," *Journal of Power Sources*, vol. 264, pp. 168–183, 2014.
- [72] M. Jørgensen, K. Norrman, and F. C. Krebs, "Stability/degradation of polymer solar cells," *Solar Energy Materials and Solar Cells*, vol. 92, no. 7, pp. 686–714, 2008.
- [73] W. Huang, E. Gann, L. Thomsen, A. Tadich, Y.-B. Cheng, and C. R. McNeill, "Metal evaporation-induced degradation of fullerene acceptors in polymer/fullerene solar cells," *ACS Applied Materials & Interfaces*, vol. 8, no. 3, pp. 2247–2254, 2016.
- [74] C. Mu, P. Liu, W. Ma, K. Jiang, J. Zhao, K. Zhang, Z. Chen, Z. Wei, Y. Yi, J. Wang, S. Yang, F. Huang, A. Facchetti, H. Ade, and H. Yan, "High-efficiency all-polymer solar cells based on a pair of crystalline low-bandgap polymers," *Advanced Materials*, vol. 26, no. 42, pp. 7224–7230, 2014.
- [75] L. Gao, Z.-G. Zhang, L. Xue, J. Min, J. Zhang, Z. Wei, and Y. Li, "All-polymer solar cells based on absorption-complementary polymer donor and acceptor with high power conversion efficiency of 8.27%," *Advanced Materials*, vol. 28, no. 9, pp. 1884–1890, 2016.
- [76] D. Nava, Y. Shin, M. Massetti, X. Jiao, T. Biskup, M. S. Jagadeesh, A. Calloni, L. Duò, G. Lanzani, C. R. McNeill, M. Sommer, and M. Caironi, "Drastic improvement of air stability in an n-Type doped naphthalene-diimide polymer by thionation," *ACS Applied Energy Materials*, vol. 1, no. 9, pp. 4626–4634, 2018.
- [77] H. Yan, Z. Chen, Y. Zheng, C. Newman, J. R. Quinn, F. Dötz, M. Kastler, and A. Facchetti, "A high-mobility electron-transporting polymer for printed transistors," *Nature*, vol. 457, no. 7230, pp. 679–686, 2009.
- [78] D. Mori, H. Benten, I. Okada, H. Ohkita, and S. Ito, "Highly efficient charge-carrier generation and collection in polymer/polymer blend solar cells with a power conversion efficiency of 5.7%," *Energy & Environmental Science*, vol. 7, pp. 2939–2943, 2014.
- [79] E. Ahmed, G. Ren, F. S. Kim, E. C. Hollenbeck, and S. A. Jenekhe, "Design of new electron acceptor materials for organic photovoltaics: Synthesis, electron transport, photophysics, and photovoltaic properties of oligothiophene-functionalized naphthalene diimides," *Chemistry of Materials*, vol. 23, no. 20, pp. 4563–4577, 2011.
- [80] X. Wang, J. Huang, Z. Niu, X. Zhang, Y. Sun, and C. Zhan, "Dimeric naphthalene diimide based small molecule acceptors: synthesis, characterization, and photovoltaic properties," *Tetrahedron*, vol. 70, no. 32, pp. 4726–4731, 2014.
- [81] M. T. Lloyd, J. E. Anthony, and G. G. Malliaras, "Photovoltaics from soluble small molecules," *Materials Today*, vol. 10, no. 11, pp. 34–41, 2007.
- [82] S. V. Bhosale, C. H. Jani, and S. J. Langford, "Chemistry of naphthalene diimides," *Chemical Society Reviews*, vol. 37, no. 2, pp. 331–342, 2008.

- [83] O. Yushchenko, D. Villamaina, N. Sakai, S. Matile, and E. Vauthey, "Comparison of charge-transfer dynamics of naphthalenediimide triads in solution and  $\pi$ -stack architectures on solid surfaces," *The Journal of Physical Chemistry C*, vol. 119, no. 27, pp. 14999–15008, 2015.
- [84] T. He, M. Stolte, and F. Würthner, "Air-stable n-channel organic single crystal field-effect transistors based on microribbons of core-chlorinated naphthalene diimide," *Advanced Materials*, vol. 25, no. 48, pp. 6951–6955, 2013.
- [85] Z. Li, L. Ying, P. Zhu, W. Zhong, N. Li, F. Liu, F. Huang, and Y. Cao, "A generic green solvent concept boosting the power conversion efficiency of all-polymer solar cells to 11%," *Energy and Environmental Science*, vol. 12, no. 1, pp. 157–163, 2019.
- [86] P. S. Rao, A. Gupta, D. Srivani, S. V. Bhosale, A. Bilic, J. Li, W. Xiang, R. A. Evans, and S. V. Bhosale, "An efficient non-fullerene acceptor based on central and peripheral naphthalene diimides," *Chemical Communications*, vol. 54, no. 40, pp. 5062–5065, 2018.
- [87] A. Welford, S. Maniam, E. Gann, L. Thomsen, S. J. Langford, and C. R. McNeill, "Thionation of naphthalene diimide molecules: Thin-film microstructure and transistor performance," *Organic Electronics*, vol. 53, pp. 287–295, 2018.



# Chapter 2

## Literature Review

### 2.1 Introduction

The past fifteen years have seen significant improvements in both OPV device efficiencies and processing techniques, made possible by an increased understanding of the working principles of organic semiconductors, breakthroughs in device engineering, and the development of new, highly efficient light-absorbing materials.<sup>1-7</sup> In order to appreciate the complex operation of an organic solar cell, it is imperative to first understand the mechanisms that give rise to semiconducting behavior in organic materials. This, as well as subsequent optoelectronic properties, will be discussed in Section 2.2. Section 2.3 then focuses on OPV device operation, discusses donor materials and why significant early research efforts focused on p-type materials, followed by a review of recent progress made in novel acceptor materials. This chapter aims to survey the existing literature in order to highlight gaps in modern research, which will be addressed in the topics of subsequent results chapters in this thesis.

### 2.2 Organic semiconductors

As was discussed in Section 1.3, the introduction of a heterojunction between materials of different electron affinity by C. W. Tang in 1986 provided a key step in the advancement of organic photovoltaics.<sup>8</sup> However, a proper introduction to the working principles of organic semiconductors (OSCs) is required to fully appreciate the ingenuity of this strategy for producing highly efficient organic solar cells and will be discussed first. This is followed by a review of the electronic structure of organic semiconductors, which is vital to understanding the optoelectronic properties of these materials.

#### 2.2.1 Working principles

In the ground state, carbon has the following electronic configuration:  $1s^2 2s^2 2p^2$ , with the outer shell containing two s electrons, which are paired, and two p electrons, which are unpaired.<sup>10</sup> These outer shell electrons are essential for the formation of interatomic bonds because of their potential to hybridize, of which there are the following three possible configurations: sp,  $sp^2$  and  $sp^3$ . For reference, the geometry of s and p orbitals are shown in Figure 2.1 (a) and (b), respectively. sp hybridization is

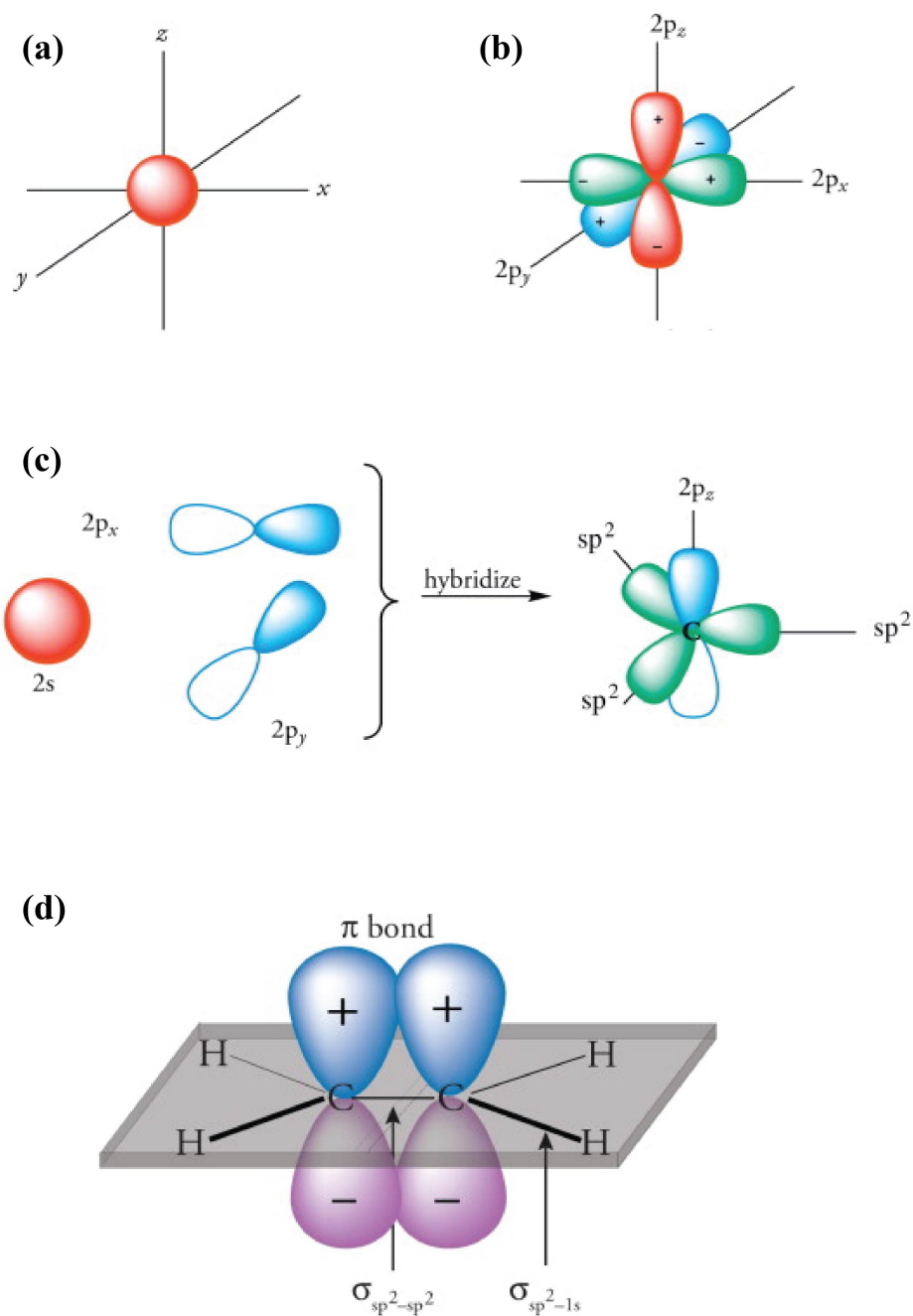


Figure 2.1: Depictions of s and p orbitals are shown in (a) and (b), respectively. The  $sp^2$  hybridization process is shown in (c). A side view depicts three  $sp^2$  orbitals and one  $2p$  orbital, oriented in the z-direction. The bonding structure of ethylene is shown in (d), which illustrates out-of-plane  $\pi$ -bonding and in-plane  $\sigma$  bonding between both the carbon and hydrogen atoms. Reproduced from Organic Chemistry, R. Ouellette and D. Rawn, Structure and Bonding in Organic Solids, 1-39, Copyright (2014), with permission from Elsevier.<sup>9</sup>

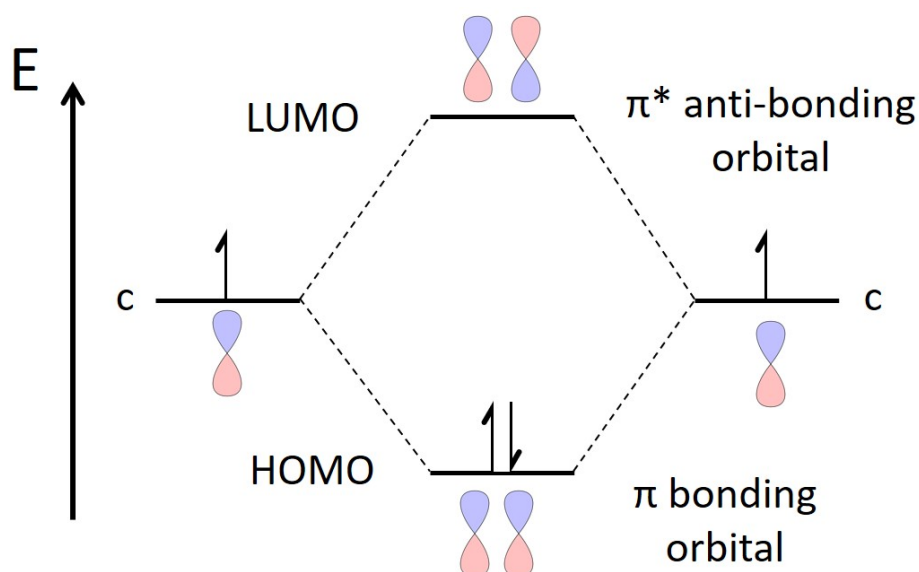


Figure 2.2: Schematic molecular orbital energy diagram for two carbon atoms. The central arrows denote two electrons with different spin.

the simplest of the three, with one s orbital and one p orbital hybridizing to form two new orbitals, which maintain  $180^\circ$  between them. Four tetrahedrally oriented  $sp^3$  orbitals are formed in  $sp^3$  hybridization, when the 2s and three 2p orbitals are combined. For conjugated materials,  $sp^2$  hybridization is vital to achieving interesting electronic properties within the material and will be described in most detail here. When the s orbital is mixed with two of the 2p orbitals, three  $sp^2$  orbitals are formed (Figure 2.1 (c)). One of the p orbitals, for example the  $p_z$  orbital, remains unaltered while the s orbital hybridizes with the  $p_x$  and  $p_y$  orbitals. This gives rise to three planar orbitals that are oriented  $120^\circ$  from one another.

In a conjugated molecule, the hybridized orbitals are located in the plane of the carbon atoms and form  $\sigma$ -bonds, while the  $p_z$  orbital is perpendicular to the plane of carbon atoms, and is able to form a  $\pi$ -bond with the neighboring, overlapping  $p_z$  orbital of an adjacent carbon atom. Figure 2.1 (d) depicts this bonding environment in ethylene, a simple example. The formation of a  $\pi$ -bond delocalizes the electron density of the molecule above and below the plane of carbon atoms, and removes the electron density from the plane of the molecule, allowing for electronic charge carriers to move freely along the backbone of the conjugated material.

When orbitals hybridize, they can do so either by constructive or destructive interference. As two unbound atoms move closer to one another and meet, the orbitals associated with their valence electrons hybridize and a bond is formed, resulting in a lowering of the orbital energy of both atoms to a state termed the  $\pi$ -bonding molecular orbital: a consequence of constructive interference between the individual atomic orbitals. The  $\pi^*$ -antibonding orbital is formed by destructive interference of the hybridized orbitals and lies at an energy higher than that of the individual atoms. It is therefore energetically unfavorable for an electron to occupy the antibonding orbital. In an organic semiconductor, multiple atoms are brought together to create several  $\pi$  and  $\pi^*$  orbitals, where the highest-energy  $\pi$ -bonding orbital is referred to as the Highest Occupied Molecular Orbital (HOMO) while the lowest-energy  $\pi^*$ -antibonding



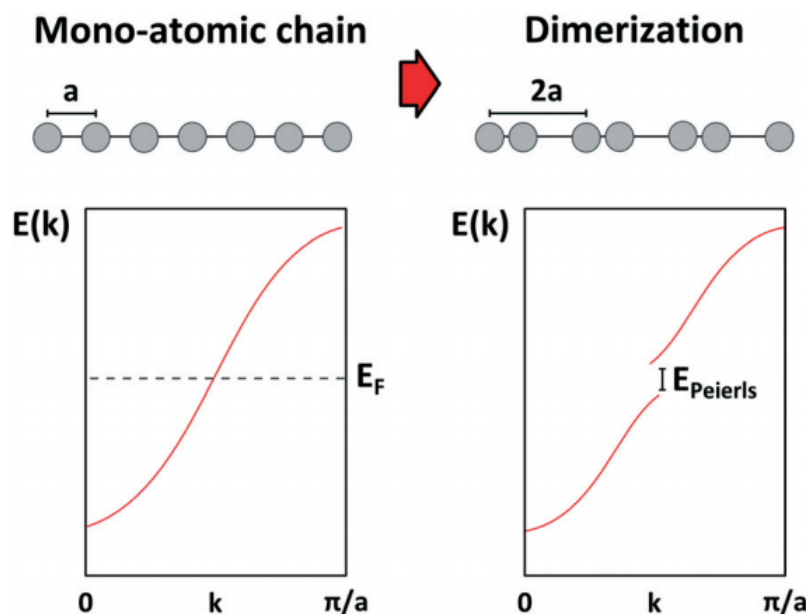


Figure 2.3: Schematic band diagrams showing the electronic stability gained by dimerization of a mono-atomic chain for a half-filled band. Reproduced from Boschker et al.<sup>11</sup> with permission from The Royal Society of Chemistry.

molecular orbital is termed the Lowest Unoccupied Molecular Orbital (LUMO). A schematic is shown in Figure 2.2. A conjugated small molecule or polymer has enough atomic orbitals to create bands of bonding and anti-bonding orbitals which are analogous to the valence and conduction bands, respectively, in inorganic semiconductors, although charge transport kinetics are fundamentally different in organic compared to inorganic materials. The transport of charge carriers along the backbone of a conjugated material is discussed in more detail in 2.2.2.2.

### 2.2.1.1 Electronic structure of organic semiconductors

In order to fully understand the mechanisms that result in semiconducting behavior arising in conjugated materials – most notably the formation of a band gap – it is important to provide an overview of the Peierls Instability, first introduced by Peierls<sup>12</sup> and Fröhlich<sup>13</sup> in the 1950s. Briefly, a conjugated polymer is considered to be a long chain that is made up of repeating single units (similar to a string of pearls in a necklace where each pearl is a single unit) while a conjugated small molecule is considered as an individual, single unit. With these assumptions, a polymer that consists of, for example,  $2N$  atoms, can be modeled as a one-dimensional chain of length  $L$  with  $2N$  electrons. At first glance, an intuitive reader may assume the ground state has a periodicity of  $L/2N$ , however the Peierls Instability Theorem states that this 1D, equally spaced chain of ions, with one electron per ion, is *unstable*.<sup>12</sup> In order to form a stable material, a distortion to the periodicity of the chain is required, with some atoms being spaced closer together while others are further apart. To achieve this, Peierls and Fröhlich proposed a model in which there are two periods: Period 1 with periodicity  $L/N$  and Period 2 with periodicity  $L/2N$ . Alternating these two periods breaks the symmetry from one period to the other, reducing the overall ground-state

energy of the chain.<sup>14</sup> This is termed a dimerism, a schematic of which is shown at the top of Figure 2.3. Below, Figure 2.3 shows energy diagrams for the two different scenarios, plotted with respect to the wave vector,  $k$ . For the case of a mono-atomic chain, the energy diagram represents that of a metal, in which there is a continuous band with the Fermi energy in the middle of the band. For the dimer, the energy diagram is representative of a semiconductor, with the Fermi energy in the middle of the band gap. Energetically, the dimerization stabilizes this system by simultaneously lowering the energy of the occupied states and raising the energy of the unoccupied states, which causes the band gap to form at the Fermi energy level. This band gap is responsible for inducing interesting optical and electronic behavior in OSCs, enabling them to be used in a multitude of applications that were previously limited to inorganic semiconductors. Practically, OSCs are made by synthesizing materials with alternating single and double bonds, where atoms bonded by a double bond are closer together than single-bonded atoms.<sup>15</sup> A detailed explanation of the ensuing optoelectronic properties of organic semiconductors is provided in the next section.

## 2.2.2 Optoelectronic properties

In contrast to conventional semiconductors, where strong covalent bonds are responsible for the material's energetic properties, the strong covalent bonds that bind atoms in organic semiconductors play a lesser role in the materials' energetics, which are dominated by van der Waals bonds between adjacent molecules. This weaker bonding environment results in wavefunctions that are notably more localized, with excited-state electrons and holes being confined to the same molecule, directly influencing the optical and transport properties in OSCs. This section focuses on the interesting optical and charge transport properties as they relate to organic semiconductors, which are fundamentally different to the properties observed in inorganic semiconductors.

Following the formation of a band gap, conjugated organic materials exhibit interesting optical and electronic properties, made possible by the delocalized  $\pi$  orbitals which enable electronic polarizability.<sup>16</sup> Integral to explaining how organic solar cells operate is a basic understanding of the fundamental optical and electronic properties of organic semiconductors. For example, the electronic excited states in OSCs directly relate to processes including light absorption and emission, photoconductivity and electroluminescence, all of which are pertinent to solar cell operation.<sup>17</sup> This section provides an overview of the interaction of OSCs with light, followed by an introduction to charge transport in OSCs, both of which will facilitate understanding of Section 2.3: Organic solar cells.

### 2.2.2.1 Light absorption in organic semiconductors

When organic semiconductors are exposed to light, a strong optical response arises in the UV-visible energy range ( $\sim 300 - 770$  nm) as absorbed photons enable  $\pi - \pi^*$  transitions from bonding to anti-bonding orbitals (for example, an excitation from the HOMO to the LUMO), creating an excited state.<sup>18</sup> Excited molecules can exist in two distinct spin states: a singlet state with spin 0 and a triplet state with spin 1.<sup>18,19</sup> The singlet state comprises one electron in the  $\pi^*$  orbital and one electron in the  $\pi$  orbital, which have anti-parallel spin, summing to 0. Conversely, the triplet state electrons have parallel spin, adding up to a total spin of 1.<sup>18</sup> Because optical excitation preserves

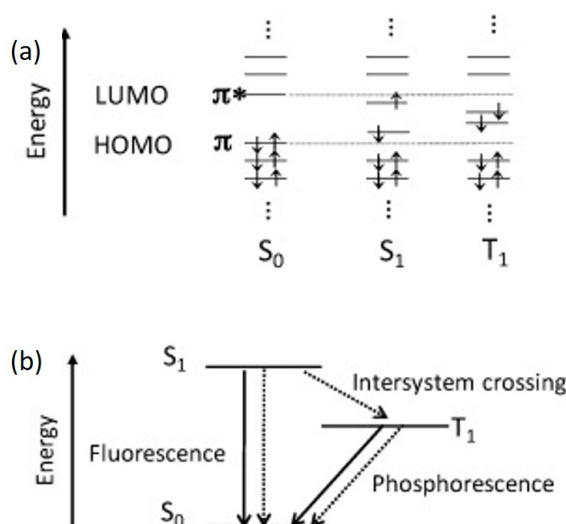


Figure 2.4: (a) Singlet and triplet states for an isolated molecule. Electron spin is indicated by arrows, which show the anti-parallel singlet spin states and parallel triplet spin states. (b) A state diagram indicating radiative (solid lines) and non-radiative (dotted lines) relaxation channels.<sup>18</sup> Reproduced from *Materials Science and Engineering: Reports*, A. Köhler and H. Bässler, *Triplet States in Organic Semiconductors*, 71-109, Copyright (2009), with permission from Elsevier.<sup>18</sup>

spin, photon absorption only generates singlet excitons that are excited from the singlet ground state ( $S_0$ ) to the first unoccupied singlet excited state ( $S_1$ ).<sup>20</sup> Due to the very short lifetime ( $\sim 1 - 10$  ns) of this excited state, there is usually a rapid transition back to the ground state via either fluorescence or a non-radiative decay process. There is, however, a small probability that while in the excited state, the system will cross over to a triplet state ( $T_1$ ) (see Figure 2.4) where it can exist for significantly longer (on the order of milliseconds) due to radiative recombination to the ground state being forbidden.<sup>20</sup> From the triplet state, the charge can relax to the ground state either via phosphorescence or non-radiatively, although phosphorescence is not normally observed at room temperature for conjugated organic molecules.<sup>21</sup> While radiative decay processes are imperative for efficient OLED operation, the opposite is true for OPVs, where an efficient device operates by maintaining an excited state long enough for free carriers to be extracted as current.

Due to the low atomic number and density of carbon-based materials, the dielectric constant is low for organic semiconductors ( $\epsilon_r \sim 2 - 4$ ). As a result, the excited state exists as a quasiparticle known as an exciton – a coulombically bound (in both energy and space) electron-hole pair. Spatially, the separation distance between the electron and hole that comprise an exciton is very small ( $\sim 1$  nm) and the charges are normally confined to the same molecule or conjugated segment.<sup>22</sup> The relative attractive force between charges is disputed and varies from one OSC to another, however, it is generally accepted that the binding energy for a singlet exciton is  $\sim 0.3 - 0.5$  eV.<sup>17</sup> The triplet exciton binding energy is generally larger due to the attractive exchange interaction between an electron and hole with the same spin orientation (see Figure 2.4).<sup>18</sup>

Imperative to the operation of organic solar cells is that the exciton is dissociated into an electron and hole pair, and that these charges are separated, enabling sub-

sequent extraction as current in a photovoltaic device.<sup>23</sup> This is discussed in more detail in Section 2.3.1, however, briefly, in organic solar cells this exciton dissociation and subsequent charge separation is achieved by combining materials with differing electron affinities. At the interface between such materials, the large difference in electronic energy levels produces a local electric field, or “driving force,” which is large enough to dissociate charges into electrons and holes. Dissociated charges may then be separated, and hop to their respective electrodes, described in more detail below.

### 2.2.2.2 Introduction to charge transport

Following exciton dissociation or charge injection, electrons and holes can move along the backbone of a polymer or small molecule. Unlike conventional semiconductors such as silicon or germanium, whose covalent bonds (high bonding energy) enable charges to move at high mobilities ( $\sim 1,500$  cm/Vs) as delocalized plane waves, the van der Waals bonding environment in OSCs results in weak electronic coupling between molecules or conjugated segments, and thus charges are primarily transported via a hopping mechanism, which is typically associated with significantly lower mobilities, usually around  $10^{-3}$  cm/Vs.<sup>24,25</sup>

There are several factors that influence the efficient transport of charges in an organic semiconductor. These include molecular packing, disorder, impurities, and charge carrier densities within the system.<sup>26</sup> First, the molecular packing can strongly influence charge carrier mobility due to anisotropy: charges are able to move most efficiently along the backbone of a conjugated material, where  $\pi$  orbitals of neighboring atoms overlap. Additionally, when oligomers or molecules are spaced closely, the  $\pi$  orbitals of neighboring oligomers or molecules may be close enough to allow charges to hop across molecules. If, however, the molecular packing in a material is widely-spaced, charges may be unable to move between adjacent molecules, greatly hindering charge mobility.

Building upon this, disorder within the organic semiconductor also strongly influences charge transport. Disorder is classified in two ways: diagonal disorder describes disorder along the *same* polymer chain or molecule, and mobility is reflective of fluctuations in site energies along the chain, while off-diagonal disorder is related to fluctuations in interactions between adjacent molecules or polymer chains. Off-diagonal disorder is largely responsible for the charge transport experienced in the bulk of the material, and can either enable high mobility through well-conducting pathways, or extremely low mobility if many traps are present.<sup>26</sup>

As in inorganic semiconductors, impurities in organic semiconductors can greatly influence charge carrier mobility. These impurities include compounds with a slightly different chemical structure to the rest of the organic semiconductor, which can arise as side products from synthesis. These impurities can greatly hinder charge transport and carrier mobility if their HOMO or LUMO energies fall within the gap of the HOMO and LUMO energies of the organic semiconductor because this can lead to the formation of traps – classified as either deep traps with energy  $\gg K_B T$ , or shallow traps with energy  $\ll K_B T$ , in which case detrapping can occur thermally. For example, it was shown by Jurchescu and coworkers,<sup>27</sup> that pentacene, which had an impurity concentration of 0.7% after synthesis, exhibited a hole mobility of  $35$  cm<sup>2</sup>/Vs<sup>27</sup> at room temperature, after the impurity concentration was reduced to 0.07%. For comparison, other research has shown hole mobilities that are an order of magnitude less, at 0.45

$\text{cm}^2/\text{Vs}^{28}$  at room temperature, for pentacene that has not been purified so carefully.

Finally, the charge carrier concentration greatly influences free carrier mobility in organic semiconductors. This is discussed in more detail in Section 2.3.1.1 as it pertains to organic photovoltaic operation, however, briefly: at low carrier densities, mobility is largely affected by the number of trap states that arises from the parameters mentioned earlier (namely the disorder within the material and the impurity concentration), with many charge carriers being lost to traps. However, if charge carrier density is large enough, only some of the carriers are lost to traps within the material, while the rest are able to move through the organic semiconductor, experiencing trap-free transport.<sup>26</sup>

The exact mechanisms of charge hopping in OSCs are still under debate, as there are two schools of thought to describe charge transport in organic semiconductors: one pertaining to the influence of polarons (or electron-phonon coupling) and the other pertaining to disorder. Today, it is generally believed that both polaron and disorder-based transport can occur simultaneously, however disorder-based transport often dominates, and charge transport within organic semiconductors can phenomenologically be treated as effects due to disorder because these are more dominant than polaronic effects. Several models exist for both polaron and disorder-based models, however here, the 1959 Holstein small-polaron model<sup>29</sup> will be introduced first, as it is the most common hopping model applied to organic semiconductors,<sup>30</sup> followed by a brief introduction to the Marcus disorder model, which is the most commonly used disorder model to describe charge transport in organic semiconductors.<sup>31</sup>

The Holstein small-polaron model built on one fundamental assumption: the propagation of charges is dependent upon electron-phonon coupling.<sup>24</sup> A polaron is a quasiparticle that is used to describe electron (or hole) interactions with atoms in a solid lattice. The presence of polarons in OSCs means that charge transport requires both charge movement as well as lattice distortion. This means that charge transport by hopping is much less efficient compared to band transport, because free electrons (or holes) are predominantly trapped on a molecule and only move to the next adjacent lattice site when they obtain enough energy to hop there.<sup>29</sup> Holstein simplified this premise by only considering a 1D, one-electron model. The total energy in this system is comprised of three elements: (1) the total lattice energy, which is the sum of  $N$  harmonic oscillators, all with frequency  $\omega_0$ , (2) the energy dispersion of the electron, and (3) the electron-lattice coupling. Additionally, the polaron binding energy,  $E_b$ , is an important consideration, as it describes the type of transport model appropriate for a system: large polarons (low  $E_b$ ) are used when describing band-like transport while small polarons (high  $E_b$ ) are appropriate for systems that undergo hopping transport mechanisms.<sup>29</sup> Given these assumptions, the following relationship can be used to describe the charge mobility,  $\mu$ :

$$\mu = \sqrt{\frac{\pi}{2}} \frac{ea^2}{\hbar} \frac{J^2}{\sqrt{E_b}} (kT)^{-3/2} \exp\left(\frac{-E_b}{2kT}\right) \quad (2.1)$$

where  $\hbar$  is the reduced Plank's constant ( $\hbar = \frac{h}{2\pi}$ ),  $J$  is the electron transfer energy,  $a$  is the lattice constant, and  $e$  is the charge of an electron;  $\frac{ea^2}{\hbar}$  has the dimension of a carrier mobility.<sup>24</sup>

The Marcus disorder model is largely based on the Miller-Abrahams disorder model that was originally conceptualized for charge transport in doped inorganic materials.<sup>32</sup> However, the Marcus model also accounts for the off-diagonal disorder arising from in-

equivalent electronic couplings along the backbone of the organic semiconductor. This disorder is introduced into the system by randomly generating a disorder energy from a Gaussian distribution of states. Charge carriers are then treated to exist on localized states on distinct molecules, and are allowed to hop to their nearest neighboring site if their energy is high enough. The hopping rate from site  $i$  to site  $j$ ,  $v_{ij}$ , is given by:

$$v_{ij} = \frac{|I_{ij}|^2}{\hbar} \sqrt{\frac{\pi}{\lambda kT}} \exp\left(-\frac{(\Delta G_{ij} + \lambda)^2}{4\lambda kT}\right) \quad (2.2)$$

where  $I_{ij}$  is the transfer integral that describes when the wavefunction overlaps between sites  $i$  and  $j$ ,  $\lambda$  is the reorganization energy, which relates to phonon relaxation, and  $\Delta G_{ij}$  is the change in the Gibbs free energy between sites  $i$  and  $j$ , which arises from the different energetic contributions from both sites.

From the relationships in both Equation 2.1 and 2.2, it is clear that carrier mobility is also strongly dependent on another factor not mentioned above: temperature. Interestingly, the mobility in organic semiconductors has a positive dependence on temperature, which is opposite that of inorganic semiconductors.<sup>24</sup> This is particularly useful in solar cell applications, because one limiting factor in silicon-based photovoltaics is a negative relationship between temperature and efficiency, with PCE decreasing by roughly half a percent with every increasing degree above 25 °C.<sup>33</sup> In certain climates, solar panels can reach temperatures up to 65 °C, at which they operate at a significantly reduced efficiency. This is not true, however, for organic solar cells. Although studies pertaining to more novel materials are scarce, the short-circuit current density dependence on temperature for solar cells fabricated with a P3HT:PCBM blend indicates a constant increase in current density up to approximately 50 °C, after which the current density declines.<sup>34</sup> This implies that organic solar cells may be more appropriate in high-temperature climates compared to silicon solar cells, if hurdles such as lower efficiencies and shorter lifetimes can be overcome. Further details on charge transport, as it pertains to solar cell operation, are given in Section 2.3.1.1.

This concludes the overview of the basic working principles of organic semiconductors. The following section provides an introduction to organic solar cells, and how the principles outlined above affect them, and must be accounted for, in order to realize efficient solar cell operation.

## 2.3 Organic solar cells

The following section covers the basic operating principles of organic solar cells, followed by solar cell properties, such as active layer morphology and device architecture, that can be optimized to improve device performance. Characterization methods to quantify solar cell performance and properties are covered next, followed by a detailed discussion of the materials commonly used in OPV research, as well as recent progress that has been made in the area of NDI-based small molecule acceptors.

### 2.3.1 OPV Operation

Conventional, inorganic solar cells employ a doped semiconductor — typically silicon — with an internal electric field formed by a p-n junction, across which a built-in field is generated. Incident photons absorbed within the bulk of the silicon generate

electrons and holes that diffuse towards the p-n junction. In the p-doped side, holes are attracted to the negative charge of the N-doped side and diffuse towards the p-n junction, where they are swept across the junction and removed, causing other holes to diffuse towards it. The opposite is true for electrons in the n-doped side.<sup>35</sup> However, as was explained in the previous section, absorbed photons in OSCs generate bound electron-hole pairs – excitons – due to the low dielectric constant of the absorbing material ( $\epsilon_r \sim 2 - 4$ ).<sup>23,36</sup> Because these electrons and holes are electrically bound to one another by approximately 0.3 – 0.5 eV, organic semiconductors pose a unique problem, in that the excitons must first be dissociated into free carriers, before they are able to diffuse or hop to their respective electrodes in a photovoltaic device.<sup>37,38</sup> Excitons dissociate at the interface between materials of sufficiently different electron affinities (i.e. between donor (D) and acceptor (A) materials), and are able to diffuse on the order of 10 nm before relaxing to the ground state.<sup>23,39</sup> This means that an ideal organic solar cell should offer a junction between donor and acceptor materials every 10 nm, or so (described in more detail in Section 2.3.1.2). At this interface, the donor material (p-type) retains the hole while the acceptor material (n-type) accepts the electron, offering a means for charge separation following exciton dissociation. Specifically, electron transfer from the donor to the acceptor is possible through so-called charge-transfer (CT) states, which exist at picosecond time scales, and are described as excited, delocalized band states.<sup>40,41</sup> Following exciton interaction with a D/A interface, but prior to the charges being dissociated, the exciton exists in a charge-transfer state. Although this state is short lived ( $< 1$  ps), it enables charges to override the coulombic attractive forces binding the exciton, enabling exciton dissociation into electrons and holes. Subsequently, these charges are able to be separated, with the driving force needed for separation arising from the energy needed to reach the delocalized band states.<sup>41</sup> Following charge separation, free carriers can move through the device to their respective electrodes.<sup>41</sup> The electronic separation between the electrons and holes results in a photovoltage, which can be predicted by the separation in energy between the HOMO of the donor and the LUMO of the acceptor. Current through the device is then produced by the drift and diffusion of free carriers to their respective electrodes.

Although it is possible for the acceptor to absorb photons, fullerenes - the historic n-type material - have very low absorption in the visible range, contributing minimally to the number of excitons formed. One method to increase the current output of the solar cell is to implement acceptor materials that also contribute to the number of excitons formed by strongly absorbing photons in the visible range. This is discussed in more detail in Section 2.3.3.2. However, in this introduction, it is assumed that charge generation occurs after photoexcitation of the donor material. Figure 2.5 illustrates the current generation process in three steps: (1) a photon is absorbed by the donor, creating an  $S_1$  singlet exciton state, (2) the  $S_1$  state is quenched (or dissociated) into an electron-hole pair at the donor/acceptor interface, which generates an interfacial charge-transfer state, and (3) the CT state undergoes interfacial separation into free electrons and holes, which are able to diffuse to the cathode and anode, respectively.<sup>43</sup> Following step 2 (exciton dissociation), the electron and hole maintain a proximity of 0.5 - 1 nm, where they experience a significant Coulomb binding energy preventing them from separating. Step 3 (charge separation) is therefore only possible when there is enough energy in the system to overcome the binding energy.<sup>44</sup> In fact, a large loss mechanism in current generation by organic solar cells is the failure to successfully

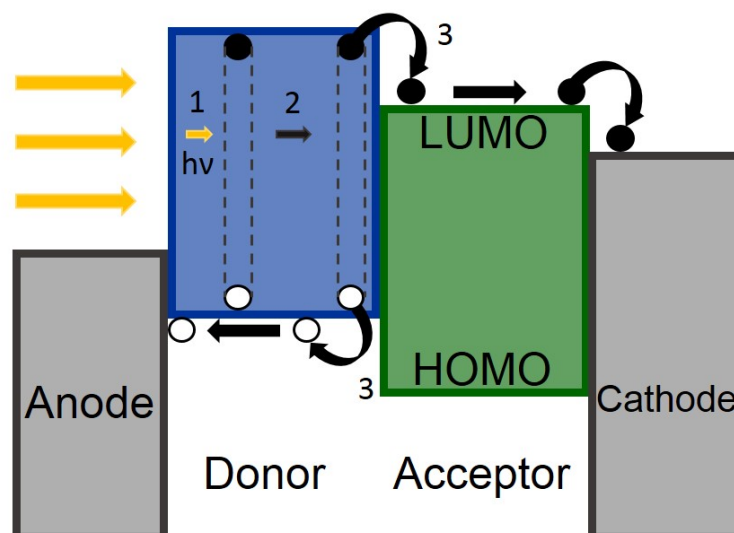


Figure 2.5: Energy diagram of an organic solar cell. After a photon is absorbed by the active layer (step 1), it diffuses to the interface between donor and acceptor materials where the energy difference between the LUMO levels of the donor and acceptor acts as a driving force for exciton dissociation (step 2). The charges are then separated (step 3) as the electron is transferred to the acceptor, losing some energy, where it remains until it is transferred, again losing some energy, to the cathode. Similarly, the hole migrates in the opposite direction towards the anode, also losing energy after dissociating from the electron. Adapted with permission from *Polymeric Solar Cells: Materials, Design, Manufacture*. 2010. Lancaster, PA: DEStech Publications, Inc.<sup>42</sup>

separate charges after exciton dissociation. This is referred to as geminate recombination, which is the recombination and subsequent annihilation of a dissociated exciton whose charges were not quickly separated after dissociation due to the inherent electrostatic attraction between electrons and holes, occurring within approximately 100 ns of photon absorption.<sup>45</sup> If, however, the steps demonstrated in Figure 2.5 are followed, electrons and holes are transported to their respective electrodes via percolated donor and acceptor pathways, giving rise to a photocurrent.<sup>35</sup>

Additional limiting factors in the output current of the solar cell include losses due to recombination of separated electrons and holes, as well as excitons that fail to come in contact with a D/A interface and never dissociate and separate into free carriers before relaxing to the ground state. Non-geminate, or bimolecular, recombination is the recombination of an electron and hole that were completely separated, occurring either between electrons and holes stemming from the same or different excitons and is often the dominant loss mechanism in organic solar cells.<sup>24</sup> The rates of bimolecular and geminate recombination are both dependent on light intensity, however while geminate recombination is linearly dependent on light intensity, bimolecular recombination is superlinear, being proportional to the square of the charge density.<sup>46</sup>

There are several mechanisms that can reduce the solar cell's losses due to recombination including utilizing donor and acceptor materials with similar hole and electron mobilities, and forming a favorable active layer morphology for free carrier transport through the bulk (see Section 2.3.1.2).<sup>47</sup> With regards to the first mechanism, the material with lower mobility is responsible for increasing non-geminate recombination by causing a build-up of one type of carrier (typically, donor polymers have lower mo-



bility than acceptor fullerenes).<sup>48</sup> This accumulation of, for example, holes, facilitates recombination of free charges because the device becomes space-charge limited, which can significantly lower the amount of current produced by the solar cell.<sup>35,42</sup> If, however, the electron and hole mobilities are balanced and charges have clear networks to their respective electrodes, efficient charge transport can take place within the active layer, the working principles of which are discussed in the next section.

### 2.3.1.1 Charge transport

There are three possible directions free carriers can move through the bulk of either the donor or acceptor material: (1) along the backbone of the conjugated material, (2) between backbones of adjacent materials ( $\pi - \pi$  stacking direction), or (3) across the side chains of the material.<sup>49-52</sup> The conductivity of conjugated polymers is highest along the backbone (in-plane direction) of the molecule, due to the strong coupling of electronic states in this direction, resulting from overlapping  $p_z$  orbitals of neighboring carbon atoms. In a bulk film, the transfer of charge from one polymer or molecule to its adjacent neighbor is possible due to weak inter-chain binding, which allows charges to be transferred intermolecularly.<sup>53</sup> This is referred to as the  $\pi - \pi$  direction, and is depicted in Figure 2.6. In order to allow for solution-processability, non-conjugated alkyl side-chains are added to the structure. Due to the nature of these side chains, and especially their lack of conjugation, they are non-conducting, resulting in anisotropy of charge mobility through the material: it is possible for charges to move only along the backbone of the polymer and between polymers in the  $\pi$ -direction, but not between chains in the alkyl chain direction, as shown in Figure 2.6.

The fastest direction of charge movement is along the backbone of the donor and/or acceptor material, followed by movement in the  $\pi$ - $\pi$  stacking direction. It is therefore clear that the orientation of the donor and acceptor materials throughout the bulk of the active layer plays an important role in achieving high performance in organic solar cells. Due to the device architecture of these solar cells (see Section 2.3.1.3), free carriers travel in the vertical direction. The “edge-on” orientation depicted in Figure 2.6 is therefore unfavorable for charge transport, because polymers are vertically separated by insulating alkyl chains. In a device, materials should either be oriented in a “face-on” or, ideally, a “chain-on” configuration in order to promote efficient charge transport to the anode and cathode.

In contrast to inorganic semiconductors, where band transport occurs, charge transport within organic semiconductors occurs by carriers hopping between localized states.<sup>54</sup> This is due to the strong coupling between electrons and phonons - quantized lattice vibrations - in organic semiconductors, which are, in some cases, larger than electron-electron interactions. This is described in more detail in Section 2.2.2.2, however, for comparison, the mobility for electrons and holes in crystalline silicon is approximately 1300 and 450  $\text{cm}^2/\text{Vs}$ , respectively, while carrier mobilities in organic semiconductors are orders of magnitude less, typically being below 1  $\text{cm}^2/\text{Vs}$ .<sup>10,55</sup>

Additionally, the introduction of a second material (either the donor or acceptor) to the organic semiconductor can influence the charge transport and carrier mobility in several ways: (1) it can effect the disorder within the system, (2) it can change the impurity concentration which can result in increased trap states, and (3) it can change the charge carrier density in the active layer. For example, efficient solar cell operation requires balanced charge transport between the donor and acceptor materials.

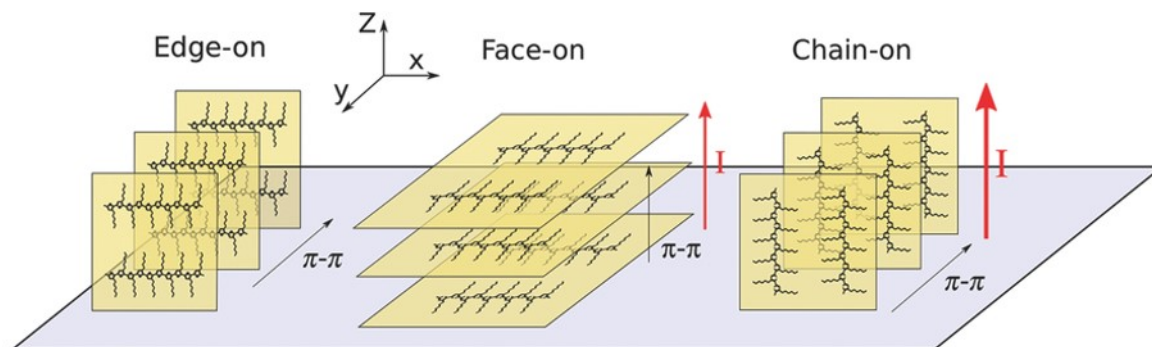


Figure 2.6: Possible polymer chain orientations of P3HT, with respect to the substrate. The red arrow shows intensity of possible charge transport in the Z direction with the chain-on orientation resulting in the most efficient charge transport, along the backbone of the polymer, followed by the face-on orientation, along the  $\pi$ - $\pi$  direction. In this configuration, the edge-on orientation is insulating in the Z-direction, as transport across alkyl chains is not possible. Adapted and reproduced with permission from Skrypnichuk et al. *Advanced Materials*, 28(12,) 2016, 2359-2366.<sup>50</sup>

Otherwise, the accumulation of the charge carrier in the lower-mobility material will result in non-uniformity in the applied electric field within the device. If the mobility of the donor material is lower than that of the acceptor, for example, holes will accumulate within the device while electrons are largely removed. This results in a larger electric field near the anode, and a smaller electric field at the cathode, limiting the further extraction of electrons. Once the system reaches steady-state, the extraction of holes and electrons must be equal, and is therefore limited by the mobility of the lower-mobility material.<sup>56</sup>

Despite the lower charge carrier mobility in organic semiconductors over their inorganic counterparts, and the additional limitations that arise from the introduction of a second material in the active layer, it is still possible to produce efficient solar cells, although special attention must be paid to the processing conditions used in their fabrication. Amongst the most important parameters in an efficient organic solar cell is the active layer morphology formed in the bulk-heterojunction of the device. The requirements for a successful active layer that allows for both exciton dissociation and efficient charge collection at the electrodes are discussed in the next section, as well as strategies that are commonly employed to achieve these.

### 2.3.1.2 Active layer morphology

The active, light-absorbing layer in organic solar cells has been extensively studied and progressively improved upon through meticulous device engineering.<sup>1,6,36,57</sup> As was mentioned in the Introduction Chapter, the first organic solar cells employed single-material active layers that demonstrated power conversion efficiencies of  $\sim 0.2\%$ .<sup>58,59</sup> However, due to the need for a driving force to separate electrons and holes into free carriers, a second material is required to induce charge transfer, and because excitons are limited to a 10 nm diffusion length, that second material should be thoroughly intermixed with the first. Typically, organic solar cells are fabricated by co-dissolving the donor and acceptor materials, usually in common organic solvents such as chloroben-

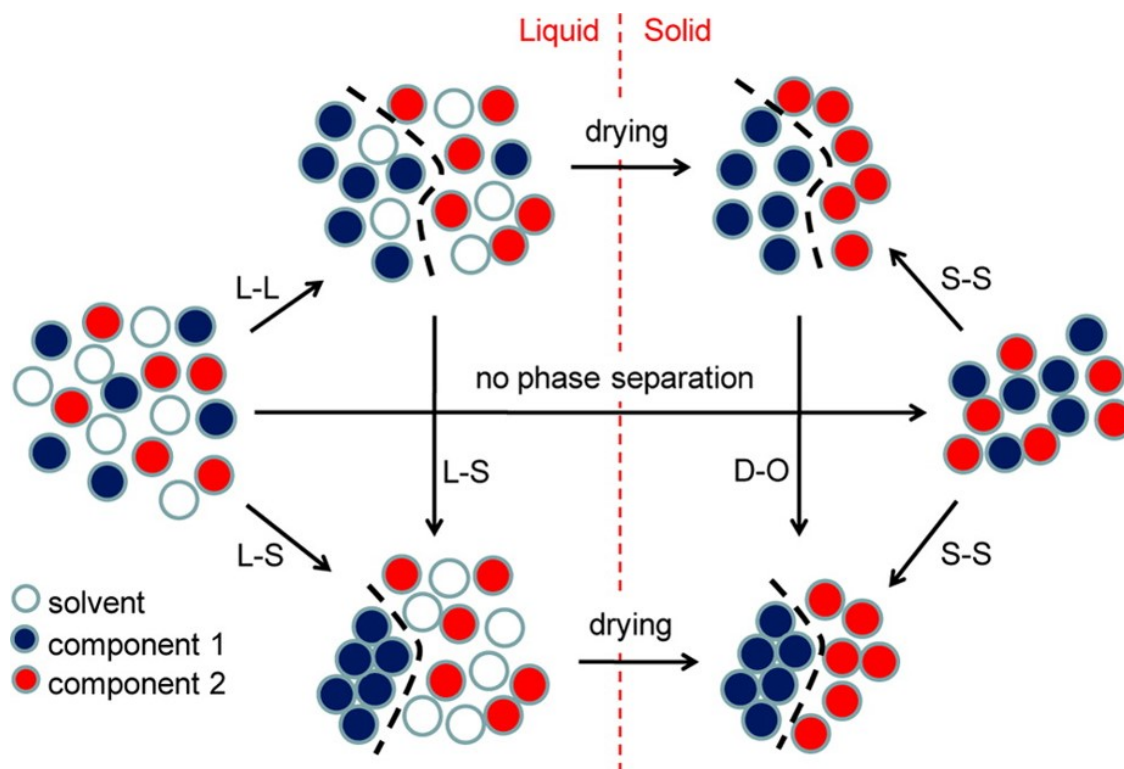


Figure 2.7: Schematic overview of the phase separation processes that may occur during drying of a solution that contains two components. L-L, L-S, and S-S are liquid-liquid, liquid-solid, and solid-solid phase separations, respectively, and D-O is disorder-order transition. Reprinted with permission from *Journal of American Chemical Society* 135, 32, 12057-12067. Copyright (2013) American Chemical Society.<sup>60</sup>

zene or chloroform, to create a solution for spin casting (described in more detail in Section 3.3.1). The thin-film morphology obtained from this solution is influenced by the level of interaction between the conjugated components as well as their interaction with the solvent used. Figure 2.7 gives a schematic overview of the phase separation processes that are possible in both the solution and solid-state phases of such a system.<sup>60</sup> The figure describes that the final film morphology is largely influenced by the different types of phase separation that can occur as the solution dries, following deposition. From a mixed state in the solution, the two components can either undergo a liquid-liquid (L-L) phase separation, a liquid-solid (L-S) phase separation, or no phase separation, as the film dries. After L-L phase separation, the film undergoes a disorder-order (D-O) transition and is left in a de-mixed state. The L-S phase separation results directly in a de-mixed state, while a drying process that undergoes no phase separation during solvent evaporation will result in a mixed solid-state film. Therefore, the drying kinetics are intrinsically related to the degree of mixing between the two conjugated materials in the solid-state and it is essential to select materials whose kinetics will result in preferential morphologies, described in more detail below.

The thermodynamics of phase separation within a two-component system can be described by the Flory-Huggins Theory,<sup>61,62</sup> which enables insight into whether mixing or demixing is the preferred equilibrium morphology between two organic materials. This theory operates under a straight-forward lattice model that assumes (1) poly-

mers can be divided into their smallest repeat unit, monomers, (2) small molecules are the same size as individual polymeric monomer units, and (3) all lattice sites are occupied, either by polymer units or small molecules, and have a constant volume,  $v_o$ . For example, given a blend that contains two conjugated materials, Polymer  $A$  and Small Molecule  $B$ , the number of lattice sites occupied by each chain of Polymer  $A$  is equal to the number of monomers that make up the polymer,  $N_A$ , and each molecule of Small Molecule  $B$  takes up one lattice site ( $N_B = 1$ ). The Flory-Huggins theory defines the equilibrium state of the solid-state donor:acceptor blend and whether it will be mixed or demixed. For example, the two materials will only mix if doing so lowers the overall Gibbs free energy of the system,  $\Delta F_{mix}$ , as follows:

$$\Delta F_{mix} = F_{A+B} - (F_A + F_B) = \Delta H_{mix} - T\Delta S < 0 \quad (2.3)$$

where  $F_{A+B}$  is the free energy of the blend,  $F_A$  and  $F_B$  are the free energy of  $A$  and  $B$ , respectively,  $\Delta H$  is the enthalpy of mixing,  $\Delta S$  is the entropy of mixing and  $T$  is the temperature of the solution. Thus, it can be seen that, in order to determine whether two materials are miscible, the entropy and enthalpy of the system must be determined. Flory and Huggins calculate the entropy of mixing for a two-component system as:

$$\Delta S_{mix} = -K_b \left( \frac{\varphi_A}{N_A} \ln \varphi_A + \frac{\varphi_B}{N_B} \ln \varphi_B \right) \quad (2.4)$$

where  $K_b$  is the Boltzmann constant and  $\varphi_A$  and  $\varphi_B$  are the composition fraction of  $A$  and  $B$ , respectively. The enthalpy of mixing is calculated as:

$$\Delta H_{mix} = K_b T \chi_{AB} \varphi_A \varphi_B \quad (2.5)$$

where  $\chi_{AB}$  is the Flory-Huggins interaction parameter which parameterizes the strength of pair-wise interactions between monomers of  $A$  and  $B$ . Given these relationships for the entropy and enthalpy of the system, the Flory-Huggins equation can be re-written as follows:

$$\frac{\Delta F_{mix}}{K_b T} = \frac{\varphi_A}{N_A} \ln \varphi_A + \frac{\varphi_B}{N_B} \ln \varphi_B + \chi \varphi_A \varphi_B \quad (2.6)$$

The entropic contribution in the Flory-Huggins equation encompasses the first two terms, and always prefers a mixed state, meaning its contribution is negative. The deciding factor, then, for whether the dry film will be in a mixed or de-mixed state, relies on the sign and magnitude of the third term – the enthalpic contribution. More specifically, this will be determined by the sign and magnitude of  $\chi$ : a negative value predicts the blend will be mixed, and a positive value that is large enough to overcome the negative enthalpic term will result in a de-mixed film.<sup>61,62</sup> Additionally, it should be noted that the Flory-Huggins Theory does not account for crystallization effects on the mixing of organic semiconductors, so this mean-field assumption ignores changes in energy due to crystallization and can thus fail for more complex material systems.

Kouijzer and coworkers<sup>60</sup> determined that, for a particular polymer:fullerene blend, the Flory interaction parameter is 1, which resulted in a blend morphology containing lateral globular phases of fullerene, dispersed throughout a polymer matrix. However, this cannot be generalized to all polymer:fullerene systems, because, as was shown by Nilsson et al.,<sup>63</sup> the fullerene interacts differently with various polymers, depending on the polymer's surface energy. They show, for example, that a polymer with a

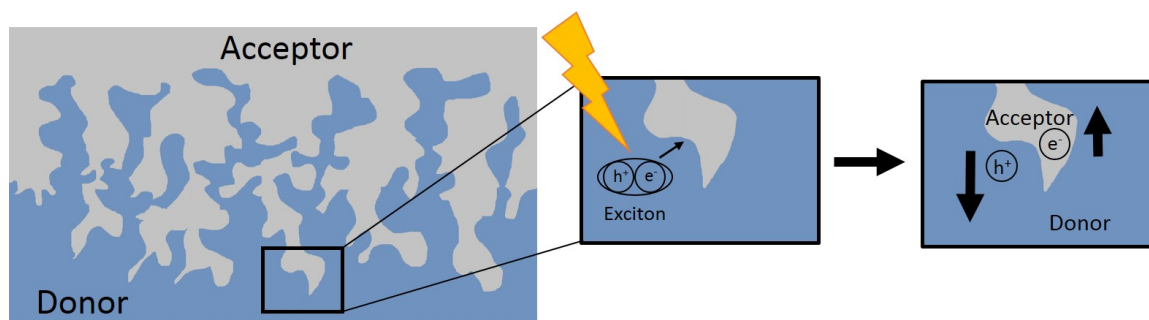


Figure 2.8: Incident photons are absorbed, creating excitons, which require materials of different electron affinity to dissociate into free electrons and holes. At the interface between donor and acceptor materials, holes are retained in the donor phase while electrons are transferred to the acceptor. In conventional polymer donor, fullerene acceptor systems, photons are typically absorbed in the donor phase due to low absorption by the fullerene. The interpenetrating donor/acceptor network provides more interfaces, increasing the likelihood of exciton dissociation.

lower surface energy will induce phase separations at lower concentrations of PCBM, compared to a polymer with higher surface energy. They found that the polarity of the polymers is largely influential over the differences in Flory interaction parameters within polymer:fullerene systems. Further strategies that can be used in order to achieve favorable active layer morphologies for blends of various conjugated materials are described below.<sup>64–66</sup>

A mixed active layer morphology is referred to as a bulk heterojunction, because the junctions between materials are distributed throughout the bulk of the film. Figure 2.8 gives a schematic representation of an ideal bulk heterojunction morphology. While there is some vertical phase separation of the donor and acceptor, the interfaces between materials are thoroughly mixed and widely distributed throughout the bulk of the layer. This ensures absorbed photons have access to an interface within their 10 nm diffusion length regardless of the depth at which they are absorbed within the active layer - a significant improvement over the bilayer heterojunction discussed in the Introduction Chapter, which is limited to a single interface between donor and acceptor materials.

Ideally, there should also be some degree of vertical phase separation in the bulk film, to aid in directing free carriers to their respective electrodes. This is due to the vertical architecture of the device, which is discussed in more detail in the next section. Depending on the configuration, electrons and holes must diffuse and/or drift either upwards or downwards towards the cathode and anode, respectively. It is thus useful to have a small degree of interfacial enrichment at the bottom and top of the active layer, to avoid a build-up of charges near the wrong electrode. For example, it is known that blends of P3HT (donor) and PCBM (acceptor) incur vertical phase separation, with the P3HT typically separating to the top of the film and PCBM to the bottom, after thermal annealing.<sup>66,67</sup> This behavior is attributed to supplying the system with a driving force – thermal energy – above the glass transition temperature of the P3HT, which gives the polymer enough mobility to rearrange, reaching a thermodynamically favorable demixed state.<sup>68</sup> Karagiannidis et al.<sup>66</sup> demonstrated this behavior in 2011, by comparing P3HT:PCBM blend films before and after annealing.

They used atomic force microscopy (AFM), Figure 2.9, to show the change in surface topography before (left) and after (right) annealing the film for 30 minutes at 140 °C. The AFM phase images show a major change in the surface of the film, with the authors describing a “rice-like” morphology consisting of polymeric crystalline domains, indicative of high-molecular weight P3HT, appearing following the heat treatment. They further conclude vertical phase separation occurred during the annealing process by comparing the root mean square (RMS) surface roughness (see Section 3.4.3) of the film before and after annealing: 7.2 and 5.5 nm, respectively. The decrease in RMS, they conclude, is due to a decrease in the PCBM phase at the surface of the film, as well as increased crystallization of the P3HT phase, resulting in a more dense crystalline structure. This observed phase separation is noteworthy because of the vertical orientation of the solar cell: in an inverted device (Section 2.3.1.3), holes, being transported by the P3HT, must reach the top contact, making the nature of the phase separation ideal for charge transport to the electrodes.

Besides thermal annealing, another strategy that is commonly used to achieve a preferential active layer morphology is solvent vapor annealing (SVA). This involves exposing the solid-state film to vapor of a suitable solvent, which penetrates the film and enables the donor and acceptor materials to reorganize to a more crystalline morphology.<sup>69</sup> SVA has been demonstrated to greatly influence the performance of organic solar cells, often significantly improving their PCE.<sup>70,71</sup> For example, Sun et al.<sup>65</sup> demonstrated that, for a blend of small molecule donor and acceptors, an SVA treatment increased solar cell performance over 9 times, from 0.55% without SVA, to 5.16% after SVA treatment with carbon disulfide, CS<sub>2</sub>. Additionally, they demonstrated consistent improvement in PCE utilizing several different solvents, including tetrahydrofuran (THF), chlorobenzene (CB), and acetone, all with varying degrees of success over devices that were not exposed to any solvent vapors. A benefit to SVA, over thermal annealing, is that the treatment is extremely fast, often improving efficiency after exposing the films for less than 30 seconds with the most efficient devices only requiring exposure to CS<sub>2</sub> for seven seconds.<sup>65</sup>

Although thermal annealing and SVA have both been demonstrated to significantly improve the performance of bulk heterojunction solar cells, these methods require a post-deposition step, which can add time to, and complicate the fabrication of, these devices. Ideally, a preferential morphology should be obtained simultaneously with active layer deposition, eliminating the need for an additional step in the fabrication process. In order to achieve this, solvent additives (comprising approximately 1-5% of the solution volume) have been widely used since their coincidental discovery in 2006.<sup>72</sup> Although not the first, the most widely used solvent additive today is 1,8-diiodooctane (DIO), which was first reported to improve the efficiency of a polymer:fullerene system from 3.35% to 5.15% in 2008.<sup>73</sup> The main requirement of the solvent additive is simple: have a boiling point higher than that of the solvent in order to remain in the film after deposition. This then provides either the donor or acceptor materials (or both) a degree of mobility, which they can utilize to crystallize, forming preferential interpenetrating networks throughout the bulk heterojunction. Today, most demonstrations of high-performing novel OPV material systems utilize some form of solvent additive in order to achieve ideal morphologies for high efficiency.

This review has introduced three techniques that can be used either during or after active layer deposition in order to form an ideal morphology for solar cell operation. The following section provides details about device architecture and how this plays a



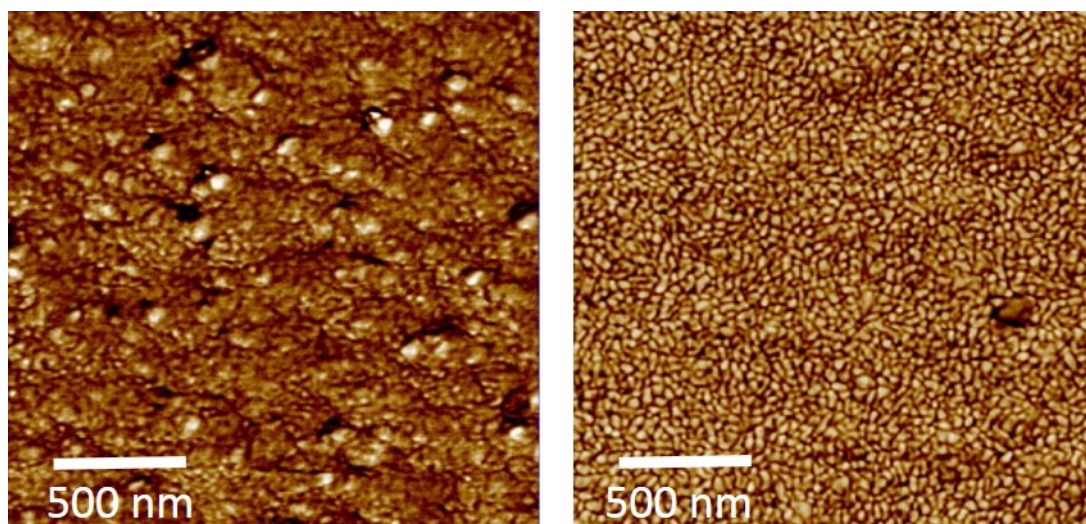


Figure 2.9: AFM phase images before (left) and after (right) annealing P3HT:PCBM films at 140 °C for 30 minutes. Post annealing, the sample shows significant changes in the topography, attributed to vertical phase separation, with P3HT crystallizing and separating towards the top of the film. Adapted and reproduced from *Materials Chemistry and Physics*, 129, Karagiannidis et al., Evolution of vertical phase separation in P3HT:PCBM thin films induced by thermal annealing, 1207-1213, Copyright (2011), with permission from Elsevier.<sup>66</sup>

role in efficient OPV device operation.

### 2.3.1.3 Device architecture

Device architecture has played an integral role in the optimization of organic solar cells, as it significantly influences charge collection efficiency at the device's electrodes.<sup>74-76</sup> Apart from the active layer, the addition of energetically selective layers (1-50 nm) between the active layer and electrodes has been shown to improve device efficiency by selectively blocking either holes at the cathode or electrons at the anode as well as decreasing the likelihood of exciton recombination at the semiconductor/metal interface as a result of having fewer surface defects that lead to recombination.<sup>23,77,78</sup> Additionally, interlayers have been used to improve the wettability and compatibility between typically polar contacts with typically non-polar organic active layers.<sup>79</sup> Though useful in these aspects, additional interlayers add to the complexity of OPVs, with some devices reportedly being comprised of six or more layers in total.<sup>80</sup>

In OPV devices, there are two types of charge selective layers: hole-selective and electron-selective layers. After charge separation, electrons and holes are physically as well as energetically separated, with holes relaxing to a lower energy. It is thus possible to incorporate materials with differing Fermi energy levels to bring selectivity to the anode and cathode of the device.<sup>81</sup> When a bulk heterojunction is sandwiched between electron and hole-selective materials, an analog to the p-i-n junction in amorphous silicon solar cells is created. In such a case, an intrinsic semiconductor (i) is situated between heavily p-doped and n-doped materials, creating ohmic contacts between the materials, allowing for electron and hole transfer between layers.<sup>82,83</sup>

Figure 2.10 gives an overview of the energetic properties of commonly used in-

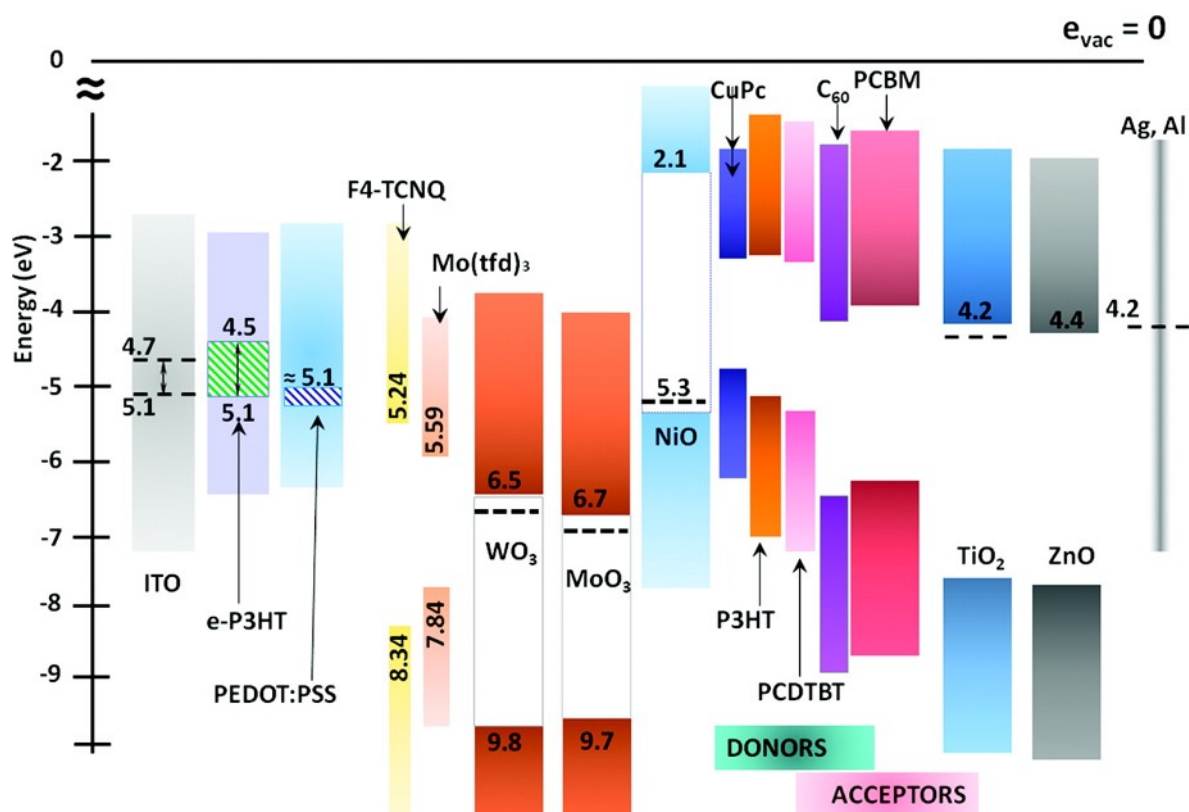


Figure 2.10: Schematic view of the energy gaps and frontier orbital energies of some common OPV materials. The colored areas represent the approximate valence and conduction bands for the various materials, using estimates from the ionization potential and electron affinity and, where available, estimates for the Fermi energy (dashed lines). Reprinted with permission from Ratcliff et al. *Journal of Physical Chemistry Letters* 2011. 2(11) 1337-1350. Copyright (2011) American Chemical Society.<sup>81</sup>



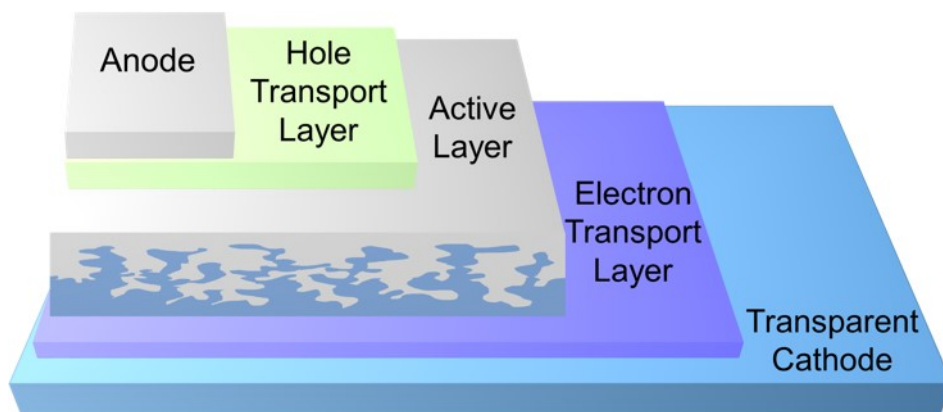


Figure 2.11: Architecture of an inverted solar cell.

terlayers and active layer materials for organic solar cells. It shows, for example, the high-lying conduction band of zinc oxide (ZnO), located just below the LUMO of PCBM, indicating a susceptibility for electron transfer at the interface between these two materials. Additionally, ZnO is known to have higher electron than hole mobility, enabling electrons to be quickly transported to the anode.<sup>84</sup> Conversely, molybdenum oxide ( $\text{MoO}_x$ ) is commonly used as a hole-selective interlayer due to its high work function.<sup>85</sup> When  $\text{MoO}_3$  is sandwiched between an organic semiconductor and a conducting contact, band bending at the interface is observed, with the oxide effectively doping the first 10 nm of the organic layer at the oxide/organic interface. This band bending induces an internal electric field at the interface, which enhances hole extraction from the organic to the oxide layer.<sup>86</sup>

Because light is absorbed in the semiconducting active layer of the organic solar cell, which is located in the middle of the sandwich structure, one of the device electrodes must be optically transparent. Lab-based organic solar cells are typically built on top of a transparent conductive oxide (TCO)-coated glass substrate. There are several TCO materials including aluminum-doped zinc oxide, the conducting polymer poly(3,4-ethylenedioxythiophene)-poly(styrenesulfonate) (PEDOT:PSS), and tin oxide ( $\text{SnO}_2$ ).<sup>87</sup> The most common TCO, however, is indium tin oxide (ITO), which is sputtered onto a glass slide, creating a layer that is approximately 60 – 150 nm thick, has a sheet resistance of 15 - 50  $\Omega/\square$  and a transparency greater than 78%.<sup>88</sup> Subsequent layers are then deposited either via vacuum evaporation or spin coating to form the completed device. Conventionally, a hole transport layer is first deposited onto the ITO slide, followed by the cell's light-absorbing active layer, an electron transport layer, and finally, the top electrode. Although this conventional architecture is still popular in lab scale devices today, several materials typically used as hole transporting and cathode layers have disadvantageous characteristics that hinder solar cell performance. Most notably, the common hole transport polymer, poly(3,4-ethylenedioxythiophene)-poly(styrenesulfonate) (PEDOT:PSS) has been shown to degrade solar cell efficiency by corroding at the ITO interface.<sup>89</sup> Similarly, aluminum, which is typically used as an electrode in conventional devices and has a low work function necessary for electron collection, is susceptible to rapid oxidation, contributing to device instability.<sup>90,91</sup> In an effort to mitigate the use of these materials and thus attempt to improve device stability, an inverted device architecture that exchanged the position of electron and hole transporting layers in the sandwich configuration was introduced.<sup>92–94</sup>

### 2.3.1.3.1 Inverted architecture

The architecture of an inverted solar cell is displayed in Figure 2.11. Despite lower power conversion efficiencies when this configuration was first introduced, solar cells employing an inverted device architecture have recently demonstrated higher stability as well as improved efficiencies over their conventional counterparts.<sup>95,96</sup> A low work function material replaces the acidic PEDOT:PSS as the first material deposited onto the ITO glass slide. Typically, zinc oxide (ZnO) is employed as the electron transporting material and has been shown to increase device performance by: (1) enhancing light absorption by redistributing the optical electric field inside the device, (2) reducing recombination losses by improving the nano-morphology at the transport layer/active layer interface and (3) having a higher conductivity than PEDOT:PSS, enabling thicker layers to be used, facilitating large-scale device fabrication.<sup>4,97,98</sup> Additionally, it has been shown that incorporating an insulating material such as the polymer polyethylenimine ethoxylated (PEIE) as a layer between the ITO and active layer, can improve the performance of organic solar cells as a surface modifier to reduce the work function of the electrode.<sup>99</sup> Alternatively, a very thin ( $< 20$  nm) layer of PEIE can be sandwiched between the ZnO and active layer to decrease the series resistance of the device by decreasing the surface roughness of the ZnO layer.<sup>100</sup> In any case, the inverted architecture replaces low work function metals as the top electrode for more air-stable high work function metals such as silver or gold.<sup>101</sup> Due to the increased stability and device performance of solar cells employing the inverted architecture, this is the preferred architecture for organic solar cells fabricated in this thesis.

## 2.3.2 Characterization

Solar cell characterization methods have been standardized in order to draw direct comparisons between materials studied by different groups in different laboratory environments. These Standard Test Conditions (STC) are: irradiance of  $1,000 \text{ W/m}^2$ , solar spectral distribution, or global air mass of 1.5, “AM 1.5G,” and a module temperature of  $25^\circ\text{C}$ .<sup>102</sup> Arguably, the most important characterization measurement for solar cells is their current density ( $J$ ) – voltage ( $V$ ) characteristics. This measures the solar cell’s response to a potential load under STC. A solar simulator is used to induce photon absorption within the device, while an applied voltage is scanned across the cell. The cell’s current response is measured and plotted against the applied voltage. Current is then converted to current density if the cell’s active area is known, facilitating direct comparison in performance between solar cells fabricated in various settings and to different cell dimensions. An example  $J - V$  curve is given in Figure 2.12. From the information given by the  $J - V$  characterization, the power conversion efficiency, PCE, can be computed as the ratio of power produced by the solar cell to the total power incident upon the cell (i.e. power out over power in).

Some parameters must be defined before the power output of the cell can be computed. The current produced by the cell at zero voltage divided by the cell’s total active area is the short circuit current density,  $J_{SC}$ , while the voltage at which zero current is detected is termed open circuit voltage,  $V_{OC}$ .  $V_{OC}$  can be predicted by the offset between the donor material’s HOMO and the acceptor material’s LUMO energy levels (taking into account a loss of approximately  $0.2 - 0.4 \text{ V}$  due to energy losses

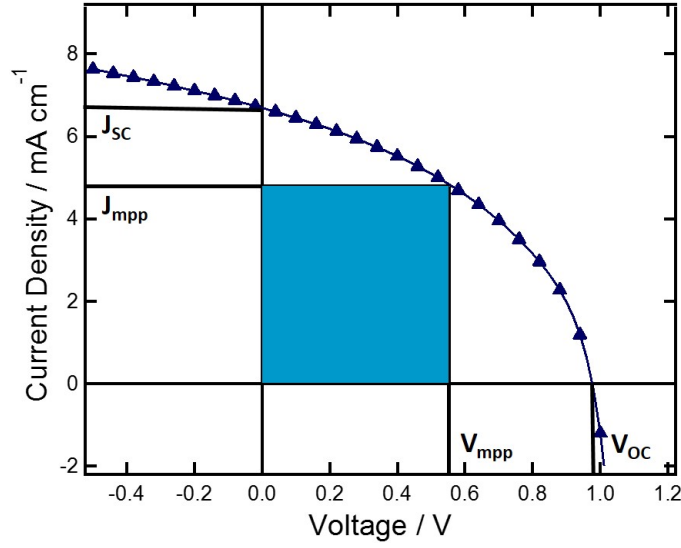


Figure 2.12: Example  $J - V$  curve for an organic solar cell measured under STC. The area in the blue box summarizes the maximum power produced by the cell, as well as giving a visual representation of the fill factor.  $J_{mpp}$  and  $V_{mpp}$  are the current and voltage maximum power points respectively.

that are described in more detail elsewhere<sup>103</sup>), while the short circuit current,  $I_{SC}$ , is a direct measurement of how well the cell can convert and extract incident photons to usable electric current.<sup>104</sup> To an extent, this can also be predicted based on the absorption spectrum of the active layer materials.<sup>105</sup> Figure 2.12 depicts the maximum power point which is used to calculate a solar cell's third important parameter: the fill factor (FF). FF gives a quantification for how “square” the current-voltage output of the cell is, giving insight into the charge extraction efficiency of the device. A higher FF corresponds to a  $J - V$  curve displaying strong square behavior, with a perfectly rectangular  $J - V$  curve representing a fill factor of 100%.<sup>106</sup> For reference, the cell pictured in Figure 2.12 has a fill factor of  $\sim 43\%$ . The PCE,  $\eta$ , of the solar cell is determined by calculating the ratio of maximum power output of the cell,  $P_{mpp}$ , to the input power,  $P_{in}$ , as follows:

$$\eta = \frac{P_{mpp}}{P_{in}} = \frac{AJ_{mpp}V_{mpp}}{P_{in}} = \frac{AJ_{SC}V_{OC}FF}{P_{in}} \quad (2.7)$$

where the fill factor is defined as:

$$FF = \frac{P_{mpp}}{AJ_{SC}V_{OC}} = \frac{J_{mpp}V_{mpp}}{J_{SC}V_{OC}} \quad (2.8)$$

where  $A$  is the active area of the solar cell.

A second useful characterization parameter for solar cells is plotting the external quantum efficiency (EQE), which quantifies the proportion of incident photons that are successfully collected as electrons at the device's electrodes. For a given wavelength, the EQE is defined as:

$$EQE = \frac{\# \text{ of collected electrons}}{\# \text{ of incident photons}} \quad (2.9)$$

EQE is important to the characterization of solar cells because the measurement quantifies a cell's spectral response, indicating whether or not a material system will respond highly to the solar spectrum.

Additionally, the spot size of the EQE measurement should be less than the active area of the solar cell device. Measuring EQE is especially useful because the  $J_{SC}$  for the solar cell can also be estimated by integrating the EQE spectrum over all measured wavelengths with the AM1.5G spectrum. This theoretical  $J_{SC}$  can then be compared to that measured under solar simulation to account for current measured from light absorbed outside the assumed active area of the cell, which may provide a boost in the measured  $J_{SC}$  value obtained from the  $J - V$  curve.

This concludes the discussion pertaining to the working principles and characterization of organic solar cells. The subsequent two sections will focus on developments of the donor and acceptor materials used in OPV research. The focus of this thesis is novel NDI-based acceptor materials, and the same donor polymer was used for all solar cells fabricated in this work, so the survey of existing literature pertaining to donor materials, Section 2.3.3.1, will be brief. This is then followed by a more in-depth overview of the recent progress in the development and performance of acceptor materials in Section 2.3.3.2.

### 2.3.3 Materials

A solution-processable organic semiconductor is composed of two essential components: a conjugated backbone and side chains. One of the key advantages of organic solar cells is their ability to be made using roll-to-roll processing techniques to reduce production costs and production time scales.<sup>107</sup> In order to ensure the solution processability of conjugated polymers in common organic solvents such as chlorobenzene and chloroform, flexible alkyl side chains are introduced to the polymer's structure. After the introduction of these solubility groups to the polymer's structure, it was believed the side chains only contribute to solubility in the solution-state, and have minimal effects on the final conformation or electronic properties of the polymer once it has been coated onto a substrate.<sup>108</sup> However, studies of the length and substituents used in side-chain groups have shown that they play a significant role in the final properties exhibited by the polymer.<sup>109–112</sup> For example, Piliago et al.<sup>109</sup> demonstrated that the configuration and length of the alkyl side chains influence several material properties. First, they synthesized *N*-alkylthieno[3,4-*c*]pyrrole-4,6-dione (TPD)-based polymers with various side chain configurations (Figure 2.13 (a)), and then compared their optical and photovoltaic properties. The side chain configurations included both linear (**P3**) and branched (**P1** and **P2**) geometries, with increasing side-chain lengths. As can be seen in Figure 2.13 (b), both the side chain geometry and length impact the final photovoltaic performance of the polymer. **P3**, which utilized linear side chains, exhibited the highest average power conversion efficiency of 6.6%, while **P1** only demonstrated an efficiency of 3.9%. The authors attribute these drastic differences in photovoltaic efficiency to changes in structural order and orientation of the polymer backbones, which are both responsible for influencing charge mobility in the device (see 2.3.1.1 for more information). While the work done by Piliago and coworkers was successful in demonstrating that side chains can have different geometries and lengths, both of which impact the final photovoltaic properties of the polymer, unfortunately they were not able to conclude that the side chains used for **P3** will always

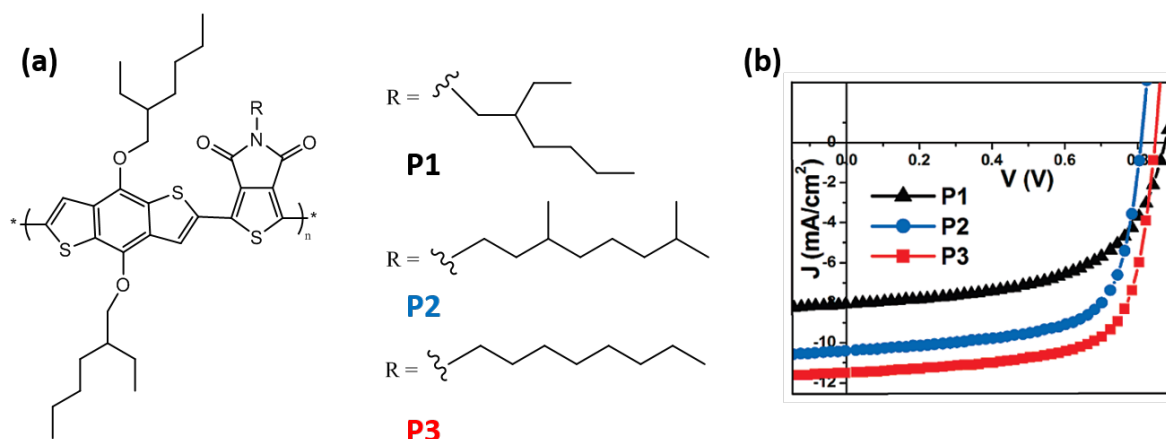


Figure 2.13: TPD-based polymers synthesized by Piliego and coworkers. Adapted with permission from *Journal of American Chemical Society*, 2010, 132 (22), pp 7595–7597. Copyright 2010 American Chemical Society.<sup>109</sup>

result in the most efficient performance for any polymeric material used in a solar cell. Several materials have been introduced since then, which have exhibited higher performance than 6.6%,<sup>3,113</sup> despite utilizing other side chain configurations, and while the side chains do play an important role in the final performance of a material, work has focused primarily on polymeric backbone design and substituent atoms.<sup>110,114</sup>

### 2.3.3.1 Donor materials

Most commonly paired with a C<sub>60</sub> derivative as the acceptor, polymeric materials have been the subject of extensive investigation when developing novel donor materials for organic solar cells.<sup>115–117</sup> There are several design strategies that have been employed in order to increase polymer performance, such as structure, side chain length and shape, and building blocks of the polymer.<sup>104,109,117,118</sup>

From 1993, when it was first introduced by Havinga and coworkers, a donor-acceptor framework has been widely used when developing novel donor materials.<sup>119</sup> This design strategy involves utilizing alternating electron-rich (donor) and electron-deficient (acceptor) units along the polymer's backbone. While it was originally developed to significantly reduce the polymers' band gap to less than 1 eV, in order to realize metallic behavior, the donor-acceptor framework has since been used to broaden the polymer's optical absorption spectrum to increase exciton generation.<sup>118</sup> The mechanisms behind the reduction in band gap are similar to the molecular orbital formation described in Section 2.2.1.1 and are as follows: after polymerization, there is an interaction between the HOMO of the donor unit with the HOMO of the acceptor unit, effectively creating two new HOMO energy states – one at a higher and one at a lower energy than the original HOMO energies. The same is true for the LUMO energy levels of the donor and acceptor units. After polymerization, the electrons are redistributed from their non-interacting orbitals to new, hybridized, orbitals of the polymer, which have a higher HOMO and lower LUMO energy, resulting in a narrower band gap.<sup>120</sup> This process is shown schematically in Figure 2.14. These so-called low-band gap polymers exhibit low onset absorption, between 800 and 900 nm, making them ideal absorbers for solar energy conversion, especially because fullerene-based

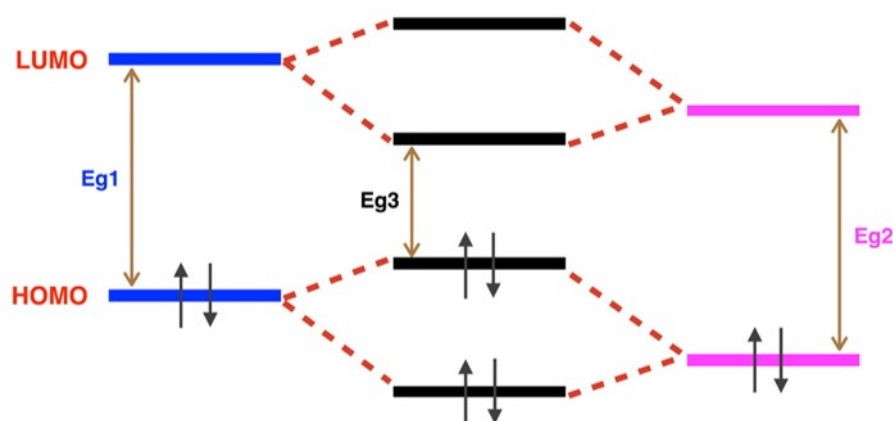


Figure 2.14: Simplified mechanism of band gap lowering by donor–acceptor interaction. The energy levels of the donor and acceptor units are shown on the left and right side of the diagram, respectively. Adapted with permission from Duo et al. *Chemical Reviews* 2015. 115(23) 12633-12665. Copyright (2015) American Chemical Society.<sup>120</sup>

acceptors contribute only marginally to the active-layer absorption spectrum.<sup>120–122</sup>

The most important donor polymer design strategy is arguably the proper selection of building blocks that make up the donor–acceptor framework. Several building blocks have been widely used to demonstrate high power conversion efficiencies, including: thieno[3,4-*b*]thiophene (TT), benzodithiophene (BDT), diketopyrrolopyrrole (DPP) and isoindigo (I).<sup>120</sup> Of these, the combination of TT and BDT is amongst the most successful, having been incorporated in polymers that have exhibited power conversion efficiencies above 10%.<sup>123–125</sup> This structure was first introduced in 2009 by Liang and coworkers, when they developed poly-((4,8-bis (octyloxy)-benzo-(1,2-*b*:4,5-*b'*) dithiophene-2,6-diyl)-(2-((dodecyloxy) carbonyl)-thieno-(3,4-*b*)-thiophenediyl)), or PTB1.<sup>126</sup> The molecular structure is shown in Figure 2.15 and follows the classic donor–acceptor, or push–pull, architecture, with the electron-accepting TT unit pictured on the left side of the polymer and the electron-donating BDT unit pictured on the right side.<sup>127</sup> The idea behind the design of this BDT-based polymer encapsulated four key rules: (1) it had to have a low band gap to ensure efficient visible absorption, (2) when paired with a fullerene-based acceptor, the LUMO of the polymer had to have sufficient alignment with the acceptor’s LUMO for efficient exciton dissociation, (3) the polymer had to have high hole mobility (i.e. the charge mobilities for the donor and acceptor materials had to be balanced), and (4) the energy difference between the donor polymer’s HOMO and acceptor material’s LUMO had to be sufficiently large in order to maximize the  $V_{OC}$  of the device.<sup>128</sup> Additionally, the TT unit was selected because its quinoidal structure (realized by incorporating additional flanking oxygen atoms to the side-chain) stabilized the planarity along the polymer’s backbone, leading to the key design-criteria of having a low-energy band gap, mentioned previously.<sup>126</sup> The rigid backbone also aided in improving the polymer’s  $\pi - \pi$  stacking efficiency, reducing the spacing between polymer backbones, which facilitates charge transfer between polymers and increases hole mobility in the material. At the time of initial publication, PTB1:PC<sub>71</sub>BM devices were amongst the most efficient, exhibiting power conversion efficiencies around 5.6%. Additionally, small changes to the structure of PTB1 led to an entire class of polymers which continue to be amongst the highest performing donor materials in organic solar cells, realizing device efficiencies surpassing

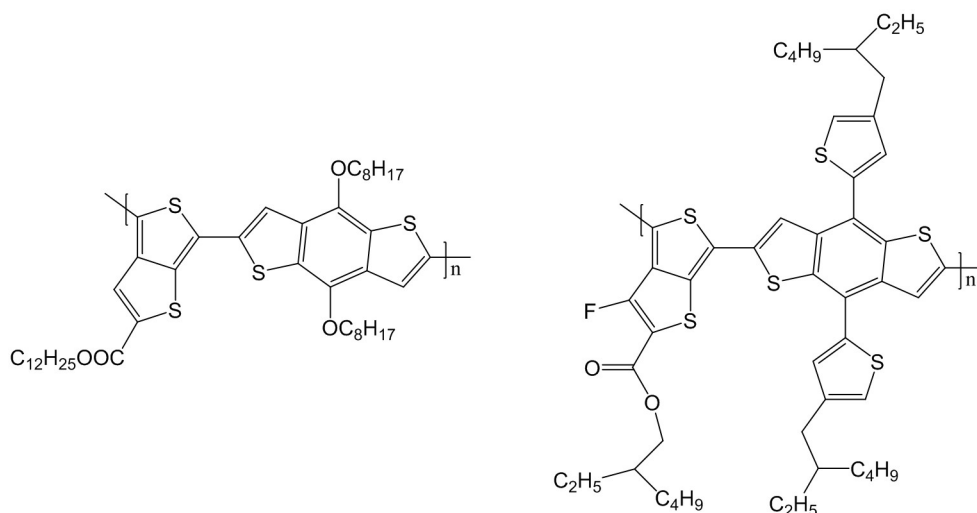


Figure 2.15: Molecular structures for PTB1 (left) and PTB7-Th (right).

14% in 2018.<sup>125, 128</sup>

One such high-performance material is poly[4,8-bis(5-(2-ethylhexyl)thiophene-2-yl)benzo[1,2-b;4,5-b']dithiophene-2,6-diyl-alt-(4-(2-ethylhexyl)-3-fluorothieno[3,4-b]thiophene)-2-carboxylate-2,6-diyl], or PTB7-Th, also known as PBDTTT-EFT (shown in Figure 2.15).<sup>113</sup> First introduced in 2013, PBDTTT-EFT is amongst the most popular donor polymers, with initial efficiencies reported approaching 10%. In fact, hundreds of research publications can be found that report work involving this material. For the novel acceptor materials studied in this thesis, all solar cells were fabricated using PBDTTT-EFT as the donor material due to: (1) its low optical band gap which results in a broad absorption profile, allowing for maximum visible photon absorption, (2) enhanced hole mobility due to increased  $\pi - \pi$  stacking efficiency resulting from the flanking thiophene units in the side chains, and (3) its lower HOMO energy level compared to other BDT and TT-containing polymers, which increases the energy difference between the HOMO of the donor and LUMO of the acceptor material resulting in a higher  $V_{OC}$ .<sup>113</sup> These reasons, along with the commercial availability of PBDTTT-EFT, make it an attractive donor material to use in conjunction with emerging acceptor materials.

### 2.3.3.2 Recent progress in acceptor materials

For many years, the active layer of a typical organic solar cell comprised a polymeric donor material and a fullerene-based acceptor.<sup>129</sup> This material combination has shown excellent device efficiencies throughout the history of organic solar cells exhibiting power conversion efficiencies up to 11.7%.<sup>130</sup> Despite these high efficiencies, there are several drawbacks associated with employing fullerene-based acceptors in organic solar cells. Despite having excellent electron mobilities, fullerene derivatives are costly, difficult to synthesize, have poor light-harvesting abilities, and low stability in air.<sup>1, 131, 132</sup> These pitfalls have a significant influence on the ability to fabricate organic solar cells that are competitive with other, more established forms of solar conversion technologies already on the market.

One potential alternative to costly fullerene acceptors are polymeric-based electron acceptor materials.<sup>133</sup> Around 2010, significant numbers of publications started

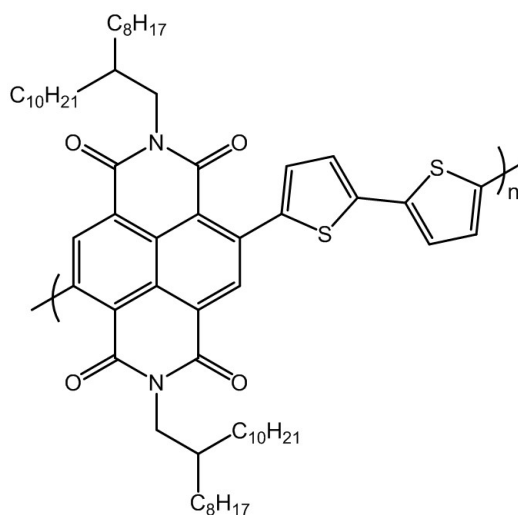


Figure 2.16: Molecular structure of PNDIT2, also known as N2200 or P(NDI2OD-T2).

to emerge that replaced fullerene-based acceptors with polymeric acceptors. These so-called all-polymer solar cells initially reported lower power conversion efficiencies than their fullerene-based counterparts,<sup>133</sup> however some systems soon started rivaling the efficiencies reported for polymer:fullerene systems. One such polymeric n-type material is PNDIT2, also known as N2200 or P(NDI2OD-T2), shown in Figure 2.16. This n-type polymer employs a naphthalene diimide moiety, with a bithiophene bridge as a linker. In 2009, PNDIT2 was first introduced in *Nature* as a high-mobility electron transporting material for organic field-effect transistors (OFETs), with transistors exhibiting electron mobilities  $> 0.1 \text{ cm}^2\text{V}^{-1}\text{s}^{-1}$ .<sup>134</sup> Additionally, due to its high electron mobility, PNDIT2 was soon employed as an acceptor material in all-polymer organic solar cells, with P3HT as the donor.<sup>135</sup> Unfortunately, this material combination exhibited very poor performance, with a maximum PCE of just 0.2%, which the authors attributed to significant geminate recombination and a non-ideal active layer morphology that exhibited domains as large as 1 micron. Fortunately, the search for an appropriate material blend that incorporated PNDIT2 did not end after these initial unfavorable results, and today, PNDIT2 is considered amongst the highest performing n-type polymeric materials for use in all-polymer organic solar cells. For example, in 2017, it was reported by Fan and coworkers<sup>136</sup> that it is possible to create an organic solar cell with greater than 10% efficiency when using PNDIT2 as an acceptor with a donor polymer that was designed specifically with the acceptor material in mind, ensuring the energy levels were properly aligned for maximized power conversion efficiency. Additionally, several other material systems have emerged that boast similar performance, further motivating the search for polymeric, non-fullerene acceptors.<sup>136, 137</sup>

However, there are notable drawbacks to employing polymeric acceptors in organic solar cells. For example, the synthesis of semiconducting polymers is cumbersome and complicated, influencing the quality of synthesized polymers, which are known to have high batch-to-batch variation, and thus limited reproducibility within devices.<sup>138</sup> The molecular weight of polymers used in organic solar cells is also known to significantly influence the device performance, impacting the appreciable optimization of these materials within solar cell devices.<sup>139</sup> The exploration of additional material classes for



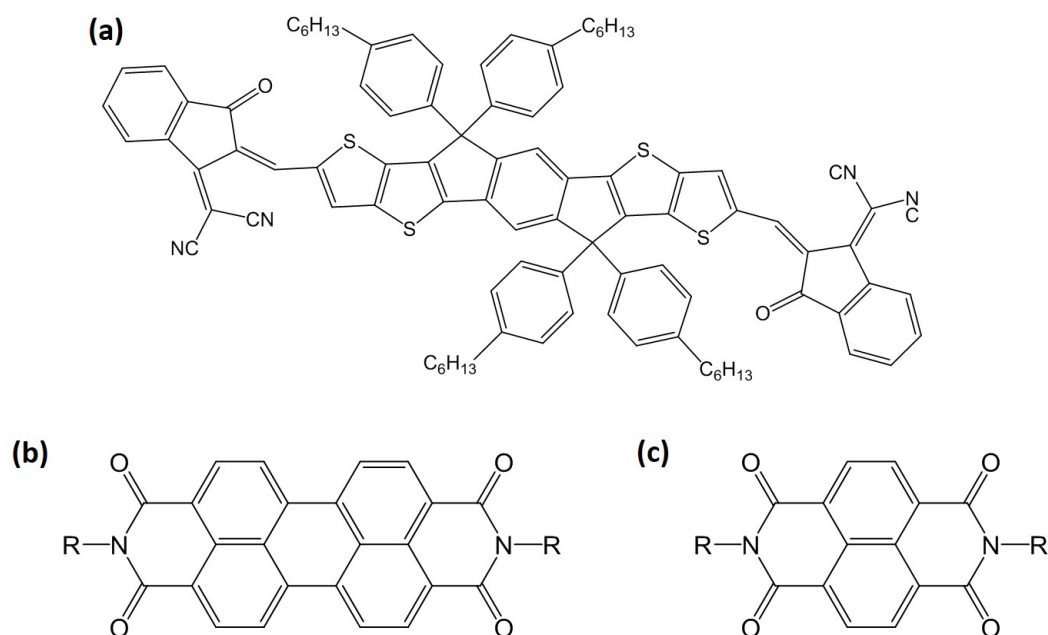


Figure 2.17: Molecular structures of (a) ITIC, (b) perylene diimide (PDI) and (c) naphthalene diimide (NDI).

use as acceptors in OPV is therefore warranted.

An alternative to both fullerene and polymeric acceptors are organic acceptor materials based on small molecular structures,<sup>131</sup> which have several advantages over fullerene-based acceptors. These include lower costs, relatively straight-forward synthesis, energy-level control, and, recently, it has been reported that small molecule acceptors are significantly less prone to degradation in air, compared to fullerenes.<sup>140</sup> They also have defined molecular structures limiting batch-to-batch variation, increased electron mobilities, and structural variation compared with their polymeric counterparts.<sup>141</sup> Further – and perhaps most importantly of all – small molecule-based acceptor materials have recently surpassed the performance of fullerene-based acceptors in several materials systems, including ones that employ BDT-based donor polymers. In fact, the present record single-junction organic solar cell power conversion efficiency is 15.7%, in a device that employs a donor-polymer, molecular-acceptor active layer.<sup>142</sup> These benefits over other types of acceptors, and especially the recently realized improved performance of small molecule over fullerene acceptors, warrant further investigation into novel small molecule materials as acceptors in organic solar cells.

As with polymeric donor materials, there are several popular conjugated building blocks used in small molecule acceptors (SMAs), including 9,9'-bifluorenylidene, benzothiadiazole (BT), diketopyrrolopyrrole (DPP), thieno[3,2-b]thiophene (TT), perylene diimide (PDI), and naphthalene diimide (NDI).<sup>141,143–145</sup> SMAs are classified by their building blocks and can be grouped into several different families including benzothiadiazole-based acceptors, rylene-based acceptors (under which NDI and PDI-based acceptors are classified) and acceptors based on an acceptor-donor-acceptor (A-D-A) skeleton.<sup>146,147</sup>

To-date, the most successful small molecule acceptors are part of the A-D-A family, which borrow a similar framework to donor-acceptor type polymers by incor-

porating alternating acceptor and donor-type building blocks along the backbone of the molecule.<sup>147</sup> In 2015, a novel A-D-A small molecule called 3,9-bis(2-methylene-(3-(1,1-dicyanomethylene)-indanone))-5,5,11,11-tetrakis(4-hexylphenyl)-dithieno[2,3-d:2',3'-d']-s-indaceno[1,2-b:5,6-b']dithiophene, or ITIC, was first published in a paper titled “An electron acceptor challenging fullerenes for efficient polymer solar cells.”<sup>145</sup> While the first publication relating to ITIC, the molecular structure of which is pictured in Figure 2.17, did not outperform the conversion efficiency of solar cells fabricated using a fullerene acceptor (6.8% compared to 7.5% PCE), systematic device optimization did indeed lead to higher efficiencies than fullerene-based solar cells.<sup>148</sup> The  $J-V$  and EQE curves for fully optimized devices using ITIC as the acceptor, with a DBT-based polymeric donor, are shown in Figure 2.18. Here, it is clearly demonstrated that both the  $J-V$  characteristics, as well as EQE curves exhibit stronger performance for solar cells fabricated using ITIC, compared to those made with PC<sub>71</sub>BM, and indeed PCE was optimized to 10.8%, compared to 7.5% for the fullerene-based device.<sup>148</sup>

There are several reasons why ITIC outperforms fullerene-based solar cells. First, the alternating A-D-A framework reduces the band gap of the molecule, which – as with polymeric donors – leads to increased absorption of visible photons. This means that, unlike fullerene-based acceptors, ITIC absorbs photons that contribute to the overall number of generated excitons. This is clearly visible in the EQE curve shown on the right side of Figure 2.18. The enhanced spectral response of ITIC therefore drastically increases the  $J_{SC}$  observed in solar cells, from 12.80 mA cm<sup>-2</sup> to 16.80 mA cm<sup>-2</sup> for PC<sub>71</sub>BM and ITIC-based devices, respectively. Second, the electronic tunability offered by SMAs enables favorable LUMO<sub>A</sub>-HOMO<sub>D</sub> energy level alignment, reducing loss and therefore resulting in an improvement in  $V_{OC}$ . Finally, the authors attribute the increase in FF for ITIC-based devices, from 68.2% in PC<sub>71</sub>BM-based devices, to 74.2%, to balanced charge mobilities between the donor and acceptor materials, reducing recombination events due to the build-up of charge carriers in the lower-mobility donor material. The demonstration of a non-fullerene acceptor that outperforms devices employing PC<sub>71</sub>BM justifies the continued search for materials that can push the PCE of organic solar cells to levels where commercialization is possible.

Another interesting, and widely studied molecular acceptor building block is PDI.<sup>144, 146, 147</sup> Prior to the discovery of ITIC, PDI-based SMAs received much attention due to initially high power conversion efficiencies when paired with established polymeric donor materials.<sup>131, 149–152</sup> Similarly to ITIC, the lower-lying LUMO energies of PDIs results in efficient exciton dissociation at the donor/acceptor interface with minimal energy loss, reflected in high  $V_{OC}$  values. Additionally, high mobilities associated with PDIs lead to efficient charge extraction at the electrodes.<sup>153</sup> Their planar molecular structure, depicted in Figure 2.17(b), however, promotes strong aggregation of these molecules in thin films, leading to domains much larger than the exciton diffusion length, impacting device performance.<sup>154</sup> Despite this, intuitive modification of the structure of PDI-based molecular acceptors to decrease aggregation has seen record device efficiencies above 10% PCE.<sup>155</sup> When paired with PBDTTT-EFT as the donor material, PDI-based acceptors have shown efficiencies approaching 9%.<sup>156</sup> One commonality between both these high-performing PDI-based molecular acceptors is their star shape, which incorporates a core donor-unit that is bound to three or four flanking PDI molecules. This molecular structure is key to achieving high efficiencies, because it distorts the planarity of the lone PDI molecule, disabling the efficient pack-

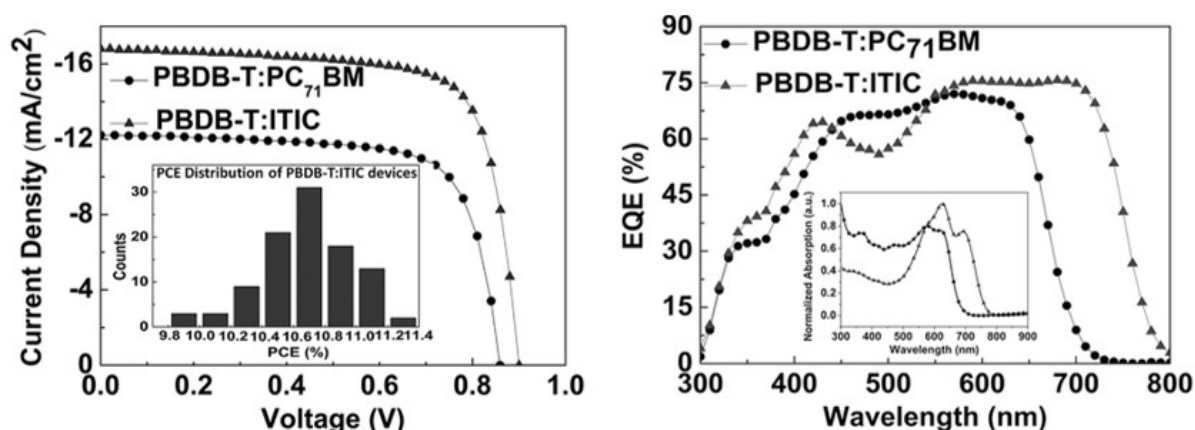


Figure 2.18: Current density versus voltage ( $J$ - $V$ ) curves histogram of PCE counts for 100 pieces of PBDB-T:ITIC-based cells (left). EQE curves and absorption spectra of PBDB-T:PC<sub>71</sub>BM and PBDB-T:ITIC blend film (right). Adapted with permission from Zhao, W. et al. *Advanced Materials*, 28, 2016, 4734–4739.<sup>148</sup>

ing that results in large domain sizes.

This concludes the general overview of the current status of emerging small molecule alternatives to fullerene acceptors for organic solar cells. The following subsection provides a more detailed review of the progress that has been made in the area of naphthalene diimide-based acceptors before and during the research presented in subsequent results chapters of this thesis was conducted.

### 2.3.3.3 Overview of NDI-based small molecule acceptors

As was mentioned in the Introduction Chapter, NDI-based small molecule acceptors are pertinent to this thesis. The NDI structure is shown in Figure 2.17(c). Although NDI-based polymeric acceptors have been studied extensively, primarily due to the high performance achieved using PNDIT2,<sup>136</sup> small molecule NDI acceptors have not received as much attention.<sup>152</sup> This is due to the significantly lower device efficiencies reported for polymeric donor:small molecule NDI acceptor active layers. For example, in a recent review article of small molecule acceptors, NDI-based acceptors are only briefly mentioned at the end of the extensive review, with the following statement: “Compared to the PDI-based molecules, the smaller fused-ring unit naphthalene diimide (NDI)-based small molecules were less successful as electron acceptors in solution-processed OPVs.”<sup>146</sup> A second review article states that “despite their success in polymeric materials, NDI-based small molecule acceptors are not widely studied. On the other hand, perylene diimide, another rylene-type dye, has reached impressive performances as a small molecule non-fullerene acceptor.”<sup>131</sup> This section provides an overview of a selection of NDI-based small molecule acceptors that have been reported in the literature, with the evolution of molecular architectures shown in Figure 2.19. Table 2.1 provides a summary of this overview by listing device performance parameters for the materials shown in Figure 2.19.

Until recently (2017), NDI-based small molecule acceptors showed little promise as n-type materials in organic solar cells, with device efficiencies rarely surpassing 2% PCE. These lower power conversion efficiencies are typically attributed to the efficient

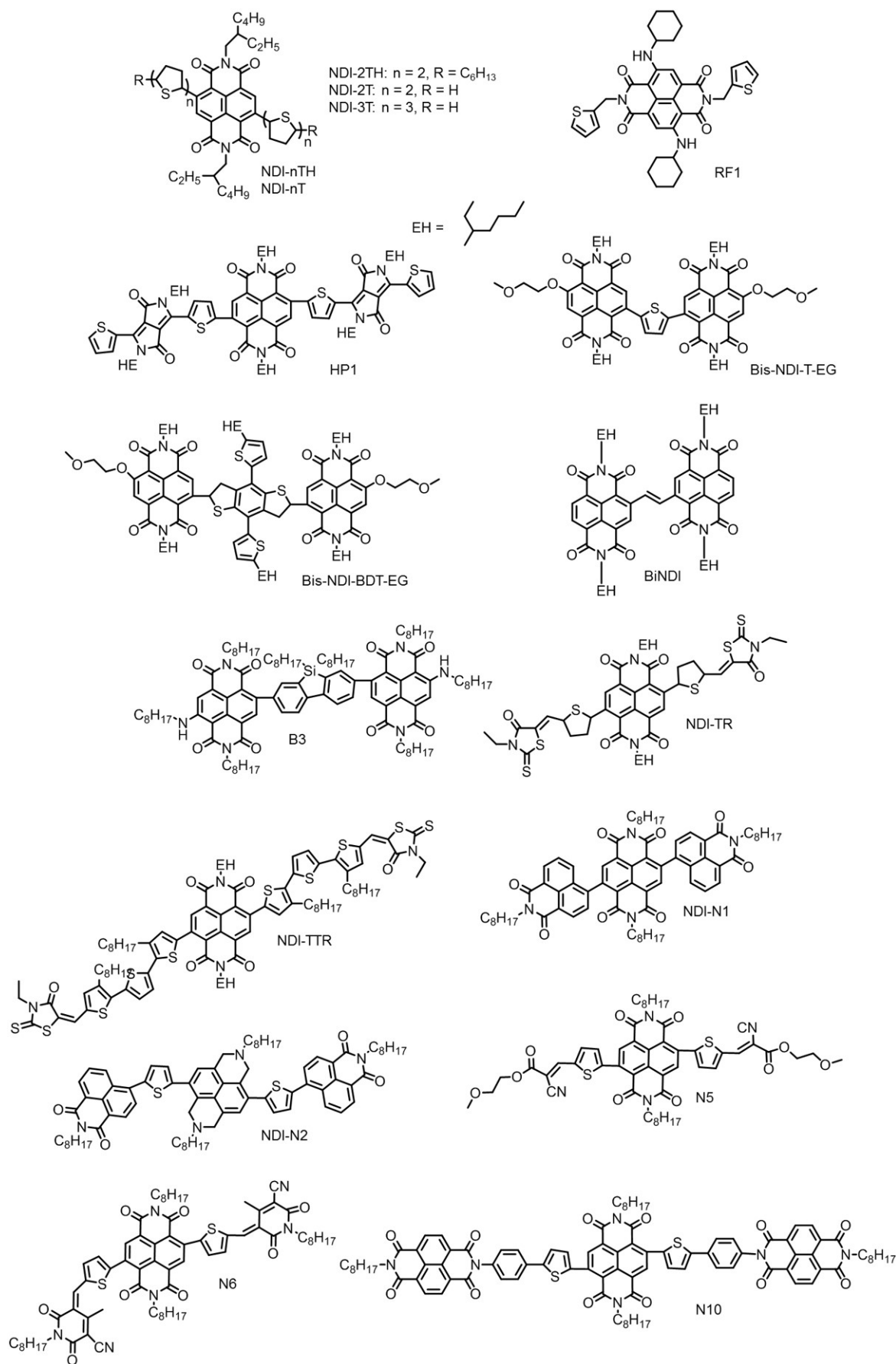


Figure 2.19: Molecular structures of NDI-based small molecule acceptors from the literature. Performance of devices fabricated with these acceptors are given in Table 2.1.

| Acceptor                      | Donor      | D:A   | Jsc<br>(mA cm <sup>-2</sup> ) | Voc<br>(V) | FF<br>(%) | PCE<br>(%) | Year |
|-------------------------------|------------|-------|-------------------------------|------------|-----------|------------|------|
| NDI-2T <sup>157</sup>         | P3HT       | 1:2   | 0.81                          | 0.71       | 34        | 0.17       | 2011 |
| NDI-3T <sup>157</sup>         | P3HT       | 1:3   | 0.45                          | 0.64       | 33        | 0.09       | 2011 |
| NDI-2TH <sup>157</sup>        | P3HT       | 1:1   | 3.43                          | 0.82       | 53        | 1.45       | 2011 |
| RF1 <sup>158</sup>            | P3HT       | 1:2.5 | 3.07                          | 0.69       | 45        | 0.96       | 2014 |
| HP1 <sup>159</sup>            | P3HT       | 1:1   | 2.15                          | 1.05       | 45        | 1.02       | 2014 |
| Bis-NDI-T-EG <sup>160</sup>   | PBDTTT-C-T |       | 2.70                          | 0.96       | 51        | 1.31       | 2014 |
| Bis-NDI-BDT-EG <sup>160</sup> | PBDTTT-C-T |       | 3.26                          | 0.95       | 40        | 1.24       | 2014 |
| BiNDI <sup>154</sup>          | PTB7       | 1:1   | 5.28                          | 0.75       | 60        | 2.31       | 2015 |
| B3 <sup>161</sup>             | P3HT       | 1:1   | 3.40                          | 0.64       | 53        | 1.16       | 2015 |
| NDI-TR <sup>162</sup>         | PBDTTT-EFT |       | 7.01                          | 0.64       | 69        | 2.97       | 2017 |
| NDI-TTR <sup>162</sup>        | PBDTTT-EFT |       | 2.24                          | 0.78       | 38        | 0.62       | 2017 |
| NDI-N1 <sup>163</sup>         | P3HT       | 1:1   | 6.13                          | 0.84       | 56        | 2.91       | 2017 |
| NDI-N2 <sup>163</sup>         | P3HT       | 1:1   | 8.58                          | 0.81       | 58        | 4.04       | 2017 |
| N5 <sup>164</sup>             | P3HT       | 1:1.2 | 7.03                          | 0.97       | 59        | 4.03       | 2017 |
| N6 <sup>164</sup>             | P3HT       | 1:1.2 | 10.78                         | 0.9        | 63        | 6.11       | 2017 |
| N10 <sup>165</sup>            | P3HT       | 1:1.2 | 12.08                         | 0.99       | 64        | 7.60       | 2018 |

Table 2.1: Average device parameters for previously published NDI-based small molecule acceptors, corresponding to the materials shown in Figure 2.19. The device architecture for all devices listed in the table was conventional, with PEDOT:PSS serving as the hole transporting material, with a top electrode made from aluminum.

packing of NDI molecules, which is even higher than that of PDI molecules, ensuing from their smaller size, which enables better planarity and stronger intermolecular interactions.<sup>146</sup> For example, Eilaf et al.<sup>157</sup> introduced a series of NDI-based small molecule acceptors that employs thiophene arms of various lengths (2-4 thiophene units) to an NDI core. They found that, for devices employing P3HT as the donor, the NDI acceptors with either two or four thiophenes as arms resulted in no photo-voltaic response, while an NDI acceptor with three thiophenes in the arms produced a device efficiency of 1.5%, after thermal annealing and adding 0.2% DIO to the active layer solution. The authors attribute this to a bicontinuous nanoscale morphology observed in the blends using the terthiophene arms, while bithiophene and tetrathiophene arms resulted in microscale phase separation, which hinders efficient exciton dissociation. Another example, from Liu and coworkers,<sup>154</sup> is an NDI-based acceptor that is comprised of two NDI moieties with a vinyl linker. At the time, in 2015, this material (paired with PTB7 as the donor) held the record for highest power conversion efficiency for this type of acceptor, with a maximum PCE of 2.4%. Spin cast active layer films initially showed large-scale phase separation, resulting in device efficiencies below 0.5%. However, the addition of just 0.5% DIO to the active layer solution enabled the acceptor-rich domains to form fibrillary crystals, significantly improving the electron mobility measured in space-charge limited current (SCLC) devices.

More recently, NDI-based small molecule acceptors have exhibited device efficiencies surpassing 6%,<sup>164</sup> and even 7%,<sup>165</sup> in 2018, by modifying the molecular structure to optimize active layer morphology. Interestingly, these high-performance NDI-based small molecule acceptors performed best in devices employing P3HT as the electron donating material, with devices exhibiting far higher efficiencies than conventional

P3HT:PCBM devices, which showed an efficiency of just over 3%,<sup>165</sup> and also significantly higher than the P3HT:PNDIT2 devices mentioned previously. For the case of the highest-performing material to-date, shown in Figure 2.19 as N10, the use of three NDI moieties linked via a thiophene exhibited exceptional device performance due to the acceptor's strong light harvesting ability, complimentary energy levels to P3HT, and its ability to form a favorable blend morphology for charge generation and extraction.<sup>165</sup> Ultimately, this led to device efficiencies surpassing 7.6% PCE, demonstrating that NDI-based small molecule acceptors have the potential to be competitive with not only fullerenes, but other non-fullerene acceptors such as the high-performing NDI-based polymer mentioned earlier.

In addition to unfavorable morphologies resulting from the high level of planarity in NDI-based molecules, lower device performance for NDI molecules is also attributed to a weak optical response in the visible region, due to a larger band gap compared to, for example, PDI-based molecules.<sup>146</sup> Here, the use of substituents, which are discussed below, can have a strong impact on the optical properties, resulting in extended absorption behavior into the visible range. Overall, despite their initial lower performance, the record-setting efficiencies achieved in NDI-based polymeric acceptors,<sup>136</sup> along with the benefits of employing small molecule acceptors, warranted further investigation into small-molecular architectures when the research reported in this thesis began, in the hopes of improving photovoltaic performance, as well as principle investigations into the NDI structure itself, to better understand how improvements in performance can be achieved through chemical modification of the structure.

#### 2.3.3.3.1 Substituent atoms

In chemistry, a substituent is an atom or group of atoms that replaces a different atom in a molecule. Research in materials used in organic electronic applications has highlighted the significance that such substituents can have on the optoelectronic properties of a material.<sup>114,166</sup> Substituents can be used to modify the behavior of almost every aspect of an organic material, from its energy levels<sup>167</sup> and resulting absorption profile,<sup>168</sup> to its morphology.<sup>169</sup> Often, the substitution of one atom for another can adjust the properties of the material to suit the application. This is because, sometimes, altering something as basic as the atomic size in a molecule, or its electronegativity, can significantly alter the local chemistry around the substitution, which can have ramifications when scaled up to the macro-scale. Over the past decade, functionalization of the NDI moiety through substituent atoms has received particular attention, primarily because it requires little synthetic effort.<sup>170</sup>

One potential location of substituent atoms or groups of atoms in NDIs is at the core of the molecule, at a flanking hydrogen position.<sup>162,163,167</sup> These are labeled as R<sub>1</sub> - R<sub>4</sub> in Figure 2.20. Commonly, a thiophene unit is placed here, either alone, or in conjunction with additional blocks such as benzoisoquinoline-dione, an example of which is shown in Figure 2.19 with NDI-N1 and NDI-N2.<sup>163</sup> In the case of adding a thiophene-benzoisoquinoline-dione unit (NDI-N2), the optical properties of the NDI-based small molecule are greatly effected. Thin-film absorption spectra show the modified molecule begins absorbing at ~680 nm,<sup>163</sup> while the parent molecule is known to begin absorbing at energies greater than ~415 nm.<sup>171</sup> This lowering in energy of the band gap is a result of both an increase in the HOMO, from -6.94 eV to

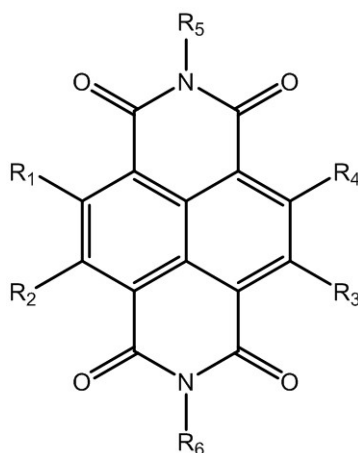


Figure 2.20: Molecular structure of the NDI moiety, with labeled core (R<sub>1</sub> - R<sub>4</sub>) and imide (R<sub>5</sub>, R<sub>6</sub>) positions suitable for functionalization.

-5.86 eV, and a decrease in the LUMO, from -3.67 eV to -4.10 eV, compared to the parent molecule. In devices, as stated previously, a reduction in band gap is favorable because additional photons that are absorbed by the acceptor can contribute to the current density. For the modified NDI molecule, atomic force microscopy images showed that the addition of a thiophene-benzisoquinoline-dione unit to the NDI moiety resulted in a donor:acceptor blend that exhibited “interweaving” and a smooth morphology. However, further characterization into the blend morphology is lacking. The good photovoltaic performance of this acceptor (>4% PCE when used in conjunction with P3HT as the donor) is attributed to a lower-energy absorption onset in blends, compared with blends employing PCBM. Additionally, the favorable energy level alignment between P3HT and the NDI-based SMA, compared to PCBM, resulted in improved  $V_{OC}$  (0.81 V compared to 0.56 V) values. Finally, the highest efficiency to-date for an organic solar cell comprised of a polymeric donor:NDI small molecule acceptor active layer utilizes N10 as the acceptor, pictured in Figure 2.19. Again, this material showed exceptional performance when paired with P3HT at over 7.6% – more than double the performance reported when PCBM is used as the acceptor. N10 incorporates three NDI moieties, linked via a thiophene-benzene bridge. The excellent performance of this acceptor is attributed to strong light-harvesting abilities, a favorable blend morphology, and preferential energy level alignment with P3HT. Work to improve the performance of N10 in fullerene-free devices is ongoing.<sup>165</sup>

Apart from molecular units such as thiophene, substituent atoms can also be incorporated at the flanking hydrogen positions.<sup>167, 172</sup> For example, Lee and coworkers,<sup>172</sup> introduced a series of core-chlorinated NDIs that showed improved field-effect mobilities and air stability compared to the parent molecule. The higher air stability is attributed to a lowering of the LUMO through electron-withdrawing chlorine groups, while improved electron mobility is attributed to reduced  $\pi - \pi$  stacking distance between molecules, facilitating charge transfer between adjacent molecules. Additional core-substituents that have been successfully incorporated into the NDI moiety include tin,<sup>173</sup> cyanide,<sup>174</sup> oxygen,<sup>175</sup> amine<sup>167, 176</sup> and sulfur,<sup>177</sup> all of which influence the optical and electronic properties of the NDI moiety. To expand upon this, Chapter 4 of this thesis focuses on the effect that oxygen, sulfur and amine have on NDI properties.

In addition to core substitution, it is possible to replace the imide oxygen atoms

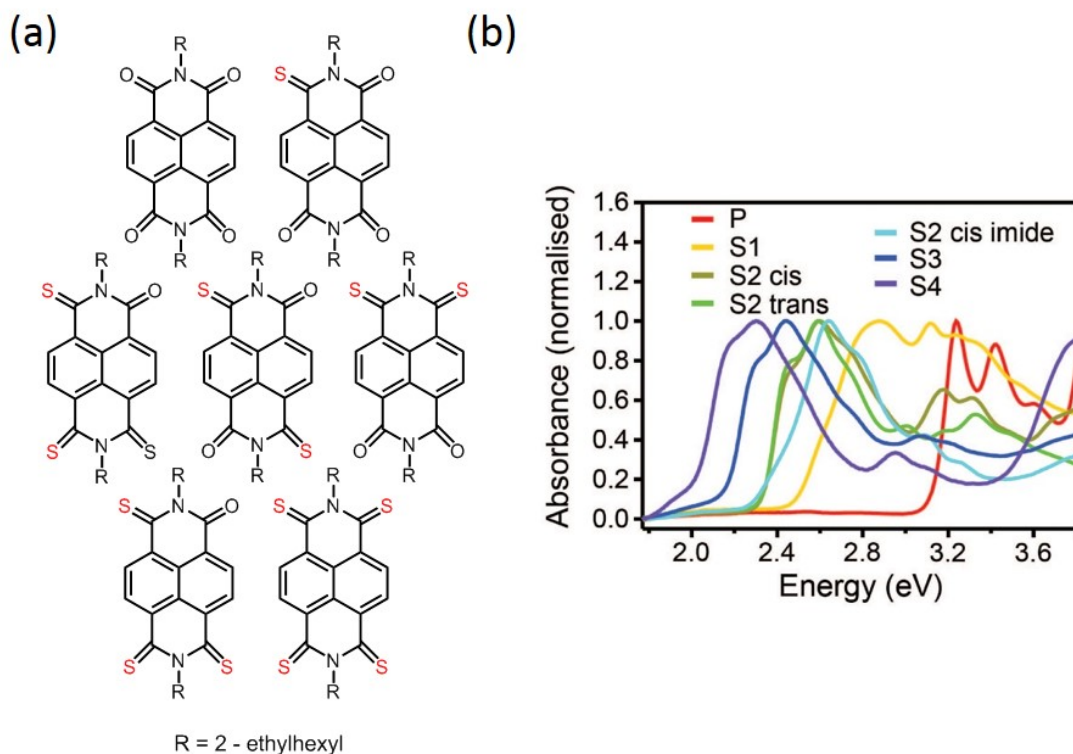


Figure 2.21: (a) The series of thionated NDI molecules, including the parent (top, left), 1S (top, right), 2S-*cis* (middle, left), 2S-*trans* (middle, center), 2S-*cis imide*, 3S (bottom, left) and 4S (bottom, right). (b) The thin-film UV-visible absorption spectra for the molecules. Adapted from Thionation of naphthalene diimide molecules: Thin-film microstructure and transistor performance, Adam Welford, et al., *Organic Electronics*, 53, Pages 287-295, Copyright (2018), with permission from Elsevier.<sup>171</sup>

in the NDI moiety. When sulfur replaces these oxygens, this modification is termed thionation. Thionation is useful because it is very controlled, meaning not all the oxygen atoms must necessarily be replaced. For NDI, this results in 7 possible configurations: the parent, with all four imide oxygens, 1S, with one sulfur substitution, 2S in a *cis*, *trans*, and *cis imide* configuration, 3S and 4S. These are shown in Figure 2.21 (a). Figure 2.21 (b) provides the solid-state UV-visible absorption spectra (discussed in more detail in Section 3.2.1.2), which clearly demonstrates strong changes in the optical response of NDI-based molecules with various degrees of thionation.<sup>171</sup> Thionation can therefore be seen as a potential strategy to manipulate the energy levels of the NDI moiety, in order to improve performance as acceptors in organic solar cells. Chapter 6 of this thesis experimentally explores the effect that thionation has on the performance of NDI-based solar cells, while Chapter 7 utilizes DFT-based calculations to predict and understand the changes in electronic structure with increasing thionation.

This concludes the review of the literature that is pertinent to this thesis. The following chapter, Chapter 3, provides an introduction and details on the experimental methods used in this thesis.





# References

- [1] J. Roncali, "Molecular bulk heterojunctions: An emerging approach to organic solar cells," *Accounts of Chemical Research*, vol. 42, no. 11, pp. 1719–1730, 2009.
- [2] Z. He, C. Zhong, S. Su, M. Xu, H. Wu, and Y. Cao, "Enhanced power-conversion efficiency in polymer solar cells using an inverted device structure," *Nature Photonics*, vol. 6, no. 9, pp. 593–597, 2012.
- [3] Y. Liang, Z. Xu, J. Xia, S. T. Tsai, Y. Wu, G. Li, C. Ray, and L. Yu, "For the bright future-bulk heterojunction polymer solar cells with power conversion efficiency of 7.4%," *Advanced Materials*, vol. 22, no. 20, pp. 135–138, 2010.
- [4] J. Gilot, I. Barbu, M. M. Wienk, and R. a. J. Janssen, "The use of ZnO as optical spacer in polymer solar cells: Theoretical and experimental study," *Applied Physics Letters*, vol. 91, no. 11, pp. 1–4, 2007.
- [5] G. Li, C.-W. Chu, V. Shrotriya, J. Huang, and Y. Yang, "Efficient inverted polymer solar cells," *Applied Physics Letters*, vol. 88, no. 10, pp. 253503–233303, 2006.
- [6] G. Yu, J. Gao, J. C. Hummelen, F. Wudl, and A. J. Heeger, "Polymer photovoltaic cells - enhanced efficiencies via a network of internal donor-acceptor heterojunctions," *Science*, vol. 270, pp. 1789–1791, 1995.
- [7] V. Shrotriya, G. Li, Y. Yao, C.-W. Chu, and Y. Yang, "Transition metal oxides as the buffer layer for polymer photovoltaic cells," *Applied Physics Letters*, vol. 88, no. 7, p. 073508, 2006.
- [8] C. W. Tang, "Two-layer organic photovoltaic cell," *Applied Physics Letters*, vol. 48, no. 2, p. 183, 1986.
- [9] R. J. Ouellette and J. D. Rawn, "Structure and bonding in organic compounds," in *Organic Chemistry*, pp. 1–39, Elsevier, 2014.
- [10] M. Pope and C. E. Swenberg, "Optical properties of organic molecules and crystals," in *Electronic Processes in Organic Crystals and Polymers*, pp. 1–180, New York City: Oxford University Press, 2nd ed., 1999.
- [11] J. E. Boschker, R. Wang, and R. Calarco, "GeTe: a simple compound blessed with a plethora of properties," *CrystEngComm*, vol. 19, no. 36, pp. 5324–5335, 2017.
- [12] R. Peierls, *Quantum Theory of Solids*. London: Oxford University Press, 1955.

- [13] H. Frohlich, “On the Theory of Superconductivity: The One-Dimensional Case,” *Proceedings of the Royal Society A: Mathematical, Physical and Engineering Sciences*, vol. 223, no. 1154, pp. 296–305, 1954.
- [14] T. Kennedy and E. Lieb, “Proof of the Peierls instability in one dimension,” *Physical Review Letters*, vol. 59, no. 12, pp. 1309–1312, 1987.
- [15] J. Pouget and B. Hennion, “The charge-density wave instability in quasi one-dimensional conductors,” *Phase Transitions*, vol. 30, no. 1-4, 1991.
- [16] S. Günes, H. Neugebauer, and N. S. Sariciftci, “Conjugated polymer-based organic solar cells,” *Chemical Reviews*, vol. 107, no. 4, pp. 1324–1338, 2007.
- [17] M. Knupfer, “Exciton binding energies in organic semiconductors,” *Applied Physics A: Materials Science and Processing*, vol. 77, no. 5, pp. 623–626, 2003.
- [18] A. Köhler and H. Bässler, “Triplet states in organic semiconductors,” *Materials Science and Engineering: R*, vol. 66, no. 4-6, pp. 71–109, 2009.
- [19] G. Klein, R. Voltz, and M. Schott, “On singlet exciton fission in anthracene and tetracene at 77°K,” *Chemical Physics Letters*, vol. 19, pp. 391–394, apr 1973.
- [20] W. Brutting, C. Adachi, and R. J. D. Holmes, *Physics of Organic Semiconductors*. Wiley-VCH, 2012.
- [21] N. J. Turro, V. Ramamurthy, and J. C. Scaiano, “Modern molecular photochemistry of organic molecules,” *Photochemistry and Photobiology*, vol. 88, no. 4, pp. 1033–1033, 2012.
- [22] J. Benduhn, F. Piersimoni, G. Londi, A. Kirch, J. Widmer, C. Koerner, D. Beljonne, D. Neher, D. Spoltore, and K. Vandewal, “Impact of triplet excited states on the open-circuit voltage of organic solar cells,” *Advanced Energy Materials*, vol. 8, no. 21, p. 1800451, 2018.
- [23] L. Dou, J. You, Z. Hong, Z. Xu, G. Li, R. A. Street, and Y. Yang, “25th anniversary article: A decade of organic/polymeric photovoltaic research,” *Advanced Materials*, vol. 25, no. 46, pp. 6642–6671, 2013.
- [24] N. Zhou and A. Facchetti, “Charge Transport and Recombination in Organic Solar Cells (OSCs),” in *Organic and Hybrid Solar Cells*, pp. 19–52, Cham: Springer, 2014.
- [25] J. Nelson, “Polymer:fullerene bulk heterojunction solar cells,” *Materials Today*, vol. 14, no. 10, pp. 462–470, 2011.
- [26] V. Coropceanu, J. Cornil, D. A. da Silva, Y. Olivier, R. Silbey, and J. L. Bredas, “Charge transport in organic semiconductors,” *Chemical Reviews*, vol. 107, no. 5, p. 2165, 2007.
- [27] O. D. Jurchescu, J. Baas, and T. T. M. Palstra, “Effect of impurities on the mobility of single crystal pentacene,” *Applied Physics Letters*, vol. 84, no. 16, pp. 3061–3063, 2004.

- [28] A. A. Günther, J. Widmer, D. Kasemann, and K. Leo, “Hole mobility in thermally evaporated pentacene: Morphological and directional dependence,” *Applied Physics Letters*, vol. 106, no. 23, 2015.
- [29] T. Holstein, “Studies of polaron motion,” *Annals of Physics*, vol. 8, no. 3, pp. 343–389, 1959.
- [30] G. Horowitz, “Organic field-effect transistors,” *Advanced Materials*, vol. 10, no. 5, pp. 365–377, 1998.
- [31] R. A. Marcus, “Electron Transfer Reactions in Chemistry: Theory and Experiment (Nobel Lecture),” *Angewandte Chemie International Edition in English*, vol. 32, no. 8, pp. 1111–1121, 1993.
- [32] A. Miller and E. Abrahams, “Impurity conduction at low concentrations,” *Physical Review*, vol. 120, no. 3, pp. 745–755, 1960.
- [33] S. Applications and M. A. Green, “Solar cells - operating principles, technology and system applications,” *Solar Energy*, vol. 28, no. 5, p. 447, 1982.
- [34] D. Chirvase, Z. Chiguvare, M. Knipper, J. Parisi, V. Dyakonov, and J. C. Hummelen, “Temperature dependent characteristics of poly(3 hexylthiophene)-fullerene based heterojunction organic solar cells,” *Journal of Applied Physics*, vol. 93, no. 6, pp. 3376–3383, 2003.
- [35] P. W. M. Blom, V. D. Mihailetschi, L. J. A. Koster, and D. E. Markov, “Device physics of polymer:fullerene bulk heterojunction solar cells,” *Advanced Materials*, vol. 19, no. 12, pp. 1551–1566, 2007.
- [36] J. C. Bernède, “Organic photovoltaic cells: History, principle and techniques,” *Journal of the Chilean Chemical Society*, vol. 53, no. 3, pp. 1549–1564, 2008.
- [37] J.-L. Bredas, “When electrons leave holes in organic solar cells,” *Science*, vol. 343, no. 6170, pp. 492–493, 2014.
- [38] R. M. Metzger, *Unimolecular and supramolecular electronics I*, vol. 312. Springer, 2012.
- [39] H. Spanggaard and F. C. Krebs, “A brief history of the development of organic and polymeric photovoltaics,” *Solar Energy Materials and Solar Cells*, vol. 83, no. 2-3, pp. 125–146, 2004.
- [40] N. S. Sariciftci, L. Smilowitz, A. J. Heeger, and F. Wudi, “Photoinduced electron transfer from a conducting polymer to buckminsterfullerene,” *Science*, vol. 258, no. 5087, pp. 1474–1476, 1992.
- [41] A. A. Bakulin, A. Rao, V. G. Pavelyev, P. H. Van Loosdrecht, M. S. Pshenichnikov, D. Niedzialek, J. Cornil, D. Beljonne, and R. H. Friend, “The role of driving energy and delocalized states for charge separation in organic semiconductors,” *Science*, vol. 335, no. 6074, pp. 1340–1344, 2012.
- [42] F. C. Krebs, *Polymeric solar cells : materials, design, manufacture*. Lancaster, Pennsylvania: DEStech Publications, Inc., 2010.

- [43] T. M. Clarke and J. R. Durrant, "Charge photogeneration in organic solar cells," *Chemical Reviews*, vol. 110, no. 11, pp. 6736–6767, 2010.
- [44] A. C. Jakowetz, M. L. Böhm, J. Zhang, A. Sadhanala, S. Huettnner, A. A. Bakulin, A. Rao, and R. H. Friend, "What controls the rate of ultrafast charge transfer and charge separation efficiency in organic photovoltaic blends," *Journal of the American Chemical Society*, vol. 138, no. 36, pp. 11672–11679, 2016.
- [45] S. K. Pal, T. Kesti, M. Maiti, F. Zhang, O. Inganäs, S. Hellström, M. R. Andersson, F. Oswald, F. Langa, T. Osterman, T. Pascher, A. Yartsev, and V. Sundström, "Geminate charge recombination in polymer/fullerene bulk heterojunction films and implications for solar cell function," *Journal of the American Chemical Society*, vol. 132, no. 35, pp. 12440–12451, 2010.
- [46] D. Credgington, F. C. Jamieson, B. Walker, T. Q. Nguyen, and J. R. Durrant, "Quantification of geminate and non-geminate recombination losses within a solution-processed small-molecule bulk heterojunction solar cell," *Advanced Materials*, vol. 24, no. 16, pp. 2135–2141, 2012.
- [47] J.-T. Shieh, C.-H. Liu, H.-F. Meng, S.-R. Tseng, Y.-C. Chao, and S.-F. Horng, "The effect of carrier mobility in organic solar cells," *Journal of Applied Physics*, vol. 107, no. 8, p. 084503, 2010.
- [48] M. M. Mandoc, L. J. A. Koster, and P. W. M. Blom, "Optimum charge carrier mobility in organic solar cells," *Applied Physics Letters*, vol. 90, no. 93, pp. 133504–133508, 2007.
- [49] H. Dong, X. Fu, J. Liu, Z. Wang, and W. Hu, "25th anniversary article: Key points for high-mobility organic field-effect transistors," *Advanced Materials*, vol. 25, no. 43, pp. 6158–6183, 2013.
- [50] V. Skrypnichuk, G.-J. Wetzelaer, P. Gordiichuk, S. Mannsfeld, A. Hermann, M. Toney, and D. Barbero, "Ultrahigh mobility in an organic semiconductor by vertical chain alignment," *Advanced Materials*, vol. 28, no. 12, pp. 2359–2366, 2016.
- [51] Y. Yao, H. Dong, and W. Hu, "Charge transport in organic and polymeric semiconductors for flexible and stretchable devices," *Advanced Materials*, pp. n/a–n/a, 2015.
- [52] A. Salleo, "Charge transport in polymeric transistors," *Materials Today*, vol. 10, no. 3, pp. 38–45, 2007.
- [53] T. A. Skotheim, *Handbook of conducting polymers*. M. Dekker, 1986.
- [54] H. Spanggaard and F. C. Krebs, "A brief history of the development of organic and polymeric photovoltaics," *Solar Energy Materials & Solar Cells*, vol. 83, pp. 125–146, 2004.
- [55] D. Caughey and R. Thomas, "Carrier mobilities in silicon empirically related to doping and field," *Proceedings of the IEEE*, vol. 55, no. 12, pp. 2192–2193, 1967.

- [56] V. D. Mihailetschi, J. Wildeman, and P. W. Blom, "Space-charge limited photocurrent," *Physical Review Letters*, vol. 94, no. 12, p. 126602, 2005.
- [57] Y. Zang, C. Z. Li, C. C. Chueh, S. T. Williams, W. Jiang, Z. H. Wang, J. S. Yu, and A. K. Y. Jen, "Integrated molecular, interfacial, and device engineering towards high-performance non-fullerene based organic solar cells," *Advanced Materials*, pp. 5708–5714, 2014.
- [58] B. R. Weinberger, M. Akhtar, and S. C. Gau, "Polyacetylene photovoltaic devices," *Synthetic Metals*, vol. 4, no. 3, pp. 187–197, 1982.
- [59] J. Tsukamoto, H. Ohigashi, K. Matsumura, and A. Takahashi, "A schottky barrier type solar cell using polyacetylene," *Japanese Journal of Applied Physics*, vol. 20, pp. L127–L129, 1981.
- [60] S. Kouijzer, J. J. Michels, M. van den Berg, V. S. Gevaerts, M. Turbiez, M. M. Wienk, and R. A. J. Janssen, "Predicting morphologies of solution processed polymer:fullerene blends," *Journal of the American Chemical Society*, vol. 135, no. 32, pp. 12057–12067, 2013.
- [61] P. J. Flory, "Thermodynamics of high polymer solutions," *Journal of Chemical Physics*, vol. 10, no. 51, pp. 51–61, 1941.
- [62] M. L. Huggins, "Thermodynamic properties of solutions of long-chain compounds," *Annals of the New York Academy of Sciences*, vol. 43, no. 1, pp. 1–32, 1942.
- [63] S. Nilsson, A. Bernasik, A. Budkowski, and E. Moons, "Morphology and Phase Segregation of Spin-Casted Films of Polyfluorene/PCBM Blends," *Macromolecules*, vol. 40, no. 23, pp. 8291–8301, 2007.
- [64] Z. Xu, L.-M. Chen, G. Yang, C.-H. Huang, J. Hou, Y. Wu, G. Li, C.-S. Hsu, and Y. Yang, "Vertical phase separation in poly(3-hexylthiophene):fullerene derivative blends and its advantage for inverted structure solar cells," *Advanced Functional Materials*, vol. 19, no. 8, pp. 1227–1234, 2009.
- [65] K. Sun, Z. Xiao, E. Hanssen, M. F. G. Klein, H. H. Dam, M. Pfaff, D. Gerthsen, W. W. H. Wong, and D. J. Jones, "The role of solvent vapor annealing in highly efficient air-processed small molecule solar cells," *Journal of Materials Chemistry A*, vol. 2, no. 24, p. 9048, 2014.
- [66] P. Karagiannidis, D. Georgiou, C. Pitsalidis, A. Laskarakis, and S. Logothetidis, "Evolution of vertical phase separation in P3HT:PCBM thin films induced by thermal annealing," *Materials Chemistry and Physics*, vol. 129, no. 3, pp. 1207–1213, 2011.
- [67] A. J. Parnell, A. J. Cadby, O. O. Mykhaylyk, A. D. F. Dunbar, P. E. Hopkinson, A. M. Donald, and R. A. L. Jones, "Nanoscale phase separation of P3HT:PCBM thick films as measured by small-angle X-ray scattering," *Macromolecules*, vol. 44, no. 16, pp. 6503–6508, 2011.

- [68] J. Klein, T. Kerle, F. Zink, and E. Eiser, "Segmental interaction parameters of binary polymer mixtures evaluated from binodals and from surface-degregation profiles: comparison with small-angle neutron scattering," *Macromolecules*, vol. 33, no. 4, pp. 1298–1305, 2000.
- [69] W. H. Lee, D. H. Kim, J. H. Cho, Y. Jang, J. A. Lim, D. Kwak, and K. Cho, "Change of molecular ordering in soluble acenes via solvent annealing and its effect on field-effect mobility," *Applied Physics Letters*, vol. 91, no. 9, p. 092105, 2007.
- [70] H. Tang, G. Lu, L. Li, J. Li, Y. Wang, and X. Yang, "Precise construction of PCBM aggregates for polymer solar cells via multi-step controlled solvent vapor annealing," *Journal of Materials Chemistry*, vol. 20, no. 4, pp. 683–688, 2010.
- [71] S. Miller, G. Fanchini, Y.-Y. Lin, C. Li, C.-W. Chen, W.-F. Su, and M. Chhowalla, "Investigation of nanoscale morphological changes in organic photovoltaics during solvent vapor annealing," *Journal of Materials Chemistry*, vol. 18, no. 3, pp. 306–312, 2008.
- [72] J. Peet, C. Soci, R. C. Coffin, T. Q. Nguyen, A. Mikhailovsky, D. Moses, and G. C. Bazan, "Method for increasing the photoconductive response in conjugated polymer/fullerene composites," *Applied Physics Letters*, vol. 89, no. 25, p. 252105, 2006.
- [73] J. K. Lee, W. L. Ma, C. J. Brabec, J. Yuen, J. S. Moon, J. Y. Kim, K. Lee, G. C. Bazan, and A. J. Heeger, "Processing additives for improved efficiency from bulk heterojunction solar cells," *Journal of the American Chemical Society*, vol. 130, no. 11, pp. 3619–3623, 2008.
- [74] G. Li, C. W. Chu, V. Shrotriya, J. Huang, and Y. Yang, "Efficient inverted polymer solar cells," *Applied Physics Letters*, vol. 88, no. 25, pp. 23–25, 2006.
- [75] Y. Yang, *Progress in High-Efficient Solution Process Organic Photovoltaic Devices*. Heidelberg: Springer, 1 ed., 2015.
- [76] P. Heremans, D. Cheyns, and B. P. Rand, "Strategies for increasing the efficiency of heterojunction organic solar cells: Material selection and device architecture," *Accounts of Chemical Research*, vol. 42, no. 11, pp. 1740–1747, 2009.
- [77] M. Y. Chan, C. S. Lee, S. L. Lai, M. K. Fung, F. L. Wong, H. Y. Sun, K. M. Lau, and S. T. Lee, "Efficient organic photovoltaic devices using a combination of exciton blocking layer and anodic buffer layer," *Journal of Applied Physics*, vol. 100, no. 89, pp. 243905–163501, 2006.
- [78] M. D. Irwin, D. B. Buchholz, A. W. Hains, R. P. H. Chang, and T. J. Marks, "p-Type semiconducting nickel oxide as an efficiency-enhancing anode interfacial layer in polymer bulk-heterojunction solar cells," *Proceedings of the National Academy of Sciences*, vol. 105, no. 8, pp. 2783–2787, 2008.
- [79] S. A. Paniagua, P. J. Hotchkiss, S. C. Jones, S. R. Marder, A. Mudalige, F. S. Marrikar, J. E. Pemberton, and N. R. Armstrong, "Phosphonic acid modification of indium tin oxide electrodes: Combined XPS/UPS/contact angle studies," *The Journal of Physical Chemistry C*, vol. 112, no. 21, pp. 7809–7817, 2008.

- [80] R. Steim, F. R. Kogler, and C. J. Brabec, "Interface materials for organic solar cells," *Journal of Materials Chemistry*, vol. 20, no. 13, p. 2499, 2010.
- [81] E. L. Ratcliff, B. Zacher, and N. R. Armstrong, "Selective interlayers and contacts in organic photovoltaic cells," *Journal of Physical Chemistry Letters*, vol. 2, no. 11, pp. 1337–1350, 2011.
- [82] P. Würfel, *Physics of Solar Cells: from Principles to New Concepts*. Weinheim, Germany: Wiley-VCH, 2005.
- [83] H. Taniguchi, M. Konagai, K. S. Lim, P. Sichanugrist, K. Komori, and K. Takahashi, "Junction Properties of nip and pin amorphous Si solar cells prepared by a glow discharge in pure silane," *Japanese Journal of Applied Physics*, vol. 21, no. S2, pp. 219–224, 1982.
- [84] F. M. Li, G.-W. Hsieh, S. Dalal, M. C. Newton, J. E. Stott, P. Hiralal, A. Nathan, P. A. Warburton, H. E. Unalan, P. Beecher, A. J. Flewitt, I. Robinson, G. Amaratunga, and W. I. Milne, "Zinc oxide nanostructures and high electron mobility nanocomposite thin film transistors," *IEEE Transactions on Electron Devices*, vol. 55, no. 11, pp. 3001–3011, 2008.
- [85] F. Wang, X. Qiao, T. Xiong, and D. Ma, "The role of molybdenum oxide as anode interfacial modification in the improvement of efficiency and stability in organic light-emitting diodes," *Organic Electronics*, vol. 9, no. 6, pp. 985–993, 2008.
- [86] K. Walzer, B. Maennig, M. Pfeiffer, and K. Leo, "Highly efficient organic devices based on electrically doped transport layers," *Chemical Reviews*, vol. 107, no. 4, pp. 1233–1271, 2007.
- [87] J. Meiss, C. L. Uhrich, K. Fehse, S. Pfuetzner, M. K. Riede, and K. Leo, "Transparent electrode materials for solar cells," in *Photonics for Solar Energy Systems II* (A. Gombert, ed.), vol. 7002, p. 700210, International Society for Optics and Photonics, 2008.
- [88] Aldrich, "Indium tin oxide coated glass slide," <https://www.sigmaaldrich.com/catalog/product/aldrich/636916?lang=en&region=AU>, 2018.
- [89] M. P. de Jong, L. J. van IJzendoorn, and M. J. A. de Voigt, "Stability of the interface between indium-tin-oxide and poly(3,4-ethylenedioxythiophene)/poly(styrenesulfonate) in polymer light-emitting diodes," *Applied Physics Letters*, vol. 77, no. 14, p. 2255, 2000.
- [90] Y. Şahin, S. Alem, R. De Bettignies, and J. M. Nunzi, "Development of air stable polymer solar cells using an inverted gold on top anode structure," *Thin Solid Films*, vol. 476, no. 2, pp. 340–343, 2005.
- [91] J. Feng-Xing, X. Jing-Kun, L. Bao-Yang, X. Yu, H. Rong-Jin, and L. Lai-Feng, "Thermoelectric Performance of Poly(3,4-ethylenedioxythiophene):Poly(styrenesulfonate)," *Chinese Physical Letters*, vol. 25, no. 6, pp. 2202–2205, 2008.



- [92] T. Nyberg, “An alternative method to build organic photodiodes,” *Synthetic Metals*, vol. 140, no. 2, pp. 281–286, 2004.
- [93] A. C. Arias, M. Granström, D. S. Thomas, K. Petritsch, and R. H. Friend, “Doped conducting-polymer–semiconducting-polymer interfaces: Their use in organic photovoltaic devices,” *Physical Review B*, vol. 60, no. 3, pp. 1854–1860, 1999.
- [94] S. Lattante, “Electron and hole transport layers: Their use in inverted bulk heterojunction polymer solar cells,” *Electronics*, vol. 3, no. 1, pp. 132–164, 2014.
- [95] T. Ameri, G. Dennler, C. Waldauf, P. Denk, K. Forberich, M. C. Scharber, C. J. Brabec, and K. Hingerl, “Realization, characterization, and optical modeling of inverted bulk-heterojunction organic solar cells,” *Journal of Applied Physics*, vol. 103, no. 8, p. 084506, 2008.
- [96] J. Yuan, X. Huang, H. Dong, J. Lu, T. Yang, Y. Li, A. Gallagher, and W. Ma, “Structure, band gap and energy level modulations for obtaining efficient materials in inverted polymer solar cells,” *Organic Electronics*, vol. 14, no. 2, pp. 635–643, 2013.
- [97] V. Papamakarios, E. Polydorou, A. Soultati, N. Droseros, D. Tsikritzis, A. M. Douvas, L. Palilis, M. Fakis, S. Kennou, P. Argitis, and M. Vasilopoulou, “Surface modification of ZnO layers via hydrogen plasma treatment for efficient inverted polymer solar cells,” *ACS Applied Materials & Interfaces*, vol. 8, no. 2, pp. 1194–1205, 2015.
- [98] T. Stubhan, H. Oh, L. Pinna, J. Krantz, I. Litzov, and C. J. Brabec, “Inverted organic solar cells using a solution processed aluminum-doped zinc oxide buffer layer,” *Organic Electronics*, vol. 12, pp. 1539–1543, 2011.
- [99] Y. Zhou, C. Fuentes-Hernandez, J. Shim, J. Meyer, A. J. Giordano, H. Li, P. Winget, T. Papadopoulos, H. Cheun, J. Kim, M. Fenoll, A. Dindar, W. Haske, E. Najafabadi, T. M. Khan, H. Sojoudi, S. Barlow, S. Graham, J. L. Brédas, S. R. Marder, A. Kahn, and B. Kippelen, “A universal method to produce low-work function electrodes for organic electronics,” *Science*, vol. 336, no. 6079, pp. 327–332, 2012.
- [100] H. Zeng, X. Zhu, Y. Liang, and X. Guo, “Interfacial layer engineering for performance enhancement in polymer solar cells,” *Polymers*, vol. 7, no. 2, pp. 333–372, 2015.
- [101] C. Y. Jiang, X. W. Sun, D. W. Zhao, A. K. K. Kyaw, and Y. N. Li, “Low work function metal modified ITO as cathode for inverted polymer solar cells,” *Solar Energy Materials and Solar Cells*, vol. 94, no. 10, pp. 1618–1621, 2010.
- [102] J. Kroon, M. Wienk, W. Verhees, and J. Hummelen, “Accurate efficiency determination and stability studies of conjugated polymer/fullerene solar cells,” *Thin Solid Films*, vol. 403, pp. 223–228, 2002.
- [103] S. M. Menke, N. A. Ran, G. C. Bazan, and R. H. Friend, “Understanding energy loss in organic solar cells: Toward a new efficiency regime,” 2018.

- [104] M. C. Scharber, D. Mühlbacher, M. Koppe, P. Denk, C. Waldauf, A. J. Heeger, and C. J. Brabec, "Design rules for donors in bulk-heterojunction solar cells—Towards 10% energy-conversion efficiency," *Advanced Materials*, vol. 18, no. 6, pp. 789–794, 2006.
- [105] B. Beyer and K. Leo, "Efficiency increase of organic solar cells with emissive light-in-coupling layers," *Journal of Materials Chemistry C*, vol. 3, no. 41, pp. 10830–10836, 2015.
- [106] B. Qi and J. Wang, "Fill factor in organic solar cells," *Physical Chemistry Chemical Physics*, vol. 15, no. 23, pp. 8972–82, 2013.
- [107] R. Søndergaard, M. Hösel, D. Angmo, T. T. Larsen-Olsen, and F. C. Krebs, "Roll-to-roll fabrication of polymer solar cells," *Materials Today*, vol. 15, no. 1, pp. 36–49, 2012.
- [108] R. L. Uy, S. C. Price, and W. You, "Structure-property optimizations in donor polymers via electronics, substituents, and side chains toward high efficiency solar cells," *Macromolecular Rapid Communications*, vol. 33, no. 14, pp. 1162–1177, 2012.
- [109] C. Piliego, T. W. Holcombe, J. D. Douglas, C. H. Woo, P. M. Beaujuge, and J. M. J. Frechet, "Synthetic control of structural order in N-alkylthieno[3,4-c]pyrrole-4,6-dione-based polymers for efficient solar cells," *Journal of the American Chemical Society*, vol. 132, no. 22, pp. 7595–7597, 2010.
- [110] H. N. Tsao, D. M. Cho, I. Park, M. R. Hansen, A. Mavrinskiy, D. Y. Yoon, R. Graf, W. Pisula, H. W. Spiess, and K. Mullen, "Ultrahigh mobility in polymer field-effect transistors by design," *Journal of the American Chemical Society*, vol. 133, no. 8, pp. 2605–2612, 2011.
- [111] S. Liu, Z. Kan, S. Thomas, F. Cruciani, J.-L. Brédas, and P. M. Beaujuge, "Thieno[3,4-c]pyrrole-4,6-dione-3,4-difluorothiophene polymer acceptors for efficient all-polymer bulk heterojunction solar cells," *Angewandte Chemie International Edition*, vol. 55, no. 42, pp. 12996–13000, 2016.
- [112] N. Wang, Z. Chen, W. Wei, and Z. Jiang, "Fluorinated benzothiadiazole-based conjugated polymers for high-performance polymer solar cells without any processing additives or post-treatments," *Journal of the American Chemical Society*, vol. 135, no. 45, pp. 17060–17068, 2013.
- [113] S. H. Liao, H. J. Jhuo, Y. S. Cheng, and S. A. Chen, "Fullerene derivative-doped zinc oxide nanofilm as the cathode of inverted polymer solar cells with low-bandgap polymer (PTB7-Th) for high performance," *Advanced Materials*, vol. 25, no. 34, pp. 4766–4771, 2013.
- [114] J. Liu, B. Walker, A. Tamayo, Y. Zhang, and T. Q. Nguyen, "Effects of heteroatom substitutions on the crystal structure, film formation, and optoelectronic properties of diketopyrrolopyrrole-based materials," *Advanced Functional Materials*, vol. 23, no. 1, pp. 47–56, 2013.

- [115] G. Li, R. Zhu, and Y. Yang, “Polymer solar cells,” *Nature Photonics*, vol. 6, no. 3, pp. 153–161, 2012.
- [116] F. Huang, K.-S. Chen, H.-L. Yip, S. K. Hau, O. Acton, Y. Zhang, J. Luo, and A. K.-Y. Jen, “Development of new conjugated polymers with donor- $\pi$ -bridge-acceptor side chains for high performance solar cells,” *Journal of the American Chemical Society*, vol. 131, no. 39, pp. 13886–13887, 2009.
- [117] A. Facchetti, “ $\pi$ -Conjugated polymers for organic electronics and photovoltaic cell applications,” *Chemistry of Materials*, vol. 23, no. 3, pp. 733–758, 2011.
- [118] P. M. Beaujuge, W. Pisula, H. N. Tsao, S. Ellinger, K. Mullen, and J. R. Reynolds, “Tailoring structure-property relationships in dithienosilole-benzothiadiazole donor-acceptor copolymers,” *Journal of the American Chemical Society*, vol. 131, no. 22, pp. 7514–7515, 2009.
- [119] E. Havinga, W. ten Hoeve, and H. Wynberg, “Alternate donor-acceptor small-band-gap semiconducting polymers; Polysquaraines and polycroconaines,” *Synthetic Metals*, vol. 55, no. 1, pp. 299–306, 1993.
- [120] L. Dou, Y. Liu, Z. Hong, G. Li, and Y. Yang, “Low-bandgap near-IR conjugated polymers/molecules for organic electronics,” *Chemical Reviews*, vol. 115, no. 23, pp. 12633–12665, 2015.
- [121] R. Kroon, M. Lenes, J. C. Hummelen, P. W. M. Blom, and B. de Boer, “Small bandgap polymers for organic solar cells (polymer material development in the last 5 years),” *Polymer Reviews*, vol. 48, no. 3, pp. 531–582, 2008.
- [122] B. V. Lobanov and A. I. Murzashev, “Optical absorption of fullerene C60 within the concept of a strongly correlated state,” *Russian Physics Journal*, vol. 59, no. 6, pp. 856–861, 2016.
- [123] J. D. Chen, C. Cui, Y. Q. Li, L. Zhou, Q. D. Ou, C. Li, Y. Li, and J. X. Tang, “Single-junction polymer solar cells exceeding 10% power conversion efficiency,” *Advanced Materials*, vol. 27, no. 6, pp. 1035–1041, 2015.
- [124] C. Liu, C. Yi, K. Wang, Y. Yang, R. S. Bhatta, M. Tsige, S. Xiao, and X. Gong, “Single-junction polymer solar cells with over 10% efficiency by a novel two-dimensional donor-acceptor conjugated copolymer,” *ACS Applied Materials & Interfaces*, vol. 7, no. 8, pp. 4928–4935, 2015.
- [125] H. Zhang, H. Yao, J. Hou, J. Zhu, J. Zhang, W. Li, R. Yu, B. Gao, S. Zhang, and J. Hou, “Over 14% efficiency in organic solar cells enabled by chlorinated nonfullerene small-molecule acceptors,” *Advanced Materials*, vol. 30, no. 20, p. 1800868, 2018.
- [126] Y. Liang, Y. Wu, D. Feng, S.-T. Tsai, H.-J. Son, G. Li, and L. Yu, “Development of new semiconducting polymers for high performance solar cells,” *Journal of the American Chemical Society*, vol. 131, no. 1, pp. 56–57, 2009.
- [127] M. Zhang, X. Guo, W. Ma, H. Ade, and J. Hou, “A large-bandgap conjugated polymer for versatile photovoltaic applications with high performance,” *Advanced Materials*, vol. 27, no. 31, pp. 4655–4660, 2015.

- [128] L. Lu and L. Yu, “Understanding low bandgap polymer PTB7 and optimizing polymer solar cells based on it,” *Advanced Materials*, vol. 26, no. 26, pp. 4413–4430, 2014.
- [129] B. C. Thompson and J. M. J. Fréchet, “Polymer-fullerene composite solar cells,” *Angewandte Chemie International Edition*, vol. 47, no. 1, pp. 58–77, 2008.
- [130] J. Zhao, Y. Li, and E. Al, “Efficient organic solar cells processed from hydrocarbon solvents,” *Nature Energy*, vol. 1, no. 2, p. 15027, 2016.
- [131] S. M. McAfee, J. M. Topple, I. G. Hill, and G. C. Welch, “Key components to the recent performance increases of solution processed non-fullerene small molecule acceptors,” *Journal of Materials Chemistry A*, vol. 3, no. 32, pp. 16393–16408, 2015.
- [132] M. Jørgensen, K. Norrman, and F. C. Krebs, “Stability/degradation of polymer solar cells,” *Solar Energy Materials and Solar Cells*, vol. 92, no. 7, pp. 686–714, 2008.
- [133] A. Facchetti, “Polymer donor-polymer acceptor (all-polymer) solar cells,” *Materials Today*, vol. 16, no. 4, pp. 123–132, 2013.
- [134] H. Yan, Z. Chen, Y. Zheng, C. Newman, J. R. Quinn, F. Dötz, M. Kastler, and A. Facchetti, “A high-mobility electron-transporting polymer for printed transistors,” *Nature*, vol. 457, no. 7230, pp. 679–686, 2009.
- [135] J. R. Moore, S. Albert-Seifried, A. Rao, S. Massip, B. Watts, D. J. Morgan, R. H. Friend, C. R. McNeill, and H. Sirringhaus, “Polymer blend solar cells based on a high-mobility naphthalenediimide-based polymer acceptor: device physics, photophysics and morphology,” *Advanced Energy Materials*, vol. 1, no. 2, pp. 230–240, 2011.
- [136] B. Fan, L. Ying, P. Zhu, F. Pan, F. Liu, J. Chen, F. Huang, and Y. Cao, “All-polymer solar cells based on a conjugated polymer containing siloxane-functionalized side chains with efficiency over 10%,” *Advanced Materials*, vol. 29, no. 47, 2017.
- [137] Y. Guo, Y. Li, O. Awartani, H. Han, J. Zhao, H. Ade, H. Yan, and D. Zhao, “Improved performance of all-polymer solar cells enabled by naphthodiperylenetetraimide-based polymer acceptor,” *Advanced Materials*, vol. 29, no. 26, 2017.
- [138] H. K. H. Lee, Z. Li, I. Constantinou, F. So, S. W. Tsang, and S. K. So, “Batch-to-batch variation of polymeric photovoltaic materials: its origin and impacts on charge carrier transport and device performances,” *Advanced Energy Materials*, vol. 4, no. 16, p. 1400768, 2014.
- [139] P. Schilinsky, U. Asawapirom, U. Scherf, M. Biele, and C. J. Brabec, “Influence of the molecular weight of poly(3-hexylthiophene) on the performance of bulk heterojunction solar cells,” *Chemistry of Materials*, vol. 17, no. 8, pp. 2175–2180, 2005.

- [140] C. Wang, S. Ni, S. Braun, M. Fahlman, and X. Liu, “Effects of water vapor and oxygen on non-fullerene small molecule acceptors,” *Journal of Materials Chemistry C*, 2018.
- [141] J. Zhou, Y. Zuo, X. Wan, G. Long, Q. Zhang, W. Ni, Y. Liu, Z. Li, G. He, C. Li, B. Kan, M. Li, and Y. Chen, “Solution-processed and high-performance organic solar cells using small molecules with a benzodithiophene unit,” *Journal of Materials Chemistry A*, vol. 135, pp. 8484–8487, 2013.
- [142] J. Yuan, Y. Zhang, L. Zhou, G. Zhang, H.-L. Yip, T.-K. Lau, X. Lu, C. Zhu, H. Peng, P. A. Johnson, M. Leclerc, Y. Cao, J. Ullmann, Y. Li, and Y. Zou, “Single-Junction Organic Solar Cell with over 15% Efficiency Using Fused-Ring Acceptor with Electron-Deficient Core,” *Joule*, 2019.
- [143] Y. Li, X. Liu, F.-P. Wu, Y. Zhou, Z.-Q. Jian, B. Song, Y. Xia, S.-G. Zhang, F. Gao, O. Inganäs, and L.-S. Liao, “Non-fullerene acceptor with low energy loss and high external quantum efficiency: towards high performance polymer solar cells,” *Journal of Materials Chemistry A*, 2016.
- [144] Q. He, T. Li, C. Yan, Y. Liu, J. Wang, M. Wang, Y. Lin, and X. Zhan, “Cracking perylene diimide backbone for fullerene-free polymer solar cells,” *Dyes and Pigments*, vol. 128, pp. 226–234, 2016.
- [145] Y. Lin, J. Wang, Z.-g. Zhang, H. Bai, Y. Li, D. Zhu, and X. Zhan, “An electron acceptor challenging fullerenes for efficient polymer solar cells,” *Advanced Materials*, vol. 27, no. 7, pp. 1170–1174, 2015.
- [146] Y. Lin and X. Zhan, “Non-fullerene acceptors for organic photovoltaics: an emerging horizon,” *Materials Horizons*, vol. 1, no. 5, pp. 470–488, 2014.
- [147] G. Zhang, J. Zhao, P. C. Y. Chow, K. Jiang, J. Zhang, Z. Zhu, J. Zhang, F. Huang, and H. Yan, “Non-fullerene acceptor molecules for bulk heterojunction organic solar cells,” *Chemical Reviews*, vol. 118, no. 7, pp. 3447–3507, 2018.
- [148] W. Zhao, D. Qian, S. Zhang, S. Li, O. Inganäs, F. Gao, and J. Hou, “Fullerene-free polymer solar cells with over 11% efficiency and excellent thermal stability,” *Advanced Materials*, vol. 28, no. 32, pp. 4734–4739, 2016.
- [149] S. Li, W. Liu, M. Shi, J. Mai, T.-K. Lau, J. Wan, X. Lu, C.-Z. Li, and H. Chen, “A spirobifluorene and diketopyrrolopyrrole moieties based non-fullerene acceptor for efficient and thermally stable polymer solar cells with high open-circuit voltage,” *Energy & Environmental Science*, vol. 9, pp. 604–610, 2016.
- [150] J. Zhao, Y. Li, H. Lin, Y. Liu, K. Jiang, C. Mu, T. Ma, J. Yuk, L. Lai, H. Hu, D. Yu, and H. Yan, “High-efficiency non-fullerene organic solar cells enabled by a difluorobenzothiadiazole-based donor polymer combined with a properly matched small molecule acceptor,” *Energy & Environmental Science*, vol. 8, p. 520, 2015.
- [151] X. Zhang, J. Yao, and C. Zhan, “A selenophenyl bridged perylene diimide dimer as an efficient solution-processable small molecule acceptor,” *Chemical Communications*, vol. 51, no. 6, pp. 1058–61, 2014.

- [152] H.-W. Luo and Z.-T. Liu, "Recent developments of di-amide/imide-containing small molecular non-fullerene acceptors for organic solar cells," *Chinese Chemical Letters*, vol. 27, no. 8, pp. 1283–1292, 2016.
- [153] Y. Zhao, Y. Guo, and Y. Liu, "25th anniversary article: Recent advances in n-type and ambipolar organic field-effect transistors," *Advanced Materials*, vol. 25, no. 38, pp. 5372–5391, 2013.
- [154] Y. Liu, L. Zhang, H. Lee, H.-W. Wang, A. Santala, F. Liu, Y. Diao, A. L. Briseno, and T. P. Russell, "NDI-based small molecule as promising nonfullerene acceptor for solution-processed organic photovoltaics," *Advanced Energy Materials*, vol. 5, no. 12, p. 1500195, 2015.
- [155] J. Zhang, Y. Li, J. Huang, H. Hu, G. Zhang, T. Ma, P. C. Y. Chow, H. Ade, D. Pan, and H. Yan, "Ring-fusion of perylene diimide acceptor enabling efficient non-fullerene organic solar cells with a small voltage loss," *Journal of the American Chemical Society*, vol. 139, no. 45, pp. 16092–16095, 2017.
- [156] Y. Duan, X. Xu, H. Yan, W. Wu, Z. Li, and Q. Peng, "Pronounced effects of a triazine core on photovoltaic performance-efficient organic solar cells enabled by a PDI trimer-based small molecular acceptor," *Advanced Materials*, vol. 29, no. 7, p. 1605115, 2017.
- [157] E. Ahmed, G. Ren, F. S. Kim, E. C. Hollenbeck, and S. A. Jenekhe, "Design of new electron acceptor materials for organic photovoltaics: Synthesis, electron transport, photophysics, and photovoltaic properties of oligothiophene-functionalized naphthalene diimides," *Chemistry of Materials*, vol. 23, no. 20, pp. 4563–4577, 2011.
- [158] Z. Mao, T. P. Le, K. Vakhshouri, R. Fernando, F. Ruan, E. Muller, E. D. Gomez, and G. Sauve, "Processing additive suppresses phase separation in the active layer of organic photovoltaics based on naphthalene diimide," *Organic Electronics: Physics, Materials, Applications*, vol. 15, no. 11, pp. 3384–3391, 2014.
- [159] H. Patil, A. Gupta, A. Bilic, S. V. Bhosale, and S. V. Bhosale, "A solution-processable electron acceptor based on diketopyrrolopyrrole and naphthalenediimide motifs for organic solar cells," *Tetrahedron Letters*, vol. 55, no. 32, pp. 4430–4432, 2014.
- [160] X. Wang, J. Huang, Z. Niu, X. Zhang, Y. Sun, and C. Zhan, "Dimeric naphthalene diimide based small molecule acceptors: synthesis, characterization, and photovoltaic properties," *Tetrahedron*, vol. 70, no. 32, pp. 4726–4731, 2014.
- [161] A. Gupta, R. V. Hangarge, X. Wang, B. Alford, V. Chellapan, L. A. Jones, A. Rananaware, A. Bilic, P. Sonar, and S. V. Bhosale, "Crowning of dibenzosilole with a naphthalenediimide functional group to prepare an electron acceptor for organic solar cells," *Dyes and Pigments*, vol. 120, pp. 314–321, 2015.
- [162] M. J. Sung, M. Huang, S. H. Moon, T. H. Lee, S. Y. Park, J. Y. Kim, S.-K. Kwon, H. Choi, and Y.-H. Kim, "Naphthalene diimide-based small molecule acceptors for fullerene-free organic solar cells," *Solar Energy*, vol. 150, pp. 90–95, 2017.

- [163] D. Srivani, A. Gupta, D. D. La, R. S. Bhosale, A. L. Puyad, W. Xiang, J. Li, S. V. Bhosale, and S. V. Bhosale, "Small molecular non-fullerene acceptors based on naphthalenediimide and benzoisoquinoline-dione functionalities for efficient bulk-heterojunction devices," *Dyes and Pigments*, vol. 143, pp. 1–9, 2017.
- [164] D. Srivani, A. Agarwal, S. Bhssale, A. L. Puyad, W. Xiang, R. A. Evans, A. Gupta, and S. Bhosale, "Naphthalene diimide-based non-fullerene acceptors flanked by open-ended and aromatizable acceptor functionalities," *Chemical Communications*, vol. 53, no. 2017, pp. 11157–11160, 2017.
- [165] P. S. Rao, A. Gupta, D. Srivani, S. V. Bhosale, A. Bilic, J. Li, W. Xiang, R. A. Evans, and S. V. Bhosale, "An efficient non-fullerene acceptor based on central and peripheral naphthalene diimides," *Chemical Communications*, vol. 54, no. 40, pp. 5062–5065, 2018.
- [166] S. Li, L. Ye, W. Zhao, S. Zhang, S. Mukherjee, H. Ade, and J. Hou, "Energy-level modulation of small-molecule electron acceptors to achieve over 12% efficiency in polymer solar cells," *Advanced Materials*, vol. 28, no. 42, pp. 9423–9429, 2016.
- [167] F. S. Etheridge, R. Fernando, J. A. Golen, A. L. Rheingold, and G. Sauve, "Tuning the optoelectronic properties of core-substituted naphthalene diimides by the selective conversion of imides to monothioimides," *RSC Advances*, vol. 5, no. 58, pp. 46534–46539, 2015.
- [168] N. Pearce, E. S. Davies, R. Horvath, C. R. Pfeiffer, X.-Z. Sun, W. Lewis, J. McMaster, M. W. George, and N. R. Champness, "Thionated naphthalene diimides: Tuneable chromophores for applications in photoactive dyads," *Physical Chemistry Chemical Physics*, vol. 20, pp. 752–764, 2018.
- [169] S. Dai, F. Zhao, Q. Zhang, T.-K. Lau, T. Li, K. Liu, Q. Ling, C. Wang, X. Lu, W. You, and X. Zhan, "Fused nonacyclic electron acceptors for efficient polymer solar cells," *Journal of the American Chemical Society*, vol. 139, no. 3, pp. 1336–1343, 2017.
- [170] S. L. Suraru and F. Würthner, "Strategies for the synthesis of functional naphthalene diimides," *Angewandte Chemie International Edition*, vol. 53, no. 29, pp. 7428–7448, 2014.
- [171] A. Welford, S. Maniam, E. Gann, L. Thomsen, S. J. Langford, and C. R. McNeill, "Thionation of naphthalene diimide molecules: Thin-film microstructure and transistor performance," *Organic Electronics*, vol. 53, pp. 287–295, 2018.
- [172] W. Y. Lee, J. H. Oh, S. L. Suraru, W. C. Chen, F. Würthner, and Z. Bao, "High-mobility air-stable solution-shear-processed n-channel organic transistors based on core-chlorinated naphthalene diimides," *Advanced Functional Materials*, vol. 21, no. 21, pp. 4173–4181, 2011.
- [173] L. E. Polander, A. S. Romanov, S. Barlow, D. K. Hwang, B. Kippelen, T. V. Timofeeva, and S. R. Marder, "Stannyl derivatives of naphthalene diimides and their use in oligomer synthesis," *Organic Letters*, vol. 14, no. 3, pp. 918–921, 2012.

- [174] B. A. Jones, A. Facchetti, T. J. Marks, and M. R. Wasielewski, "Cyanonaphthalene diimide semiconductors for air-stable, flexible, and optically transparent n-channel field-effect transistors," *Chemistry of Materials*, vol. 19, no. 11, pp. 2703–2705, 2007.
- [175] C. Röger and F. Würthner, "Core-tetrasubstituted naphthalene diimides: Synthesis, optical properties, and redox characteristics," *Journal of Organic Chemistry*, vol. 72, no. 21, pp. 8070–8075, 2007.
- [176] C. Thalacker, C. Röger, and F. Würthner, "Synthesis and optical and redox properties of core-substituted naphthalene diimide dyes," *Journal of Organic Chemistry*, vol. 71, no. 21, pp. 8098–8105, 2006.
- [177] J. Míšek, A. Vargas Jentzsch, S. I. Sakurai, D. Emery, J. Mareda, and S. Matile, "A chiral and colorful redox switch: Enhanced  $\pi$  acidity in action," *Angewandte Chemie*, vol. 49, no. 42, pp. 7680–7683, 2010.





# Chapter 3

## Experimental

### 3.1 Introduction

This chapter has three functions: (1) to introduce the theory behind the characterization methods used in this thesis, (2) to introduce the processes involved in sample and device preparation, and (3) to identify the specific equipment and tools used for characterization. In general, the sections for each method begin with a theoretical introduction to a technique, followed by the specifications used in an experimental or theoretical context pertaining to the work done in subsequent results chapters. This chapter first outlines the materials used in this thesis, followed by the characterization used to evaluate their materials properties. This includes background on both experimental as well as theory-based approaches to understanding material properties. Specifications regarding solar cells, including device fabrication and characterization, are given next, followed by characterization methods used to evaluate the active layer morphology for blends.

### 3.2 Materials

This thesis explores the effect that substituent and substitutional atoms have on the materials properties of naphthalene diimide, for applications as acceptors in organic solar cells. In order to achieve this, a wide range of molecular structures, including small molecule and polymeric structures, were used. The synthesis of the materials studied in Chapters 4 (Figure 3.1) and 5 (Figure 3.2) was conducted by Dr. Subashani Maniam from the School of Chemistry at Monash University. Details pertaining to the synthesis of these materials are given in either the results chapter itself or the relevant appendix. The small molecules studied in Chapter 6 were also supplied by Dr. Subashani Maniam, while the polymers were supplied by the group of Professor Michael Sommer at the Chemnitz University of Technology, the synthesis of which has previously been published elsewhere.<sup>1</sup>

Initial studies in this thesis focus on the effect that substituent and substitutional atoms have on the NDI molecule. In the first case, oxygen, sulfur, and nitrogen heteroatoms are introduced to the NDI molecule at core positions, studied in Chapter 4. These structures are shown in Figure 3.1. The materials studied in Chapter 5, shown in Figure 3.2, build upon the substituent heteroatoms shown in Figure 3.1, however in this chapter, preferential molecular structures, which were designed specifically to

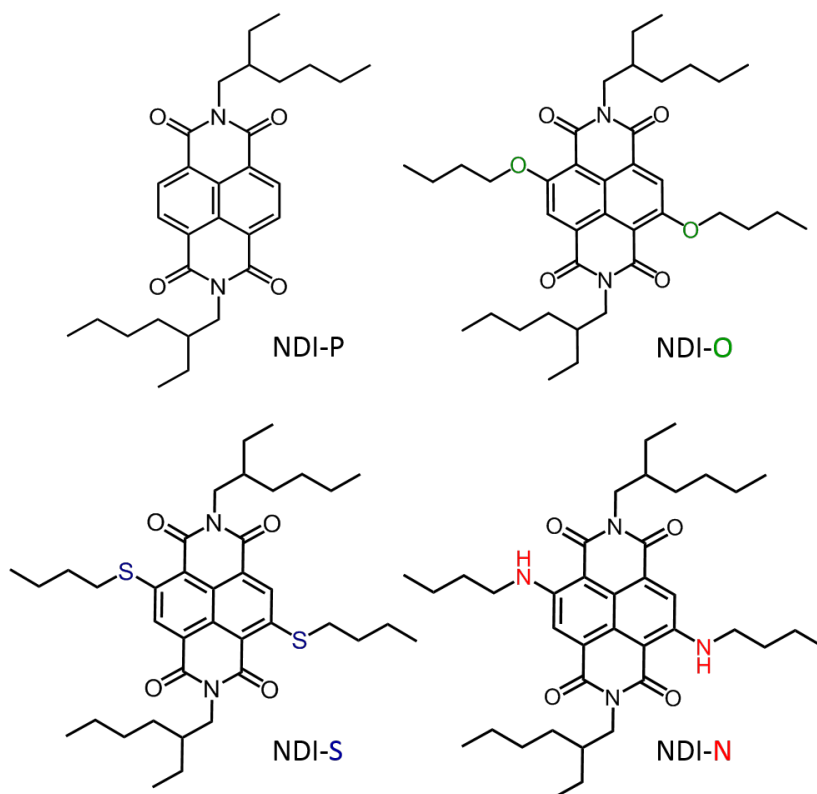


Figure 3.1: Molecular structures of the NDI-based small molecule acceptors studied in Chapter 4 including NDI-P, NDI-O, NDI-S, and NDI-N.

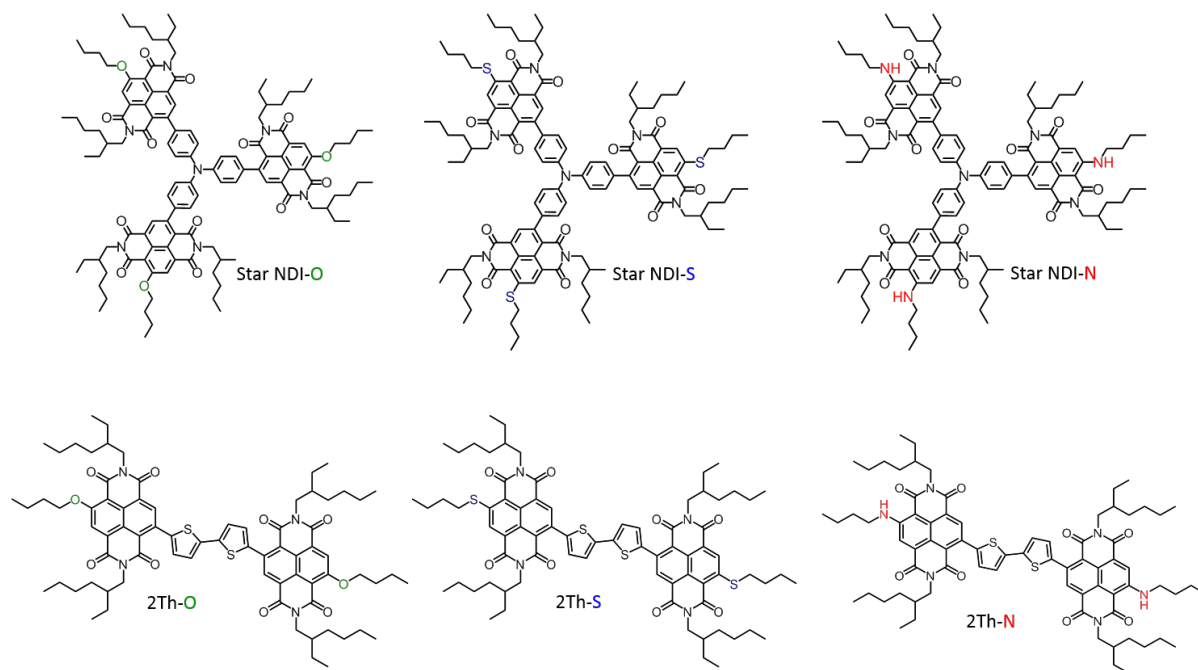


Figure 3.2: Molecular structures of the NDI-based small molecule acceptors studied in Chapter 5 including Star NDI-O, Star NDI-S, Star NDI-N, 2Th-O, 2Th-S and 2Th-N.

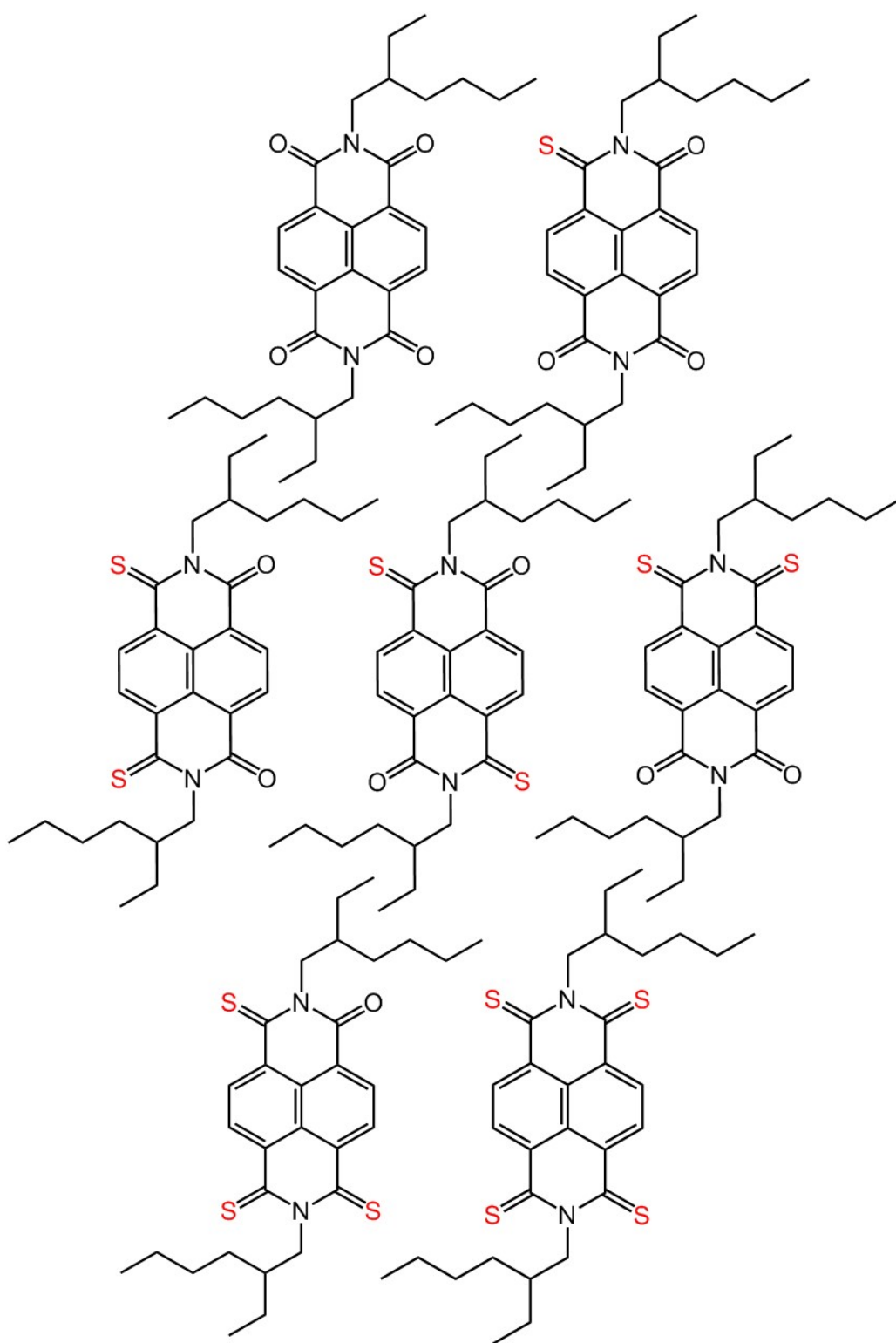


Figure 3.3: Molecular structures of the series of NDI-based small molecules with increasing degree of thionation. The parent, 1S, 2S-*trans*, and 3S molecules were used as small molecule acceptors in Chapter 4, and the effect thionation has on the NEXAFS spectra of all the materials shown was studied in Chapter 7.

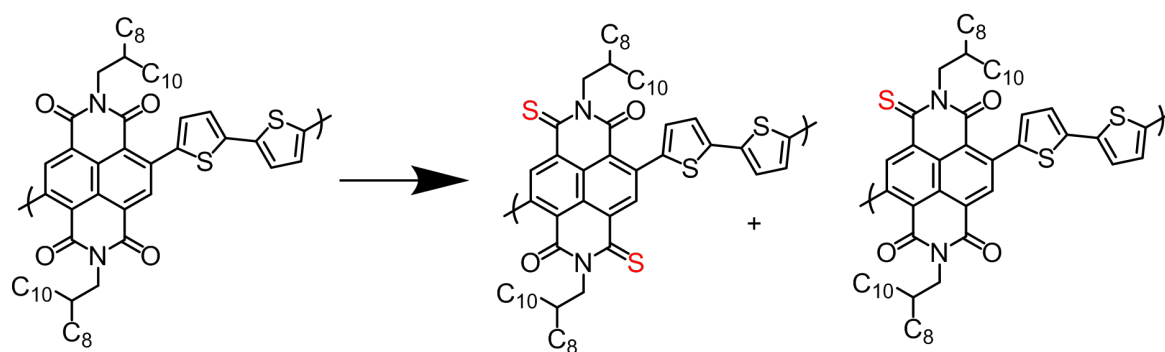


Figure 3.4: Synthetic route to the thionated polymers studied in Chapter 6, which include three ratios of 2S-*trans* to 1S: 85:15, 93:7, and 95:5.

disrupt the strong aggregation and molecular packing of the NDI moiety, as well as promote electron delocalization along the backbone, were used. Additionally, the effect that sulfur substitutional atoms (i.e. thionation) have on the performance of NDI-based acceptors is explored in Chapter 6, shown in Figure 3.3, with the Parent, 1S, 2S-*trans* and 3S materials used as molecular acceptors in solar cells. Chapter 6 also explores the effect of thionation on a polymeric acceptor material, which was chosen to provide the preferential material geometry for organic solar cells. These materials are shown in Figure 3.4. Finally, Chapter 7 refers back to the materials shown in Figure 3.3, focusing on the effect thionation has on their near-edge X-ray absorption fine structure spectra (refer to Section 3.2.1.3), through the use of X-ray absorption spectroscopy calculations.

### 3.2.1 Material Properties

A detailed analysis and understanding of the optical and electronic properties of materials utilized in organic solar cell applications is imperative to interpreting photovoltaic performance in devices. This section covers the methods used to characterize these properties, including, but not limited to, cyclic voltammetry to determine the HOMO and LUMO energies for acceptor materials, solid-state electronic fine structure and absorption characterization.

#### 3.2.1.1 Measuring Energy Levels

In this thesis, the HOMO and LUMO energy levels for various materials were determined either electrochemically, through cyclic voltammetry, or the HOMO was determined spectroscopically through photoelectron spectroscopy in air (PESA). This section covers the working principles of both techniques, followed by experimental specifications.

Electrochemistry offers convenient methods for measuring the bulk energetics of materials used in organic solar cells. In particular, cyclic voltammetry (CV), where a linear voltage is applied to the working electrode as a function of time in an electrochemical cell, can be used to measure the reduction-oxidation (redox) characteristics of organic semiconductors.<sup>2</sup> The redox behavior, then, is used to extract HOMO and LUMO energy values for the material. Typically, three electrodes are used in the set-up of the electrochemical cell: a working electrode, counter electrode, and a refer-

ence electrode. In the three-electrode cell set-up, a potential is applied to the working electrode by a potentiostat, which measures the resulting current passing through the working electrode. The electrochemical cell employs the three electrodes, as well as an electrolyte solution, which must be conductive because the mass transport process through the cell is diffusion driven.<sup>3</sup> Selection of the counter electrode material is dependent on its conductivity, as well as its ability to refrain from reacting with the bulk electrolyte solution. The reference electrode is designed to have a high impedance, to avoid conducting current. The current at the working electrode is then plotted as a function of applied potential, which reveals the oxidation and reduction potentials for a given material. The first reduction potential for an organic material corresponds with that material's LUMO level. Similarly, the first oxidation potential represents the material's HOMO energy level.

For the cyclic voltammetry measurements reported in this thesis, a Powerlab ML160 potentiostat interfaced via a Powerlab 4/20 controller to a PC running Echem for Windows was used for solution-based cyclic voltammetry measurements. Argon-purified dichloromethane was used as the solvent for tetrabutylammonium hexafluorophosphate ( $\text{Bu}_4\text{NPF}_6$ ) (0.1 M), the supporting electrolyte. 0.05 M of each acceptor material was then added to this solution prior to measurements. All CV measurements were made at room temperature using a glassy carbon working electrode (2.0 mm diameter), a platinum wire counter electrode and a second platinum wire as a quasi-reference electrode, separated from the bulk of the solution by a frit. This system was internally calibrated with ferrocene/ferrocenium ( $\text{Fc}/\text{Fc}^+$ ). A scan rate of 100 mV/s was used for all measurements, with voltammograms recorded within a range from -2000 to 1500 mV. LUMO values were extracted from the first reduction peak using the following equations, assuming the  $\text{Fc}/\text{Fc}^+$  redox reaction takes place at 4.8 eV with respect to vacuum:

$$E_{1/2} = \frac{E_{p1, red} + E_{p1, ox}}{2} - E_{1/2 \text{ Fc/Fc}^+} \quad (3.1)$$

$$E_{LUMO} = -(E_{1/2} + 4.8) \quad (3.2)$$

Additionally, PESA was used to determine the HOMO energy levels of the acceptor polymers studied in Chapter 7. PESA, first introduced in 1981,<sup>4</sup> is a common technique that is used to identify the ionization potential of a material, with the convenience of being performed in air. A typical set-up includes a cylindrical, air-filled counter, with two grids (a Suppressor grid,  $G_s$ , and a Quenching grid,  $G_q$ ) used to detect and measure the low-energy electrons emitted following UV excitation.<sup>4</sup> Emitted electrons are accelerated by the suppressor grid, during which they attach to oxygen molecules in the air. These ions are directed towards the cylindrical component, where they are further accelerated towards the anode. The electron detaches from any ion reaching the anode, where it causes a voltage reduction that can be detected and counted by the quenching grid. An energy diagram illustrating this process is shown in Figure 3.5. Because PESA is performed on materials in the solid-state, samples were prepared by spin casting the polymers from chlorobenzene at 3000 RPM, onto cleaned, ITO-coated glass substrates (see Section 3.3.1). Although this is an advantage over measurements performed using CV, in which case the materials are in solution and therefore not in a device-equivalent state, one limitation of PESA experiments is that they are only surface sensitive to the first few nanometers ( $< 20$  nm) of the film.<sup>5</sup>

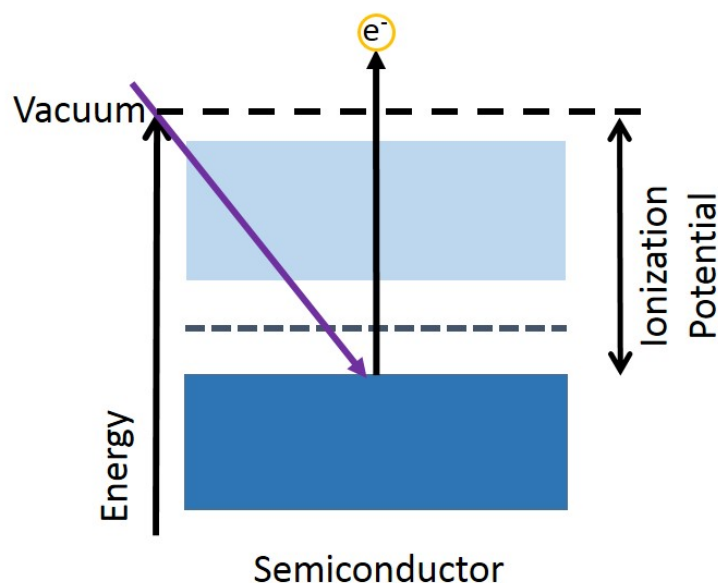


Figure 3.5: Diagram illustrating the photoemission of an electron during a PESA measurement: a UV light source is used to excite an electron from an occupied state to an energy above the vacuum level. This electron is then emitted from the sample's surface and its energy is detected by an electron detector. Because, for semiconductors, the ionization potential is the same energy as the material's HOMO energy, the HOMO is thus determined by the ionization potential.

Additionally, PESA measurements and data analysis are relatively straight forward and fast, compared with CV measurements.<sup>5</sup> During the measurement, the number of electrons that is detected by the instrument is determined as a function of incident photon energy, which is produced by a deuterium lamp, with energies ranging from 3.4 to 6.1 eV. This data is typically plotted as energy as a function of the square root of the electron count. Initially, at lower energies, the number of electrons is low and close to zero. However, at energies above the ionization potential, the number of detected electrons increases dramatically, as the incident photon energy is high enough to liberate electrons in occupied orbitals. The inflection point at which the slope of the output changes is therefore determined to be the ionization potential, or HOMO for organic semiconductors, because this is the lowest energy at which an occupied orbital emits an electron. PESA experiments were performed on samples fabricated using neat solutions of the materials studied in Chapter 7, dissolved in chlorobenzene. A Riken Keiki Model AC-2 photoelectron spectrometer with a power intensity of 5 nW was used for all samples.

### 3.2.1.2 UV-visible absorption spectroscopy

When studying materials used in solar cell applications, it is imperative to quantify and evaluate their response to the solar spectrum and, ideally, the active layer materials should exhibit broad absorption over the energy range from  $\sim 350 - 900$  nm. Typically, an ultraviolet – visible (UV-vis) spectrometer is used to quantify not only a material's spectral absorption, but also how light interacts with that material in the following ways: reflection, transmission, refraction, and scatter. This is shown schematically in

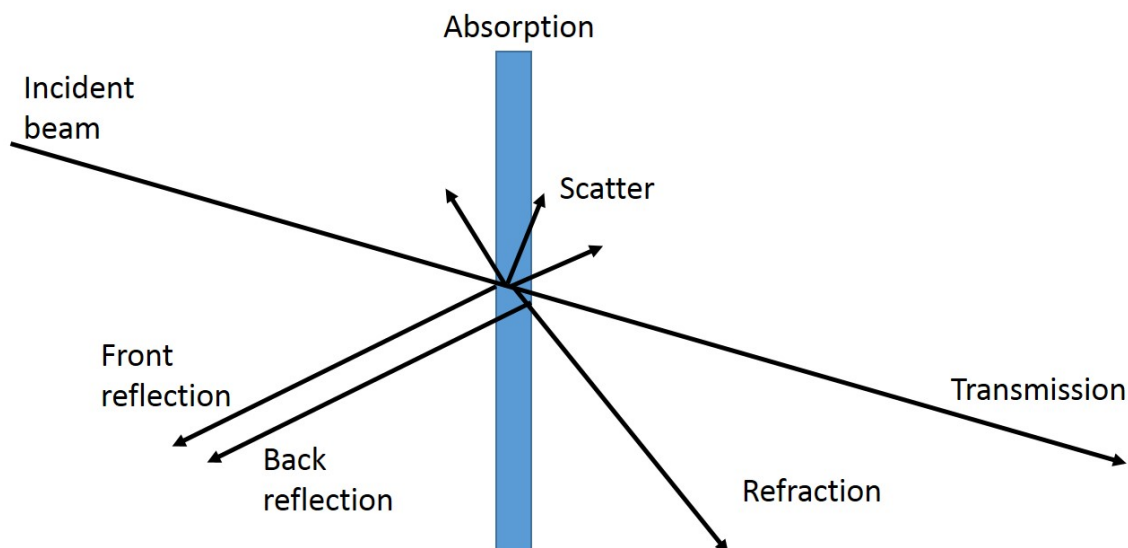


Figure 3.6: Schematic showing the various ways light can interact with a material. All light is refracted within the medium, which is not shown for clarity.

Figure 3.6. In an optical absorption measurement, the spectrometer actually measures the fraction of light that is reflected (%R) and transmitted (%T), or just the fraction of transmitted light, to determine the fraction of light that is absorbed (%A) as follows (assuming no scatter):

$$100\% = \%R + \%T + \%A \quad (3.3)$$

$$\%A = \%R + \%T - 100\% \quad (3.4)$$

The spectrometer is comprised of the following three components: an emission source that produces light with a broad emission spectrum, an optical component that collimates and disperses the spectrum, and a detector that measures the intensities of light after it has interacted with the sample. A combination of two lamps, made from deuterium and tungsten, is an example of an emission source that produces light in a suitable range from 175 – 3300 nm.<sup>6</sup> After emission, the light travels through a series of lenses and mirrors in order to be collimated into a beam, which minimizes convergence and divergence before interacting with a monochromator. The monochromator is used to disperse light into its distinct wavelengths using a diffraction grating, before it exits through a slit, which selects the wavelength prior to entering the sample chamber. Behind the sample chamber is a detector, such as a photomultiplier tube, which amplifies low light intensities by absorbing photons that are converted and multiplied into several electrons per absorbed photon.

In this thesis, a quartz vial was used for all solution, and fused silica substrates with minimal reflectance were used for all solid-state UV-visible absorption measurements. The advantage of fused silica over common glass is superior transparency, particularly in the UV energy range. These were both cleaned sequentially via sonication in acetone and 2-propanol for ten minutes. The polymers or small molecules in solution were measured with a concentration of 0.05 g/l in chlorobenzene, while films were spin cast following the optimized device film conditions. For example, for all NDI-based small molecule acceptors, neat and blend thin films were spin cast at 6000 RPM from a 30 g/l solution in chlorobenzene. There were two UV-visible absorption



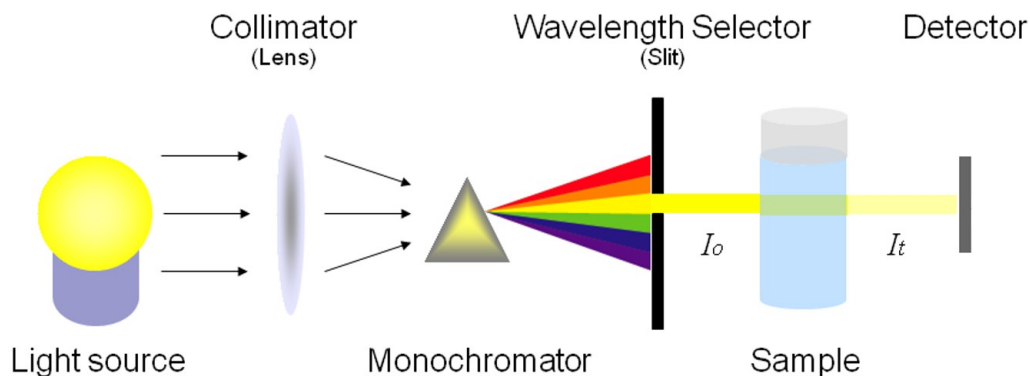


Figure 3.7: Schematic showing the basic instrumentation of a spectrometer. Reproduced with permission from LibreTexts.<sup>7</sup>

spectrometers used in this thesis. A Perkin Elmer Lambda 950 UV-Vis spectrometer was used for all measurements which were taken in the range from 350 nm to 900 nm for small molecule acceptors. In Chapter 7, which focuses on thionated polymer acceptors whose absorption profile extends beyond 900 nm, a Perkin Elmer Lambda 1050 was used to measure absorption from 300 – 1500 nm. In order to account for slight variations in film thickness, and to be better able to compare absorption profiles between materials, all absorption spectra were normalized to the largest absorption peak, usually near or above 350 nm for NDI-based acceptors.

### 3.2.1.3 Near edge X-ray absorption fine structure spectroscopy

Apart from determining whether a material is appropriate for photovoltaic applications, studying the absorption behavior of organic semiconductors can reveal information regarding the interfacial orientation and alignment of conjugated materials, as well as the material's electronic structure. Near edge X-ray absorption fine structure (NEXAFS) spectroscopy measures the X-ray absorption spectra of a material over X-ray energies close to the binding energy of elements that make up the material. In organic semiconductors, the carbon K-shell is particularly useful because the materials are primarily comprised of carbon. The resulting spectra directly reflect the chemical environment of the atom corresponding to a particular transition, which is dependent on other elements present. This is particularly useful for analyzing materials used in organic photovoltaics because a material's NEXAFS spectra provides a unique "fingerprint" that enables contrast within blends of two or more carbon-based materials. This contrast is especially useful in determining the size and purity of domains in a blend film, described in more detail in Section 3.4.6, or for determining the surface composition for a film comprised of two or more constituents. However, interpreting the NEXAFS spectra and assigning resonant features to specific transitions measured by NEXAFS spectroscopy is difficult due to a lack of reference spectra, and complex because of the delocalization of unoccupied electronic orbitals.<sup>8</sup> In order to interpret and assign spectral features to specific resonant transitions in an organic semiconductor, first-principles calculations, such as the eXcited electron and Core Hole (XCH) approach,<sup>9</sup> are useful tools that can be employed to unpack the atom-specific

contributions to a resonant transition.<sup>10–13</sup> This section first provides an overview of the principles behind NEXAFS spectroscopy, followed by an introduction to the XCH approach, which was used in this thesis to calculate X-ray absorption spectra for NDI-based molecules.

### 3.2.1.3.1 Experimental

NEXAFS spectroscopy probes a material’s response to soft X-ray radiation (62 – 620 eV) close to one of its absorption edges (e. g. the carbon K-edge at  $\sim 284$  eV). Specifically, NEXAFS is used to measure resonant transitions that correspond to exciting electrons from core levels (such as the carbon 1s orbital) to unoccupied electronic states in the  $\pi^*$  and  $\sigma^*$  anti-bonding orbitals that were first introduced in Section 2.2.1. There are two types of transitions associated with a NEXAFS measurement: ionizing transitions that remove electrons from core levels to continuum states above the vacuum level, and non-ionizing, resonant transitions to  $\pi^*$  anti-bonding orbitals at energies below the ionization potential and  $\sigma^*$  anti-bonding orbitals at energies above the ionization potential. The first type of excitation, to the continuum states, provides a step-like contribution, while the resonant transitions correspond to specific peaks in the NEXAFS spectrum.<sup>8,14</sup> For materials that contain multiple chemical species, assignment of these peaks to specific transitions is challenging, which is why the use of theoretical calculations can be especially helpful in associating particular peaks with specific transitions. This is discussed in more detail in the next section.

Figure 3.8 provides a schematic energy diagram that shows some of the possible electronic transitions from core to anti-bonding and continuum states in a conjugated material. The NEXAFS spectrum associated with such transitions is also shown. This illustration makes clear that low-energy peaks observed at the resonance energy for carbon are associated with transitions to the  $\pi^*$  anti-bonding orbitals, while higher-energy transitions are associated with a combination of excitations to the continuum (shown as the step-edge in the figure) as well as to  $\sigma^*$  anti-bonding orbitals. Due to the nature of conjugated materials with non-conjugated side-chains added for solubility, the excitations in the  $\pi^*$  manifold are particularly useful in characterizing the orientation of the polymer backbone or conjugated core, because these transitions stem from the conjugated backbone of the material. To realize this, the NEXAFS spectrum of a conjugated material is measured at different incident polarizations, and the resulting changes in resonant intensity of a transition are then used to deduce the transition dipole moment. The quantified variation in resonant intensity as a function of polarization is referred to as the transition dichroism, and if this dichroism is known, as well as the orientation of the transition dipole moment with respect to the molecular structure, it is possible to determine the orientation of a polymer or molecule, with respect to the substrate surface. For example, for common organic semiconductor building blocks such as thiophene and phenyl rings, the C 1s  $\rightarrow \pi^*$  transition dipole moment is oriented perpendicular to the plane of the rings, because the  $\pi$  molecular orbitals are oriented perpendicular to the C=C bond axis. Therefore, the molecular orientation of a material containing either thiophene or phenyl rings can be quantified by measuring the NEXAFS spectra at different incident beam polarizations, and the resulting dichroism can be used to deduce the material’s orientation.<sup>14</sup>

NEXAFS spectra can be further analyzed through the fitting of Gaussian peaks to reproduce the spectrum. This is illustrated in Figure 3.9, which shows experimental

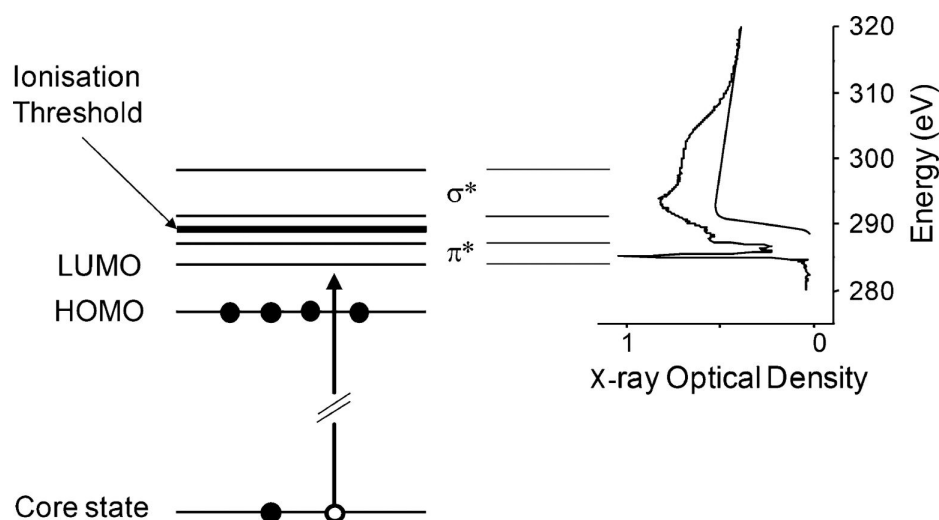


Figure 3.8: Energy diagram showing potential electronic transitions from a core state to anti-bonding and continuum states after X-ray absorption (left) and the associated NEXAFS spectrum (right). Reproduced with permission from Nahid et al. *European Polymer Journal*, 81, 2016, 5343-554.<sup>14</sup>

data (black squares) that has been fitted with a combination of a step-edge, providing the contribution to the spectra of transitions to continuum states, and Gaussian peaks, which represent resonant transitions to  $\pi^*$  states below the step-edge and  $\sigma^*$  states above it. However, because this approach is semi-empirical, it does not provide information regarding the underlying physical transitions due to limitations in the experimental energy resolution ( $\sim 30 - 100$  meV at the carbon K edge),<sup>15</sup> which results in a broadening of measured peaks. In fact, the resolution of a NEXAFS experiment is not good enough to distinguish between distinct transitions from atoms in a molecule that have slightly different chemical environments arising from their nearest neighbors. For example, referring to Figure 3.3, the resonant energy of a core  $1s \rightarrow \pi^*$  transition for a carbon atom bonded to a nitrogen or oxygen atom is different to the resonant energy of such a transition for a carbon atom bonded only to other carbon atoms. However, the limited resolution offered by a NEXAFS experiment renders the exact peak assignment of such different transitions difficult. Conventionally, general distinctions between transitions for atoms in different chemical environments are developed by measuring NEXAFS spectra of several materials with slight differences in chemical structure. This is used to build up intuition,<sup>16</sup> and while this method can provide insight into how chemical modification of an organic semiconductor influences its absorption behavior, synthesizing multiple materials is costly from both a time and financial perspective, and even when materials with slight chemical modification are available for NEXAFS experiments, the underlying reasons for changes in absorption behavior may still be elusive.<sup>17</sup> This is the case for the materials that are discussed in Chapter 7, in which systematic changes in the NEXAFS spectra were observed following increasing levels of thionation of the NDI moiety, however these were unable to be explained by experimental measurements alone. This thesis aims also to expand upon these observations by utilizing X-ray absorption spectroscopy calculations to simulate the NEXAFS spectra of these materials, in order to explain the underlying phenomena responsible for the systematic changes observed in the experimental data. These calculations are described in more detail in the subsequent section.

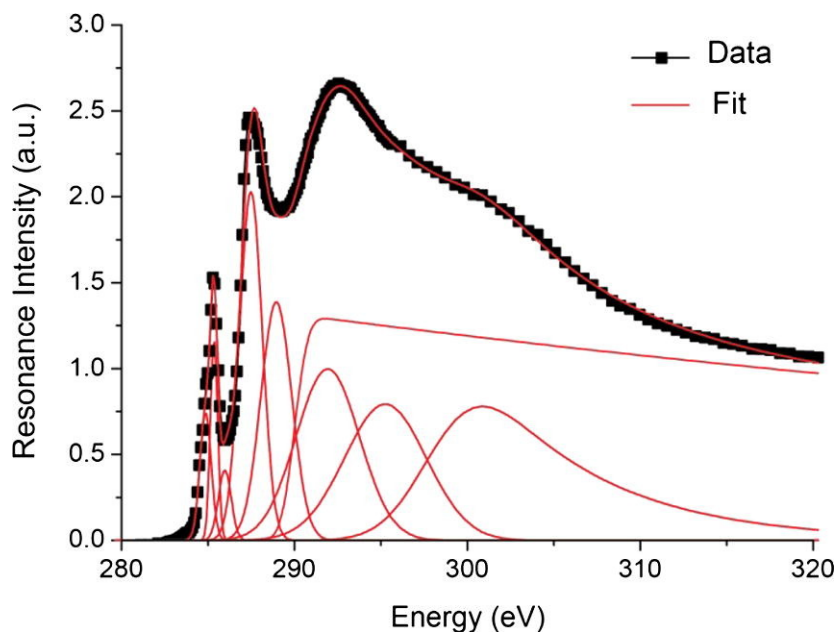


Figure 3.9: Experimental NEXAFS spectrum of P3HT (black, squares). A series of Gaussian peaks and a step-edge are used to generate a fit, which can be helpful in defining a NEXAFS spectra for a specific material. Reproduced with permission from Nahid et al. *European Polymer Journal*, 81, 2016, 5343-554.<sup>14</sup>

In this thesis, NEXAFS samples were prepared using solutions from optimized devices for blend NEXAFS measurements, and neat solutions were made using the same concentration as optimized blend solutions. Degenerately doped silicon wafers, which were sonicated for ten minutes, sequentially, in acetone and IPA prior to a plasma treatment, were used as the substrate. Either neat or blend films were deposited using the optimized spin speed for devices: 6000 RPM in a nitrogen atmosphere. Next, these substrates were cut to fit and mounted (with carbon tape) onto a sample holder. NEXAFS spectroscopy experiments were performed at the Soft X-ray beamline of the Australian Synchrotron<sup>15</sup> using a nearly perfectly linearly polarized X-ray beam. Total electron yield data was acquired by measuring the drain current flowing to the sample under X-ray illumination while partial electron yield data was acquired using a channeltron detector with a retarding voltage of 210 V. X-ray angles of incidence of 20°, 40°, 55°, 70° and 90° were used for all spectra. The sample was moved to a new spot following each measurement to avoid beam damage. The signal probed from the sample was compared with a reference highly ordered pyrolytic graphite (HOPG) and the variation of the photon flux was monitored by using a gold mesh. The NEXAFS spectrum of the HOPG was measured at the same time as samples to calibrate the photon energy. The recorded signal was normalized by the “stable monitor method”,<sup>18</sup> by setting the pre-edge to 0 and the intensity at 320 eV to 1. NEXAFS data were analyzed with QANT.<sup>19</sup>

In Chapter 6, the NEXAFS spectra of blend films were used to determine the surface composition for PBDTTT-EFT-based devices, with increasing levels of thionation in the PNDIT2 polymer. This required first measuring NEXAFS spectra for all neat polymers, and then determining, through the use of Gaussian peak fitting, the unique NEXAFS “fingerprint” for each material. QANT enables peak fitting through the use of the least-squares Lavenberg-Marquardt algorithm with an interactive multi peak fit,

using user-defined constraints. This is important initially, to ensure multiple narrow transitions are appropriately described as opposed to being approximated by a single, wide peak. Through QANT, it is then possible to analyze the blend film spectra against the spectra of the neat components, and determines a ratio of donor:acceptor content in the spectra of the blend film.

### 3.2.1.3.2 Calculations

As was mentioned in the previous section, due to limitations in the energy resolution of a NEXAFS experiment, interpreting NEXAFS spectra can be challenging. However, the use of theoretical calculations, which compute X-ray absorption behavior for every excited atom in a molecule individually, before summing these and displaying an average curve, can provide information on how local chemistry influences the X-ray absorption energy for individual atoms in a molecule. An example of how chemistry influences specific transitions is shown in Figure 3.10, which shows a schematic diagram for a resonant transition from a  $1s$  core orbital in the carbon K-shell to the LUMO, ignoring core-hole effects (top, center). However, due to the complex interaction between the core hole that is created and the excited electron, calculations of the actual resonant transition for an excited atom must take into account changes in the initial-state core-orbital energy as well as in the final excited-state energy, as is done within the energy alignment scheme applied using the XCH approach.<sup>20,21</sup> Furthermore, this thesis explores the effect that heteroatoms have on material properties, which aims to highlight that differences in chemical environment lead to differences in the initial and final-state energies for every inequivalent atom in the material. This heterogeneity in the chemistry manifests as multiple contributions to the measured NEXAFS at varying energies and intensities, adding to the complexity of the spectrum and the difficulty of its interpretation. An example of a core-level excitation to the LUMO for inequivalent carbon atoms in the same molecule is also shown in Figure 3.10, and demonstrates the, potentially, dramatic influence an atom's chemical environment has on a resonant transition energy. In the schematic, the reference atom can be considered as a benchmark for comparison. As in all cases, the creation of a core-hole on this atomic site, following the X-ray excitation, induces changes in the electronic structure of the system as a whole, but especially so around the excited atom. Generally, we expect ground state orbitals that originally overlapped the atomic site of the excitation to become more localized on that site and for their energies to shift accordingly – typically to lower energies than their ground state equivalents. This is demonstrated in the figure by the “LUMO” energy label for the reference atom, which is shifted to a lower energy, compared to the ground state LUMO. Figure 3.10 also indicates excitations of two other atoms which are oxidized (reduced) with respect to the reference atom. For example, if the reference atom was a C atom bound to another C atom, then a relatively oxidized (reduced) atom might be bound to a nitrogen (boron) atom (anything with a significantly different electronegativity). In cases where an available, unoccupied molecular orbital (such as the LUMO) overlaps the core orbitals of each of these atoms with the correct local symmetry (as required by the dipole selection rule) – even in their core-excited states – then transitions to the “same” orbital from these different atoms will appear at different photon energies. This is akin to the so-called chemical shift observable in X-ray photoemission spectra (XPS), with more oxidized (reduced) atoms of the same element evident as absorption peaks at higher

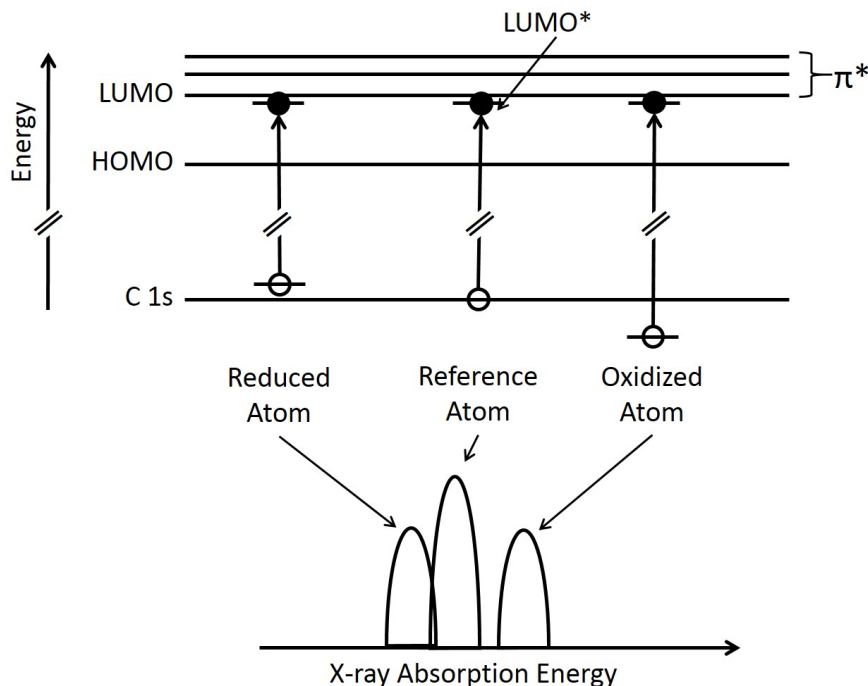


Figure 3.10: Schematic showing the changes in resonant transitions to  $\pi^*$  states for carbon atoms in different chemical environments.

(lower) photoabsorption energies, albeit typically with smaller shifts than their XPS equivalents. The use of calculations to simulate NEXAFS spectra was found to be particularly useful for the series of thionated NDI molecules shown in Figure 3.3, for which experimental data showed systematic changes in the NEXAFS spectra of the series, that were not able to be explained by experiment alone. Chapter 7 of this thesis builds upon the previously published NEXAFS data for this series,<sup>17</sup> by simulating NEXAFS spectra and breaking down these curves into individual atomic contributions in order to understand the role local chemistry plays in systematic changes observed in the NEXAFS spectra with increasing thionation.

The calculations used to predict NEXAFS spectra in this thesis rely on Density Functional Theory (DFT). This section serves to introduce DFT and other computational approximations used in the eXcited-electron and Core Hole (XCH) approach, which was used for all NEXAFS calculations in this thesis. Specifications pertaining to the calculations themselves are given in the experimental section of Chapter 7. An overview of other theories used to calculate NEXAFS spectra is also provided.

DFT is a mathematical method used to calculate an approximate solution to the Schrödinger equation for a many-body system. Practically, DFT can be used to predict structural, magnetic, and electronic properties of materials in the ground state.<sup>22,23</sup> The Schrödinger equation was derived in 1926, by Erwin Schrödinger, following the discovery that the motion of electrons, similarly to photons, can be described by waves. In its simplest form, the Schrödinger equation is:

$$\hat{H}\Psi = E\Psi \quad (3.5)$$

where  $\Psi$  is the wavefunction,  $E$  is the energy of the system and  $\hat{H}$  is the Hamiltonian operator, comprised of three terms: the kinetic energy,  $\hat{T}$ , the external potential,  $\hat{V}$ ,

and the electron-electron interaction,  $\hat{U}$ .

$$\hat{H} = \hat{T} + \hat{V} + \hat{U} \quad (3.6)$$

There are several sophisticated methods that approximate solutions to the Schrödinger equation, such as the Hartree-Fock method,<sup>24</sup> shown below:

$$\Psi(r_1, r_2, \dots, r_N) = \psi_1(r_1)\psi_2(r_2)\dots\psi_N(r_N) \quad (3.7)$$

where  $\psi(r_1)$  is a wavefunction that satisfies a one-electron Schrödinger equation. However, these methods are computationally expensive, making it almost impossible to apply to larger, more complex systems such as the molecules studied in this thesis. This is because, for every electron in the system, there are three spatial coordinates to describe its location: x, y, and z. In order to drastically simplify the determination of the ground-state energy of the system, it is useful to define the electron density of the entire system, reducing the number of variables from  $3N$  (that is, three directions for  $N$  atoms comprising the system) to simply 3: x, y, and z for the entire system.

In 1965, the Kohn-Sham equation was first introduced, which provided a breakthrough in the approach to solving DFT calculations, by providing a method for handling the kinetic energy functional,  $\hat{T}$ , previously neglected by other approximations of solutions to the Schrödinger equation. Kohn and Sham postulated that the kinetic energy of  $N$  interacting electrons in a system could be approximated by a fictitious system of  $N$  non-interacting electrons with the same density. This provided a practical way to solve and find the ground state density using fictitious, non-interacting so-called Kohn-Sham orbitals. However, the Kohn-Sham equation lacks detail on the exact exchange-correlation potential, which is generally approximated by other methods.<sup>25</sup> The breakthrough in determining electronic structure in multi-atomic systems that was offered by the Kohn-Sham equation is still widely used today, including in the calculations of the first core-excited state determined by the XCH method.

Following “excitation,” the XCH method represents the excited atom in a molecule as a modified pseudopotential, with the electron excited from the atom placed in the first available valence orbital, analogous to the LUMO of the ground state, to reduce computational cost. The excitation of an electron from a core orbital (described hereafter as a core hole) into the available LUMO and its resulting “relaxation” due to the Coulomb interaction between the electron and hole, defines the final state.<sup>9</sup> Unoccupied energy levels higher than the first available valence orbital are generated from the self-consistent potential of the system. The core excitation is moved from one atom to another of the same species, which enables the accumulation of the full X-ray absorption spectroscopy spectrum. The calculations rely on the Perdew-Burke-Ernzerhof (PBE) generalized gradient approximation,<sup>26</sup> which is known to underestimate band gaps.<sup>27</sup> To account for these discrepancies, a dilation factor of 1.1 is applied to the carbon K-edge simulations. The final line shape of the XAS spectra is generated via a numerical convolution of the simulated transitions with Gaussian line shapes. Peak widths are set to 0.2 eV and the heights are proportional to the oscillator strength calculated for a given transition.

Apart from the XCH method, there are other methods used to calculate the X-ray absorption spectra of conjugated organic materials. For example, a widely-used method is the Transition Potential (TP) approach, which assumes a localized core hole in the description of the excitation, termed a “one-center approximation.”<sup>28–30</sup>

Although also based on DFT in the Kohn-Sham scheme as the XCH approach is, in this method, a transition state for one excitation center (i.e. for the carbon K-edge) is introduced as a representative for all excitations to unoccupied orbitals. For the carbon K-edge, this is characterized by the C 1s core orbital, and has a fractional occupation number of 0.5, calculated self-consistently. This approach treats electronic excitation as being located “half-way” between the initial and final state, accounting for some of the excited state relaxation. Additionally, the transition energies are known to be approximately 1.5 – 2.0 eV too large, which is commonly addressed by an established correction function.<sup>28</sup>

The XCH method was developed in part by David Prendergast of the Molecular Foundry at the Lawrence Berkeley National Laboratory in Berkeley, California. Access to the XCH code developed by Dr. Prendergast was made available through the Molecular Foundry User Access Program. Calculations were performed by the candidate under the supervision of Dr. Prendergast. The candidate traveled to the Lawrence Berkeley National Laboratory for a 5 week visit, continuing the calculations remotely at Monash University.

This concludes the methodology for experiments used to characterize materials properties of the organic semiconductors studied in this thesis. The following section outlines the methods used to fabricate and characterize solar cells.

### 3.3 Solar cell fabrication and characterization

The following section outlines the equipment and methods used to fabricate organic solar cells, as well as to characterize current-voltage characteristics and external quantum efficiency for all the devices mentioned in this thesis. Results Chapters 4-6 feature NDI-based small molecule acceptors with the same optimized solar cell fabrication conditions, while Chapter 7 introduces NDI-based polymeric acceptors. These different systems required slightly different optimum device processing conditions, compared to the small molecule acceptors, which are described in detail in the experimental part of Chapter 7. Here, the material systems used in Chapters 4-6 are used as an example for the device fabrication methods employed in this thesis.

#### 3.3.1 Device fabrication

Devices fabricated with an inverted architecture (shown in Figure 3.11) in general were found to perform better compared to conventional devices. This was concluded following device optimization for a materials system that involved work during this PhD but is not featured in this thesis. Results pertaining to this system can be found elsewhere.<sup>31</sup> The inverted device architecture was optimized for each material system and is specified in each results chapter. As an example, optimized devices featured in Chapter 5 utilize the following architecture: ITO/ZnO/PEIE/Active Layer/MoO<sub>x</sub>/Ag.

Devices were fabricated onto pre-patterned ITO glass slides with a sheet resistance of 50  $\Omega/\square$ , supplied by Luminescence Technology Corporation. As is shown in Figure 3.11, the ITO-coated slides have a total area of 11.95 mm<sup>2</sup>, and a thickness of 1.1 mm, with the ITO covering an area of 7.5 mm  $\times$  11.95 mm. The fabrication process for all devices began in the same way: ITO-coated glass slides were sequentially sonicated in acetone and 2-propanol for ten minutes, followed by an oxygen-derived plasma treatment (using a Harrick PDC-FMG plasma cleaner) for ten minutes. The



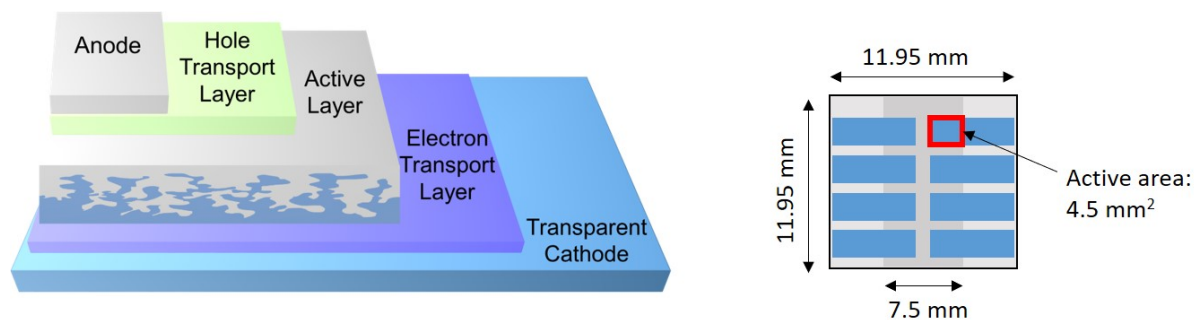


Figure 3.11: Schematic of an inverted solar cell (left) and diagram of completed device (right).

zinc oxide precursor was prepared by dissolving zinc acetate dihydrate (220 mg) in 10 ml 2-methoxyethanol to form a 0.1 M solution. Ethanolamine (61 mg) was added as a stabilizer and the solution was stirred at 60 °C overnight in ambient conditions. A 0.4% PEIE solution was prepared by further diluting 40 mg of PEIE already dissolved in water, in 10 mL of 2-methoxyethanol. Both solutions were filtered (using 0.45  $\mu\text{m}$  polytetrafluoroethylene (PTFE) filters) before use and spin cast in ambient conditions. ZnO (4000 RPM) and PEIE (5000 RPM) films were annealed at 200 °C for thirty minutes and 120 °C for twenty minutes respectively. All materials and solvents were acquired from Sigma Aldrich and used as received. Following ZnO and PEIE deposition, substrates were transferred to a glove box under nitrogen atmosphere where active layers were spin cast to form films with thicknesses of approximately 80 nm (6000 RPM) for all NDI-based small molecule acceptors (this varies slightly to the thicknesses attained for the polymeric acceptors used in Chapter 7, which were  $\sim 50$  nm thick). PBDTTT-EFT was used as the donor material for all devices fabricated in this thesis. It was purchased from 1-Material (batch number YY8126,  $M_n = 25$  kg/mol) and used as received. A 1:1 weight ratio of PBDTTT-EFT:acceptor was determined to be optimal for all systems. All systems were cast from 30 g/l solutions in anhydrous chlorobenzene, with solutions heated overnight at 70 °C prior to spin coating. Immediately after films were deposited, the substrates were transferred to an Angstrom Engineering Covap vacuum evaporator where 12 nm of molybdenum oxide (supplied by sigma Aldrich, purity: 99%), at a deposition rate of 0.3  $\text{\AA}/\text{s}$ , followed by 100 nm of silver (supplied by R.D. Mathis Company, purity: 99.999%), at a deposition rate of 1.0  $\text{\AA}/\text{s}$ , were vacuum evaporated onto the substrates with the vacuum level remaining below  $10^{-6}$  mbar. A mask was used to produce eight identical pixels per device ( $4.5 \text{ mm}^2$  active area each) during evaporation. The right side of Figure 3.11 provides a diagram of a completed device, in which the dimensions of the substrate and active-area are shown. Prior to characterization, devices were fitted with edge clips and encapsulated by ITW Devcon 2T epoxy and glass. The epoxy was left to cross-link overnight and devices were typically characterized within 24 hours of being fabricated.

### 3.3.2 Device characterization

The theory introducing both  $J - V$  and EQE measurements is given in Section 2.3.2. This section specifies the equipment used in experiments.

### 3.3.2.1 $J - V$ measurements

A Photo Emission Tech model SS50AAA solar simulator (calibrated using a PV Measurements silicon reference cell with a KG3 glass filter) was used to simulate sunlight (AM 1.5 spectrum) at an intensity of  $100 \text{ mW cm}^{-2}$  while a Keithley 2635 source meter characterized the device's photovoltaic performance. Because devices employed an inverted architecture, voltage was swept from -0.5 to 1.0 V, in 0.02 V increments.

A spectroradiometer from PV Measurements was used to characterize the output of the solar simulator. The spectral mismatch, characterized by the mismatch factor,  $M$ , was determined as follows, and subtracted from reported device efficiencies:

$$M = \frac{\int E_R(\lambda) S_R(\lambda) \partial\lambda}{\int E_S(\lambda) S_R(\lambda) \partial\lambda} \times \frac{\int E_S(\lambda) S_T(\lambda) \partial\lambda}{\int E_R(\lambda) S_T(\lambda) \partial\lambda} \quad (3.8)$$

where  $E_S$  is the spectral irradiance of the solar simulator,  $E_R$  is the AM1.5G standard spectral irradiance,  $S_T$  is the spectral responsivity of the test cell, and  $S_R$  is the spectral responsivity of the reference silicon cell used when calibrating the solar simulator. Typical  $M$  values range from 0.02 - 0.04, indicating only minimal deviations of the solar simulator from the AM 1.5 spectrum.

### 3.3.2.2 EQE measurements

Following  $J - V$  characterization, the EQE of working pixels was measured as a function of wavelength using a spot size less than the active area of the pixel. A monochromator (Oriel Cornerstone 130) was used to disperse light from a tungsten filament (Newport 250 W QTH). Prior to measurement, the system was calibrated with a photodiode (Thorlabs FDS-100CAL) placed at the exact location devices occupy during measurements. The light intensity was measured simultaneously as measurements were obtained using a second silicon photodiode that continually measured a portion of the beam using a beam splitter. EQE was measured from 350 to 900 nm in 5 nm increments, where the monochromator was controlled by a LabView-based program, which also recorded the current from the solar cell and the signal from the silicon reference photodiode. The spectral responsivity for the devices was related to the EQE as follows:

$$EQE = \frac{1240 J_{SC}}{\lambda E} = \frac{1240 s(\lambda)}{\lambda} \quad (3.9)$$

where  $J_{SC}$  is the short-circuit current,  $E$  is the irradiance, and  $\lambda$  is the wavelength in nanometers. This equation allows for the devices'  $J_{SC}$  to be estimated using a spot size smaller than the active area of the cell, thereby minimizing the boost in  $J_{SC}$  sometimes observed in  $J - V$  characterization due to edge effects occurring as a result of illuminating over the entire area of the cell. Without the use of a mask to prevent charges generated outside of the defined active area of the cell contributing to the current, it was observed that the  $J_{SC}$  determined from  $J - V$  characterization was often higher than the  $J_{SC}$  determined by integrating the EQE spectrum.

### 3.3.2.3 Intensity dependent measurements

By varying the optical excitation intensity used to illuminate a solar cell, it is possible to measure steady-state, intensity-dependent  $J - V$  characteristics. Extracting the short-circuit current, and plotting this as a function of light intensity, it is possible to

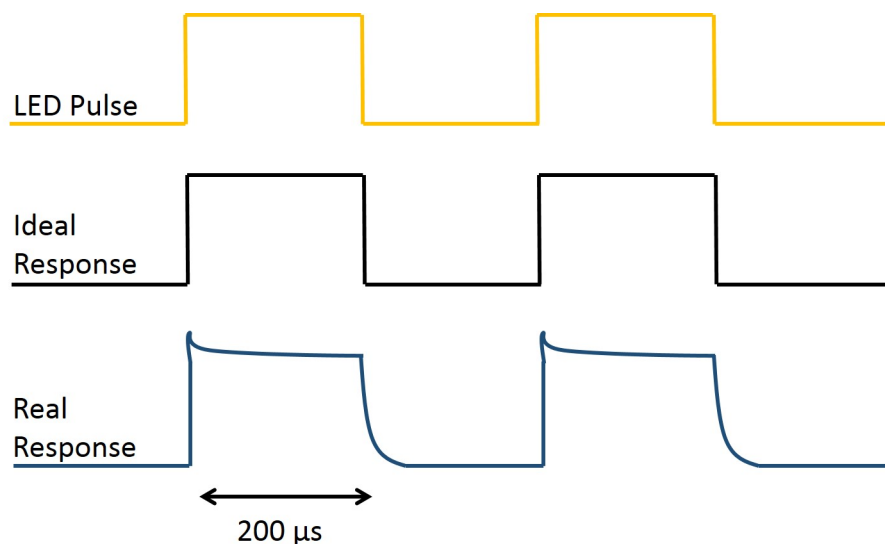


Figure 3.12: Schematic of an ideal and real response to a pulsed light source during a transient photocurrent measurement.

determine  $\alpha$ , a parameter used to quantify the degree of non-linearity in the following power law relationship:  $J_{SC} \propto I^\alpha$ . An ideal solar cell would have an  $\alpha$  value of 1, however deviances from the ideal case result in lower  $\alpha$  values. Intensity dependent measurements were conducted using the same equipment described previously for  $J-V$  measurements, however instead of a solar simulator, the light source was a Thorlabs MWWHL3 white light LED, driven by a Thorlabs DC2200 driver.

### 3.3.2.4 Transient photocurrent measurements

Transient photocurrent measurements can be used to probe the charge carrier dynamics in an organic solar cell. One approach is to pulse a device with a square pulse of light with a duration long enough for the device to reach steady state but with a pulse frequency low enough such that the device is depleted of charge prior to the arrival of the next pulse. Current is measured as a function of time, which enables the characterization of a device's response time to the pulsed light. Ideally, the output current vs. time curve should reflect that of the light source: a sudden, fast rise to maximum current at a given light intensity, which remains stable during the time of the pulse, followed by a rapid decay back to zero current when the light source is off. This is shown schematically in Figure 3.12. However, non-ideal behavior may arise as a result of imbalanced charge mobilities in the donor and acceptor materials, or an abundance of trap states in either or both material. Non-ideal behavior may be indicated by an over-shoot in the turn-on of the photocurrent at the start of the pulse, as well as a tail that extends beyond the time when the LED source is turned off (shown in Figure 3.12). Measuring transient photocurrent as a function of LED light intensity is also useful, as this provides information about charge trapping and de-trapping. Non-ideal behavior can be indicative of bimolecular recombination competing with charge extraction, both of which negatively impact solar cell performance.<sup>32,33</sup>

In this work, transient photocurrent measurements were conducted using a 200  $\mu$ s square Kingbright L-7104VGC-H green LED pulse (with a wavelength of 525 nm and pulse frequency of 100 Hz) which was driven by an Agilent 3522A function generator.

An Agilent Technologies InfiniiVision DSO-X 3032A digital oscilloscope (DOSC) was used to record transient photocurrent measurements, with the solar cell connected in series with a 50  $\Omega$  terminated output of the oscilloscope. A set of density filters were used to alter the intensity of the LED source. Current was plotted as a function of time for all light intensities in the transient photocurrent measurements.

### 3.3.3 Space-charge limited current devices

A common method to quantify the mobility of a donor/acceptor blend is to fabricate devices that become space-charge limited, with the limited carriers being either electrons or holes.<sup>34</sup> These are termed space-charge limited current (SCLC) devices, and are termed either hole-only or electron-only, depending on the charge that becomes space-charge limited in the device. In order to control this, devices are fabricated using only hole-injecting and electron-blocking electrodes in hole-only devices, and electron-injecting and hole-blocking electrodes in electron-only devices. In the device, at least one electrode must efficiently inject the desired carrier, while the other electrode must block injection of the other carrier. Applying a voltage to the device injects unipolar charges, which builds up space-charge in the device. The relationship between the voltage applied to the parallel plates of the electrodes and the amount of space-charge that can be sustained determines the current that is produced, influenced in turn by the carrier mobility. Then, the steady-state current density,  $J_{SCLC}$ , can be determined using the Murgatroyd equation,<sup>35</sup> which accounts for the voltage-dependence of mobility often seen in organic semiconductors:

$$J_{SCLC} = \frac{9}{8} \epsilon_0 \epsilon_r \mu_0 \exp(0.89\beta \sqrt{V - V_{bi}/d}) \frac{V^2}{d^3} \quad (3.10)$$

where  $V$  is the voltage,  $d$  is the active layer thickness,  $\mu_{SCLC}$  is the mobility of the device, and  $\epsilon$  is the permittivity of the film. In this way, it is possible to determine both the hole and electron mobility of an active layer, by fabricating hole and electron-only devices, and extracting the mobility of each through the relationship above, from steady-state  $J - V$  curves.

## 3.4 Active layer morphology characterization

To fully characterize the active layer morphology in an organic solar cell, it is necessary to probe the characteristic domain size and crystallinity, the degree of mixing between donor and acceptor materials, the amount of phase separation (if any) between materials, and the interfacial structure.<sup>36</sup> Unfortunately, there is no single technique that can be used to fully characterize the active layer morphology in solar cells. Instead, morphology is characterized using a combination of complimentary techniques including optical, X-ray and electron-based methods. Together, these techniques can assist in developing a comprehensive understanding of the active layer morphology in the organic systems described in this thesis. Unless otherwise stated, the fabrication methods used to prepare samples for the following techniques utilized the optimized blend film parameters described in the previous section.

### 3.4.1 Surface Profiler

Although not strictly a morphology characterization technique, a surface profiler is used to determine the active layer thickness in organic solar cells. This is an important parameter, as the active layer thickness influences both the number of photons that are absorbed by the solar cell, as well as how efficiently the free charge carriers that are generated following absorption are extracted from the device.

In order to determine the active layer thickness, films are deposited following optimized device conditions onto a cleaned glass substrate. A scalpel is used to remove the soft organic material without scratching the substrate by gently removing the film. The surface profiler then uses a fine-tipped stylus to scan across the surface of the film, perpendicular to the direction of the channels of removed film. In this way, a profile of the surface of the film, including the exposed substrate, is measured, and the difference between the height of the film and height of the substrate is taken to be the active layer thickness. A Dektak-150 Surface Profiler (Veeco Instruments Inc.) was used for all active layer thickness measurements reported in this thesis.

### 3.4.2 Photoluminescence quenching

Efficient solar cell operation requires that (1) the neutral excitons that are created following photon absorption are dissociated into electron-hole pairs, (2) that these electron-hole pairs are separated, and (3) that these then free carriers are transported out of the device without recombining with an oppositely charged carrier. Photoluminescence (PL) quenching is a technique that can be used to probe the first requirement. As was outlined in Section 2.2.2.1, the excited-state singlet exciton that is created after photon absorption decays either radiatively (via photoluminescence) or non-radiatively within 1-10 ns following excitation. If the singlet exciton is dissociated into a free electron-hole pair, the charges will no longer be able to decay to the ground state, in which case the photoluminescence is quenched. PL quenching measurements probe the efficiency of exciton dissociation for a given material or blend of materials by detecting the number of photons that are emitted by the material(s) over a certain energy range, following an optical excitation.<sup>37</sup>

In OPV research, it is useful to measure the PL spectra of the donor and acceptor materials separately, as well as in a blend film. In this way, it can be determined if the addition of an n-type material to a p-type material enhances the exciton dissociation efficiency, which is determined by the number of photons detected. This, in conjunction with other techniques, can give valuable insight into the size, dispersion, and purity of donor and acceptor-rich domains within the blend.<sup>37</sup>

The experimental set-up for a PL quenching measurement is similar to that described for UV-visible absorption spectroscopy in the previous section. However, instead of being located directly behind the sample, the highly sensitive detector is located at a 90° angle from the source, to avoid overexposure. PL quenching measurements were performed in the research group of Justin M. Hodgkiss at the MacDiarmid Institute for Advanced Materials and Nanotechnology, at the Victoria University of Wellington in New Zealand for the materials presented in Chapter 6 and at Monash University for the materials presented in Chapter 7. Experimental details are given in the relative results chapters. As with solid-state UV-vis, neat samples used for PL quenching measurements were prepared using the optimized active layer processing conditions for OPV devices, and were deposited onto fused silica substrates.

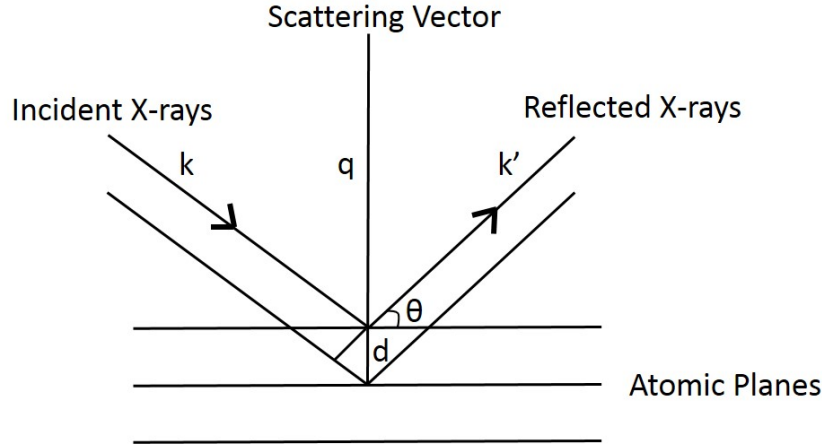


Figure 3.13: Schematic diagram demonstrating Bragg reflections off a crystalline material.

### 3.4.3 Atomic force microscopy

Atomic force microscopy (AFM) is a relatively simple, lab-based technique that is commonly used to characterize the surface topography of the active layer.<sup>38–40</sup> AFM utilizes a sharp cantilever tip to scan the surface of a sample, detecting minute differences in force of the cantilever on the surface to draw a surface topography map that shows nanometer-length differences in surface height across the film.<sup>41</sup> AFM can be useful in determining whether vertical or lateral phase separation occurs between the two materials comprising the active layer, assuming the surface characteristics of both materials are known.<sup>42</sup> This technique is used to image the surface topography of a thin film by measuring the roughness of features on the surface of a film. AFM can also be useful in determining domain size within the active layer, if the domains are very large. Being able to picture domains using AFM generally means the active layer materials are not heterogeneously mixed, resulting in an active layer that does not favor exciton dissociation.

In this thesis, AFM images were obtained from the Melbourne Centre for Nanofabrication using a Bruker Dimension Icon in ScanAsyst mode. Bruker Company AFM tips (MPP-11120-10) were used for all AFM measurements. All films measured by AFM were blends, processed using the optimized conditions for solar cells.

### 3.4.4 Grazing incidence wide-angle X-ray scattering

X-rays are useful for characterizing the active layer morphology in organic solar cells because X-ray radiation encompasses wavelengths on the order of the physical features in blend organic films. Typically, X-ray diffraction (XRD) is used to examine the crystal structure of highly ordered materials, generally relying on the periodic spacing of atoms or molecules in three dimensions.<sup>43</sup> Figure 3.13 illustrates the interactions of X-rays with such a material, indicating that arrangement and spacing between planes of atoms can be determined through Bragg's Law:

$$2d\sin\theta = n\lambda \quad (3.11)$$

where  $d$  is the spacing between atomic planes,  $n$  is the order of reflection (an integer),  $\lambda$  is the incident wavelength, and  $\theta$  is the angle of X-ray incidence with respect to

the substrate. Most commonly, Bragg's Law is used to determine  $d$ , the spacing between atomic planes, because  $\theta$  and  $\lambda$  are known. It is possible to determine the unit cell or coherent packing formation of a molecule within the unit cell of single crystals using XRD measured at many angles of incidence. This leads to the appearance of many Bragg peaks and is typically performed on a powder sample. In real space, the orientation and spacing of the unit cell is described by the lattice vector (**a**, **b**, **c**). X-ray-based scattering techniques are well established and the physics governing scattering events is well understood, making them ideal for studying the active layer morphology in organic blends.<sup>44</sup> However, the disordered nature of materials used in organic electronics, as well as carbon-based materials having a low X-ray cross section, both lead to weak scattering, limiting the use of XRD for probing the crystallinity of an organic material.<sup>45</sup> Instead, synchrotron radiation, which has a high photon flux and brilliance, as well as strong beam collimation, enables the characterization of even weakly scattering, organic films.

One powerful and widely-used X-ray technique is grazing incidence wide-angle X-ray scattering (GIWAXS), which has become ubiquitous with active layer morphology characterization in organic solar cells.<sup>36,46</sup> In this technique, X-rays are used to probe the degree of crystallization, as well as the orientation and size of crystallites, throughout the active layer in reciprocal, or Fourier, space.<sup>45</sup> The use of X-rays to probe microstructure in a given material involves elastic scattering from the atoms in that material, and hence the spacing of the unit cell can be determined by a Fourier transform of the positions and intensities of the scattering profile, provided enough scattering peaks are seen.<sup>47</sup> Instead of the real space lattice vector, (**a**, **b**, **c**), the orientation and spacing of the unit cell is described by the lattice vector in reciprocal space:

$$\mathbf{a}^* = 2\pi \frac{\mathbf{b} \times \mathbf{c}}{\mathbf{a}(\mathbf{b} \times \mathbf{c})} \quad (3.12)$$

$$\mathbf{b}^* = 2\pi \frac{\mathbf{a} \times \mathbf{c}}{\mathbf{a}(\mathbf{b} \times \mathbf{c})} \quad (3.13)$$

$$\mathbf{c}^* = 2\pi \frac{\mathbf{a} \times \mathbf{b}}{\mathbf{a}(\mathbf{b} \times \mathbf{c})} \quad (3.14)$$

Then, the general lattice vector is:

$$\mathbf{G}^* = h\mathbf{a}^* + k\mathbf{b}^* + l\mathbf{c}^* \quad (3.15)$$

where  $h$ ,  $k$ , and  $l$  are the integer Miller indices.  $q$  is defined by the difference between  $k$  and  $k'$ , see Figure 3.13, and, in reciprocal space, diffraction is possible when  $q$ , satisfies Bragg's Law:

$$q_B = \left( \frac{4\pi}{\lambda} \right) \sin\theta_b = 2\pi |\mathbf{G}_{hkl}| \quad (3.16)$$

It is possible to revert  $\mathbf{G}_{hkl}$  to real space through the following:<sup>47</sup>

$$d_{hkl} = \frac{1}{|\mathbf{G}_{hkl}|} \quad (3.17)$$

GIWAXS limits the incident X-ray angle to very shallow, grazing angles relative to the surface of the film, in order to minimize scattering from the substrate and maximize scattering from the sample. Detection of scattering off the sample is enabled by

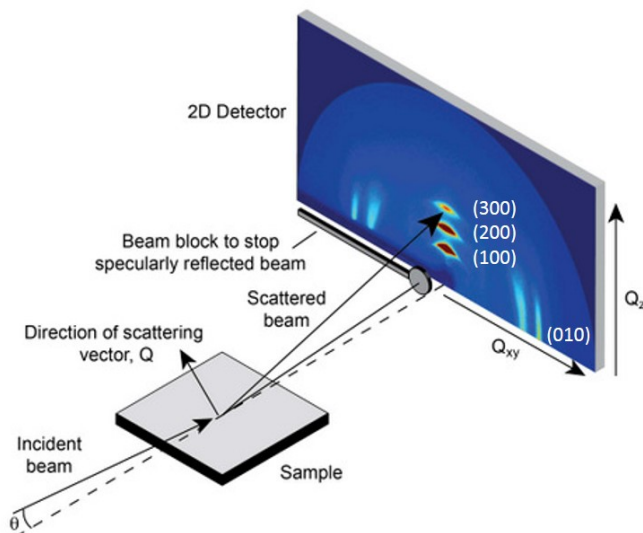


Figure 3.14: Experimental set-up of a GIWAXS measurement. The peaks in the 2D GIWAXS image have been indexed as (100), (200), and (300), in the  $Q_z$  direction, indicating 3 Bragg reflections in this direction, and the peak in the  $Q_{xy}$  direction is indexed as a (010), or  $\pi - \pi$  stacking peak. Adapted with permission from Schuettfort et al. *Journal of American Chemical Society*. 2013, 135, 1092-1101.<sup>48</sup> Copyright 2013 American Chemical Society.

implementing a beam-stop to block the direct specular reflection. GIWAXS enables the characterization of four key microstructure parameters in organic semiconductor films: (1) the repeat distances between molecules, (2) the coherence length (determined by the width of the scattering peaks), (3) information about the texture of the film (i.e. whether it is random or oriented), and (4) depth-dependent information from careful angle-resolved experiments, discussed in more detail below. A schematic diagram of the experimental set-up is shown in Figure 3.14.

An important parameter in GIWAXS measurements is the critical angle,  $\theta_c$ . At very shallow angles, X-rays incident below the critical angle of the sample result in total external reflection, essentially only probing the first several nanometers of the film, rendering it a surface-sensitive measurement. As the incident angle is increased to angles above the critical angle, X-rays penetrate the entirety of the film and measurements reflect an average scattering profile of the bulk film. For polymers, the critical angle is smaller than that of the substrate, so it is possible to simultaneously be above the critical angle of the polymer film, but below that of the substrate (which has a higher critical angle due to the larger electron density of silicon), resulting in a clean scattering profile of the sample with minimum scattering from the substrate. Furthermore, significantly increased scattering intensity can be achieved by the waveguiding of X-rays within the polymer film for angles close to the critical angle. Ideally, characterization of a thin-film by GIWAXS should include measurements at several incident angles, ranging from below the critical angle to well above it, to provide depth-sensitive information and to ensure optimum scattering signal. The critical angle is determined as follows:

$$a_c = \lambda \sqrt{\frac{r_e \rho_e}{\pi}} \quad (3.18)$$



where  $r_e$  is the Thompson scattering length of the electron,  $\lambda$  is the wavelength of the incident X-ray, and  $\rho_e$  is the electron density of the material(s).

The length scale probed is set by the sample-to-detector distance (along with the X-ray energy), which determines the  $q$ -range over which the 2D detector measures. Experiments at the Australian Synchrotron were performed with a distance of  $\sim 300$  mm, which, given the size of the Pilatus 1M detector used (and an X-ray energy of, typically, 11 to 14 keV), gives a  $q$ -range of  $0.2 \text{ \AA}^{-1}$  to  $2.5 \text{ \AA}^{-1}$ , corresponding to distances of 0.25 nm to 3.2 nm. This range is particularly useful for characterizing molecular spacings in neat and blend films, and determining whether blending materials disrupts the molecular spacing of the neat materials. However, despite its popularity, the interpretation of scattering data can be challenging (due to the few, and often poorly resolved diffraction peaks), and results are typically used qualitatively to describe whether one material is “more” or “less” ordered than another.<sup>47</sup> The amount of information that is encoded into a scattering pattern, though, is rich, and the interpretation of commonly observed features is relatively straight forward. Usually, materials used in organic solar cells exhibit multiple peaks in a GIWAXS pattern, and it can be useful to index these peaks.<sup>17</sup> For example, when measuring the GIWAXS profile for a donor-acceptor blend, it is helpful to first index the scattering peaks for the donor and acceptor materials separately, to facilitate the interpretation of the blend pattern. The same Miller indices ( $h$ ,  $k$ , and  $l$ ) that are used to characterized diffraction peaks in Bragg’s law are also used to index scattering peaks observed by GIWAXS: for a typical conjugated polymer,  $h$  is indexed as the lamellar stacking (side chain) repeat,  $k$  is indexed as the  $\pi - \pi$  stacking repeat and  $l$  is indexed as the backbone repeat. The peaks in the 2D GIWAXS pattern shown in Figure 3.14 provide an example for peak indexing. Here, the three peaks in the  $Q_z$  direction are indexed as (100), (200), and (300), indicating a high degree of order along the lamellar stacking direction. The (010) peak is also shown (in the  $Q_{xy}$  direction), indicating some  $\pi - \pi$  stacking in the film. It is worth noting that 2D GIWAXS patterns for small molecules can be more complicated than those for polymers, due to the 3D crystalline nature of some small molecules, and the diverse range of packing motifs that small molecules can adopt. It can also be difficult to index peaks from a GIWAXS pattern if there are not enough peaks in the 2D GIWAXS image.

Figure 3.15 illustrates three possible scattering profiles in the bottom row, with corresponding crystallite orientation in the top row, for increasing degrees of orientation with respect to the substrate. Scenario A exhibits a ring in the diffraction pattern, which corresponds to the presence of crystallites that are randomly oriented with respect to one another and the substrate. When the crystallites are slightly more aligned with one another, and oriented with polymer backbones parallel to the substrate, an arc is observed in the  $q_z$  direction (Figure 3.15 (B)). Finally, scenario C demonstrates an ellipse, or spot, in the scattering pattern, which is indicative of a highly oriented film with crystallites oriented parallel to the substrate. If crystallites were oriented with polymer backbones normal to the substrate surface (i.e.  $90^\circ$  from the orientations shown in Figure 3.15), the scattering features would be located in the  $q_{xy}$  direction. This enables the interpretation of not only the degree of crystallization in a given material, but also how the material is oriented with respect to the substrate, which is of great importance for efficient solar cell operation. Not shown in the figure is the case in which there is no scattering pattern at all, which is observed in films that lack any degree of crystallinity.

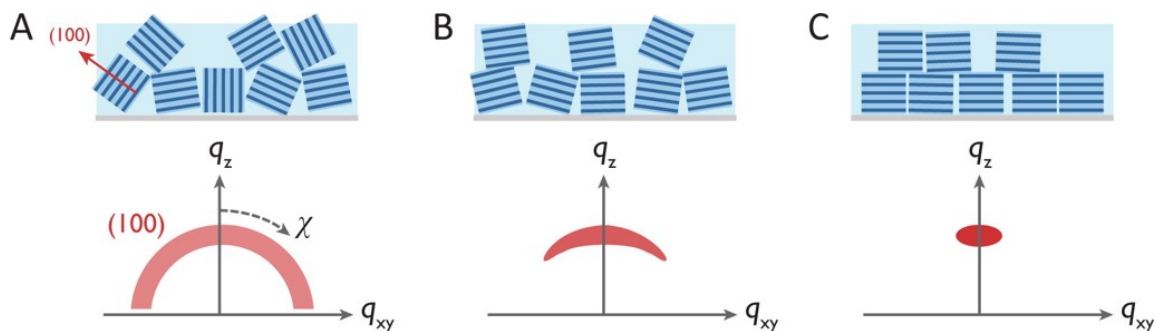


Figure 3.15: 2D GIWAXS patterns corresponding to different orientations of polymer crystallites. (A) Randomly oriented crystallites, with no preference for a specific crystallographic orientation (100) with respect to the substrate normal produce rings in the diffraction patterns. (B) Oriented films with a distribution of crystallite orientations produce arcs of diffracted intensity. (C) Highly oriented films produce spots or ellipses. Adapted with permission from Rivnay et al. *Chem. Rev.*, 2012, 112 (10), pp 5488–5519. Copyright (2012) American Chemical Society.<sup>47</sup>

Referring back to Figure 3.15, Scenario A exhibits a ring-like diffraction pattern that corresponds to lamellar stacking, labeled as a (100) peak in both the  $q_z$  and  $q_{xy}$  directions. However, as the material becomes more uniformly oriented, as is shown in Scenario C, the intensity of the (100) peak, in the  $q_{xy}$  direction is reduced dramatically. In this way, the scattering profile provides information that pertains not only to the degree of crystallinity, but also the orientation of these crystallites. This packing orientation, denoted by strong peaks in the (100) plane in the  $q_z$  direction, is referred to as “edge-on,” because the polymer backbone is oriented  $90^\circ$  from the surface of the substrate. Conversely, if the crystallites were to be turned by  $90^\circ$ , the (100) peak would be visible only in the  $q_{xy}$  direction. This orientation is referred to as “face-on.”

In this thesis, GIWAXS samples were prepared using the optimized device processing conditions for both blend and neat films, which were deposited onto cleaned silicon substrates, cut to be approximately  $1.5\text{ cm} \times 1.5\text{ cm}$  in size. GIWAXS measurements were performed at the SAXS/WAXS beamline at the Australian Synchrotron.<sup>49</sup> A Dectris Pilatus 1M detector was used to record scattering patterns from 11 keV - 14 keV (specified in each results chapter) electrons. The beam had dimensions of  $250\text{ }\mu\text{m}$  in the horizontal and  $150\text{ }\mu\text{m}$  in the vertical directions. Intermodule gaps in the detector lead to “dead space” in the image, which was overcome by taking three images for each sample with the detector slightly offset, that were stitched together in-software following measurements. Samples were aligned by adjusting the height and the polar angle of the sample stage such that the beam was cut by 50% by the sample. Background signal from substrate scatter was minimized by keeping the incident angle of the X-ray beam close to the critical angle of the polymer film but below the critical angle of the substrate. Damage to the film was avoided by limiting the total X-ray exposure time to 3 seconds. The sample-to-detector distance was calibrated using a silver behenate sample and chosen in order to obtain a  $q$  value that extended to at least  $2.0\text{ }\text{\AA}^{-1}$ , to ensure the  $\pi - \pi$  stacking peaks were included. A beam-stop was used to hinder the direct, high-intensity beam from hitting the detector. This beam-stop causes a shadow in the low- $q_z$  region of the 2D scattering pattern, so it was positioned so that the X-ray beam would hit as close to the edge of the beam-stop as possible.

The X-ray flux was constantly monitored by a photodiode, mounted on the beam-stop. Various angles were used, ranging from  $0.05^\circ$  to  $0.3^\circ$  in steps of  $0.01^\circ$ , to survey the scattering patterns above and below the critical angle of either the neat or blend films.

The results were analyzed by an altered version of the NIKA 2D data reduction package<sup>50</sup> implemented in IgorPro. 1D scattering profiles along the  $q_{xy}$  (in-plane) and  $q_z$  (out of plane) directions were extracted by integrating the 2D scattering patterns. Peak analysis was done by fitting a Gaussian curve to these 1D line-cuts, after a cubic background function was subtracted.

### 3.4.5 Transmission electron microscopy

Transmission electron microscopy (TEM) utilizes a collimated electron beam to probe the microstructure of materials. In this thesis, the active layers were floated off onto a copper mesh grid, which the electron beam transmits through, forming a 2D projection of the sample down the axis of the electron beam.<sup>51</sup> Bright field (BF) imaging mode was used, in which dark regions in the TEM image correspond to more electron scattering and hence higher electron densities. For blends utilizing a polymer:fullerene mixture, regions with higher electron density correspond with fullerene-rich areas, because fullerenes have a higher electron density than polymers ( $\sim 1.10 \text{ g cm}^{-3}$  for polymers<sup>52</sup> and  $\sim 1.50 \text{ g cm}^{-3}$  in fullerenes<sup>53</sup>). However, the material systems explored in this thesis avoid the use of fullerene acceptors, and TEM images were captured for fullerene-free blends that lack significant contrast arising from differences in electron density, due to the similar electron densities between different polymeric materials.<sup>54</sup> For such systems, contrast can be enhanced by significantly defocusing the electron beam, however this may also lead to artificial artifacts in the 2D projection, and unless the materials contain dissimilar substituent atoms, it is difficult to attain clear TEM images with enough contrast to distinguish between the donor and acceptor materials.<sup>55</sup> The following section, however, introduces a technique that allows for the characterization of non-fullerene active layers with material contrast arising from the subtle differences in NEXAFS-based contrast.

Due to the limitations of this technique, where necessary, solutions used to prepare TEM samples were slightly diluted, in order to produce films with appropriate thicknesses ( $\leq 100 \text{ nm}$ ) for measurement. Following deposition, films were floated off in deionized water onto 300 mesh square copper TEM grids from Emgrid. TEM experiments were conducted by Dr. Amelia Liu, and images were obtained using a JEOL JEM-2100F TEM operating at a voltage of 200kV. Defocused bright-field images were collected using a Gatan UltraScan 1000 ( $2k \times 2k$ ) CCD camera. A  $20 \mu\text{m}$  objective aperture and a large defocus value of  $-10,000 \text{ nm}$  were used to increase contrast between the phases.

### 3.4.6 Resonant soft X-ray scattering

As was mentioned in the previous section, due to OPV active layers being comprised of materials that largely lack strong electron density contrast, there can be difficulties that arise from trying to image morphology using typical methods such as TEM. However, through the combination of small-angle X-ray scattering (SAXS) and NEXAFS spectroscopy, 3D chemical morphology information can be extracted for fullerene-free blends using a technique termed Resonant Soft X-ray Scattering (R-SoXS). Scattering

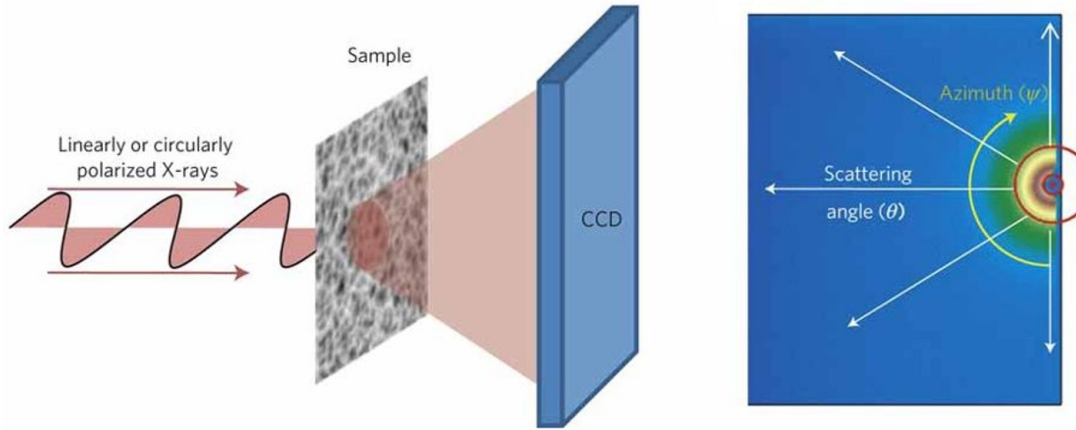


Figure 3.16: Set-up of an R-SoXS experiment. Polarized X-rays are scattered by the material onto a CCD array. Adapted with permission from Collins et al. *Nature Materials*, 2012, 11, pp. 536–543. Copyright (2012) Springer Nature.<sup>47</sup>

techniques such as R-SoXS are complimentary to previously described, highly localized techniques like AFM and TEM, because they represent a statistical average over a large sample area.<sup>56</sup> In addition, unlike in conventional SAXS experiments which are performed using hard X-rays, R-SoXS takes advantage of the enhanced scattering contrast available in the soft X-ray energy range to gain unique chemical sensitivity between different conjugated materials, on nm –  $\mu$ m length scales, making it ideal for studying the mesostructure of bulk heterojunction blends.<sup>57</sup>

R-SoXS is a transmission experiment, the set-up of which is shown in Figure 3.16.<sup>47</sup> Small-angle X-ray scattering is a widely used technique for revealing information about the size, shape, distribution and structure of disordered and partially ordered systems.<sup>58</sup> Unlike the hard X-rays used in traditional SAXS experiments, measuring SAXS in the soft X-ray range at certain resonant energies (such as about 284 eV, corresponding to the carbon K-edge) amplifies the observed scattering intensity, and provides enhanced chemical sensitivity between two very similar materials, such as the carbon-based materials used in heterojunction organic solar cells. For example, the photon energy of the X-ray beam can be tuned to maximize material contrast, enhancing the scattering intensity.<sup>59</sup> Further, the scattering effect of the measurement enables a probe of nano and mesoscale components in the blend, such as the size and purity of active layer domains. In this way, the domain size can be deduced from the position of the scattering peaks, based on the position of momentum transfer,  $q$ .

Interpretation of R-SoXS data relies on X-ray-electron interactions, which are encoded, at resonant energies, in the complex index of refraction:

$$n = 1 - \delta + i\beta \quad (3.19)$$

where  $\delta$  is the dispersive component and  $\beta$  is the absorptive component of the refractive index.<sup>60</sup> Specifically,  $\delta$  and  $\beta$  are important parameters at resonance energies, because rapid changes in  $\delta$  and  $\beta$  modulate the X-ray scattering intensity as a function of energy. Scattering contrast is thus derived from differences between  $\delta$  and  $\beta$ , even in materials with similar electron densities.<sup>61</sup>

In 2011, Wang et al.<sup>59</sup> demonstrated the powerful capabilities of R-SoXS to provide a detailed, highly resolved interpretation of the morphology of a triblock copolymer.

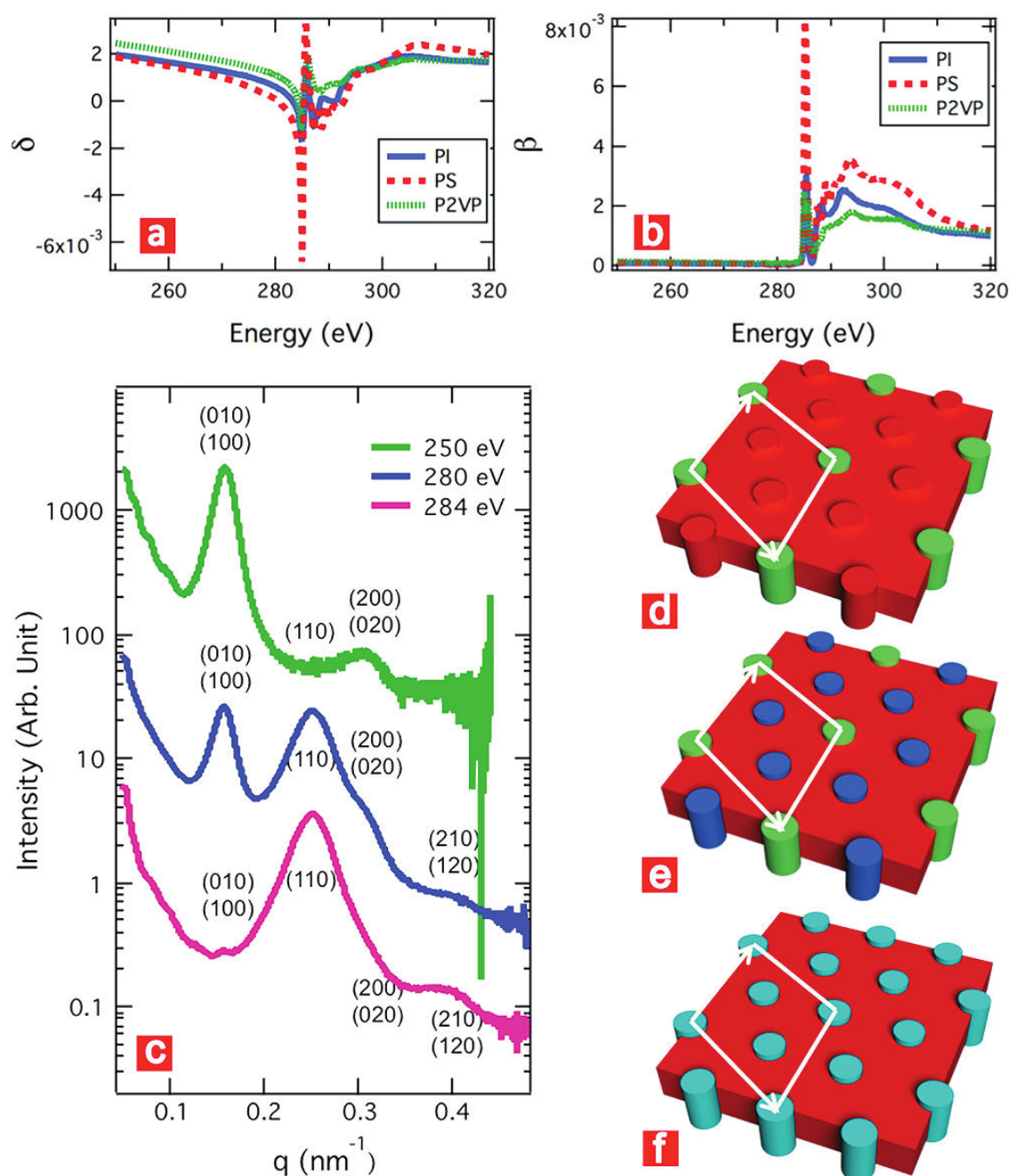


Figure 3.17: Real (a) and imaginary (b) components of the refractive index. (c) Scattering profile of the triblock copolymer film at different X-ray energies. (d-f) Sketches of the resulting matrix that was determined at the three X-ray energies used in (c). Reprinted with permission from Wang et al. *Nano Letters*, 2011, 11, pp. 3906-3911. Copyright (2011) American Chemical Society.<sup>59</sup>

Figure 3.17 shows the real (a) and imaginary (b) components of the refractive index, as well as the scattering profiles of the film at various incident X-ray energies (c). From this information, it was possible to determine the unique cylindrical morphology of the triblock copolymer. From parts (a) and (b) in the figure, it was determined that the contrast between the three components of the block copolymer arises primarily from the real part of the refractive index,  $\delta$ . At the different X-ray energies,  $\delta$  varies for the different components of the triblock copolymer. For example, at 250 eV,  $\delta = 0.0019$  for the PS block,  $\delta = 0.0024$  for the P2VP block, and  $\delta = 0.0019$  for the PI block. Due to the similar  $\delta$  for the PS and PI blocks, it was possible to determine the lattice of the P2VP component in the “PI-PS” matrix. Similarly, at 284 and 280 eV, contrast between the three components is large enough to fully characterize the morphology of the triblock copolymer, allowing for the creation of the sketches of (d-f) in Figure 3.17. Thus, by tuning of the photon energy, material-specific contrast, as well as index matching, can be achieved.

While the work by Wang et al.<sup>59</sup> illustrates the impressive level of detail with which the morphology of organic materials can be characterized using R-SoXS, not all organic semiconductor blends offer such a well-ordered morphology to probe. Instead of well-defined peaks, broader scattering profiles are typically observed, due to a broader distribution of domains sizes. However, for a polymer-donor:small molecule-acceptor blend, which is fairly intermixed and does not show a high degree of order, R-SoXS is still extremely useful in characterizing not only the size, but also the relative purity of active layer domains.<sup>61</sup>

Apart from PL quenching, TEM, and PESA experiments, R-SoXS measurements were the only measurements performed by a third party, due primarily to there being only one R-SoXS beamline in the world, at the Advanced Light Source in Berkeley, California. Samples used in R-SoXS experiments were prepared using the optimized device processing conditions for blend films, spin coated on top of a thick layer of PEIE to assist in floating off. Films were floated in deionized water, followed by transferring onto 100 nm SiN<sub>2</sub> windows. R-SoXS measurements were performed at beamline 11.0.1.2 at the Advanced Light Source.<sup>57</sup> Scattering was performed over a broad energy range. Scattered photons were collected by a Princeton PI-MTE in-vacuum CCD detector with 27.6 mm  $\times$  27.6 mm pixels. Two scattering patterns were collected, one at a 30 mm sample-to-detector distance and another at a 150 mm sample-to-detector distance, and combined in software. Two dimensional scattering patterns were reduced to one dimensional profiles by using a customized version of NIKA.



# References

- [1] Y. H. Shin, A. Welford, H. Komber, R. Matsidik, T. Thurn-Albrecht, C. R. McNeill, and M. Sommer, "Regioregular polymer analogous thionation of naphthalene diimide–bithiophene copolymers," *Macromolecules*, vol. 51, no. 3, pp. 984–991, 2018.
- [2] R. S. Nicholson, "Theory and application of cyclic voltammetry for measurement of electrode reaction kinetics," *Analytical Chemistry*, vol. 37, no. 11, pp. 1351–1355, 1965.
- [3] P. T. Kissinger and W. R. Heineman, "Cyclic voltammetry," *Journal of Chemical Education*, vol. 60, no. 9, p. 702, 1983.
- [4] H. Kirihata and M. Uda, "Externally quenched air counter for low-energy electron emission measurements," *Review of Scientific Instruments*, vol. 52, no. 1, pp. 68–70, 1981.
- [5] R. Pellissier, "Photoelectron spectrometer, manufactured by Riken Keiki," *RKI Instruments*, 2018.
- [6] *PerkinElmer Material Characterization Instrument Guide*. Waltham, MA: Perkin Elmer, 2017.
- [7] K. Vo, "Spectrophotometry," *LibreTexts*, 2018.
- [8] J. Stöhr, *NEXAFS Spectroscopy*. Berlin: Springer, 1992.
- [9] D. Prendergast and G. Galli, "X-Ray absorption spectra of water from first principles calculations," *Physical Review Letters*, vol. 96, p. 215502, 2006.
- [10] G. M. Su, S. N. Patel, C. D. Pemmaraju, D. Prendergast, and M. L. Chabiny, "First-principles predictions of near-edge X-ray absorption fine structure spectra of semiconducting polymers," *The Journal of Physical Chemistry C*, vol. 121, no. 17, pp. 9142–9152, 2017.
- [11] G. Fratesi, V. Lanzilotto, S. Stranges, M. Alagia, G. P. Brivio, and L. Floreano, "High resolution NEXAFS of perylene and PTCDI: a surface science approach to molecular orbital analysis," *Physical Chemistry Chemical Physics*, vol. 16, no. 28, pp. 14834–14844, 2014.
- [12] R. Püttner, P. Schmidt-Weber, T. Kampen, C. Kolczewski, K. Hermann, and K. Horn, "Identification of isomers in the gas phase and as adsorbates by near-edge X-ray absorption fine structure spectroscopy: cis- and trans-stilbene," *Journal of Electron Spectroscopy and Related Phenomena*, vol. 215, pp. 16–21, 2017.



- [13] C. Ehlert, M. Holzweber, A. Lippitz, W. E. S. Unger, and P. Saalfrank, “A detailed assignment of NEXAFS resonances of imidazolium based ionic liquids,” *Physical Chemistry Chemical Physics*, vol. 18, no. 12, pp. 8654–8661, 2016.
- [14] M. M. Nahid, E. Gann, L. Thomsen, and C. R. McNeill, “NEXAFS spectroscopy of conjugated polymers,” *European Polymer Journal*, vol. 81, pp. 532–554, 2016.
- [15] B. C. C. Cowie, A. Tadich, L. Thomsen, R. Garrett, I. Gentle, K. Nugent, and S. Wilkins, “The current performance of the wide range (90–2500 eV) soft X-ray beamline at the Australian synchrotron,” *AIP Conference Proceedings*, vol. 1234, no. 1, pp. 307–310, 2010.
- [16] R. D. Peters, P. F. Nealey, J. N. Crain, and F. J. Himpsel, “A near edge X-ray absorption fine structure spectroscopy investigation of the structure of self-assembled films of octadecyltrichlorosilane,” *Langmuir*, vol. 18, p. 1250, 2002.
- [17] A. Welford, S. Maniam, E. Gann, L. Thomsen, S. J. Langford, and C. R. McNeill, “Thionation of naphthalene diimide molecules: Thin-film microstructure and transistor performance,” *Organic Electronics*, vol. 53, pp. 287–295, 2018.
- [18] B. Watts, L. Thomsen, and P. Dastoor, “Methods in carbon K-edge NEXAFS: experiment and analysis,” *Journal of Electron Spectroscopy and Related Phenomena*, vol. 151, pp. 105–120, 2006.
- [19] E. Gann, C. R. McNeill, A. Tadich, B. C. C. Cowie, and L. Thomsen, “Quick AS NEXAFS Tool (QANT): a program for NEXAFS loading and analysis developed at the Australian Synchrotron,” *Journal of Synchrotron Radiation*, vol. 23, no. 1, pp. 374–380, 2016.
- [20] P. Jiang, D. Prendergast, F. Borondics, S. Porsgaard, L. Giovanetti, E. Pach, J. Newberg, H. Bluhm, F. Besenbacher, and M. Salmeron, “Experimental and theoretical investigation of the electronic structure of Cu<sub>2</sub>O and CuO thin films on Cu(110) using x-ray photoelectron and absorption spectroscopy,” *Journal of Chemical Physics*, vol. 138, no. 2, p. 024704, 2013.
- [21] A. H. England, A. M. Duffin, C. P. Schwartz, J. S. Uejio, D. Prendergast, and R. J. Saykally, “On the hydration and hydrolysis of carbon dioxide,” *Chemical Physics Letters*, vol. 514, no. 4-6, pp. 187–195, 2011.
- [22] R. G. Parr, “Density Functional Theory of Atoms and Molecules,” in *Horizons of Quantum Chemistry*, pp. 5–15, 1980.
- [23] P. Hohenberg and W. Kohn, “Inhomogeneous electron gas,” *Physical Review*, vol. 136, p. B864, 1964.
- [24] D. R. Hartree, “The wave mechanics of an atom with a non-coulomb central field. Part I. Theory and Methods,” *Mathematical Proceedings of the Cambridge Philosophical Society*, vol. 24, no. 1, pp. 89–110, 1928.
- [25] W. Kohn and L. J. Sham, “Self-consistent equations including exchange and correlation effects,” *Physical Review*, vol. 140, p. A1133, 1965.

- [26] J. P. Perdew, K. Burke, and M. Ernzerhof, “Generalized gradient approximation made simple,” *Physical Review Letters*, vol. 77, no. 18, pp. 3865–3868, 1996.
- [27] A. J. Cohen, P. Mori-Sánchez, and W. Yang, “Fractional charge perspective on the band gap in density-functional theory,” *Physical Review B - Condensed Matter and Materials Physics*, vol. 77, no. 11, 2008.
- [28] L. Triguero, L. Pettersson, and H. Ågren, “Calculations of near-edge x-ray-absorption spectra of gas-phase and chemisorbed molecules by means of density-functional and transition-potential theory,” *Physical Review B - Condensed Matter and Materials Physics*, vol. 58, no. 12, pp. 8097–8110, 1998.
- [29] C. Kolczewski, R. Püttner, M. Martins, A. S. Schlachter, G. Snell, M. M. Sant’Anna, K. Hermann, and G. Kaindl, “Spectroscopic analysis of small organic molecules: A comprehensive near-edge x-ray-absorption fine-structure study of C6-ring-containing molecules,” *Journal of Chemical Physics*, vol. 124, no. 3, 2006.
- [30] R. F. Fink, S. L. Sorensen, A. Naves De Brito, A. Ausmees, and S. Svensson, “The resonant Auger electron spectrum of C 1 s-1 $\pi^*$  excited ethene: A combined theoretical and experimental investigation,” *Journal of Chemical Physics*, vol. 112, no. 15, pp. 6666–6677, 2000.
- [31] T. T. Do, K. Rundel, Q. Gu, E. Gann, S. Manzhos, K. Feron, J. Bell, C. R. McNeill, P. Sonar, J. Nelson, I. McCulloch, S. R. Marder, and X. Zhan, “9-Fluorenone and 9,10-anthraquinone potential fused aromatic building blocks to synthesize electron acceptors for organic solar cells,” *New Journal of Chemistry*, vol. 41, no. 8, pp. 2899–2909, 2017.
- [32] Z. Li, F. Gao, N. C. Greenham, and C. R. McNeill, “Comparison of the operation of polymer/fullerene, polymer/polymer, and polymer/nanocrystal solar cells: A transient photocurrent and photovoltage study,” *Advanced Functional Materials*, vol. 21, no. 8, pp. 1419–1431, 2011.
- [33] C. R. McNeill, I. Hwang, and N. C. Greenham, “Photocurrent transients in all-polymer solar cells: Trapping and detrapping effects,” *Journal of Applied Physics*, vol. 106, no. 2, 2009.
- [34] J. C. Blakesley, F. A. Castro, W. Kylberg, G. F. Dibb, C. Arantes, R. Valaski, M. Cremona, J. S. Kim, and J. S. Kim, “Towards reliable charge-mobility benchmark measurements for organic semiconductors,” *Organic Electronics: physics, materials, applications*, vol. 15, no. 6, pp. 1263–1272, 2014.
- [35] P. N. Murgatroyd, “Theory of space-charge-limited current enhanced by Frenkel effect,” *Journal of Physics D: Applied Physics*, vol. 3, pp. 151–156, 1970.
- [36] W. Chen, M. P. Nikiforov, and S. B. Darling, “Morphology characterization in organic and hybrid solar cells,” *Energy & Environmental Science*, vol. 5, no. 8, p. 8045, 2012.
- [37] N. C. Greenham, X. Peng, and A. P. Alivisatos, “Charge separation and transport in conjugated-polymer/semiconductor-nanocrystal composites studied by photoluminescence quenching and photoconductivity,” *Physical Review B*, vol. 54, no. 24, pp. 17628–17637, 1996.

- [38] S. Li, W. Liu, M. Shi, J. Mai, T.-K. Lau, J. Wan, X. Lu, C.-Z. Li, and H. Chen, “A spirobifluorene and diketopyrrolopyrrole moieties based non-fullerene acceptor for efficient and thermally stable polymer solar cells with high open-circuit voltage,” *Energy & Environmental Science*, vol. 9, pp. 604–610, 2016.
- [39] X. Wang, J. Huang, Z. Niu, X. Zhang, Y. Sun, and C. Zhan, “Dimeric naphthalene diimide based small molecule acceptors: synthesis, characterization, and photovoltaic properties,” *Tetrahedron*, vol. 70, no. 32, pp. 4726–4731, 2014.
- [40] Z. Mao, T. P. Le, K. Vakhshouri, R. Fernando, F. Ruan, E. Muller, E. D. Gomez, and G. Sauve, “Processing additive suppresses phase separation in the active layer of organic photovoltaics based on naphthalene diimide,” *Organic Electronics: Physics, Materials, Applications*, vol. 15, no. 11, pp. 3384–3391, 2014.
- [41] G. M. McClelland, R. Erlandsson, and S. Chiang, “Atomic force microscopy: General principles and a new implementation,” in *Review of Progress in Quantitative Nondestructive Evaluation*, pp. 1307–1314, Boston, MA: Springer US, 1987.
- [42] P. Karagiannidis, D. Georgiou, C. Pitsalidis, A. Laskarakis, and S. Logothetidis, “Evolution of vertical phase separation in P3HT:PCBM thin films induced by thermal annealing,” *Materials Chemistry and Physics*, vol. 129, no. 3, pp. 1207–1213, 2011.
- [43] B. E. Warren, “X-ray diffraction methods,” *Journal of Applied Physics*, vol. 12, no. 5, pp. 375–383, 1941.
- [44] J. Als-Nielsen and D. McMorrow, *Elements of Modern X-ray Physics*. Wiley, 2 ed., 2011.
- [45] D. M. DeLongchamp, R. J. Kline, D. A. Fischer, L. J. Richter, and M. F. Toney, “Molecular characterization of organic electronic films,” *Advanced Materials*, vol. 23, no. 3, pp. 319–337, 2011.
- [46] Y. Liu, J. Zhao, Z. Li, C. Mu, W. Ma, H. Hu, K. Jiang, H. Lin, H. Ade, and H. Yan, “Aggregation and morphology control enables multiple cases of high-efficiency polymer solar cells,” *Nature Communications*, vol. 5, p. 5293, 2014.
- [47] J. Rivnay, S. C. B. Mannsfeld, C. E. Miller, A. Salleo, and M. F. Toney, “Quantitative determination of organic semiconductor microstructure from the molecular to device scale,” *Chemical Reviews*, vol. 112, no. 10, pp. 5488–5519, 2012.
- [48] T. Schuettfort, L. Thomsen, and C. R. McNeill, “Observation of a distinct surface molecular orientation in films of a high mobility conjugated polymer,” *Journal of the American Chemical Society*, vol. 135, no. 3, pp. 1092–1101, 2013.
- [49] N. M. Kirby, S. T. Mudie, A. M. Hawley, D. J. Cookson, H. D. T. Mertens, N. Cowieson, and V. Samardzic-Boban, “A low-background-intensity focusing small-angle x-ray scattering undulator beamline,” *Journal of Applied Crystallography*, vol. 46, pp. 1670–1680, 2013.
- [50] J. Ilavsky, “Nika: Software for two-dimensional data reduction,” *Journal of Applied Crystallography*, vol. 45, no. 2, pp. 324–328, 2012.

- [51] X. Yang, J. Loos, S. C. Veenstra, W. J. H. Verhees, M. M. Wienk, J. M. Kroon, M. A. J. Michels, and R. A. J. Janssen, "Nanoscale morphology of high-performance polymer solar cells," *Nano Letters*, vol. 5, no. 4, pp. 579–583, 2005.
- [52] T. J. Prosa, M. J. Winokur, J. Moulton, P. Smith, and A. J. Heeger, "X-ray structural studies of poly(3-alkylthiophenes): An example of an inverse comb," *Macromolecules*, vol. 25, no. 17, pp. 4364–4372, 1992.
- [53] C. Bulle-Lieuwma, W. van Gennip, J. van Duren, P. Jonkheijm, R. Janssen, and J. Niemantsverdriet, "Characterization of polymer solar cells by TOF-SIMS depth profiling," *Applied Surface Science*, vol. 203–204, pp. 547–550, 2003.
- [54] N. Zhou, A. S. Dudnik, T. I. Li, E. F. Manley, T. J. Aldrich, P. Guo, H. C. Liao, Z. Chen, L. X. Chen, R. P. H. Chang, A. Facchetti, M. Olvera De La Cruz, and T. J. Marks, "All-polymer solar cell performance optimized via systematic molecular weight tuning of both donor and acceptor polymers," *Journal of the American Chemical Society*, vol. 138, no. 4, pp. 1240–1251, 2016.
- [55] K. D. Deshmukh, R. Matsidik, S. K. Prasad, N. Chandrasekaran, A. Welford, L. A. Connal, A. C. Liu, E. Gann, L. Thomsen, D. Kabra, J. M. Hodgkiss, M. Sommer, and C. R. McNeill, "Impact of acceptor fluorination on the performance of all-polymer solar cells," *ACS Applied Materials and Interfaces*, vol. 10, no. 1, pp. 955–969, 2018.
- [56] G. Renaud, R. Lazzari, and F. Leroy, "Probing surface and interface morphology with Grazing Incidence Small Angle X-Ray Scattering," *Surface Science Reports*, vol. 64, no. 8, pp. 255–380, 2009.
- [57] E. Gann, A. T. Young, B. A. Collins, H. Yan, J. Nasiatka, H. A. Padmore, H. Ade, A. Hexemer, and C. Wang, "Soft x-ray scattering facility at the Advanced Light Source with real-time data processing and analysis," *Review of Scientific Instruments*, vol. 83, no. 4, 2012.
- [58] F. Liu, M. A. Brady, and C. Wang, "Resonant soft X-ray scattering for polymer materials," *European Polymer Journal*, vol. 81, pp. 555–568, 2016.
- [59] C. Wang, D. H. Lee, A. Hexemer, M. I. Kim, W. Zhao, H. Hasegawa, H. Ade, and T. P. Russell, "Defining the nanostructured morphology of triblock copolymers using resonant soft X-ray scattering," *Nano Letters*, vol. 11, no. 9, pp. 3906–3911, 2011.
- [60] C. Wang, T. Araki, and H. Ade, "Soft x-ray resonant reflectivity of low-Z material thin films," *Applied Physics Letters*, vol. 87, no. 21, p. 214109, 2005.
- [61] C. R. McNeill and H. Ade, "Soft X-ray characterisation of organic semiconductor films," *Journal of Materials Chemistry C*, vol. 1, no. 2, pp. 187–201, 2013.



## Chapter 4

# Effect of substituent atoms on the properties of naphthalene diimide

Substituent atoms have repeatedly been shown to alter the material properties of organic semiconductors. This chapter explores the effect that oxygen, sulfur, and nitrogen substitutional moieties, incorporated at core positions of a naphthalene diimide molecule with butyl chains, have on the optical and electronic properties of the NDI molecule. It is found that, for all three substitutions, the band gap is reduced, enabling visible wavelength absorption by the core-substituted molecules. Additionally, the substitutional moiety impacts the LUMO energy level of the material, with nitrogen raising the LUMO energy the most of the three substituents. It is shown that solar cell performance can be improved, over the parent molecule, with oxygen and sulfur substituents, from 0.33% to 0.60% and 0.56%, respectively, however the incorporation of nitrogen drastically reduces the PCE to 0.02%. The crystallinity of the materials was also explored by GIWAXS, indicating a reduction in crystallinity as substituent atoms are introduced to the molecule, likely a result of increased disorder due to the added butyl chains. When blended with a donor polymer, the parent NDI molecule disrupts the packing of the polymeric donor material, while the NDI molecules containing substituents do not exhibit any crystallization in the blend.

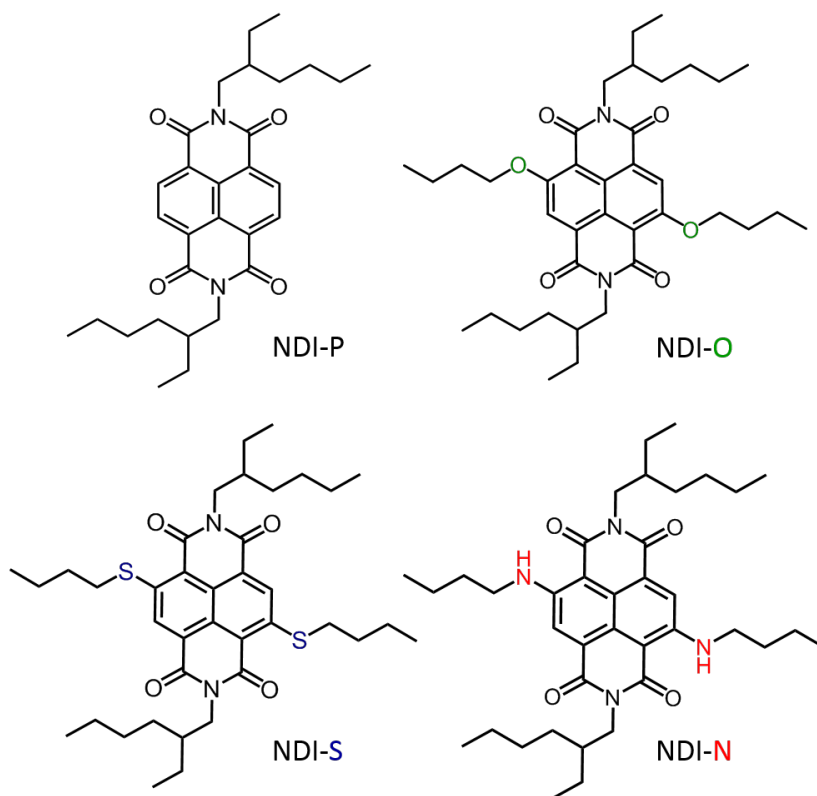


Figure 4.1: Molecular structures of the NDI-based small molecule acceptors studied in Chapter 4 including NDI-P, NDI-O, NDI-S, and NDI-N.

## 4.1 Introduction

As was mentioned in the Literature Review chapter, substituents can be used to alter the optoelectronic properties of organic semiconductors. Specifically for the naphthalene diimide moiety, substituents can be incorporated into the molecular structure at flanking core positions, or at the imide nitrogen position. Typically, soluble NDI molecules are functionalized by incorporating alkyl chains at the imide position,<sup>1</sup> although this position has also been demonstrated as a suitable location to link additional moieties to the molecule.<sup>2</sup> However, in this chapter, work has focused on functionalizing the NDI moiety by incorporating substituents at the  $R_1$  and  $R_3$  core positions, labeled in Figure 2.20.

It has previously been shown that atomic substituents at these positions can greatly influence the optical properties of NDI.<sup>3</sup> For example, if an electron donor is incorporated, the NDI exhibits a dramatic color change from white to often vibrant colors in what is termed a push-pull system.<sup>3</sup> This is the type of substitution explored in this chapter, with either oxygen, sulfur or nitrogen being incorporated at the  $R_1$  and  $R_3$  positions in conjunction with a butyl chain. There are four molecules introduced here: the parent molecule, NDI-P, and the three molecules containing substituents, NDI-O, NDI-S, and NDI-N, shown in Figure 4.1.

Adding donating substituents at core positions to the already electron-withdrawing imides in the molecule has been demonstrated to alter both the color and redox behavior of naphthalene diimide – a very attractive feature of the NDI moiety because this implies its energy levels can be tuned to fit given applications. Specifically, it is

known that increasing the donor substituent content at the core positions of the NDI moiety results in a systematic decrease in the material's band gap, with the LUMO being systematically lowered and the HOMO being systematically raised with increasing donor content.<sup>3</sup> This decrease in band gap results in a strong optical response of the material in the visible wavelength range, exemplified by vibrant colors associated with various substituent atoms. Figure 4.2 demonstrates this for the core-substituted molecules presented in this chapter: compared to the parent molecule, where the solution (chlorobenzene as solvent) is colorless, NDI-O appears yellow, NDI-S appears red, and NDI-N appears blue.

This chapter aims to understand the changes in the optical and electronic properties that occur following core substitution. As ultimately higher solar cell efficiencies were achieved with molecules with expanded molecular architectures (see Chapter 5), the characterization of these materials is not as detailed as for materials presented in subsequent results chapters. This chapter serves to demonstrate the dramatic effect substituent atoms have on the properties of NDI molecules and motivate further solar cell studies with more optimum molecular geometries.

## 4.2 Experimental Details

### 4.2.1 Cyclic Voltammetry

A VSP potentiostat from Bio-Logic Instruments with EC-Lab for Windows was used for all solution-based cyclic voltammetry measurements. A 0.1 M solution of tetrabutylammonium hexafluorophosphate ( $\text{Bu}_4\text{NPF}_6$ ) in dichloromethane (argon-purified) was used as the supporting electrolyte and solvent, respectively. CV measurements were conducted in air, where the solution was purified by gently bubbling argon gas through it for five minutes, so prior to measurement, a blank CV scan was run in order to confirm all oxygen had been removed from the solution. 0.05 M of each acceptor material was then added to the solution, and the measurement was done again. Finally, a small amount of ferrocene/ferrocenium ( $\text{Fc}/\text{Fc}^+$ ) was added to the solution and a final measurement was taken, in order to internally calibrate the system. All CV measurements were taken at room temperature (with a scan rate of 100 mV/s, from -2000 to 1500 mV) with a glassy carbon working electrode (2.0 mm diameter), a silver

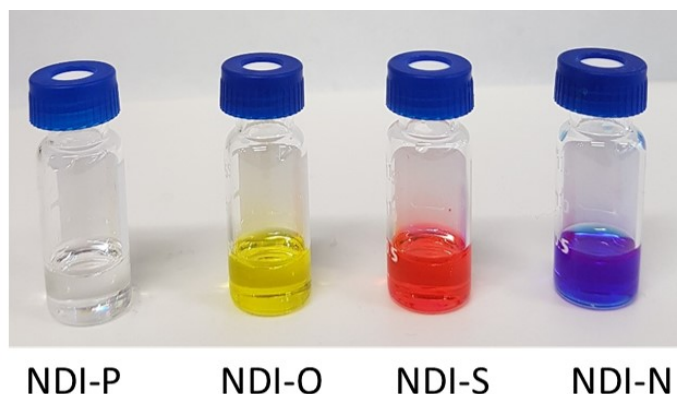


Figure 4.2: The four NDI molecules, dissolved in chlorobenzene. The addition of core substituent atoms clearly drastically alters the color of the NDI moiety.



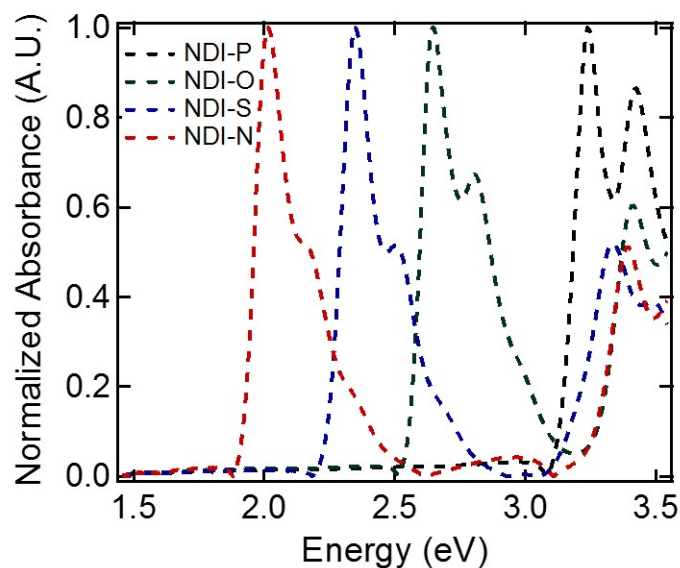


Figure 4.3: Normalized solution absorption spectra for the series of NDI-based molecules. The addition of substituent atoms to the core positions of the NDI moiety influence the size of the band gap, which is clearly demonstrated by a systematic down-shift in absorption onset energy.

wire reference electrode and a platinum wire counter electrode. The first reduction peak was used in order to estimate the LUMO energy level of the materials, as was described in the Experimental chapter.

#### 4.2.2 Organic Solar Cells

Organic solar cells were fabricated and characterized following the procedure outlined in the Experimental chapter. Active layer solutions were comprised of a 1:1 by weight blend of PBDTTT-EFT as the donor, with the NDI-based molecules as the acceptor. A solution concentration of 30 g/L was used, and devices were optimally spin cast at 6000 RPM.

### 4.3 Results and discussion

Figure 4.3 (a), shows the normalized solution UV-visible absorption spectra for the four materials. From this figure, clear shifts in absorption onset energy with the use of different substituent atoms can be seen. Similarly to what was mentioned in the previous section, it can be clearly seen that the incorporation of core substituents to the NDI moiety decreases the band-gap, allowing for increased visible light absorption, compared to the parent molecule. Importantly, the nature of the substituent atom influences this shift in absorption onset, with the more electron-donating NH group shifting the absorption onset the most, to  $\sim 1.75$  eV, compared to  $\sim 3.1$  eV for the parent molecule. Unfortunately due to the poor film forming properties of these molecules, the UV-vis spectra of neat films could not be reliably measured.

A combination of cyclic voltammetry and solution absorption was used in order to determine the energy levels of the materials, shown in Figure 4.4. The LUMO was

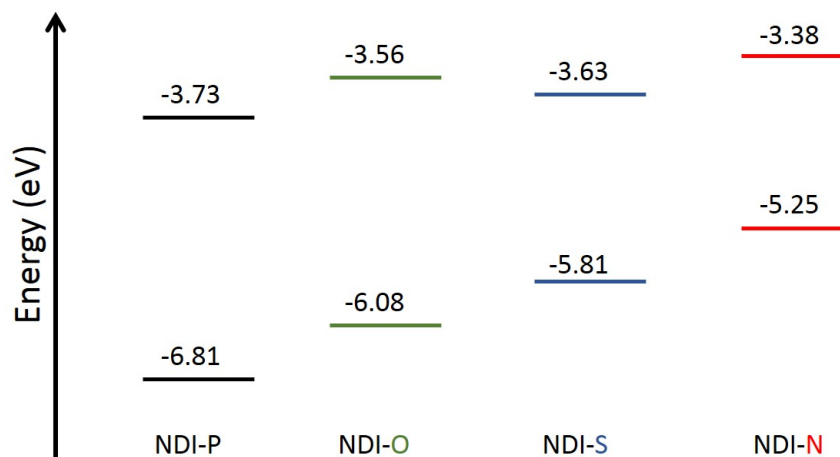


Figure 4.4: The energy levels of the series of core substituted NDI molecules, determined by a combination of cyclic voltammetry (to determine the LUMO) and solution UV-visible absorption (to determine the band gap). The HOMO is estimated as the difference between the electrochemically determined LUMO energy and the band gap, determined by the solution absorption onset energy.

estimated by the first reduction peak in the cyclic voltammogram, with the HOMO being derived from the difference between this LUMO energy and the band gap, determined by the absorption onset in solution, from Figure 4.3 (b). Note that the displayed HOMO energy level is an underestimation based on the two methods described above, and does not account for the additional energy required to fully oxidize the material. Figure 4.4 clearly demonstrates a reduction in band gap with the incorporation of substituents, for all three materials, compared to the parent molecule. Additionally, it is shown that nitrogen reduces the band gap the most, and also increases the LUMO energy, from -3.73 eV for NDI-P, to -3.38 eV for NDI-N. These changes in band gap energy are also exhibited by the colors of the materials: Figure 4.2 shows solutions of NDI-P, NDI-O, NDI-S, and NDI-N in chlorobenzene.

Figure 4.5 presents the  $J - V$  (a) and external quantum efficiency (b) plots for NDI-P, NDI-O, NDI-S, and NDI-N with the donor material, PBDTTT-EFT, pictured on the right side of Figure 2.15. All of the NDI-based acceptors exhibited poor photovoltaic performance, which is summarized in Table 4.1. Notably, both oxygen and sulfur substituents improved the efficiency of devices, primarily as a result of increased  $J_{SC}$  and  $V_{OC}$  (and at the expense of fill factor). The improvements in  $V_{OC}$  can be explained by the energy diagram shown in Figure 4.4: the LUMO for NDI-O and NDI-S is higher than that for NDI-P, which increases the  $HOMO_{donor}$ - $LUMO_{acceptor}$  energy offset, as was described in Chapter 2. Because the  $V_{OC}$  is directly related to this offset energy, the larger offset observed for NDI molecules with oxygen or sulfur substituents results in the increased  $V_{OC}$  observed, over the parent molecule. However, interestingly, the  $V_{OC}$  of the PBDTTT-EFT:NDI-N devices does not follow this trend, with a sharp reduction in  $V_{OC}$  observed in these devices. According to the literature, PBDTTT-EFT has a LUMO energy level of -3.62 eV<sup>4</sup> – quite similar to the estimated LUMO energies for the NDI-based molecules. However, the NDI-N molecule clearly exhibits the highest LUMO energy, at -3.38 eV, which is almost 0.2 eV higher than the next-highest lying LUMO energy, for NDI-O. It is possible that this 0.2 eV dif-

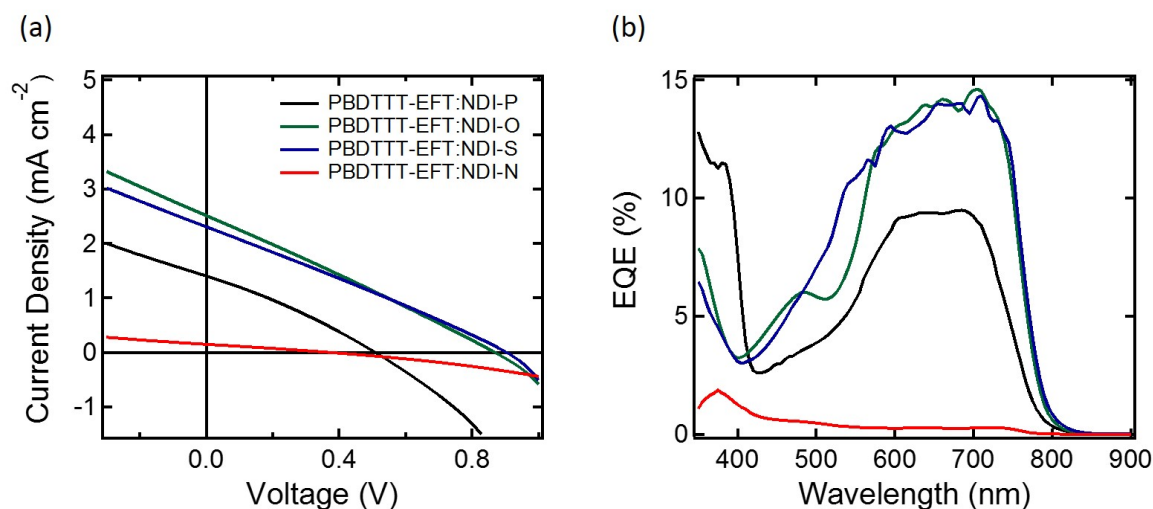


Figure 4.5:  $J - V$  characteristics (a) and EQE curves (b) for devices made employing 1:1 blends of PBDTTT-EFT:NDI acceptor. Despite a slight increase in performance after incorporating either oxygen or sulfur as core substituents, the devices still exhibit poor performance. Device parameters are given in Table 4.1.

ference is large enough to prevent the NDI-N material from acting as an acceptor in the PBDTTT-EFT:NDI-N system, as exciton dissociation would favor excited-state electron transfer from NDI-N to PBDTTT-EFT instead of the other way around. The poor charge generation due to the high LUMO of NDI-N likely explains the sharp decrease in  $V_{OC}$  observed in the PBDTTT-EFT:NDI-N system. This can further explain the dramatic reduction in EQE across the entire wavelength range shown in Figure 4.5 (b), which is likely due to inefficient charge separation.

Oxygen and sulfur substituent atoms also increase the short circuit current in devices, compared to the parent molecule, which is observed both in the  $J - V$  as well as the EQE curves pictured in Figure 4.5. This observed increase may be due to the smaller band gap for both NDI-O and NDI-S, compared to NDI-P. UV-Visible absorption profiles for these three materials blended with PBDTTT-EFT is provided in Figure 4.6 (unfortunately there was insufficient material of NDI-N to measure its blend profile with PBDTTT-EFT), and shows increased absorption for both NDI-O and NDI-S-based blends in the visible wavelength region, over the parent molecule. This improved visible absorption may lead to some current generated by the device originating from the acceptor material. Indeed, this is further demonstrated by the features in the EQE curves at  $\sim 470$  nm and  $\sim 550$  nm for NDI-O and NDI-S-based

| Acceptor | $J_{SC}$<br>( $\text{mA cm}^{-2}$ ) | $V_{OC}$<br>(V) | FF<br>(%) | PCE<br>(%) | EQE $J_{SC}$<br>( $\text{mA cm}^{-2}$ ) |
|----------|-------------------------------------|-----------------|-----------|------------|---|
| NDI-P    | 1.32                                | 0.82            | 30.5      | 0.33       | 1.68                                    |
| NDI-O    | 2.51                                | 0.90            | 26.1      | 0.60       | 2.51                                    |
| NDI-S    | 2.30                                | 0.90            | 26.8      | 0.56       | 2.61                                    |
| NDI-N    | 0.15                                | 0.34            | 29.12     | 0.02       | 0.10                                    |

Table 4.1: Solar cell parameters for devices fabricated from the NDI-based acceptors, paired with PBDTTT-EFT.

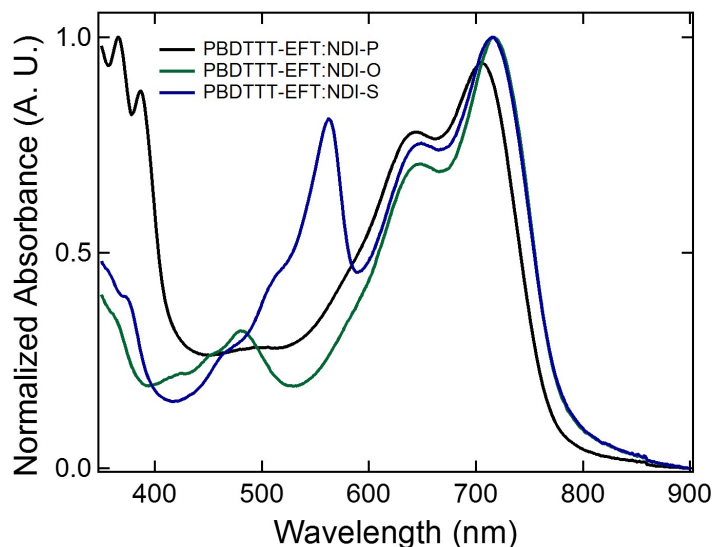


Figure 4.6: Absorption profiles for the NDI-based molecules, blended in a 1:1 by weight ratio with PBDTTT-EFT.

devices, respectively, which reflect features stemming from the NDI-based molecules in the blend absorption profiles. Conversely, the  $J_{SC}$  of NDI-N-based devices exhibits a sharp decrease, from  $1.32 \text{ mA cm}^{-2}$  for the parent molecule, to  $0.15 \text{ mA cm}^{-2}$ . This is further indicative of a strong mechanism limiting the current generation in these devices, most likely owing to the higher LUMO energy of NDI-N.

A further explanation for the improved device performance observed in both the NDI-O and NDI-S-based materials, over the parent molecule, could be due to improvements in active layer morphology. As was mentioned previously, the NDI moiety is extremely susceptible to aggregation, forming large-scale domains in blend films. However, the addition of two butyl chains that are required in order to add oxygen or sulfur substituents to the NDI core could, potentially, hinder this strong aggregation. In order to investigate this further, GIWAXS measurements were taken of both the neat and blend films.

Figure 4.7 shows the 2D GIWAXS images for neat films of the four NDI molecules. NDI-P clearly exhibits the most ordered, three-dimensional packing, most likely because the packing of the three molecules containing substituents is suppressed by the additional butyl chain flanking the molecule. The peaks displayed for NDI-P have been indexed previously,<sup>5</sup> however, briefly: NDI-P, Figure 4.7 (a), forms two distinct unit cells, which likely result from two polymorphs. This is indicated by the presence of additional Bragg spots, which also allude that the morphology is dominated by the secondary unit cell. The NDI-P molecules exhibit a triclinic unit cell which is oriented edge-on with respect to the substrate, indicated by the high intensity peak in the  $Q_z$  direction. This peak is indexed as the (001) peak, resulting from stacking along the alkyl side chains.

Figure 4.7 (b-d) shows the 2D GIWAXS images for NDI-O, NDI-S, and NDI-N, respectively. Compared to NDI-P, these materials all show suppressed aggregation, likely due to the additional butyl chains incorporated with the substituent atoms in the  $R_1$  and  $R_3$  positions. The different packing motif of these materials is, however, difficult to index due to the lack of uniform film formation of the NDI-O, NDI-S, and

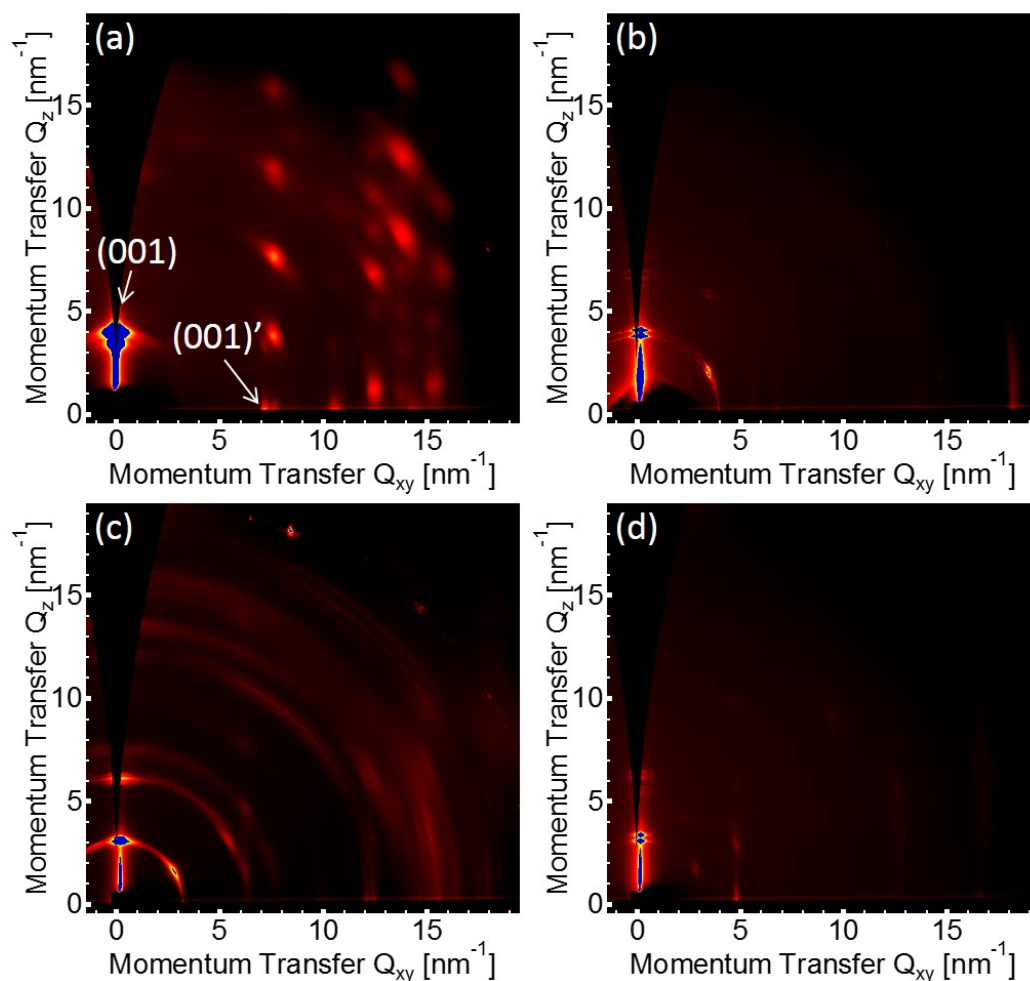


Figure 4.7: Neat 2D GIWAXS images for the parent (a), NDI-O (b), NDI-S (c), and NDI-N (d) materials. A disruption in the efficient 3D crystalline packing order of the parent material is clearly demonstrated by a reduction in scattering intensity for the molecules containing substituent atoms.

NDI-N materials.

Figure 4.8 shows the 2D GIWAXS images for NDI-P, NDI-O, NDI-S, and NDI-N blended in a 1:1 ratio with PBDTTT-EFT, following the device conditions used. For reference, a 2D GIWAXS image of a neat PBDTTT-EFT film is provided in Appendix A. The blend pictured in Figure 4.8 (a), with the NDI-P molecule exhibits features arising from both the PBDTTT-EFT and NDI-P. However, for the blend films with substituents, no crystallization features of the NDI molecules is found. Notably, the polymer maintains its characteristic  $\pi - \pi$  stacking peak, visible in the  $Q_z$  direction. The blends with NDI-O, NDI-S, and NDI-N strongly reflect the scattering profile of the neat polymer material, while the PBDTTT-EFT:NDI-P blend contains features from both materials. This could be indicative that the strong aggregation behavior of NDI-P negatively influences the ability of the blend to form a favorably mixed active layer morphology, while the molecules containing substituents, with the increased disorder arising from the added butyl chain, are able to better intermix with the polymer matrix. It is hypothesized then that the limited physical size of these NDI acceptors limits their function. Increasing the physical size of NDI-based acceptors through the



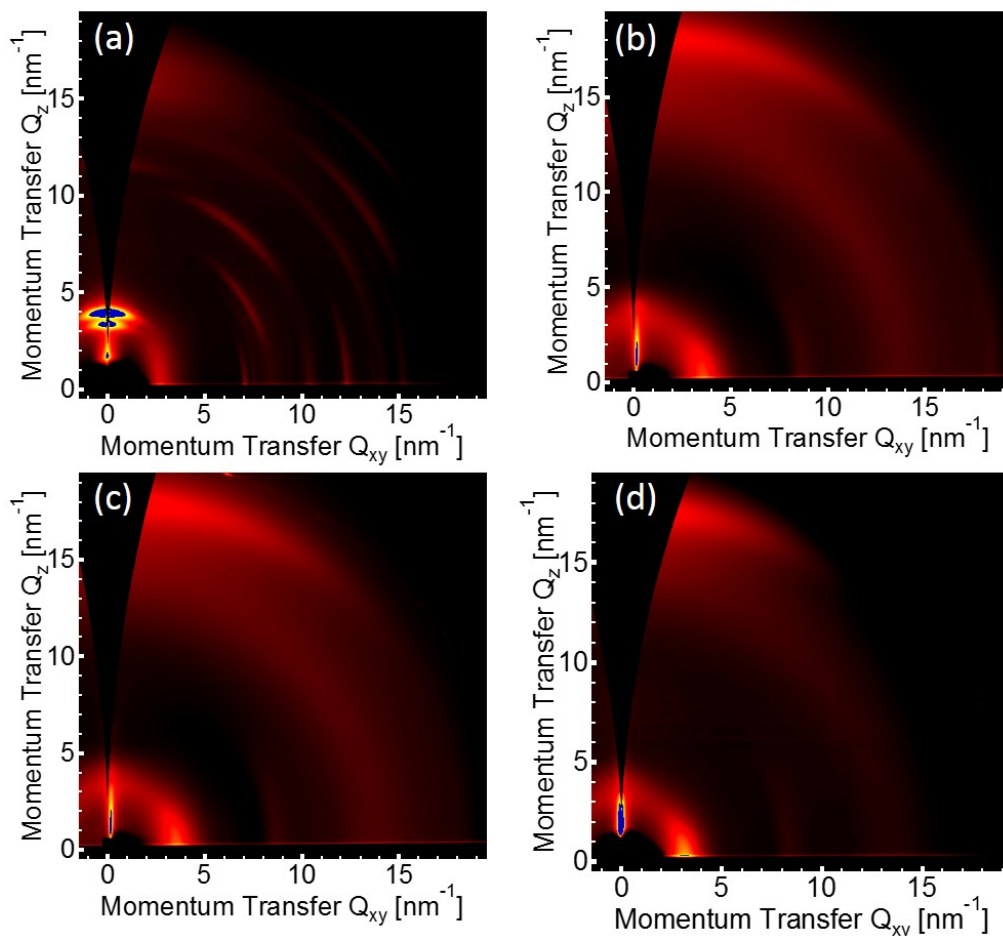


Figure 4.8: 2D GIWAXS images for the parent (a), NDI-O (b), NDI-S (c), and NDI-N (d) materials blended in a 1:1 ratio with the donor polymer, PBDTTT-EFT. While the parent material clearly disrupts the packing of the donor polymer, the blend films of NDI molecules containing core substituents with PBDTTT-EFT exhibit scattering profiles similar to that of the polymer, indicating limited disruption.

use of larger molecular architectures will be explored in the next chapter.

## 4.4 Conclusions

This chapter provided an introduction to the effects substituent atoms can have on the optical and electronic properties of the NDI moiety. It has been demonstrated that oxygen, sulfur, and nitrogen all decrease the optical band gap of the parent NDI molecule, with nitrogen resulting in the narrowest band gap observed from UV-visible absorption measurements. Additionally, cyclic voltammetry was used to estimate the LUMO energy values for the materials, and it was found that all three substituents increased the LUMO energy over the parent molecule. For NDI-O and NDI-S, this resulted in a larger  $V_{OC}$  in devices fabricated with PBDTTT-EFT, due to the larger  $HOMO_{donor}$ - $LUMO_{acceptor}$  energy offset. However, the LUMO of NDI-N was raised sufficiently to compromise its exciton dissociation ability when paired with PBDTTT-EFT, which was reflected in an extreme reduction in both  $J_{SC}$  and  $V_{OC}$ . It was also found that the additional butyl side chain that is used to incorporate either oxygen,

sulfur, or nitrogen as substituent atoms to the NDI moiety hindered the material's aggregation in the solid state. This was observed in both the neat, but particularly the blend 2D GIWAXS images for the three materials, compared with the parent molecule. Ultimately, the use of substituents was demonstrated to improve the efficiency of the parent NDI molecule, however the small conjugation length of the NDI molecule on its own may limit its effectiveness as an acceptor in organic solar cells. Increasing the conjugation length in an effort to improve OPV performance, by changing the size and shape of the acceptor molecule, is explored in more detail in the next chapter.

# References

- [1] S. V. Bhosale, C. H. Jani, and S. J. Langford, “Chemistry of naphthalene diimides,” *Chemical Society Reviews*, vol. 37, no. 2, pp. 331–342, 2008.
- [2] P. S. Rao, A. Gupta, D. Srivani, S. V. Bhosale, A. Bilic, J. Li, W. Xiang, R. A. Evans, and S. V. Bhosale, “An efficient non-fullerene acceptor based on central and peripheral naphthalene diimides,” *Chemical Communications*, vol. 54, no. 40, pp. 5062–5065, 2018.
- [3] N. Sakai, J. Mareda, E. Vauthey, and S. Matile, “Core-substituted naphthalenediimides,” *Chemical Communications*, vol. 46, no. 24, pp. 4225–4237, 2010.
- [4] S. H. Liao, H. J. Jhuo, Y. S. Cheng, and S. A. Chen, “Fullerene derivative-doped zinc oxide nanofilm as the cathode of inverted polymer solar cells with low-bandgap polymer (PTB7-Th) for high performance,” *Advanced Materials*, vol. 25, no. 34, pp. 4766–4771, 2013.
- [5] A. Welford, S. Maniam, E. Gann, L. Thomsen, S. J. Langford, and C. R. Mcneill, “Thionation of naphthalene diimide molecules: Thin-film microstructure and transistor performance,” *Organic Electronics*, vol. 53, pp. 287–295, 2018.





## Chapter 5

# Naphthalene diimide-based small molecule acceptors

This chapter introduces six novel naphthalene diimide molecular acceptors for evaluation in organic solar cells based on two different molecular architectures: a star-shaped structure with a triarylamine core flanked by three NDI moieties, and a linear molecule composed of a bithiophene bridge between two NDI moieties. For each molecular structure, the core substituents first introduced in Chapter 4, were incorporated, in order to improve device performance. Both the chemical structure and the side-chain heteroatom substitution were found to influence the optoelectronic and photovoltaic properties of these molecular acceptors. Organic solar cells were fabricated with each acceptor, utilizing PBDTTT-EFT as the donor material in inverted bulk-heterojunction devices. Nitrogen was observed to lower the solar cell performance for these acceptors by significantly decreasing the short circuit current density (similarly to observations made in Chapter 4), while sulfur increased the  $J_{SC}$  and, in the star configuration, led to the highest power conversion efficiency (PCE) of 2.8% – which was amongst the highest for any molecular NDI-based acceptor at the time of publication. Grazing incidence wide-angle X-ray scattering (GIWAXS) measurements of the star-shaped materials showed the side-chain substitutional atom significantly alters the material's packing configuration in neat films, with films blended with PBDTTT-EFT showing features characteristic of the neat donor and acceptor materials, indicating that the small molecules do not disrupt the packing of PBDTTT-EFT (and vice versa). Resonant soft X-ray scattering (R-SoXS) measurements indicate the PBDTTT-EFT:star-shaped acceptor blends are not subject to coarse phase-separation, with the average domain size for all three star-shaped acceptor blends typically being less than 100 nm. This is confirmed by similar topography for blended films in AFM images amongst the three acceptors. Photoluminescence (PL) quenching measurements, however, found large differences in PL quenching efficiency which were attributed to differences in the driving force for charge transfer, with the nitrogen substituted compound showing the lowest PL quenching and the sulfur replacement showing the highest. This is likely due to the high LUMO energy level of the Star NDI-N material, similar to NDI-N examined in Chapter 4. Following publication, additional characterization utilizing P3HT as the donor material was done, based on recent reports in the literature that demonstrate high PCE for NDI-based small molecule acceptors paired with P3HT as the donor. However, these devices exhibited far lower power conversion efficiencies compared to those fabricated with PBDTTT-EFT.

## 5.1 Context

This work builds upon the fundamental material properties discussed in Chapter 4, which showed that the substituent oxygen, sulfur, and nitrogen atoms have a notable influence over the optical and electronic properties of the NDI moiety. Two structures were chosen to explore in this chapter, both of which serve two functions: (1) to disrupt the efficient packing of the NDI moiety and (2) to increase the conjugation length of the molecule. Notably, the conjugation length of an organic semiconductor influences the material's band gap, with increasing conjugation length resulting in a smaller band gap. This can improve the spectral coverage of the NDI's UV-visible absorption, and can help improve the number of excitons that are created in the active layer of an organic solar cell. Additionally, it has recently been shown that, for an NDI-based molecule, increasing the conjugation length of the acceptor material can decrease the charge recombination rate in an OPV system.<sup>1</sup> The molecular structures are as follows: three NDI molecules joined via a triarylamine linker, termed star molecules, and two NDI molecules joined via a bithiophene bridge. The use of a donor constituent in the molecular structure was selected in order to generate a “push-pull” system, described in more detail in Chapter 2. Apart from the increased complexity in the molecular structures used in this chapter, the materials also make use of the constituent atoms studied in Chapter 4: oxygen, sulfur and nitrogen. It is shown in the publication presented in the next section, that the use of a complex molecular structure greatly improves the OPV performance of the NDI molecule, and that the substituent atoms can strongly influence the materials' performance in bulk heterojunction devices. The electronic supplementary information (ESI) mentioned in the article is provided in Appendix B, and the full citation is provided on the next page.

*Naphthalene diimide-based small molecule  
acceptors for organic solar cells*

**Kira Rundel**, Subashani Maniam, Kedar Deshmukh, Eliot Gann, Shayamal K. K. Prasad, Justin M. Hodgkiss, Steven J. Langford, and Christopher R. McNeill

*Journal of Materials Chemistry A*, 2017, **5**, 12266.

Royal Society of Chemistry | DIO: 10.1039/C7TA02749D

## 5.2 Article

# Journal of Materials Chemistry A



### PAPER

[View Article Online](#)
[View Journal](#) | [View Issue](#)


Cite this: *J. Mater. Chem. A*, 2017, 5, 12266

## Naphthalene diimide-based small molecule acceptors for organic solar cells†

Kira Rundel,<sup>a</sup> Subashani Maniam,<sup>b</sup> Kedar Deshmukh,<sup>a</sup> Eliot Gann,<sup>ac</sup> Shyamal K. K. Prasad,<sup>d</sup> Justin M. Hodgkiss,<sup>id</sup> Steven J. Langford<sup>b</sup> and Christopher R. McNeill<sup>id</sup>\*<sup>a</sup>

This work introduces six novel naphthalene diimide (NDI) molecular acceptors for evaluation in organic solar cells based on two different chemical architectures: a star-shaped structure with a triarylamine core flanked by three NDI moieties and a linear molecule composed of a bithiophene bridge between two NDI moieties. For each molecular structure, three different side chains are examined, with alkyl chains linked to the NDI core either through oxygen, sulfur, or nitrogen substituents. Both the chemical structure and the side-chain heteroatom substitution were found to influence the optoelectronic and photovoltaic properties of these molecular acceptors. Organic solar cells were fabricated with each acceptor, utilizing PBDTTT-EFT (also known as PTB7-Th) as the donor material in inverted bulk-heterojunction devices. Nitrogen was observed to lower the solar cell performance for these acceptors by significantly decreasing the short circuit current density ( $J_{SC}$ ), while sulfur increased the  $J_{SC}$  and, in the star configuration, led to the highest power conversion efficiency (PCE) of 2.8% – which is amongst the highest for any molecular NDI-based acceptor to date. Grazing incidence wide-angle X-ray scattering (GIWAXS) measurements of the star-shaped materials showed the side-chain substitutional atom significantly alters the material's packing configuration in neat films, with films blended with PBDTTT-EFT showing features characteristic of the neat donor and acceptor materials, indicating that the small molecules do not disrupt the packing of PBDTTT-EFT (and vice versa). Resonant soft X-ray scattering (R-SoXS) measurements indicate the PBDTTT-EFT:star-shaped acceptor blends are not subject to coarse phase-separation, with the average domain size for all three star-shaped acceptor blends typically being less than 100 nm. This is confirmed by similar topography for blended films in AFM images amongst the three acceptors. Photoluminescence (PL) quenching measurements, however, found large differences in PL quenching efficiency which were attributed to differences in the driving force for charge transfer, with the nitrogen substituted compound showing the lowest PL quenching and the sulfur replacement showing the highest.

Received 30th March 2017  
Accepted 19th May 2017

DOI: 10.1039/c7ta02749d

[rsc.li/materials-a](http://rsc.li/materials-a)

## Introduction

In recent years, the potential for low-cost, large-scale manufacturing of thin, flexible solar cells has been the driving force behind research in the field of organic photovoltaics

(OPV).<sup>1–3</sup> While the technology and benefits of producing solar cells through roll-to-roll printing are promising, there is still much work to be done before large-scale manufacturing of these devices is possible. Amongst the biggest obstacles to the commercialization of OPV is the lower power conversion efficiency (PCE) of organic solar cells compared with other, more mature solar technologies.<sup>4</sup> This has led to a significant research effort in improving the performance of organic photovoltaics through device engineering and material design, resulting in significant improvement in OPV performance over the past ten years.<sup>5–9</sup> Today, novel materials that exhibit PCEs near 10% or even higher are not uncommon,<sup>10–12</sup> demonstrating the competitive viability of OPV with existing solar conversion technologies.

Conventionally, organic solar cells employ a polymeric donor material and a fullerene-derivative acceptor within the light-absorbing active layer of the device.<sup>13,14</sup> Until recently, a vast majority of the effort in improving device efficiencies has focused

<sup>a</sup>Department of Materials Science and Engineering, Monash University, Wellington Road, Clayton, VIC 3800, Australia. E-mail: [christopher.mcneill@monash.edu](mailto:christopher.mcneill@monash.edu)

<sup>b</sup>School of Chemistry, Monash University, Wellington Road, Clayton, VIC 3800, Australia

<sup>c</sup>Australian Synchrotron, 800 Blackburn Road, Clayton, VIC 3168, Australia

<sup>d</sup>MacDiarmid Institute for Advanced Materials and Nanotechnology, Victoria University of Wellington, Wellington 6140, New Zealand

† Electronic supplementary information (ESI) available: Additional synthesis details of the precursors to all molecular acceptors, NMR spectra for precursor compounds as well as all molecular acceptors, cyclic voltammetry experimental procedure and voltammograms, solution absorbance experimental procedure and solution to thin film absorption comparisons, 1D GIWAXS line-cut profiles, PL spectra, device optimization data and SCLC device data. See DOI: 10.1039/c7ta02749d

on designing novel donor materials, with a fullerene derivative such as phenyl-C<sub>61</sub>-butyric acid methyl ester (PCBM) typically used as the acceptor. While there are several advantages in using PCBM as the acceptor – in particular its excellent electron mobility – fullerene derivatives are costly, difficult to synthesize, have poor light-harvesting abilities, and low stability in air,<sup>15,16</sup> calling for an investigation into alternative acceptor materials.

There are several alternatives to fullerene acceptors which employ either a polymeric or molecular structure around common electron-withdrawing building blocks including diketopyrrolopyrrole (DPP),<sup>17–19</sup> benzothiadiazole,<sup>20,21</sup> and rylene diimides, among others.<sup>22</sup> Of these alternative materials, rylene diimide-based acceptors such as perylene diimide (PDI)<sup>23–25</sup> and naphthalene diimide (NDI)<sup>26–28</sup> have shown great success in fullerene-free devices, among both polymeric and small molecular acceptors.<sup>29–31</sup> Despite initially lower performance compared with polymeric acceptors, several OPV devices comprised of a PDI-based molecular acceptor have recently exhibited device efficiencies surpassing 8% PCE in academic research,<sup>32,33</sup> while some of the highest performing molecular acceptors are comprised of a indacenodithieno[3,2-*b*]thiophene core and have exhibited efficiencies approaching 12% PCE.<sup>34</sup> Compared to their polymeric counterparts, small molecule-based acceptors have the following benefits: a defined molecular structure with lower batch-to-batch variation, increased electron mobilities, and the potential for structural variation, warranting further investigation into novel small molecule materials as acceptors in organic solar cells.<sup>35</sup>

Amongst the members of the rylene family, NDI is the smallest but a versatile aromatic compound that displays tremendous chemical, thermal and photochemical stability.<sup>36–38</sup> The NDI building block has been demonstrated to produce efficient solar cells in polymeric acceptors,<sup>39</sup> however molecular NDI-based acceptors have not been as successful, exhibiting lower performance primarily due to the naphthalene diimide's large optical band gap, weak visible absorption and strong tendency to aggregate.<sup>40</sup> These shortcomings have hindered the investigation into potential NDI-based molecular acceptors, resulting in slow progress in increasing device efficiencies. However, incorporating additional donor moieties onto the naphthalene core of the NDI allows tunable optical properties, *i.e.* lowering their optical band gap, while simultaneously disrupting strong aggregation of the NDI core. Additionally, substitutional heteroatoms have been shown to strongly influence the solid-state properties of molecular conjugated materials, providing an additional handle for tuning molecular properties which has not been explored much to date in OPV research.<sup>41</sup> In this work, we report novel NDI-based acceptors based on two different molecular architectures, and additionally explore the effect of different substitutional heteroatoms on the physical and photovoltaic properties of the molecular acceptor materials.

This paper introduces six novel NDI-based molecular acceptors (Fig. 1) that have been specifically designed to reduce strong aggregation when blended with a polymeric donor. They are: 9,9',9''-(nitrotris(benzene-4,1-diyl))tris(4-butoxy-2,7-bis(2-

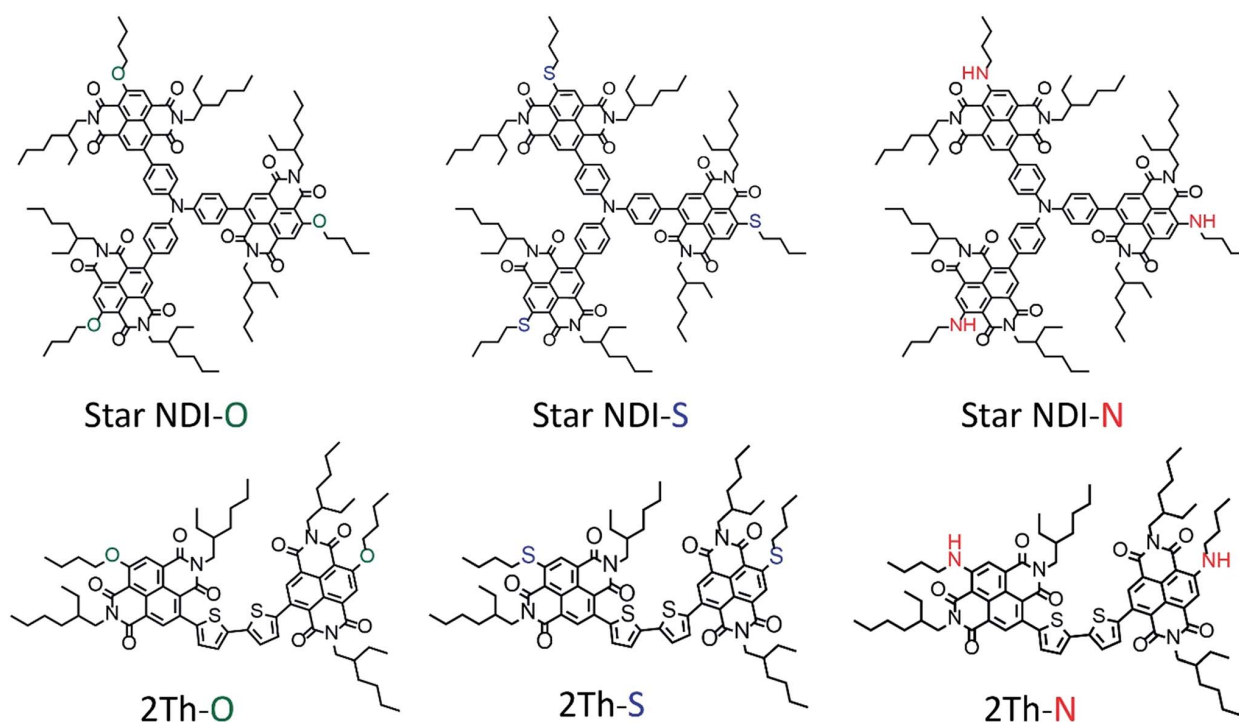


Fig. 1 Chemical structures of the six investigated materials. Materials in the top row utilize a triarylamine core to disrupt the crystalline packing tendency of the naphthalene diimides. The bottom row depicts the acceptor molecules based on the efficient P(NDI2OD-T2) polymeric acceptor.

ethylhexyl)benzo[Imn][3,8]phenanthroline-1,3,6,8(2*H*,7*H*)-tetraone) (**Star NDI-O**), 9,9',9''-(nitrilotris(benzene-4,1-diyl))tris(4-(butylthio)-2,7-bis(2-ethylhexyl)benzo[Imn][3,8]phenanthroline-1,3,6,8(2*H*,7*H*)-tetraone) (**Star NDI-S**), 9,9',9''-(nitrilotris(benzene-4,1-diyl))tris(4-(butylamino)-2,7-bis(2-ethylhexyl)benzo[Imn][3,8]phenanthroline-1,3,6,8(2*H*,7*H*)-tetraone) (**Star NDI-N**), 9,9'-([2,2'-bithiophene]-5,5'-diyl)bis(4-(butylthio)-2,7-bis(2-ethylhexyl)benzo[Imn][3,8]phenanthroline-1,3,6,8(2*H*,7*H*)-tetraone) (**2Th-O**), 9,9'-([2,2'-bithiophene]-5,5'-diyl)bis(4-(butylthio)-2,7-bis(2-ethylhexyl)benzo[Imn][3,8]phenanthroline-1,3,6,8(2*H*,7*H*)-tetraone) (**2Th-S**) and 9,9'-([2,2'-bithiophene]-5,5'-diyl)bis(4-(butylamino)-2,7-bis(2-ethylhexyl)benzo[Imn][3,8]phenanthroline-1,3,6,8(2*H*,7*H*)-tetraone) (**2Th-N**). The chemical structures for each material are depicted in Fig. 1. The increasingly popular donor-acceptor architecture<sup>42–45</sup> has been used for all six materials. The first set of acceptors utilizes a donor triarylamine core to extend the conjugation length of the molecules while simultaneously adding rotational degrees of freedom, hindering strong aggregation of the molecule. This core is flanked by three acceptor NDI moieties. A bithiophene bridge is used to link two NDI units in the second set of molecular acceptors, mimicking the popular P(NDI2OD-T2) acceptor polymer, which has demonstrated the highest performance for NDI-based acceptors with over 8% PCE.<sup>46</sup>

Sulfur, nitrogen and oxygen heteroatoms have also been substituted in the alkyl side chains. These heteroatom derivatives on the NDI core facilitate good synthetic yields and give access to compounds with widely tunable optical and electrochemical properties. Additionally, the lone pairs of electrons on these heteroatoms can undergo cross-conjugation with the electron-poor carbonyl groups, giving rise to absorption and fluorescence properties over a broad spectral range. As the nitrogen is readily oxidized, it is predicted that this substitution will raise the LUMO energy level for the molecule, reducing the driving force for exciton dissociation in bulk heterojunction devices. Alternatively, the sulfur atom has a higher electronegativity than oxygen and nitrogen.

## Experimental

### Synthesis of molecular acceptors

5,5'-Bis(4,4,5,5-tetramethyl-1,3,2-dioxaborolan-2-yl)-2,2'-bithiophene was synthesised following Hellberg *et al.*<sup>47</sup> Tris(4-(4,4,5,5-tetramethyl-1,3,2-dioxaborolan-2-yl)phenyl)amine was synthesised following Sahu *et al.*<sup>48</sup> 4,9-Dibromo-2,7-bis(2-ethylhexyl)benzo[Imn][3,8]phenanthroline-1,3,6,8(2*H*,7*H*)-tetraone was synthesised following Yuan *et al.*<sup>49</sup> 2-(2-Ethylhexyl)-1,3-dioxo-2,3-dihydro-1*H*-benzo[de]isoquinoline-6,7-dicarboxylic acid was synthesised as described in Greenland *et al.*<sup>50</sup> Analytical thin layer chromatography was performed on aluminium plates coated with silica gel (Silica 60 F254). Column chromatography was conducted using Merck silica gel 60, with a pore size between 0.063 and 0.200 mm. The eluent conditions are expressed as volume-to-volume (v/v) ratios.

Low-resolution electron impact mass spectrometry (LRMS) was performed on a Micromass Platform II API quadrupole electrospray mass spectrometer as the solutions specified.

High-resolution electron impact mass spectrometry (HR-ESI) was performed on an Agilent Technologies 6220 Accurate-Mass Time-of-Flight LC/MS as the solutions specified and Ab Sciex MALDI TOF-TOF 5800 spectrometer. For mass spectrometry  $[M]^+$  denotes the molecular ion. Melting points were recorded on a MP50 Mettler Toledo digital melting point apparatus at 5 °C min<sup>-1</sup>.

<sup>1</sup>H and <sup>13</sup>C nuclear magnetic resonance (NMR) spectra (ES2–19†) were recorded using a Bruker DRX 400 MHz NMR spectrometer (400 MHz for <sup>1</sup>H NMR, 100 MHz for <sup>13</sup>C NMR) and a Bruker AV 600 MHz NMR spectrometer (600 MHz for <sup>1</sup>H NMR, 150 MHz for <sup>13</sup>C NMR), using deuterated chloroform (CDCl<sub>3</sub>). Chemical shifts are reported relative to the resonances of residual CHCl<sub>3</sub> at  $\delta$  = 7.26 (H) and  $\delta$  = 77.2 (C). For <sup>1</sup>H NMR spectra each resonance was assigned according to the following convention: chemical shift ( $\delta$ ) measured in parts per million (ppm), multiplicity, coupling constant, (*J* Hz), number of protons and assignment. Multiplicities are denoted as (s) singlet, (d) doublet, (t) triplet, (q) quartet, (p) pentet, or (m) multiplet and prefixed (br) broad where appropriate. The <sup>13</sup>C NMR spectra were recorded using proton decoupled pulse sequence unless stated otherwise. For <sup>13</sup>C NMR each resonance was assigned according to the following convention: chemical shift ( $\delta$ ) measured in parts per million (ppm). Precursor synthesis is described in detail in the ESI.† The final synthesis of the six acceptors is given below.

**Synthesis of Star NDI-O.** 4-Bromo-9-butoxy-2,7-bis(2-ethylhexyl)benzo[Imn][3,8]phenanthroline-1,3,6,8(2*H*,7*H*)-tetraone (85 mg, 0.13 mmol), tris(4-(4,4,5,5-tetramethyl-1,3,2-dioxaborolan-2-yl)phenyl)amine (28 mg, 44.2  $\mu$ mol), tetrakis(triphenylphosphine)palladium(0) (2.3 mg, 2.0  $\mu$ mol) and potassium carbonate (2 mL, 2 M) in toluene were degassed for 15 min and then heated at reflux for 24 h. Solvent was then evaporated and the crude product was diluted with dichloromethane (30 mL) and washed with water (3  $\times$  30 mL). The organic phase was collected, dried over anhydrous MgSO<sub>4</sub> and the solvent removed under vacuum. The crude product was purified by column chromatography using dichloromethane. Then, 2% v/v acetone in dichloromethane was used to isolate desired product which was recrystallised from dichloromethane and methanol to give the title compound as a black solid (35 mg, yield 40%). Mp 263–264 °C (dec.). <sup>1</sup>H NMR  $\delta$  8.68 (s, 3H, NDI), 8.53 (s, 3H, NDI), 7.42–7.37 (m, 12H, phenyl-H), 4.50 (t, *J* = 6.8, 6H, SCH<sub>2</sub>), 4.20–4.07 (m, 12H, CH<sub>2</sub>), 2.07–1.88 (m, 12H, CH & CH<sub>2</sub>), 1.69–1.59 (m, 6H, CH<sub>2</sub>), 1.39–1.28 (m, 48H, CH<sub>2</sub>), 1.05 (t, *J* = 7.6, 9H, CH<sub>3</sub>), 0.94–0.84 (m, 36H, CH<sub>3</sub>). <sup>13</sup>C NMR ( $\delta$  163.3, 163.2, 163.0, 161.9, 161.6, 147.2, 145.0, 136.8, 129.9, 128.7, 128.5, 124.7, 124.2, 122.8, 122.6, 119.6, 111.2, 70.7, 44.4, 38.0, 37.9, 31.3, 30.8, 28.8, 28.7, 24.2, 23.24, 23.22, 19.2, 14.2, 13.9, 10.80, 10.77). MALDI *m/z* obsd  $[M - H]^+$  1925.093, calcd C<sub>120</sub>H<sub>146</sub>N<sub>7</sub>O<sub>15</sub>  $[M - H]^+$  1925.088.

**Synthesis of Star NDI-S.** 4-Bromo-9-(butylthio)-2,7-bis(2-ethylhexyl)benzo[Imn][3,8]phenanthroline-1,3,6,8(2*H*,7*H*)-tetraone (45 mg, 68.4  $\mu$ mol), tris(4-(4,4,5,5-tetramethyl-1,3,2-dioxaborolan-2-yl)phenyl)amine (15.0 mg, 22.8  $\mu$ mol), tetrakis(triphenylphosphine)palladium(0) (1.3 mg, 1.14  $\mu$ mol) and potassium carbonate (2 mL, 2 M) in toluene were degassed for



15 min and then heated at reflux for 12 h. Solvent was then evaporated and the crude product was diluted with dichloromethane (30 mL) and washed with water (3 × 30 mL). The organic phase was collected, dried over anhydrous  $\text{MgSO}_4$  and the solvent removed under vacuum. The crude product was purified by column chromatography using dichloromethane. Then, 2% v/v acetone in dichloromethane was used to isolate desired product which was recrystallised from dichloromethane and methanol to give the title compound as a dark brown solid (30 mg, yield 67%). Mp 256–257 °C (dec.).  $^1\text{H}$  NMR  $\delta$  8.78 (s, 3H, NDI), 8.69 (s, 3H, NDI), 7.44–7.38 (m, 12H, phenyl-H), 4.21–4.06 (m, 12H,  $\text{NCH}_2$ ), 3.26 (t,  $J$  = 7.6, 6H,  $\text{SCH}_2$ ), 2.01–1.85 (m, 12H, CH &  $\text{CH}_2$ ), 1.69–1.60 (m, 6H,  $\text{CH}_2$ ), 1.42–1.26 (m, 48H,  $\text{CH}_2$ ), 1.04 (t,  $J$  = 7.2, 9H,  $\text{CH}_3$ ), 0.95–0.84 (m, 36H,  $\text{CH}_3$ ).  $^{13}\text{C}$  NMR  $\delta$  164.1, 163.4, 163.0, 162.9, 150.9, 147.3, 145.6, 136.4, 135.3, 130.0, 129.2, 128.6, 127.7, 127.2, 125.4, 124.9, 124.2, 123.9, 122.7, 119.3, 44.8, 44.7, 38.0, 37.9, 32.3, 30.8, 30.1, 28.8, 28.7, 24.1, 23.26, 23.25, 22.5, 14.3, 13.9, 10.8, 10.7. MALDI  $m/z$  obsd  $[\text{M} - \text{H}]^-$  1974.650, calcd  $\text{C}_{120}\text{H}_{147}\text{N}_7\text{O}_{12}\text{S}_3$   $[\text{M} - \text{H}]^-$  1974.705.

**Synthesis of Star NDI-N.** 4-Bromo-9-(butylamino)-2,7-bis(2-ethylhexyl)benzo[*lmn*][3,8]phenanthroline-1,3,6,8(2*H*,7*H*)-tetraone (45 mg, 70.2  $\mu\text{mol}$ ), tris(4-(4,4,5,5-tetramethyl-1,3,2-dioxaborolan-2-yl)phenyl)amine (15 mg, 23.4  $\mu\text{mol}$ ), tetrakis(triphenylphosphine)palladium(0) (1.4 mg, 1.2  $\mu\text{mol}$ ) and potassium carbonate (2 mL, 2 M) in toluene were degassed for 15 min and then heated at reflux for 24 h. Solvent was then evaporated and the crude product was diluted with dichloromethane (30 mL) and washed with water (3 × 30 mL). The organic phase was collected, dried over anhydrous  $\text{MgSO}_4$  and the solvent removed under vacuum. The crude product was purified by column chromatography using dichloromethane. Then, 2% v/v acetone in dichloromethane was used to isolate desired product which was recrystallised from dichloromethane and methanol to give the title compound as a black solid (37 mg, yield 82%). Mp 285–287 °C (dec.).  $^1\text{H}$  NMR  $\delta$  10.07 (t,  $J$  = 5.6, 3H, NH), 8.59 (s, 3H, NDI), 8.29 (s, 3H, NDI), 7.39–7.33 (m, 12H, phenyl-H), 4.20–4.03 (m, 12H,  $\text{NCH}_2$ ), 3.63–3.59 (m, 6H,  $\text{HNCH}_2$ ), 1.97–1.80 (m, 12H, CH &  $\text{CH}_2$ ), 1.58–1.51 (m, 6H,  $\text{CH}_2$ ), 1.40–1.28 (m, 48H,  $\text{CH}_2$ ), 1.03 (t,  $J$  = 7.6, 9H,  $\text{CH}_3$ ), 0.95–0.84 (m, 36H,  $\text{CH}_3$ ).  $^{13}\text{C}$  NMR  $\delta$  166.8, 163.5, 163.3, 152.1, 147.0, 141.6, 136.1, 135.7, 129.9, 129.0, 128.4, 124.1, 122.6, 120.7, 120.2, 44.5, 44.1, 43.2, 38.0, 31.7, 30.89, 30.85, 28.8, 28.7, 24.21, 24.16, 23.3, 23.2, 20.4, 14.2, 13.9, 10.9, 10.8. MALDI  $m/z$  obsd  $[\text{M} + \text{H}]^+$  1925.486, calcd  $\text{C}_{120}\text{H}_{151}\text{N}_{10}\text{O}_{12}$   $[\text{M} + \text{H}]^+$  1925.585.

**Synthesis of 2Th-O.** 4-Bromo-9-butoxy-2,7-bis(2-ethylhexyl)benzo[*lmn*][3,8]phenanthroline-1,3,6,8(2*H*,7*H*)-tetraone (70 mg, 0.11 mmol), 5,5'-bis(4,4,5,5-tetramethyl-1,3,2-dioxaborolan-2-yl)-2,2'-bithiophene (23 mg, 54.5  $\mu\text{mol}$ ), tetrakis(triphenylphosphine)palladium(0) (3.2 mg, 2.73  $\mu\text{mol}$ ) and potassium carbonate (2 mL, 2 M) in toluene were degassed for 15 min and then heated at reflux for 24 h. Solvent was then evaporated and the crude product was diluted with dichloromethane (30 mL) and washed with water (3 × 30 mL). The organic phase was collected, dried over anhydrous  $\text{MgSO}_4$  and the solvent removed under vacuum. The crude product was purified by column chromatography using dichloromethane and the product obtained was recrystallised from acetone and

dichloromethane to give title compound as green brown solid (60 mg, yield 85%). Mp 225–226 °C (dec.).  $^1\text{H}$  NMR  $\delta$  8.76 (s, 2H, NDI), 8.52 (s, 2H, NDI), 7.29 (d,  $J$  = 4.0, 2H, thiophene-H), 7.22 (d,  $J$  = 4.0, 2H, thiophene-H), 4.48 (t,  $J$  = 6.8, 4H,  $\text{OCH}_2$ ), 4.19–4.05 (m, 8H,  $\text{NCH}_2$ ), 2.07–1.92 (m, 8H, CH &  $\text{CH}_2$ ), 1.69–1.60 (m, 4H,  $\text{CH}_2$ ), 1.40–1.30 (m, 32H,  $\text{CH}_2$ ), 1.05 (t,  $J$  = 7.6, 6H,  $\text{CH}_3$ ), 0.95–0.86 (m, 24H,  $\text{CH}_3$ ).  $^{13}\text{C}$  NMR  $\delta$  163.0, 162.9, 162.7, 162.1, 161.5, 140.6, 139.5, 136.9, 129.3, 129.0, 128.4, 124.7, 124.5, 123.2, 122.8, 119.8, 111.1, 70.8, 44.9, 44.5, 38.0, 31.2, 30.83, 30.80, 28.7, 24.1, 24.1, 23.3, 19.2, 14.3, 13.9, 10.8. MALDI  $m/z$  obsd  $[\text{M} + \text{H}]^+$  1288.502, calcd  $\text{C}_{76}\text{H}_{95}\text{N}_4\text{O}_{10}\text{S}_2$   $[\text{M} + \text{H}]^+$  1288.726.

**Synthesis of 2Th-S.** 4-Bromo-9-(butylthio)-2,7-bis(2-ethylhexyl)benzo[*lmn*][3,8]phenanthroline-1,3,6,8(2*H*,7*H*)-tetraone (40 mg, 60.8  $\mu\text{mol}$ ), 5,5'-bis(4,4,5,5-tetramethyl-1,3,2-dioxaborolan-2-yl)-2,2'-bithiophene (13 mg, 30.4  $\mu\text{mol}$ ), tetrakis(triphenylphosphine)palladium(0) (1.8 mg, 1.52  $\mu\text{mol}$ ) and potassium carbonate (2 mL, 2 M) in toluene were degassed for 15 min and then heated at reflux for 12 h. Solvent was then evaporated and the crude product was diluted with dichloromethane (30 mL) and washed with water (3 × 30 mL). The organic phase was collected, dried over anhydrous  $\text{MgSO}_4$  and the solvent removed under vacuum. The crude product was purified by column chromatography using dichloromethane and the product obtained was recrystallised from acetone and dichloromethane to give title compound as dark brown solid (25 mg, yield 75%). Mp 217–218 °C (dec.).  $^1\text{H}$  NMR  $\delta$  8.77 (s, 4H, NDI), 7.30 (d,  $J$  = 3.6, 2H, thiophene-H), 7.25 (d,  $J$  = 3.6, 2H, thiophene-H), 4.23–4.07 (m, 8H,  $\text{NCH}_2$ ), 3.27 (t,  $J$  = 7.6, 4H,  $\text{SCH}_2$ ), 2.01–1.85 (m, 8H, CH &  $\text{CH}_2$ ), 1.69–1.60 (m, 4H,  $\text{CH}_2$ ), 1.41–1.30 (m, 32H,  $\text{CH}_2$ ), 1.04 (t,  $J$  = 7.2, 6H,  $\text{CH}_3$ ), 0.96–0.86 (m, 24H,  $\text{CH}_3$ ).  $^{13}\text{C}$  NMR  $\delta$  163.9, 163.1, 162.70, 162.66, 151.4, 140.5, 139.7, 137.6, 136.6, 129.6, 128.8, 128.0, 125.3, 124.9, 124.6, 124.0, 123.2, 119.2, 44.9, 38.0, 37.9, 32.3, 30.8, 30.1, 28.8, 24.1, 23.28, 23.26, 22.5, 14.2, 13.9, 10.81, 10.76. HRMS (ESI)  $m/z$  obsd  $[\text{M} + \text{H}]^+$  1319.6040, calcd  $\text{C}_{76}\text{H}_{95}\text{N}_4\text{O}_8\text{S}_4$   $[\text{M} + \text{H}]^+$  1319.6027.

**Synthesis of 2Th-N.** 4-Bromo-9-(butylamino)-2,7-bis(2-ethylhexyl)benzo[*lmn*][3,8]phenanthroline-1,3,6,8(2*H*,7*H*)-tetraone (characterization described in ESI†) (50 mg, 78.0  $\mu\text{mol}$ ), 5,5'-bis(4,4,5,5-tetramethyl-1,3,2-dioxaborolan-2-yl)-2,2'-bithiophene (16 mg, 39.0  $\mu\text{mol}$ ), tetrakis(triphenylphosphine)palladium(0) (2.3 mg, 2.0  $\mu\text{mol}$ ) and potassium carbonate (2 mL, 2 M) in toluene were degassed for 15 min and then heated at reflux for 24 h. Solvent was then evaporated and the crude product was diluted with dichloromethane (30 mL) and washed with water (3 × 30 mL). The organic phase was collected, dried over anhydrous  $\text{MgSO}_4$  and the solvent removed under vacuum. The crude product was purified by column chromatography using dichloromethane and the product obtained was recrystallised from acetone and dichloromethane to give title compound as deep purple solid (40 mg, yield 80%). Mp 232–233 °C (dec.).  $^1\text{H}$  NMR  $\delta$  10.11 (t,  $J$  = 5.2, 2H, NH), 8.63 (s, 2H, NDI), 8.28 (s, 2H, NDI), 7.23 (d,  $J$  = 3.6, 2H, thiophene-H), 7.11 (d,  $J$  = 3.6, 2H, thiophene-H), 4.17–4.05 (m, 8H,  $\text{NCH}_2$ ), 3.64–3.59 (m, 4H,  $\text{HNCH}_2$ ), 1.96–1.91 (m, 4H, CH), 1.88–1.80 (m, 4H,  $\text{CH}_2$ ), 1.59–1.52 (m, 4H,  $\text{CH}_2$ ), 1.42–1.29 (m, 32H,  $\text{CH}_2$ ), 1.04 (t,  $J$  = 7.2, 6H,  $\text{CH}_3$ ), 0.95–0.86 (m, 24H,  $\text{CH}_3$ ).  $^{13}\text{C}$  NMR  $\delta$  166.6, 163.23, 163.18,



162.9, 152.2, 141.0, 139.0, 136.4, 133.3, 129.4, 128.4, 128.3, 124.1, 123.7, 122.5, 120.7, 120.4, 100.0, 44.7, 44.2, 43.2, 38.0, 31.7, 30.9, 28.8, 24.2, 24.1, 23.3, 23.2, 20.4, 14.2, 13.9, 10.84, 10.80. HRMS (ESI)  $m/z$  obsd  $[M + H]^+$  1285.6826, calcd  $C_{76}H_{97}N_6O_8S_2$   $[M + H]^+$  1285.6804.

### Device fabrication

Devices were fabricated using an inverted structure as follows: ITO/ZnO/PEIE/active layer/MoO<sub>x</sub>/Ag. ITO-patterned glass substrates were first sonicated in acetone (ten minutes) followed by 2-propanol (ten minutes). The substrates were then dried under nitrogen before a 10 minute UV-ozone treatment. Immediately thereafter, the substrates were spin-coated with a zinc acetate solution prepared as follows: zinc acetate dihydrate was dissolved in 2-methoxyethanol to form a 0.1 M solution. A small amount (60  $\mu$ L/10 mL of solution) of ethanolamine was added as a stabilizer and the solution was stirred at 60 °C overnight in ambient conditions. This ZnO interlayer was spin cast to be approximately 30 nm thick. After spin coating, the substrates were transferred to a hot plate and cured at 200 °C for 30 minutes. Subsequently, a 0.4% PEIE (polyethylenimine ethoxylated) in 2-methoxyethanol solution was spin coated onto the substrates to form a 10 nm-thick film and annealed at 120 °C for 20 minutes. All materials and solvents were acquired from Sigma Aldrich and used as received. The substrates were then transferred to a nitrogen-filled glove box where active layers were spin cast to form films that were approximately 70 nm thick. The ideal active layer solution consisted of a 1 : 1 weight ratio of donor to acceptor in chlorobenzene. The optimum concentration was 30 g L<sup>-1</sup> and all solutions were heated at 70 °C for at least 24 hours prior to being spin cast. Devices were carefully optimized with respect to active layer thickness, weight ratio, and solvent, with optimization data provided in the ESI.† Trials of solvent additives (e.g. 1,8-diiodooctane), annealing and solvent annealing were found to worsen device performance. The donor polymer PBDTTT-EFT (also known as PTB7-Th) was purchased from 1-Material (commercial name PCE-10) and used as received. After the active layer was deposited, the substrates were immediately transferred to an Angstrom Engineering Covap evaporator where 12 nm of molybdenum oxide (0.3 Å s<sup>-1</sup>) was evaporated followed by 100 nm of silver (1 Å s<sup>-1</sup>) under at most  $9 \times 10^{-7}$  Torr. A mask was used to ensure the devices each had eight identical pixels with 4.5 mm<sup>2</sup> active area each. Following the contact deposition, the devices were fitted with edge clips and encapsulated by epoxy and glass.

### Device characterization

Simulated AM1.5 G radiation with 100 mW cm<sup>-2</sup> irradiance was provided by a Photo Emission Tech model SS50AAA solar simulator with a silicon reference cell with a KG3 glass filter used to calibrate the intensity. A Keithley 2635 source meter was used to characterize the  $J$ - $V$  characteristics of devices. External quantum efficiency spectra were subsequently measured using a spot size less than the active area of the pixel in the device. This ensures that the EQE measurement is independent of the

device active area, enabling a cross-check with the measured  $J_{SC}$  under the solar simulator. An Oriel Cornerstone 130 monochromator was used to disperse light from a tungsten filament (Newport 250 W QTH). Prior to measurement, this system was calibrated using a Thorlabs FDS-100CAL photodiode placed at the exact location devices occupy during measurements.

### Thin-film morphology characterization

**Grazing incidence wide angle X-ray scattering.** GIWAXS measurements were performed at the SAXS/WAXS beamline at the Australian Synchrotron.<sup>51</sup> A Dectris Pilatus 1M detector was used to record scattering patterns from 11 keV electrons. Background signal from substrate scatter was minimized by keeping the incident angle of the X-ray beam close to the critical angle of the polymer film but below the critical angle of the substrate. Damage to the film was avoided by limiting the X-ray exposure time to 3 seconds. The sample-to-detector distance was calibrated using a silver behenate sample. The results were analysed by an altered version of the NIKA 2D data reduction package<sup>52</sup> implemented in IgorPro.

**Resonant soft X-ray scattering.** R-SoXS measurements were performed at beamline 11.0.1.2 at the Advanced Light Source.<sup>53</sup> Films were floated in deionized water, followed by transferring onto 100 nm SiN<sub>2</sub> windows. The X-ray energy of 284.0 eV was chosen by calculating the scattering materials contrast between PBDTTT-EFT and the various acceptors. Scattered photons were collected by a Princeton PI-MTE in-vacuum CCD detector with 27.6  $\mu$ m  $\times$  27.6  $\mu$ m pixels. Two scattering patterns were collected, one at a 30 mm sample to detector distance and another at a 150 mm sample to detector distance, and combined in software. Two dimensional scattering patterns were reduced to one dimensional profiles by using a customized version of NIKA.

**Photoluminescence quenching.** PL spectroscopy and PL quenching measurements were acquired using a Horiba Jobin Yvon Fluorolog spectrofluorometer.

**Atomic force microscopy.** AFM images were obtained from the Melbourne Centre for Nanofabrication using a Bruker Dimension Icon in ScanAsyst mode.

## Results and discussion

HOMO and LUMO values for each material were estimated with cyclic voltammetry and are displayed in Fig. 2. A detailed description of the measurement as well as cyclic voltammograms (ES20) for each material are given in the ESI.† The acceptors incorporating either an oxygen or sulfur in their side chains exhibited similar HOMO and LUMO values for both star and 2Th materials. The bithiophene bridge lowered both HOMO and LUMO values in these materials compared with the triarylamine core by approximately 0.1 eV. As predicted, both acceptors with nitrogen substitutional atoms exhibited high-lying HOMO and LUMO values compared with the other molecules. While the molecular structure did not greatly affect the LUMO energy level for **Star NDI-N** or **2Th-N**, there is

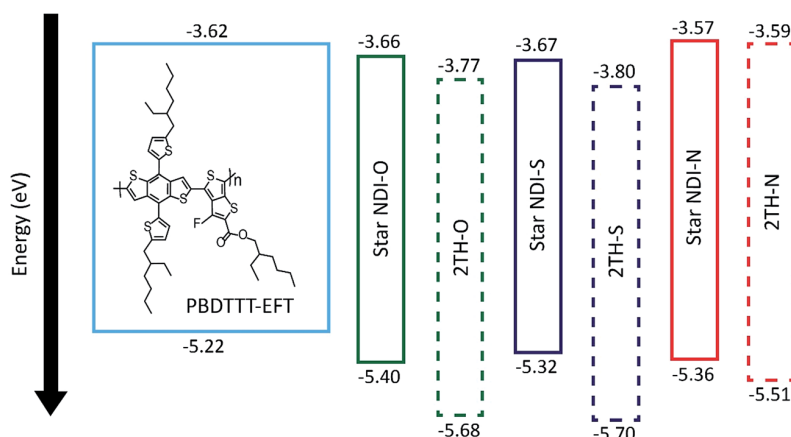


Fig. 2 HOMO and LUMO values for the six molecular acceptors. The HOMO and LUMO values for PBDTTT-EFT, as well as its chemical structure, are also given.<sup>66</sup>

a noticeable lowering of the HOMO energy in the **2Th-N** material, following the trend seen in the other 2Th materials. Due to the generally low-lying LUMO values, the popular low band-gap polymeric donor poly[4,8-bis(5-(2-ethylhexyl)thiophen-2-yl)benzo[1,2-*b*;4,5-*b'*]dithiophene-2,6-diyl-*alt*-(4-(2-ethylhexyl)-3-fluorothieno[3,4-*b*]thiophene-)-2-carboxylate-2,6-diyl] (PBDTTT-EFT) was chosen as the donor material for bulk heterojunction devices, which is known to perform well in conjunction with the NDI-based acceptor polymer P(NDI2OD-T2).<sup>54</sup> The optoelectronic properties of the materials are given in Table 1.

Each material exhibits a red-shift in its UV-visible absorption profile from the solution to the solid-state, indicative of stronger intermolecular interaction in the solid state (see Fig. ES21 in the ESI†).<sup>55</sup> The solid-state absorption profiles of neat and blend film are shown in Fig. 3. All six materials exhibited absorption coefficients ( $\alpha$ ) from  $1.7\text{--}2.0 \times 10^4 \text{ cm}^{-1}$  (Fig. ES22†). Due to the donor-acceptor character of these materials, the spectra show an extension of the absorption profile into the visible region beyond the absorption edge of NDI, which is found at  $\sim 380 \text{ nm}$ .<sup>36</sup> For the star-shaped materials, the absorption profile includes a broad absorption feature from  $\sim 550\text{--}775 \text{ nm}$ , as well as a narrower and more structured feature between  $400\text{--}550 \text{ nm}$ . Below  $400 \text{ nm}$ , absorption characteristic of  $\pi\text{--}\pi^*$  absorption in the NDI subunit is seen. For the 2Th materials, only a single, broad absorption feature in the visible is seen. The broad absorption peak at larger wavelengths is attributed to the induced charge

transfer (ICT) state of the bithiophene bridge, flanked by two NDI acceptor moieties. The broad absorption peaks exhibited by all six acceptors can be attributed to delocalized electronic transitions throughout the entire molecule.<sup>56</sup> Extending the acceptor's absorption spectrum into the visible wavelength range will, in theory, enable greater photon absorption by photovoltaic devices, increasing the photocurrent. The absorption profile of 1 : 1 blends of the acceptor molecules with the donor polymer PBDTTT-EFT strongly reflect the absorption profile of neat PBDTTT-EFT at higher wavelengths, while the absorption profiles of the acceptors are visible at wavelengths below  $550 \text{ nm}$ . The lower optical bandgap for the star-shaped materials is indicative of a longer conjugation length along the molecule compared to 2Th materials.

Following initial material investigations, inverted solar cells employing each molecular acceptor were fabricated with the following architecture: ITO/ZnO/PEIE/active layer/MoO<sub>x</sub>/Ag. Sandwiching a thin ( $\sim 10 \text{ nm}$ ) layer of the insulating polymer PEIE between the electron transporting and active layers – which elsewhere has been shown to increase the performance of polymer solar cells<sup>57</sup> – was found to enhance the performance of our NDI-based solar cells (Fig. ES23†). Active layers were spin cast at 6000 RPM from chlorobenzene solutions with a 1 : 1 PBDTTT-EFT : acceptor ratio by weight to form films approximately  $70 \text{ nm}$  thick. These were determined to be the optimum processing conditions for all six molecular acceptors. A detailed description of the device fabrication is outlined in the Experimental section and additional optimization can be found in the ESI.† Although 1,8-diiodooctane (DIO) was trialed as a solvent additive, even very low concentrations (0.2 vol%) were determined to hinder the device performance. This is in agreement with similar systems that also show the addition of DIO to NDI-based acceptor devices reduces the device performance.<sup>58</sup> The  $J\text{--}V$  characteristics and external quantum efficiency (EQE) spectra for all six acceptors are given in Fig. 4 with a summary of the performance parameters given in Table 2.

Table 1 The optoelectronic properties and melting points for the six molecular acceptors

| Acceptor   | LUMO (eV) | HOMO (eV) | $E_g$ (eV) | $E_g^{\text{opt}}$ (eV) |
|------------|-----------|-----------|------------|-------------------------|
| Star NDI-O | −3.66     | −5.40     | 1.74       | 1.83                    |
| Star NDI-S | −3.67     | −5.32     | 1.65       | 1.75                    |
| Star NDI-N | −3.57     | −5.36     | 1.79       | 1.86                    |
| 2Th-O      | −3.77     | −5.68     | 1.91       | 1.91                    |
| 2Th-S      | −3.80     | −5.70     | 1.90       | 1.88                    |
| 2Th-N      | −3.59     | −5.51     | 1.92       | 1.92                    |

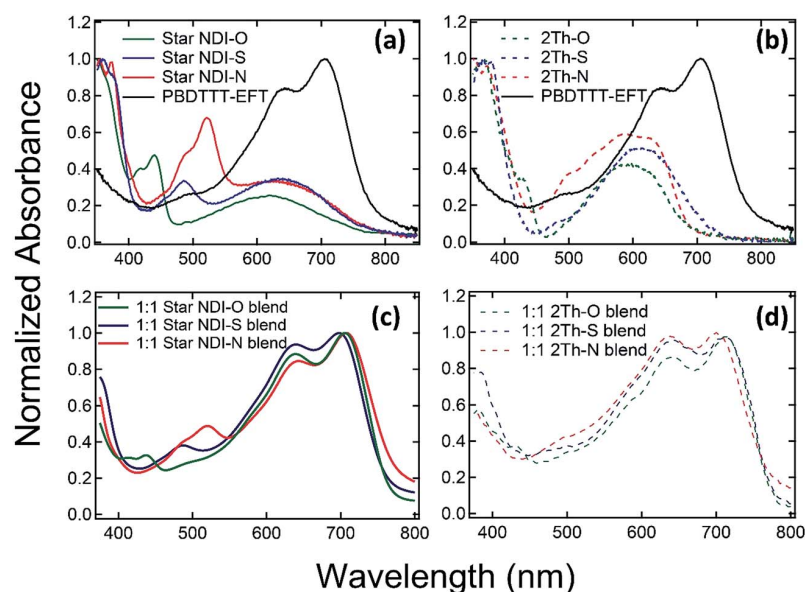


Fig. 3 Normalized neat absorbance for the star-shaped acceptors and PBDTTT-EFT (a) and 2Th molecules (b). The absorbance profiles for optimized device blends are shown in the bottom row for both the star-shaped materials (c) and 2Th materials (d).

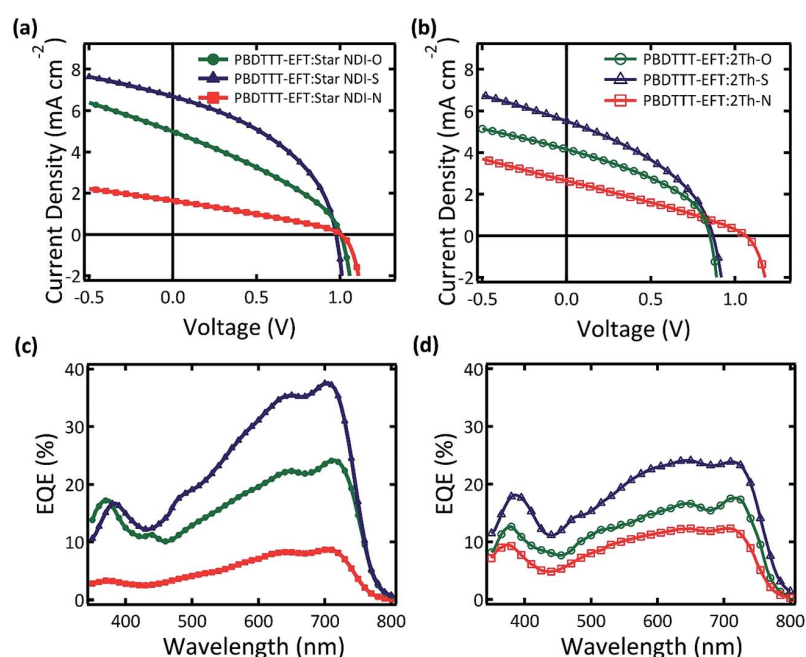


Fig. 4 Solar cell characteristics for star-shaped (a) and 2Th-based devices (b). The devices were all optimized to the following processing conditions: a 1 : 1 donor : acceptor ratio with PBDTTT-EFT in a 30 g L<sup>-1</sup> chlorobenzene solution, spin cast at 6000 RPM. EQE spectra for star-shaped (c) and 2Th-based (d) devices are also shown. The EQE spectra complement the *J*-*V* characteristics, as materials with a sulfur substitution exhibit higher EQE while the nitrogen substitution leads to a decrease in EQE.

For both star-shaped and linear molecules, there are systematic variations in performance for the different heteroatoms. For both star-shaped and linear acceptors, the sulfur substituted molecule was found to perform best, followed by the oxygen substituted molecule, with the nitrogen substituted

molecule performing the worst. For the star-shaped materials, devices based on Star-S exhibited enhanced  $J_{SC}$  and fill factors (FF) compared to Star-O based devices, with  $J_{SC}$  increasing from 5.0 to 6.7 mA cm<sup>-2</sup> and FF from 34 to 43%. Alternatively, compared to both Star-O and Star-S based devices, the Star-N

**Table 2** Photovoltaic performance for the six molecular acceptors as well as PL quenching efficiency when excited at 600 nm for the Star acceptors in a 1 : 1 blend with PBDTTT-EFT

| Acceptor   | $J_{SC}$ (mA cm <sup>-2</sup> ) | $V_{OC}$ (V) | FF (%) | PCE (%)     | EQE $J_{SC}$ (mA cm <sup>-2</sup> ) | PL quench. eff. (%) |
|------------|---------------------------------|--------------|--------|-------------|-------------------------------------|---------------------|
| Star NDI-O | 5.0 ± 0.1                       | 1.00 ± 0.01  | 34 ± 1 | 1.7 ± 0.1   | 4.4 ± 0.1                           | 71.8                |
| Star NDI-S | 6.8 ± 0.2                       | 0.98 ± 0.01  | 42 ± 3 | 2.8 ± 0.1   | 6.3 ± 0.8                           | 82.3                |
| Star NDI-N | 1.6 ± 0.1                       | 0.95 ± 0.07  | 32 ± 1 | 0.50 ± 0.05 | 1.42 ± 0.1                          | 43.2                |
| 2Th-O      | 4.6 ± 0.2                       | 0.88 ± 0.05  | 40 ± 1 | 1.6 ± 0.1   | 3.5 ± 0.3                           |                     |
| 2Th-S      | 5.1 ± 0.4                       | 0.88 ± 0.02  | 38 ± 1 | 1.7 ± 0.2   | 4.3 ± 0.6                           |                     |
| 2Th-N      | 2.7 ± 0.1                       | 1.06 ± 0.07  | 33 ± 3 | 0.84 ± 0.05 | 2.3 ± 0.2                           |                     |

devices exhibit significantly reduced  $J_{SC}$  and FF, down to 1.6 mA cm<sup>-2</sup> and 32% respectively. Similar trends are seen for the bithiophene materials.  $J_{SC}$  was also estimated by integrating the external quantum efficiency spectra which agree well in general with the measured  $J_{SC}$ , with the slightly larger  $J_{SC}$  values measured under the solar simulator likely to be due to edge effects given the small active area of the cells.

Based on the spectral features of the EQE and the absorption profiles of the donor and acceptor materials, it can be seen that acceptor materials are contributing to current, but only contributing at most 25% due to the lower absorption coefficient of these materials compared to PBDTTT-EFT (refer to the donor : acceptor ratio EQE and UV-Vis spectra analysis in the ESI†). This observation indicates that these materials do not significantly contribute to the photocurrent generated by the devices, despite the absorption edge being extended into the visible wavelength region by elongating the conjugation length of the material. Future work will include optimizing the molecular structure of acceptors in order to increase their contribution to the observed photocurrent in bulk hetero-junction devices.

As noted above, a strong dependence on the substitutional atom is reflected in the  $J_{SC}$  measured for these materials, particularly in acceptors utilizing a nitrogen substitutional atom. For the star-shaped materials, this dependence is significant, with an observed  $J_{SC}$  of just 1.6 mA cm<sup>-2</sup> for **Star NDI-N**, compared with 5.0 mA cm<sup>-2</sup> for **Star NDI-O** and 6.8 mA cm<sup>-2</sup> for **Star NDI-S**. This change in  $J_{SC}$  could be due to the reduced LUMO/LUMO offset between PBDTTT-EFT and **Star NDI-N**. This offset determines the driving force for charge transfer and charge separation, and is therefore extremely important. The same reasoning can be used to explain the reduced  $J_{SC}$  observed in PBDTTT-EFT:2Th-N devices.

It is important to note that the FF for all six acceptors blended with PBDTTT-EFT are lower than those reported for other NDI-based molecular acceptors that exhibit similar efficiencies. Reported FF for similar OPV systems are typically around 50% (ref. 27 and 28) while the systems reported here range from 32–42%. These low FF indicate that photogenerated charge carriers are not able to be efficiently extracted from the devices, which may be due to a number of reasons including large active-layer domain sizes that prohibit excitons from dissociating efficiently, a lack of clear charge pathways to the respective electrodes of the charge carriers, or an imbalance in electron and hole mobility within the active layer.<sup>59</sup> Indeed,

preliminary space-charged limited current measurements on PBDTTT-EFT:Star NDI-O blends (see Fig. ESI28†) determined the hole and electron mobilities to be  $4.6 \times 10^{-4}$  and  $1.7 \times 10^{-7}$  cm<sup>2</sup> V<sup>-1</sup> s<sup>-1</sup> respectively. The significantly lower electron mobility compared to hole mobility indicates unbalanced charge movement through the device, and may help to explain the relatively low FF observed in solar cells made from these materials.

Within the six materials discussed here, the nitrogen heteroatom lowers the FF for both the star-shaped and linear molecules, while the oxygen or sulfur heteroatoms result in higher FF. For the star-shaped materials, the sulfur heteroatom clearly demonstrates the higher FF of 42% over 34% for **Star NDI-O**. However, the oxygen heteroatom within the linear molecules results in a FF of 40%, which is higher than the 38% FF realized with the sulfur heteroatom. Despite these subtle differences, the FF reported here remain notably lower than those reported for similar systems, and further investigation into the morphology of the active layers will be discussed below, in an effort to explain these deficiencies.

Another interesting variation between the materials is the value of the  $V_{OC}$ , which is influenced by both the substitutional atoms and the molecular structure. Theoretically the maximum  $V_{OC}$  obtainable will be limited by the difference between the HOMO of the donor and LUMO of the acceptor materials.<sup>6</sup> The trends that can be observed in the measured  $V_{OC}$  agree well with those predicted by comparing LUMO values between the various acceptors. Between the star and bithiophene bridge structures, the linear configuration of the 2Th materials decreases both the HOMO and LUMO values for these materials compared with the star-shaped materials. This results in higher  $V_{OC}$  values for the star-shaped materials. For the 2Th materials, the  $V_{OC}$  for both oxygen and sulfur substitutional atoms are very similar, which reflects the very similar LUMO values for these materials. The LUMO of the 2Th-N material, however, is significantly higher, which results in an increase in the  $V_{OC}$  of 0.06 V from 0.88 V for 2Th-O and 2Th-S to 0.94 V. Interestingly, this notable increase in  $V_{OC}$  is not observed in the Star-N material over the  $V_{OC}$  values of Star-O and Star-S, despite these having lower LUMO values. With influence by kinetic factors as well as energetic factors, the lower than expected  $V_{OC}$  of the Star-N molecule could be due to higher bimolecular recombination in Star-N based devices. Additionally, the  $V_{OC}$  values observed for all three linear molecules, which were designed based on the P(NDI2OD-T2) polymer, are higher than



the  $V_{OC}$  observed when P(NDI2OD-T2) is blended with PBDTTT-EFT.<sup>60</sup> The all-polymer devices resulted in a  $V_{OC}$  of 0.80 V, which is significantly lower than the 0.88–0.94 V observed for the molecular materials. This is a reflection of the increased LUMO value for the molecular materials, from  $-3.8$  eV for P(NDI2OD-T2),<sup>40</sup> to  $-3.59$  eV for **2Th-N**. Despite an increase in  $V_{OC}$  for the **2Th** materials, a significant reduction in both  $J_{SC}$  and FF are observed when the molecular acceptors are blended with PBDTTT-EFT compared to P(NDI2OD-T2). These differences result in a typical PCE of 5.5% for PBDTTT-EFT:P(NDI2OD-T2) devices,<sup>60</sup> compared to 1.6, 1.7 and 0.84% PCE for **2Th-O**, **2Th-S** and **2Th-N** devices respectively.

Apart from the molecules with sulfur substitutions, incorporating the triarylamine core unit resulted in better device efficiency compared with the more planar bithiophene configuration. This result is most likely due to the star-shaped molecules affording a greater opportunity for charge delocalisation compared to the linear molecules.<sup>61</sup>

Ultimately, thionating the alkyl chain of the star-shaped NDI-based acceptor resulted in an average PCE of 2.8%, which is amongst the highest efficiencies for NDI-based molecular acceptors to-date.<sup>22,62</sup> (Using the lower  $J_{SC}$  from integrating the EQE spectrum yields an efficiency of 2.6%, which is still among the highest efficiencies.) As a result of the improved performance of the star-shaped materials over the bithiophene acceptors, further investigations into the morphology of these materials focused on the triarylamine-based acceptors.

Grazing incidence wide angle X-ray scattering (GIWAXS) was used to characterize the crystallinity<sup>63,64</sup> of the neat and blend films of the three star acceptors (Fig. 5). In contrast to the scattering patterns observed in soluble NDI derivatives,<sup>65</sup> the scattering patterns of neat films of the three star acceptors, in general, show few well-defined scattering features,

indicating a lack of extended three-dimensional order, demonstrating that the star architecture is effective in suppressing the crystallization of these molecules. There are, however, subtle differences in the scattering patterns of the three star acceptors indicating that the substitutional atom does have an effect on the materials' intermolecular packing. For the **Star NDI-O** material, only two weak isotropic rings at  $\sim 4.5$  nm<sup>-1</sup> and 14 nm<sup>-1</sup> are seen which are likely associated with correlated ordering (weak aggregation) on the length scale of the molecule and disordered  $\pi$ - $\pi$  packing, respectively. For the **Star NDI-S** material, only a very weak  $\pi$ - $\pi$  stacking feature can be seen in the  $Q_z$  direction. Finally, the **Star NDI-N** material appears to show some peaks at low  $Q$ , suggesting some degree of order on the length scale of the molecule, with both isotropic and anisotropic scattering features. The scattering features in the neat acceptor films are carried over into the GIWAXS patterns of 1 : 1 blends with the donor polymer. Indeed, the scattering patterns of the blends resemble a linear combination of the scattering patterns of the neat materials, indicating that both donor and acceptor materials pack in a similar fashion in the blend and, in particular, that these three acceptor materials do not appear to disrupt the packing of PBDTTT-EFT crystallites (and *vice versa*). 1D GIWAXS line cut profiles for neat donor and acceptor as well as blend films can be found in the electronic ESI (Fig. ES26†). Interestingly while there are variations in the degree of order exhibited by the three star NDI molecules, solar cell performance appears to be inversely correlated with acceptor order, with the **Star NDI-S** giving the best solar cell performance despite showing the least crystalline order. The **Star NDI-O** gives the next highest solar cell performance with some improved crystalline order, while the **Star NDI-N** molecule gives the worst solar cell performance despite showing the

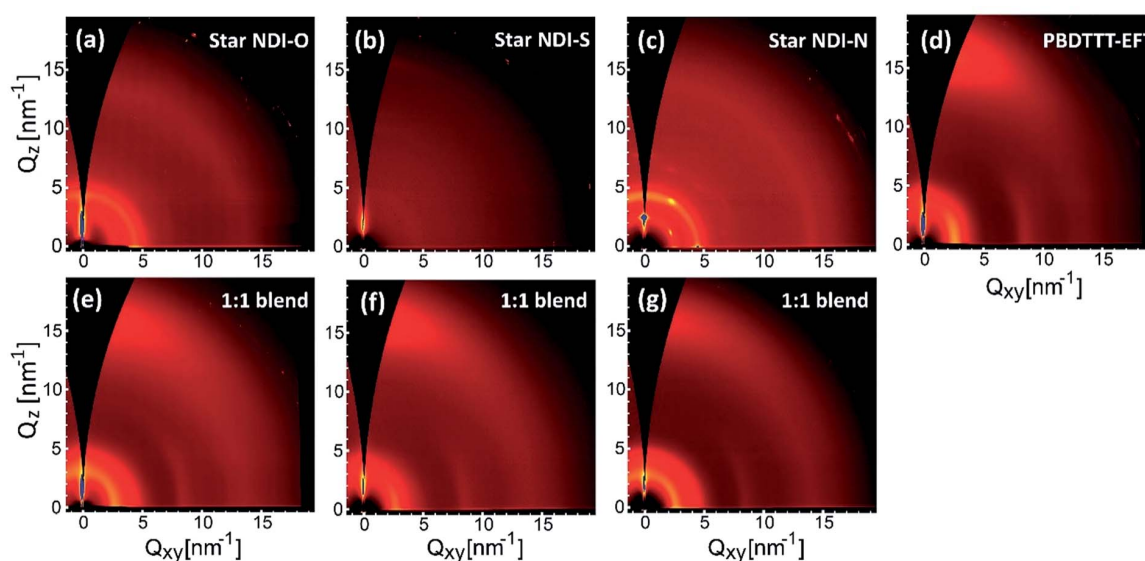


Fig. 5 2D GIWAXS spectra of neat **Star NDI-O** (a), **Star NDI-S** (b), **Star NDI-N** (c) and PBDTTT-EFT (d). The corresponding blended films of PBDTTT-EFT with **Star NDI-O** (e), **Star NDI-S** (f) and **Star NDI-N** (g) are also given.

highest level of crystallinity. Of course, crystallinity in itself may not be causing poor solar cell performance with differences in the LUMO levels of the materials likely to be more strongly influencing device behavior, as discussed above. However, the GIWAXS observations show that crystallinity does not appear to be necessary to enable device action in this class of material.

The size of domains on the 10 nm to 1  $\mu$ m length scale has been probed with resonant soft X-ray scattering (R-SoXS) with the results displayed in Fig. 6. The R-SoXS patterns show a lack of prominent scattering features for values of  $Q < 0.05 \text{ nm}^{-1}$ , indicating a lack of coarse phase separation. All three blends show similar scattering profiles suggesting a lack of a well-defined domain spacing with domains typically less than 100 nm in size. While the R-SoXS results show that the domains are not overly coarse, there is likely to be a distribution of domain sizes with some as large as 100 nm. AFM (Fig. 7) was used to confirm the homogeneity of the domain sizes for 1 : 1 blended films of all three molecular acceptors. The images show

a lack of coarse phase separation and relatively smooth film topography, indicating the substitutional heteroatom does not strongly influence the morphology of blended films, which is in agreement with the R-SoXS spectra.

Finally, PL quenching experiments were performed to assess the efficiency of charge generation in the Star NDI-based blends. Fig. ES27† presents the PL spectra used to calculate PL quenching with Table 2 summarizing the PL quenching efficiency results. The PL quenching data indicate a strong dependence of charge transfer efficiency on the substitutional heteroatom, with the sulfur substitution resulting in the largest PL quenching efficiency of 82.3% followed by the oxygen heteroatom of 71.8% and finally, the nitrogen substitutional atom resulted in the lowest PL quenching efficiency of 43.2%. These PL quenching efficiency trends nicely follow the device trends indicating that differences in exciton dissociation efficiency can largely account for the variations in  $J_{\text{SC}}$  observed. While differences in PL quenching efficiency are often associated with variations in domain size, the R-SoXS and AFM results indicate that all three blends have similar morphologies. Thus the differences in PL quenching efficiency are attributed to differences in the driving force for charge transfer, with the raised LUMO of the **Star NDI-N** molecule in particular resulting in an insufficient LUMO/LUMO offset. The PL quenching efficiency of the **Star NDI-O** and **Star NDI-S** molecules indicate there is still some room for improvement, however it is not clear what contribution morphology may be playing here.

This work has demonstrated that NDI-based small molecule acceptors have the potential to act as efficient electron acceptors in organic solar cells. While this manuscript has focused on using PBDTTT-EFT as the donor material, other donor polymers may be better suited, which will be the subject of future work. Very recently, it has been shown that poly(3-hexylthiophene-2,5-diyl) (P3HT) can successfully act as the donor polymer for NDI-based molecular acceptors, with devices reaching efficiencies greater than 4%.<sup>62</sup> The use of a heteroatom-linked side-chain attached to the NDI core also affords greater flexibility for tuning optoelectronic properties, and future work tuning the nature of these side chains will also be of interest.

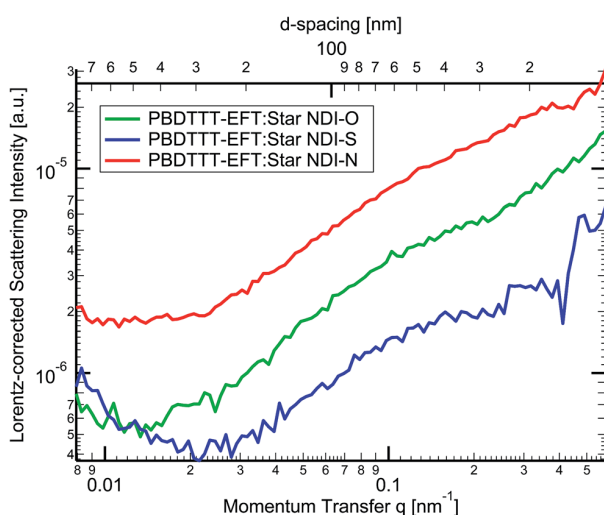


Fig. 6 R-SoXS spectra for 1 : 1 blends of PBDTTT-EFT with the three acceptors.

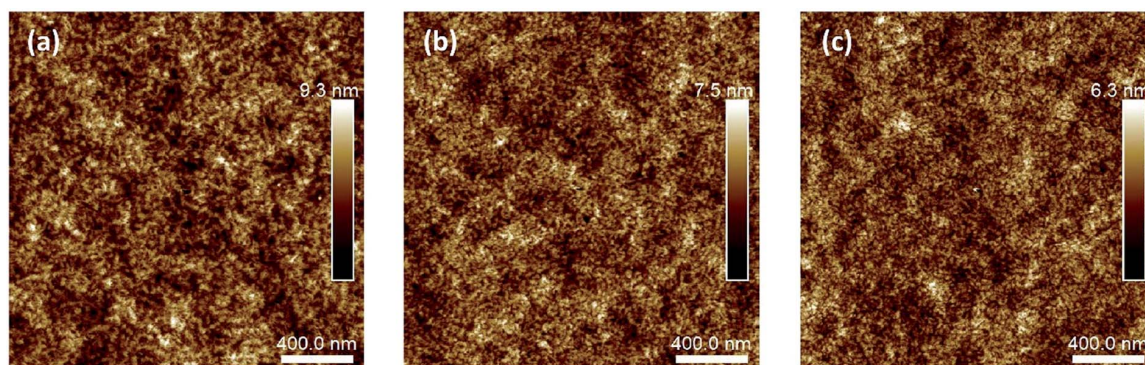


Fig. 7 AFM images for 1 : 1 blends of PBDTTT-EFT:Star NDI-O (a), Star NDI-S (b) and Star NDI-N (c).

## Conclusions

In conclusion, six novel NDI-based molecular acceptors have been synthesized. These acceptors utilize two different molecular architectures and have three different substitutional atoms in their side chains. It was found that a triarylamine core flanked by three NDI units was a favorable molecular structure compared to two NDI units connected *via* a bithiophene bridge. This is most likely due to the more extended electron delocalization afforded by the star-shaped material, as is shown by the UV-visible absorption profile. Additionally, it was found that the substitutional heteroatom plays an important role in the performance of these acceptors. The electron donating nitrogen atom significantly decreased the performance of these materials by raising the LUMO level, having an unfavorable effect on exciton dissociation and resulting in significant reductions in  $J_{SC}$ . Alternatively, substituting a readily reduced sulfur atom in place of an oxygen resulted in significantly improved  $J_{SC}$  in solar cells, leading to a PCE of 2.8%, which is amongst the highest to date for molecule NDI acceptors.

## Acknowledgements

The authors would like to thank Si-Xuan Guo for assistance in cyclic voltammetry measurements. Adam Welford is also thanked for assistance with AFM measurements. This work was performed in part on the SAXS/WAXS beamlines at the Australian Synchrotron, Victoria, Australia. It was also performed in part on the Soft X-ray beamline of the Advanced Light Source, which is a DOE Office of Science User Facility under contract no. DE-AC02-05CH11231. This work was performed in part at the Melbourne Centre for Nanofabrication (MCN) in the Victorian Node of the Australian National Fabrication Facility (ANFF). Financial support from the Australian Research Council through the Discovery Grant Scheme (DP130101861 and DP170104477) is gratefully acknowledged.

## References

- 1 C. J. Brabec and J. R. Durrant, *MRS Bull.*, 2008, **33**, 670–675.
- 2 S. Günes, H. Neugebauer and N. S. Sariciftci, *Chem. Rev.*, 2007, **107**, 1324–1338.
- 3 C. W. Tang, *Appl. Phys. Lett.*, 1986, **48**, 183.
- 4 S. B. Darling and F. You, *RSC Adv.*, 2013, **3**, 17633–17648.
- 5 Y. Liang, Z. Xu, J. Xia, S. T. Tsai, Y. Wu, G. Li, C. Ray and L. Yu, *Adv. Mater.*, 2010, **22**, 135–138.
- 6 M. C. Scharber, D. Mühlbacher, M. Koppe, P. Denk, C. Waldauf, A. J. Heeger and C. J. Brabec, *Adv. Mater.*, 2006, **18**, 789–794.
- 7 G. Yu, J. Gao, J. C. Hummelen, F. Wudl and A. J. Heeger, *Science*, 1995, **270**, 1789–1791.
- 8 Z. He, C. Zhong, S. Su, M. Xu, H. Wu and Y. Cao, *Nat. Photonics*, 2012, **6**, 593–597.
- 9 J. J. M. Halls, C. A. Walsh, N. C. Greenham, E. A. Marseglia, R. H. Friend, S. C. Moratti and A. B. Holmes, *Nature*, 1995, **376**, 498–500.
- 10 J. De Chen, C. Cui, Y. Q. Li, L. Zhou, Q. D. Ou, C. Li, Y. Li and J. X. Tang, *Adv. Mater.*, 2015, **27**, 1035–1041.
- 11 B. Kan, Q. Zhang, M. Li, X. Wan, W. Ni, G. Long, Y. Wang, X. Yang, H. Feng and Y. Chen, *J. Am. Chem. Soc.*, 2014, **136**, 15529–15532.
- 12 C. Liu, C. Yi, K. Wang, Y. Yang, R. S. Bhatta, M. Tsige, S. Xiao and X. Gong, *ACS Appl. Mater. Interfaces*, 2015, **7**, 4928–4935.
- 13 G. Dennler, M. C. Scharber and C. J. Brabec, *Adv. Mater.*, 2009, **21**, 1323–1338.
- 14 D. Gendron and M. Leclerc, *Energy Environ. Sci.*, 2011, **4**, 1225.
- 15 M. Jørgensen, K. Norrman and F. C. Krebs, *Sol. Energy Mater. Sol. Cells*, 2008, **92**, 686–714.
- 16 S. M. McAfee, J. M. Topple, I. G. Hill and G. C. Welch, *J. Mater. Chem. A*, 2015, **3**, 16393–16408.
- 17 J. W. Jung and W. H. Jo, *Chem. Mater.*, 2015, **27**, 6038–6043.
- 18 H. Shi, W. Fu, M. Shi, J. Ling and H. Chen, *J. Mater. Chem. A*, 2015, **3**, 1902–1905.
- 19 S. Li, W. Liu, M. Shi, J. Mai, T.-K. Lau, J. Wan, X. Lu, C. Z. Li and H. Chen, *Energy Environ. Sci.*, 2016, **9**, 604–610.
- 20 H. Zhou, L. Yang, A. C. Stuart, S. C. Price, S. Liu and W. You, *Angew. Chem.*, 2011, **123**, 3051–3054.
- 21 J. W. Jung and W. H. Jo, *Chem. Mater.*, 2015, **27**, 6038–6043.
- 22 H.-W. Luo and Z.-T. Liu, *Chin. Chem. Lett.*, 2016, **27**, 1283–1292.
- 23 X. Zhang, J. Yao and C. Zhan, *Chem. Commun.*, 2014, **51**, 1058–1061.
- 24 J. Zhao, Y. Li, H. Lin, Y. Liu, K. Jiang, C. Mu, T. Ma, J. Y. L. Lai, H. Hu, D. Yu and H. Yan, *Energy Environ. Sci.*, 2015, **8**, 520–525.
- 25 S. Li, W. Liu and E. Al, *J. Mater. Chem. A*, 2016, **4**, 10659–10665.
- 26 E. Ahmed, G. Ren, F. S. Kim, E. C. Hollenbeck and S. A. Jenekhe, *Chem. Mater.*, 2011, **23**, 4563–4577.
- 27 X. Wang, J. Huang, Z. Niu, X. Zhang, Y. Sun and C. Zhan, *Tetrahedron*, 2014, **70**, 4726–4731.
- 28 Y. Liu, L. Zhang, H. Lee, H.-W. Wang, A. Santala, F. Liu, Y. Diao, A. L. Briseno and T. P. Russell, *Adv. Energy Mater.*, 2015, **5**, 1500195.
- 29 H. Li, T. Earmme, G. Ren, A. Saeki, S. Yoshikawa, N. M. Murari, S. Subramanian, M. J. Crane, S. Seki and S. A. Jenekhe, *J. Am. Chem. Soc.*, 2014, **136**, 14589–14597.
- 30 Y. Zhong, M. T. Trinh, R. Chen, W. Wang, P. P. Khlyabich, B. Kumar, Q. Xu, C.-Y. Nam, M. Y. Sfeir, C. Black, M. L. Steigerwald, Y.-L. Loo, S. Xiao, F. Ng, X.-Y. Zhu and C. Nuckolls, *J. Am. Chem. Soc.*, 2014, **136**, 15215–15221.
- 31 C. Mu, P. Liu, W. Ma, K. Jiang, J. Zhao, K. Zhang, Z. Chen, Z. Wei, Y. Yi, J. Wang, S. Yang, F. Huang, A. Facchetti, H. Ade and H. Yan, *Adv. Mater.*, 2014, **26**, 7224–7230.
- 32 Y. Zhong, M. T. Trinh, R. Chen, G. E. Purdum, P. P. Khlyabich, M. Sezen, S. Oh, H. Zhu, B. Fowler, B. Zhang, W. Wang, C.-Y. Nam, M. Y. Sfeir, C. T. Black, M. L. Steigerwald, Y.-L. Loo, F. Ng, X.-Y. Zhu and C. Nuckolls, *Nat. Commun.*, 2015, **6**, 8242.
- 33 Q. Wu, D. Zhao, A. M. Schneider, W. Chen and L. Yu, *J. Am. Chem. Soc.*, 2016, **138**, 7248–7251.

- 34 Y. Yang, Z.-G. Zhang, H. Bin, S. Chen, L. Gao, L. Xue, C. Yang and Y. Li, *J. Am. Chem. Soc.*, 2016, **138**, 15011–15018.
- 35 J. Roncali, *Acc. Chem. Res.*, 2009, **42**, 1719–1730.
- 36 S. V. Bhosale, C. H. Jani and S. J. Langford, *Chem. Soc. Rev.*, 2008, **37**, 331–342.
- 37 O. Yushchenko, D. Villamaina, N. Sakai, S. Matile and E. Vauthey, *J. Phys. Chem. C*, 2015, **119**, 14999–15008.
- 38 T. He, M. Stolte and F. Würthner, *Adv. Mater.*, 2013, **25**, 6951–6955.
- 39 L. Gao, Z. G. Zhang, L. Xue, J. Min, J. Zhang, Z. Wei and Y. Li, *Adv. Mater.*, 2016, **28**, 1884–1890.
- 40 D. Trefz, A. Ruff, R. Tkachov, M. Wieland, M. Goll, A. Kiri and S. Ludwigs, *J. Phys. Chem. C*, 2015, **119**, 22760–22771.
- 41 J. Liu, B. Walker, A. Tamayo, Y. Zhang and T. Q. Nguyen, *Adv. Funct. Mater.*, 2013, **23**, 47–56.
- 42 Y. Lin, Z.-G. Zhang, H. Bai, J. Wang, Y. Yao, Y. Li, D. Zhu and X. Zhan, *Energy Environ. Sci.*, 2015, **8**, 610–616.
- 43 S. Li, H. Zhang, W. Zhao, L. Ye, H. Yao, B. Yang, S. Zhang and J. Hou, *Adv. Energy Mater.*, 2016, **6**, 1501991.
- 44 A. D. Hendsbee, S. M. McAfee, J.-P. Sun, T. M. McCormick, I. G. Hill and G. C. Welch, *J. Mater. Chem. C*, 2015, **3**, 8904–8915.
- 45 O. K. Kwon, J.-H. Park, D. W. Kim, S. K. Park and S. Y. Park, *Adv. Mater.*, 2015, **27**, 1951–1956.
- 46 L. Gao, Z. G. Zhang, L. Xue, J. Min, J. Zhang, Z. Wei and Y. Li, *Adv. Mater.*, 2016, **28**, 1884–1890.
- 47 J. Hellberg, T. Remonen, F. Allared, J. Slaett and M. Svensson, *Synthesis*, 2003, **14**, 2199–2205.
- 48 D. Sahu, C.-H. Tsai, H.-Y. Wei, K.-C. Ho, F.-C. Chang and C.-W. Chu, *J. Mater. Chem.*, 2012, **22**, 7945.
- 49 Z. Yuan, Y. Ma, T. Gessner, M. Li, L. Chen, M. Eustachi, T. R. Weitz, C. Li and K. Muellen, *Org. Lett.*, 2016, **18**, 456–459.
- 50 B. W. Greenland, S. Burattini, W. Hayes and H. M. Colquhoun, *Tetrahedron*, 2008, **64**, 8346–8354.
- 51 N. M. Kirby, S. T. Mudie, A. M. Hawley, D. J. Cookson, H. D. T. Mertens, N. Cowieson and V. Samardzic-Boban, *J. Appl. Crystallogr.*, 2013, **46**, 1670–1680.
- 52 J. Ilavsky, *J. Appl. Crystallogr.*, 2012, **45**, 324–328.
- 53 E. Gann, A. T. Young, B. A. Collins, H. Yan, J. Nasiatka, H. A. Padmore, H. Ade, A. Hexemer and C. Wang, *Rev. Sci. Instrum.*, 2012, **83**, 45110.
- 54 L. Gao, Z.-G. Zhang, L. Xue, J. Min, J. Zhang, Z. Wei and Y. Li, *Adv. Mater.*, 2016, **28**, 1884–1890.
- 55 J. Clark, C. Silva, R. H. Friend and F. C. Spano, *Phys. Rev. Lett.*, 2007, **98**, 206406.
- 56 Z. R. Grabowski and K. Rotkiewicz, *Chem. Rev.*, 2003, **103**, 3899–4032.
- 57 B. A. E. Courtright and S. A. Jenekhe, *ACS Appl. Mater. Interfaces*, 2015, **7**, 26167–26175.
- 58 M. J. Sung, M. Huang, S. H. Moon, T. H. Lee, S. Y. Park, J. Y. Kim, S.-K. Kwon, H. Choi and Y.-H. Kim, *Sol. Energy*, 2017, **150**, 90–95.
- 59 B. Qi and J. Wang, *Phys. Chem. Chem. Phys.*, 2013, **15**, 8972–8982.
- 60 D. Mori, H. Benten, I. Okada, H. Ohkita and S. Ito, *Energy Environ. Sci.*, 2014, **7**, 2939–2943.
- 61 J. Wang, K. Liu, L. Ma and X. Zhan, *Chem. Rev.*, 2016, **116**, 14675–14725.
- 62 D. Srivani, A. Gupta, D. D. La, R. S. Bhosale, A. L. Puyad, W. Xiang, J. Li, S. V. Bhosale and S. V. Bhosale, *Dyes Pigm.*, 2017, **143**, 1–9.
- 63 P. Müller-Buschbaum, *Adv. Mater.*, 2014, **26**, 7692–7709.
- 64 J. Rivnay, S. C. B. Mannsfeld, C. E. Miller, A. Salleo and M. F. Toney, *Chem. Rev.*, 2012, **112**, 5488–5519.
- 65 E. Gann, X. Gao, C. Di and C. R. McNeill, *Adv. Funct. Mater.*, 2014, **24**, 7211–7220.
- 66 S. H. Liao, H. J. Jhuo, Y. S. Cheng and S. A. Chen, *Adv. Mater.*, 2013, **25**, 4766–4771.



### 5.3 Updates and Conclusions

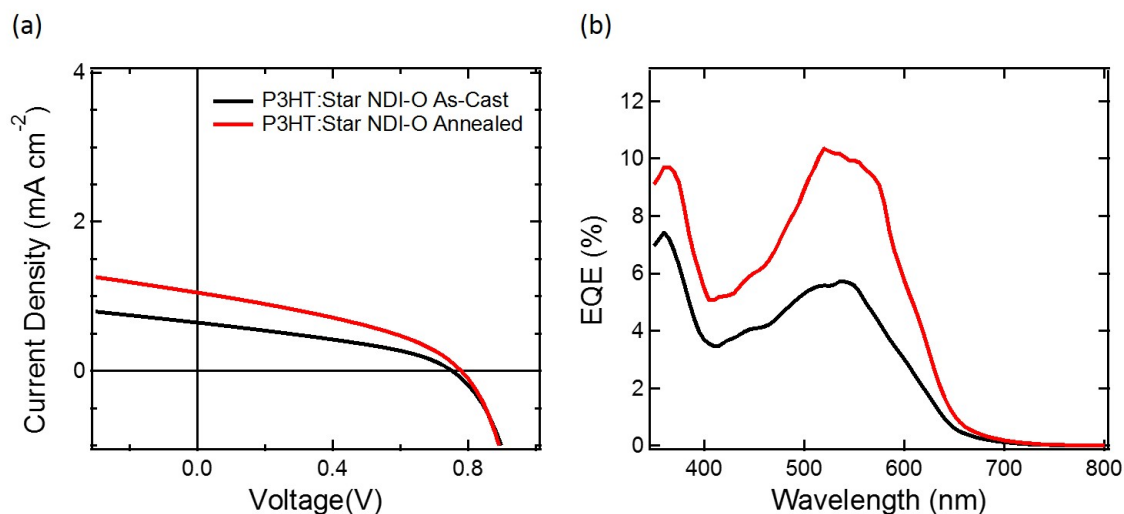


Figure 5.1: As-cast (black lines) and annealed (red lines)  $J-V$  (a) and EQE (B) curves. Although annealing does improve device performance, the use of P3HT as the donor material results in reduced power conversion efficiency, compared to PBDTTT-EFT.

Following the publication of this article in 2017, there were several interesting findings prior to the completion of this thesis. First, some of the highest reported efficiencies for organic solar cells employing NDI-based small molecule acceptors were published using P3HT as the donor material.<sup>2-4</sup> These are discussed in more detail in Chapter 2. Following these new findings, it seemed necessary to explore the device performance for the materials studied in this chapter, paired with P3HT. Due to limited availability of Star NDI-S, the highest-performing of the six acceptors, Star NDI-O was used instead, in inverted OPV devices fabricated from a 1:1.2 by weight ratio of P3HT:Star NDI-O in dichlorobenzene, with a solution concentration of 20 g/L. Following the success of annealing for devices reported in the literature, devices were either characterized as-cast, or annealed at 110 °C for 5 minutes. The  $J-V$  and external quantum efficiency curves for these devices are shown in Figure 5.1 and the device parameters are given in Table 5.1. Although annealing did lead to a doubling in power conversion efficiency observed in these devices, the use of P3HT as the donor material significantly reduced the device performance over those presented in this chapter. This is primarily due to the significantly lower  $J_{SC}$  and slightly lower  $V_{OC}$  values, compared to devices fabricated with PBDTTT-EFT.

Ultimately, this chapter presents six novel acceptors that were designed specifically to improve the performance of NDI-based small molecules in organic solar cells by hindering the formation of large, phase-separated domains and increasing the material's

| Device   | $J_{SC}$<br>(mA cm <sup>-2</sup> ) | $V_{OC}$<br>(V) | FF<br>(%) | PCE<br>(%) | EQE $J_{SC}$<br>(mA cm <sup>-2</sup> ) |
|----------|------------------------------------|-----------------|-----------|------------|--|
| As-Cast  | 0.74                               | 0.75            | 31.5      | 0.17       | 0.68                                   |
| Annealed | 1.19                               | 0.78            | 32.6      | 0.30       | 1.16                                   |

Table 5.1: Solar cell parameters for devices fabricated with P3HT.

conjugation length. Compared to the core-substituted materials explored in Chapter 4, these structural modifications significantly improved the performance of NDI-based small molecule acceptors in organic solar cells, leading to amongst the highest reported efficiencies for this class of acceptor material at the time of initial publication. The following chapter aims to build on this knowledge, by selecting a favorable material structure for thionated NDI molecules, in an effort to improve the performance of the materials studied in Chapter 5.



# References

- [1] J. Jiang, A. Alsam, S. Wang, S. M. Aly, Z. Pan, O. F. Mohammed, and K. S. Schanze, "Effect of conjugation length on photoinduced charge transfer in  $\pi$ -conjugated oligomer-acceptor dyads," *Journal of Physical Chemistry A*, vol. 121, no. 26, pp. 4891–4901, 2017.
- [2] P. S. Rao, A. Gupta, D. Srivani, S. V. Bhosale, A. Bilic, J. Li, W. Xiang, R. A. Evans, and S. V. Bhosale, "An efficient non-fullerene acceptor based on central and peripheral naphthalene diimides," *Chemical Communications*, vol. 54, no. 40, pp. 5062–5065, 2018.
- [3] D. Srivani, A. Gupta, D. D. La, R. S. Bhosale, A. L. Puyad, W. Xiang, J. Li, S. V. Bhosale, and S. V. Bhosale, "Small molecular non-fullerene acceptors based on naphthalenediimide and benzoisoquinoline-dione functionalities for efficient bulk-heterojunction devices," *Dyes and Pigments*, vol. 143, pp. 1–9, 2017.
- [4] D. Srivani, A. Agarwal, S. Bhssale, A. L. Puyad, W. Xiang, R. A. Evans, A. Gupta, and S. Bhosale, "Naphthalene diimide-based non-fullerene acceptors flanked by open-ended and aromatizable acceptor functionalities," *Chemical Communications*, vol. 53, no. 2017, pp. 11157–11160, 2017.



## Chapter 6

# Photovoltaic performance of thionated NDI-based acceptors

Thionation, or the replacement of oxygen for sulfur atoms, of the NDI moiety has previously been shown to influence the optical and electronic properties of naphthalene diimide. For example, the electron mobility in field-effect transistors was shown to vary greatly between molecules with varying degrees of thionation, and that thionation in a 2S-*trans* configuration doubles the electron mobility over the mobility for the parent molecule. This chapter first evaluates the electronic and optical properties of thionated NDI molecules, and how these influence solar cell performance. It is shown that increasing degrees of thionation result in a systematic reduction in the band gap of the molecule, which is further illustrated by a systematic lowering of the absorption onset energy in optical absorption measurements. Solar cells reflect this change with a systematic decrease in the open-circuit voltage with increasing thionation. However, higher degrees of thionation also result in improvements in short-circuit current and fill factor, and higher solar cell efficiencies are observed for the 2S-*trans* NDI molecule compared to the parent molecule, despite a reduction in  $V_{OC}$  from 0.82 V to 0.62 V. However, the overall photovoltaic performance for NDI-based small molecule acceptors is  $\sim 0.4\%$ , and a more suitable molecular architecture was selected in order to improve solar cell performance. Thionation in a 2S-*trans* configuration was therefore explored as a potential strategy to improving the performance of the polymer, PNDIT2, in all-polymer solar cells fabricated with the donor polymer PBDTTT-EFT. Solar cells were fabricated with the original polymer, PNDIT2, as a reference, and an optimized efficiency of 4.85% was achieved. Batches of the thionated analog with increasing ratios of 1S to 2S-*trans* thionation (15:85, 7:93, and 5:95) were studied, which enabled a systematic investigation of the effect thionation has on all-polymer solar cell performance. However, despite the promising results from NDI-based small molecule acceptors, devices with thionated PNDIT2 exhibited a systematic lowering of photovoltaic parameters with increasing thionation, resulting in device efficiencies of just 0.84%, 0.62%, and 0.42% PCE for 1S to 2S conversion ratios of 15:85, 7:93, and 5:95, respectively. The lower performance of the thionated blends is attributed to poor  $\pi - \pi$  stacking order in the thionated PNDIT2 phase, resulting in lower electron mobilities and finer phase separation. Evidence in support of this conclusion is provided by grazing incidence wide-angle X-ray scattering, transmission electron microscopy, photoluminescence quenching, space-charge limited current measurements, and transient photocurrent analysis.

## 6.1 Introduction and Context

Modification of the polymeric or molecular structure by substituent substitution is routinely demonstrated to alter the electronic and morphological properties of organic semiconductors.<sup>1</sup> For PNDIT2, this has recently been shown to offer a method for improving all-polymer solar cell performance, for example, when the sulfur atoms in the bithiophene bridge are replaced with selenium.<sup>2</sup> This selenophene derivative, PDNIBS, when used in conjunction with a donor material whose absorption profile perfectly complimented that of the acceptor polymer, was able to achieve power conversion efficiencies as high as 9.4%. Thionation of rylene diimide-based materials has also been shown to be an attractive strategy for tuning material properties without the need to synthesize a new compound from scratch.<sup>3–7</sup> The replacement of oxygen for sulfur can significantly affect the material’s optical and electronic properties. For example, it has been shown to reduce LUMO energy of the material and increase the HOMO energy, resulting in a systematic lowering of the material’s band gap with thionation.<sup>5,8</sup> Reducing the band gap can thus promote broad-spectrum light absorption, as lower energy photons in the solar spectrum will also be absorbed. In organic solar cells, thionation of the acceptor material has the potential to increase the  $J_{SC}$  for two reasons: (1) smaller band gaps promote additional photon absorption, allowing the acceptor to contribute to the number of excitons generated in the active layer of the solar cell and (2) a larger offset between the LUMO energies for the donor and acceptor will result in an increased driving force for exciton dissociation and charge separation, leading to a higher number of free charge carriers being created following photon absorption.<sup>9,10</sup> However, because the open circuit voltage,  $V_{OC}$ , of the device is dependent on the difference in energy between the donor’s HOMO ( $HOMO_D$ ) and acceptor’s LUMO ( $LUMO_A$ ) levels, a lower  $V_{OC}$  is to be expected with thionation, requiring the additional current generation to outweigh the energy loss due to a lower  $HOMO_D - LUMO_A$  offset. Nevertheless, other strategies such as acceptor fluorination have resulted in higher overall PCE despite a lowering of  $V_{OC}$  due to improvements in fill factor and  $J_{SC}$ .<sup>11</sup> All-polymer solar cells also, in general, exhibit lower fill factors than fullerene-based cells, so exploring different strategies to boost cell FF is of interest.

With regards to thionated NDI-based molecules, Welford et al.<sup>5</sup> showed that thionation of an NDI molecule systematically lowers the optical absorption onset, with the unthionated parent molecule exhibiting no absorption in the visible energy range, while the fully thionated NDI-4S molecule demonstrated an absorption onset at as low as 2.0 eV (620 nm). Additionally, in organic field-effect transistors (OFETs), improved electron mobilities were observed when using the thionated derivatives of the parent molecule, although these were not systematic, with the molecules that had two or three sulfur atoms outperforming the NDI-1S and NDI-4S molecules with 1 and 4 oxygen substitutions, respectively. The largest improvement was observed in the NDI 2S-*trans* and NDI 3S molecules, with electron mobilities of  $1.8 \times 10^{-1} \text{ cm}^2/\text{Vs}$  and  $1.2 \times 10^{-1} \text{ cm}^2/\text{Vs}$ , respectively – more than double that measured for the parent molecule, which exhibited an electron mobility of  $0.68 \times 10^{-1} \text{ cm}^2/\text{Vs}$ . These results indicate thionation could be a potential strategy to improve the performance of NDI-based acceptors for organic solar cells through tuning the band gap and improving charge carrier mobility. Here, the effects of thionation on both small molecule as well as polymeric NDI-based acceptors are explored, however focus is placed on the thionation of the NDI-based

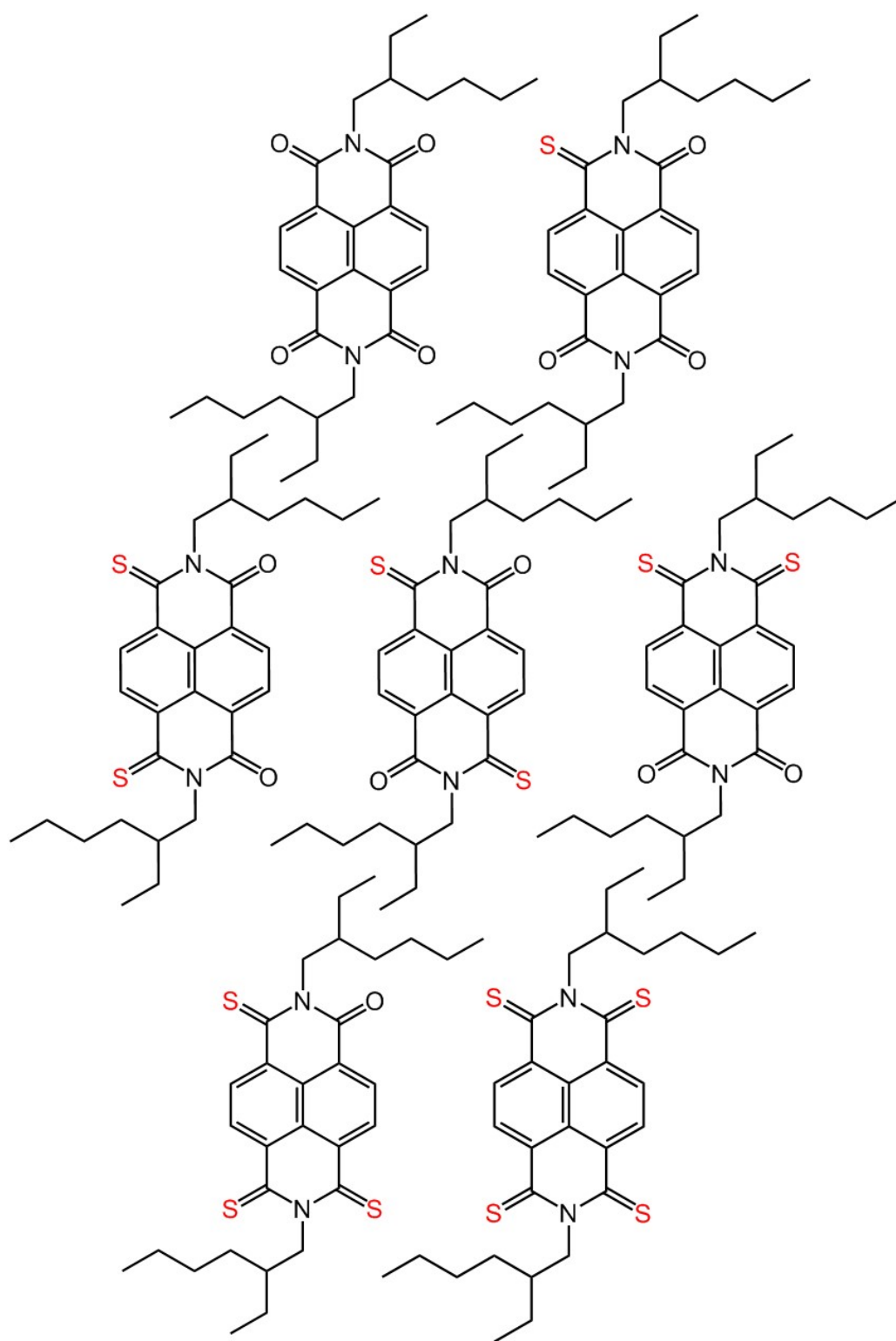


Figure 6.1: Molecular structures of the series of NDI-based small molecules with increasing degree of thionation. The parent, 1S, 2S-*trans*, and 3S molecules were used as small molecule acceptors in Chapter 4, and the effect thionation has on the NEXAFS spectra of all the materials shown was studied in Chapter 7.



acceptor polymer PNDIT2, which has been shown to exhibit exceptional performance in organic electronic applications, demonstrating amongst the highest mobilities in n-type OFETs and enabling all-polymer solar cell efficiencies approaching 10%.<sup>12,13</sup> Three different ratios of 2S-*trans*:1S thionation in polymeric form are used: 85:15, 93:7 and 95:5. The degree of thionation for each polymer is denoted by the percentage of 2S-*trans* (i.e. the polymer containing a 2S-*trans* to 1S ratio of 85:15 is termed 2S-*trans*-PNDIT2-85%). (Note that due to synthetic limitations it is not possible to produce pure, 2S-*trans*-PNDIT2 with 100% 2S units.<sup>14</sup>) It is shown, however, that thionation reduces the photovoltaic efficiency for all-polymer solar cells, compared to PBDTTT-EFT:PNDIT2 blends. The reduction in efficiency stems primarily from systematic decreases in open circuit voltage and short circuit current. The  $V_{OC}$  reduction is a result of the reduced  $HOMO_D - LUMO_A$  offset following thionation, and the  $J_{SC}$  reduction stems from a suppressed  $\pi - \pi$  stacking order in the thionated materials compared to PNDIT2, which prevents efficient electron extraction in the acceptor, and gives rise to severe electron trapping (low electron mobility). Suppressed  $\pi - \pi$  stacking in the thionated polymer also leads to finer phase separation hindering charge separation and extraction.

## 6.2 Experimental Details

### 6.2.1 Materials

The donor polymer, PBDTTT-EFT, commercial name PCE-10, was purchased from 1-Material and was employed for all devices reported in this chapter and used as received. The synthesis of the NDI-based small molecule acceptors has been reported previously.<sup>5</sup> The reference acceptor polymer, PNDIT2, was purchased from Raynergy Tek and used as received. Three samples of the thionated analog to PNDIT2 were used,<sup>14</sup> composed of different ratios of 2S-*trans* to 1S: 85:15 (85%), 93:7 (93%), and 95:5 (95%). Details of the preparation of these thionated polymers can be found elsewhere.<sup>14</sup>

### 6.2.2 Solar Cell Fabrication

All organic solar cells reported in this chapter were fabricated using a 1:1 weight ratio of donor to acceptor using chlorobenzene as the solvent. The following inverted device architecture led to the highest performing solar cells: ITO/PEIE/Active Layer/ $MoO_x$ /Ag, with the solution used for spin-coating the active layer having a concentration of 15 g/l for PBDTTT-EFT:PNDIT2 blends and 30 g/l for PBDTTT-EFT:thionated acceptor and PBDTTT-EFT:small molecule acceptor blends (due to very thin films and low current values for devices cast from a 15 g/l solution). All active layers were deposited at 6000 RPM, resulting in active layer thicknesses of approximately 110 nm for all devices. Following active layer deposition, 12 nm of  $MoO_x$  (0.3 Å/s) and 100 nm of Ag (1 Å/s) were vacuum deposited below  $9 \times 10^{-7}$  torr using an Angstrom Engineering Covap evaporator. Devices were attached with edge clips and encapsulated prior to being removed from the nitrogen atmosphere for characterization. All solvents pertaining to solar cell fabrication were purchased from Sigma-Aldrich and used as received.

### 6.2.3 Optoelectronic Properties Measurements

UV-visible-NIR absorption was measured using a Perkin Elmer Lambda 950 Spectrometer for NDI-based molecular acceptors from 350 – 900 nm, and a 1050 Spectrometer for thionated PNDIT2 acceptors, with the integrating sphere attachment, from 300 – 1500 nm. For the neat UV-Visible absorption spectra for thionated PNDIT2 acceptors, absorption is expressed as an absorption coefficient,  $\alpha$ . Blend films from active layer solutions were deposited onto fused silica glass slides using the optimum device conditions, described under solar cell fabrication. Photoelectron spectroscopy in air (PESA) measurements were performed using a Riken Keiki AC-2 spectrometer. For all samples a power intensity of 5 nW was used.

### 6.2.4 Photoluminescence Quenching

Photoluminescence spectra were obtained using an Ocean Optics spectrometer (FLAME-S-VIS-NIR-ES) coupled to an integrating sphere (Horiba Quanta-phi). A 520 nm diode laser (Thorlabs) was used for excitation with samples coated onto fused silica substrates.

### 6.2.5 Space-charge limited current devices

Space charge limited current devices utilizing both the PBDTTT-EFT:acceptor blend films as well as neat films for the acceptors explored in this chapter were made with the following device structure: ITO/PEDOT:PSS/Al/Active Layer/Ca/Al.<sup>15</sup> The same patterned ITO substrates used for solar cells were used for all SCLC devices, following the same cleaning method. High conductivity grade PEDOT:PSS solution was purchased from Sigma Aldrich and spin-cast as received at 5000 RPM prior to curing at 130 °C for 30 minutes. Aluminum was subsequently vacuum evaporated at a rate of 1 Å/s to form a 35 nm thick layer prior to either the blend or neat active layer films being spin cast at 6000 RPM. 20 nm of Ca at 0.5 Å/s and 80 nm of Al at 1 Å/s were evaporated next, to complete devices, which were fitted with edge clips and encapsulated by epoxy and glass prior to characterization. Mobility values were extracted from the current density-voltage plots using the Murgatroyd equation.

## 6.3 Results and Discussion

The results and discussion section in this chapter is separated in to two parts: the first explores the effect of thionation on the performance of NDI-based small molecule acceptors, while the second explores how thionation impacts the performance of PNDIT2 in all-polymer solar cells.

### 6.3.1 Thionated NDI-based Small Molecule Acceptors

The synthesis and OFET performance of the series of systematically thionated NDI molecules presented in this chapter, shown in Figure 6.1, has previously been reported.<sup>5</sup> The HOMO and LUMO values, estimated with cyclic voltammetry, are presented in the energy diagram in Figure 6.2.<sup>5</sup> It shows that increasing the degree of thionation systematically narrows the band gap of the material by both increasing the HOMO

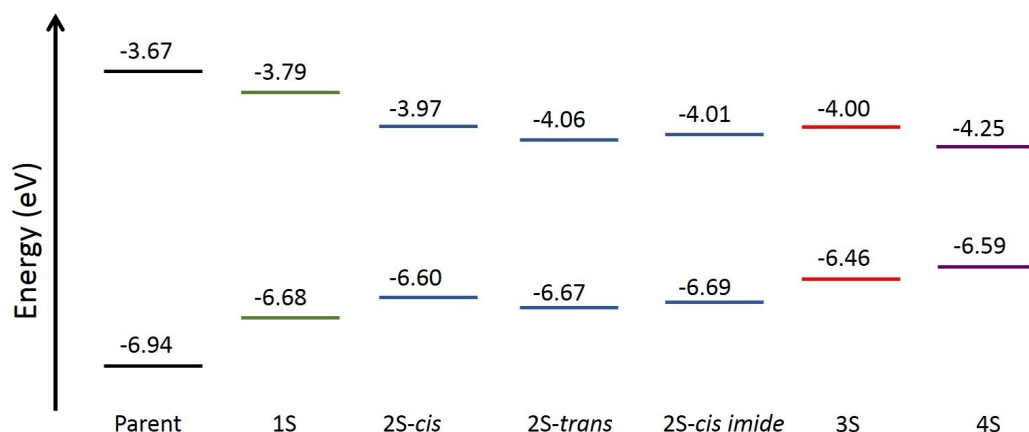


Figure 6.2: Energy diagram showing the change in HOMO and LUMO energy levels with increasing thionation of the NDI moiety.<sup>5</sup>

and decreasing the LUMO energy. This is exemplified for a selection of the thionated materials, shown in Figure 6.3 (a), which gives the normalized UV-visible absorption spectra of thin films spin cast from chlorobenzene.

In order to quantify how the energetics affect solar cell performance, devices were fabricated utilizing PBDTTT-EFT as the donor material. OPV device data for a selection of thionated molecules (the parent, 1S, 2S-*trans*, and 3S, chosen because of their availability and performance in OFET devices) is shown in Figure 6.4, which provides  $J - V$  and external quantum efficiency curves. The  $J - V$  curves indicate systematic changes in solar cell performance with increasing thionation. For example, the devices'  $V_{OC}$  is systematically reduced with increasing thionation, which is in line with predictions made in Chapter 2 about the relationship between the donor material's HOMO and the acceptor material's LUMO: namely that the  $HOMO_{donor} - LUMO_{acceptor}$  energy offset dictates the maximum possible device  $V_{OC}$ . It is therefore

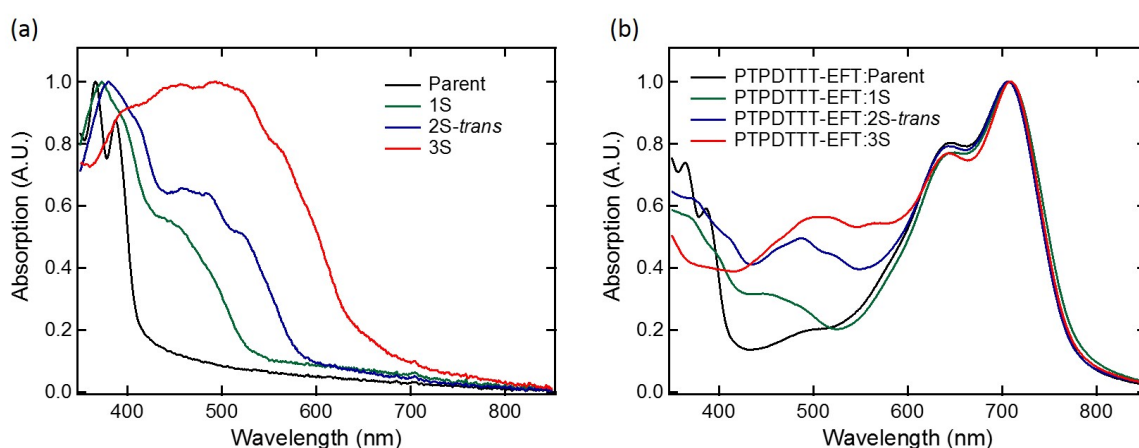


Figure 6.3: Normalized neat (a) and blend (b) UV-visible absorption spectra for thin films cast from chlorobenzene. Increasing thionation results in a narrowing of the material's band gap, illustrated by the increase in absorption onset wavelength with increasing thionation. Similarly, the blend films, with PBDTTT-EFT, show increased absorption of visible wavelengths with increasing thionation.

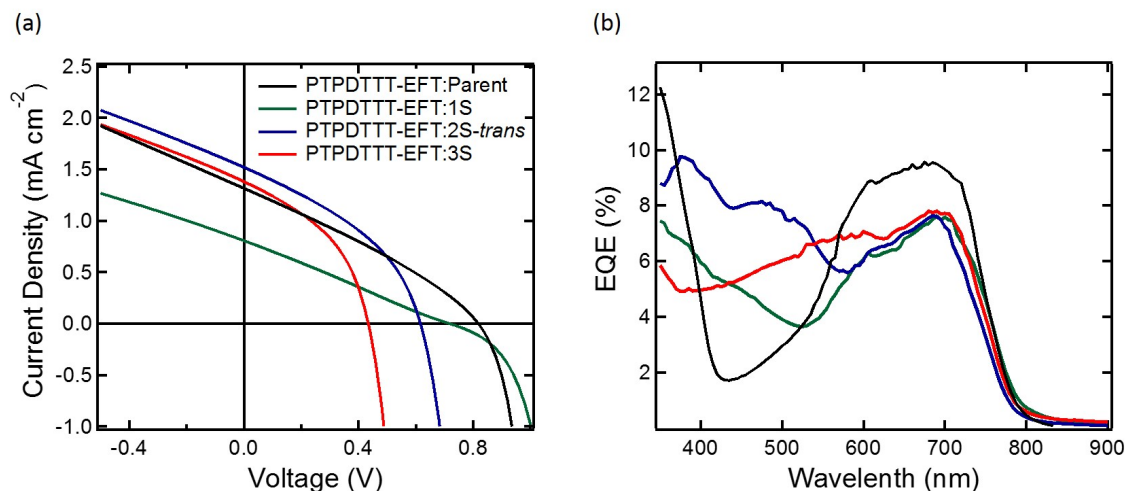


Figure 6.4: Solar cell data for a selection of molecules from the series. The data indicate that increasing the degree of thionation systematically lowers the  $V_{OC}$ , in line with the reduced  $HOMO_D - LUMO_A$  offset resulting from the decreased LUMO energy level with observed following thionation

logical, given the energy diagram shown in Figure 6.2, that the device  $V_{OC}$  decreases with increasing thionation. However, due to the narrowing of the band gap with thionation, it is possible to compensate for the loss in  $V_{OC}$  by increasing the  $J_{SC}$ . This is potentially possible due to the narrowing of the NDI-based material’s band gap as thionation is increased. Figure 6.3 (b) illustrates that PBDTTT-EFT blended with 2S-*trans* and 3S, for example, results in broader absorption of visible wavelengths, compared to PBDTTT-EFT blended with the Parent or 1S materials. Indeed, the external quantum efficiency curves, pictured in Figure 6.4 (b), demonstrate broader absorption across the visible wavelength spectrum with increasing thionation.

Further, there appears to be a “sweet spot” of two sulfur atoms, which results in maximum power conversion efficiency in organic solar cells. Despite a lower  $V_{OC}$ , compared to the parent molecule, the 2S-*trans* acceptor increases the  $J_{SC}$  and fill factor sufficiently in order to exhibit the highest PCE of 0.36%, compared to 0.33% for the parent. Another systematic change in performance is reflected in the devices’ fill factor. Which, following an initial decrease between the parent and 1S molecules, increases with increasing thionation, up to 40.1% for 3S, compared to 30.5% for the Parent. The fill factor has been related to many factors, with the efficiency of charge separation being one of them. Thus thionation could be a strategy to boost the charge separation efficiency in NDI-based acceptors resulting from a deeper LUMO.

| Acceptor         | $J_{SC}$<br>(mA cm <sup>-2</sup> ) | $V_{OC}$<br>(V) | FF<br>(%) | PCE<br>(%) | EQE $J_{SC}$<br>(mA cm <sup>-2</sup> ) |
|------------------|------------------------------------|-----------------|-----------|------------|--|
| Parent           | 1.32                               | 0.82            | 30.5      | 0.33       | 1.68                                   |
| 1S               | 0.81                               | 0.72            | 25.1      | 0.15       | 1.3                                    |
| 2S- <i>trans</i> | 1.51                               | 0.62            | 38.5      | 0.36       | 1.69                                   |
| 3S               | 1.39                               | 0.44            | 40.1      | 0.25       | 1.92                                   |

Table 6.1: Solar cell parameters for devices fabricated from the thionated NDI molecules, paired with PBDTTT-EFT.

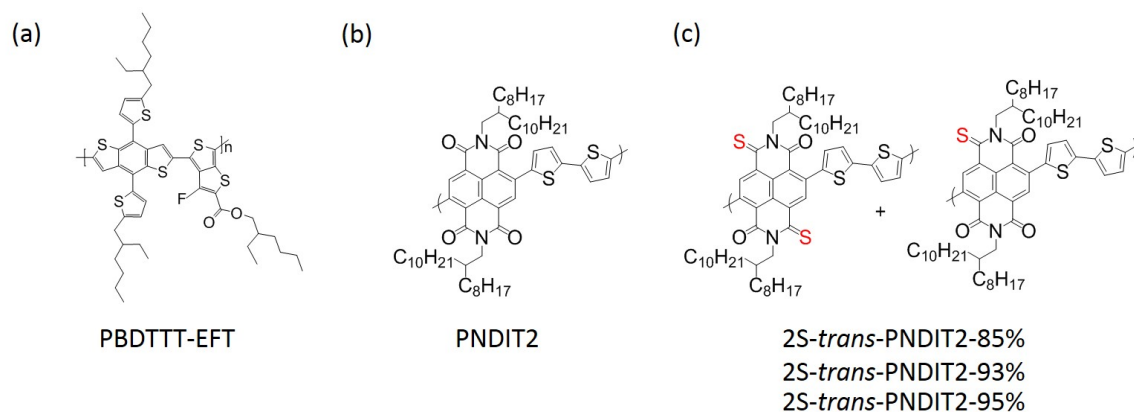


Figure 6.5: Molecular structures for PBDTTT-EFT (a), PNDIT2 (b), and 2S-*trans*-PNDIT2 (c), with three ratios of 2S-*trans* to 1S: 85:15 (85%), 93:7 (93%), and 95:5 (95%).

Although power conversion efficiencies for these NDI-based small molecule acceptors remains low (most likely due to the strong aggregation and unfavorable active layer morphology formed by the NDI molecule), the systematic changes in electronic structure, which lead to notable difference in organic solar cell performance, warrant further investigation of the thionated NDI motif in expanded molecular geometries. Therefore, following the promising OPV results for the 2S-*trans* thionated NDI molecule, it was attempted to synthesize a star-shaped material (following the star-shaped geometry from Chapter 5) that incorporated 2S-*trans* thionated NDI molecules. However, the yield of this synthesis was extremely low, as well as the material being unstable in ambient conditions. It was therefore not possible to further explore whether the use of a more complex, star-shaped molecular structure could also improve the performance of thionated NDI molecules.

### 6.3.2 Effect of Thionation on PNDIT2

In this section, the effect of thionation on the performance of all-polymer solar cells by increasing the degree of thionation across three PNDIT2 analogs is investigated. Polymer-analogous 2S-*trans* thionation was used partly due to synthetic restrictions<sup>14</sup> and because 2S-*trans* small molecule derivatives have shown good performance in OFETs,<sup>5</sup> as well as the promising results from the previous section. Figure 6.5 shows the molecular structures of the polymers studied in this work. PBDTTT-EFT is used as the donor polymer and PNDIT2 is used as the non-thionated reference acceptor polymer. The series of thionated polymers utilizes increasing ratios of 2S-*trans* to 1S: 85% is 85:15, 93% is 93:7 and 95% is 95:5 2S-*trans* to 1S.

The thin-film optical absorption profiles of the materials are shown in Figure 6.6, with thionation resulting in a reduction of the photon absorption onset energy due to a reduction in band gap with thionation.<sup>5,7,8</sup> This reduction in band gap is mostly due to a reduction in the LUMO energy of the polymer with thionation, though a modest increase in HOMO energy is also seen. Table 6.2 summarizes the previously published<sup>14,16</sup> electrochemically-determined band gap and LUMO values for the thionated materials, as well as optical band gaps based on the absorption profiles in Figure 6.6. HOMO values for all polymers are also reported in Table 6.2, which were measured

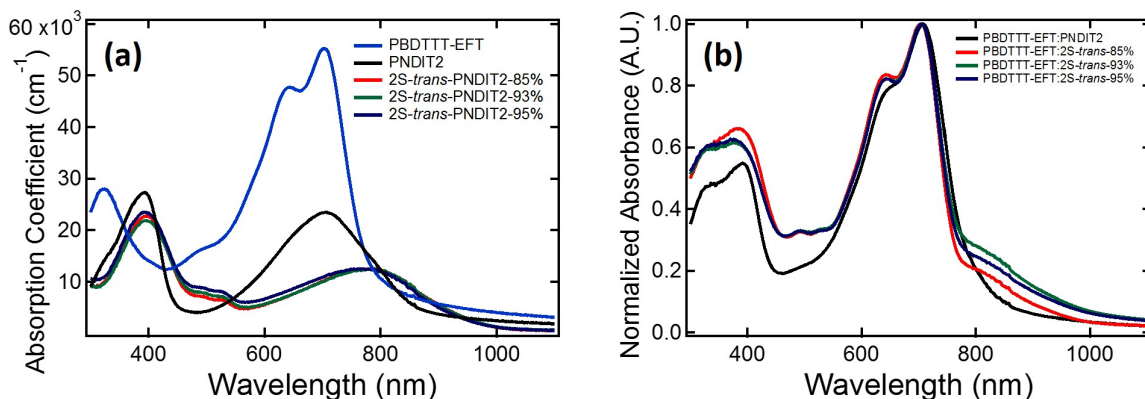


Figure 6.6: Absorption spectra for the neat materials, expressed as absorption coefficient (a) and normalized 1:1 blend (b) materials used in organic solar cells. The shift in absorption onset following thionation can clearly be seen in both the neat and blend films.

on fresh samples with PESA, at the same time. In the absorption spectra of the neat materials (Figure 6.6(a)), a strong shift in the absorption onset wavelength is observed, from 882 nm for PNDIT2 to  $\sim 970$  nm for the thionated derivatives. This corresponds to a reduction in the optical band gap of 0.13 eV, from 1.41 eV for PNDIT2 to 1.28 eV for the thionated versions. Although a lower optical band gap enables more visible photons to be absorbed by the active layer in an organic solar cell, and the reduction of the acceptor's LUMO induces a larger driving force for exciton dissociation, the reduction in  $\text{LUMO}_A$  also has the potential to reduce the devices' open-circuit voltage. Apart from lowering the band gap of the material which improves absorption beyond 800 nm, thionation also results in increased absorption between 450 – 550 nm.

In order to determine the effect of thionation on the performance of all-polymer solar cells, devices employing PNDIT2 in conjunction with the donor polymer, PBDTTT-EFT, were made as a reference. Additionally, devices using the series of thionated PNDIT2 analogs with increasing 2S-*trans* concentration were fabricated to determine the effect that increasing the proportion of 2S-*trans* thionation has on the performance. The  $J - V$  and EQE characteristics for each material fabricated with PBDTTT-EFT are shown in Figure 6.7. A summary of the  $J - V$  characteristics are given in Table 6.3. The commercially available PNDIT2 that was used for reference devices has a molecular weight of  $M_n = 77$  kDa, compared to  $M_n = 12$  kDa of the thionated

| Material                     | $E_g^{14}$<br>(eV) | Abs. Onset<br>(nm) | $E_g^{opt}$<br>(eV) | HOMO<br>(eV) | LUMO<br>(eV)       |
|------------------------------|--------------------|--------------------|---------------------|--------------|--------------------|
| PBDTTT-EFT                   | -                  | 786                | 1.58                | -5.03        | -3.6 <sup>17</sup> |
| PNDIT2                       | 1.68               | 882                | 1.41                | -5.79        | -3.7 <sup>14</sup> |
| 2S- <i>trans</i> -PNDIT2-85% | 1.49               | 971                | 1.28                | -5.75        | -4.0 <sup>14</sup> |
| 2S- <i>trans</i> -PNDIT2-93% | 1.48               | 966                | 1.28                | -5.71        | -4.0 <sup>14</sup> |
| 2S- <i>trans</i> -PNDIT2-95% | 1.49               | 970                | 1.28                | -5.69        | -4.0 <sup>14</sup> |

Table 6.2: Optoelectronic properties of the materials. Electrochemical estimates of the band gap and LUMO energy levels have been determined previously.<sup>14</sup> HOMO values were determined using PESA.



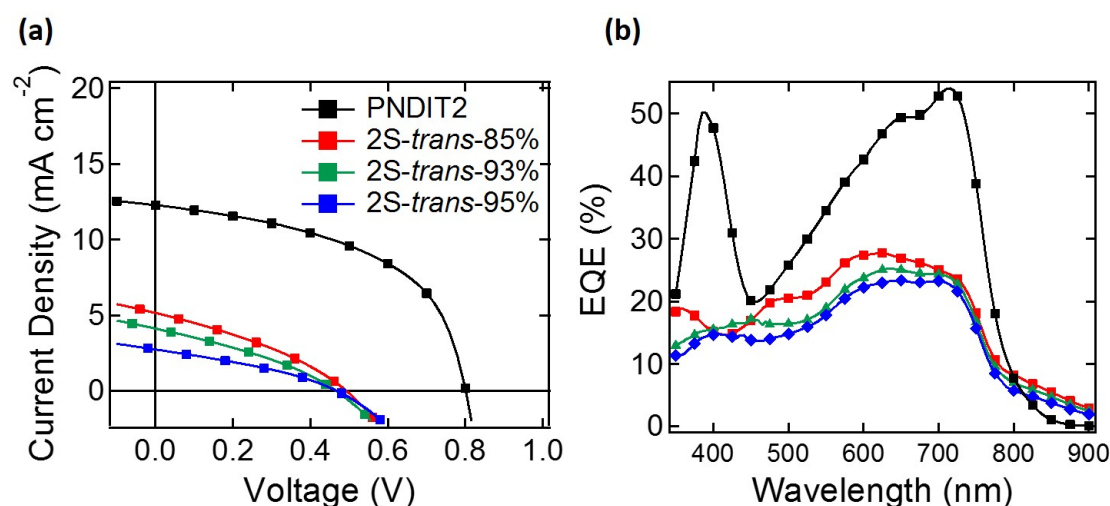


Figure 6.7: (a) Current-voltage characteristics for solar cells fabricated with PNDIT2, and its thionated derivatives, as the acceptor and with PBDTTT-EFT used as donor. (b) Corresponding external quantum efficiency curves. The response for thionated acceptors above 800 nm indicates that both the donor and acceptor contribute to current produced by the devices.

analogues. Devices utilizing a low molecular weight version of PNDIT2 ( $M_n = 9.4$  kDa) were also fabricated, and these results are available in Appendix C. As anticipated, it can be seen that thionation of the PNDIT2 material reduces the solar cell's  $V_{OC}$ . The optimized PBDTTT-EFT:PNDIT2 device exhibits a  $V_{OC}$  of 0.80 V, while the thionated materials result in devices with  $V_{OC}$  values of 0.49 V, 0.47 V, and 0.47 V, for 2S-*trans*-PNDIT2-85%, 2S-*trans*-PNDIT2-93%, and 2S-*trans*-PNDIT2-95%, respectively, illustrating a decrease in  $V_{OC}$  with increasing degree of thionation. This reduction in  $V_{OC}$  is roughly in line with the previously published changes in LUMO energy with thionation, where a reduction of the polymer's LUMO energy level from -3.7 eV for PNDIT2 to -4.0 eV for the thionated analogues was observed.<sup>14</sup> However, thionation also systematically reduces the devices' short circuit current,  $J_{SC}$ , and dramatically reduces the FF, contrary to the results presented in the previous section, for small molecule-based acceptors. In particular, the  $J_{SC}$  of the thionated materials is systematically lowered to 5.2 mA cm<sup>-2</sup>, 4.1 mA cm<sup>-2</sup>, and 2.7 mA cm<sup>-2</sup> for 2S-*trans*-PNDIT2-85%, 2S-*trans*-PNDIT2-93%, and 2S-*trans*-PNDIT2-95%, respectively, compared to 11.9 mA cm<sup>-2</sup> for the reference polymer. Finally, the fill factor for the thionated polymers is dramatically decreased, from over 50% in PNDIT2 to less than 35% for all three thionated derivatives. Overall, thionation of the PNDIT2 polymer systematically reduces the power conversion efficiency of organic solar cells from 4.85% to 0.84%, 0.62%, and 0.42% for 2S-*trans*-PNDIT2-85%, 2S-*trans*-PNDIT2-93%, and 2S-*trans*-PNDIT2-95%, respectively. Although devices made with the low molecular weight PNDIT2 sample showed lower performance compared to devices made from with the high molecular weight PNDIT2 (Figure C.1), the fill factor,  $J_{SC}$  and  $V_{OC}$  were all still superior to the best thionated cells. Thus, apart from molecular weight, the thionation of PNDIT2 dramatically reduces the performance of all-polymer solar cells.

External quantum efficiency curves are shown in Figure 6.7 (b), which illustrate

| Acceptor                   | $J_{SC}$<br>(mA cm <sup>-2</sup> ) | $V_{OC}$<br>(V) | FF<br>(%) | PCE<br>(%)  | EQE $J_{SC}$<br>(mA cm <sup>-2</sup> ) |
|----------------------------|------------------------------------|-----------------|-----------|-------------|--|
| <b>PNDIT2</b>              | 11.9 ± 0.3                         | 0.80 ± 0.01     | 51 ± 1    | 4.85 ± 0.17 | 10.1                                   |
| <b>2S-<i>trans</i>-85%</b> | 5.2 ± 0.2                          | 0.49 ± 0.01     | 33 ± 1    | 0.84 ± 0.04 | 6.1                                    |
| <b>2S-<i>trans</i>-93%</b> | 4.1 ± 0.5                          | 0.47 ± 0.02     | 33 ± 1    | 0.62 ± 0.06 | 5.5                                    |
| <b>2S-<i>trans</i>-95%</b> | 2.3 ± 0.2                          | 0.47 ± 0.01     | 33 ± 1    | 0.42 ± 0.02 | 5.0                                    |

Table 6.3:  $J - V$  characteristics for solar cells fabricated from PNDIT2, including its optimized processing conditions and those optimized for the thionated polymers, as well as characteristics for the thionated derivatives.

that the thionation of PNDIT2 dramatically reduces the number of extracted charge carriers broadly across the visible spectrum, apart from a slight increase for wavelengths above 800 nm, where the 2S-*trans* polymers absorb light that contributes to the current produced by the solar cells. This is indicative of significantly increased recombination in the thionated blends, further illustrated by the large decrease in fill factor compared to PNDIT2 devices. The EQE spectra were integrated over the measured wavelength range in order to estimate the short circuit current density, the values of which are given in Table 6.3. Interestingly, the estimated  $J_{SC}$  for devices fabricated from the thionated polymers is higher than that measured in the  $J - V$  curve, while the estimated  $J_{SC}$  for PNDIT2 devices is lower than the  $J_{SC}$  value extracted from the  $J - V$  curve. An overestimation in  $J_{SC}$  from the  $J - V$  curve is possible due to edge effects, as the surrounding area of a device pixel is also illuminated by the solar simulator, and charges generated there can be extracted, although not originating from the defined active area of the device. An underestimation reflects increased recombination under solar simulator illumination compared to the lower light intensities used for EQE measurement, confirmed by intensity dependent measurements presented below.

Further analysis into the active layer morphology was performed in order to explain the large discrepancy in performance between PNDIT2 and the thionated polymers. The dramatic reduction in  $J_{SC}$  and fill factor indicate increased recombination in the active layer, which could be linked to the size and degree of crystallinity within the donor and acceptor-rich domains. Another explanation for the low  $J_{SC}$  could be that the thionated polymers form large domains throughout the active layer, unfavorable for exciton dissociation. Atomic force microscopy (AFM), Figure 6.8 and Figure C.2, transmission electron microscopy (TEM), Figure 6.9, and near-edge X-ray absorption fine structure (NEXAFS) spectroscopy (Figure C.4) were used to compare the surface and bulk morphologies of the polymer blends. Samples for AFM and NEXAFS experiments were prepared under the optimized device processing conditions while slightly thinner blends were used for TEM analysis. The AFM images for blends in Figure 6.8 show similar surface topographies, with a relatively smooth surface characterized by a fibrillary morphology. This fibrillar morphology is characteristic of PNDIT2<sup>18</sup> with the surface of blends with PBDTTT-EFT known to be PNDIT2-rich.<sup>19</sup> Thionation of the acceptor material appears to maintain this fibrillar morphology, however it is less pronounced. AFM images of neat PNDIT2 and neat thionated samples confirm a suppressed fibrillar order in the thionated samples, see Appendix C. A slight increase in surface roughness is also seen with thionation with the root-mean-square (RMS) roughness increasing from 0.67 nm for the PNDIT2 blend to 1.06 nm, 0.93 nm, and 1.00 nm for the 2S-*trans*-PNDIT2-85%, 2S-*trans*-PNDIT2-



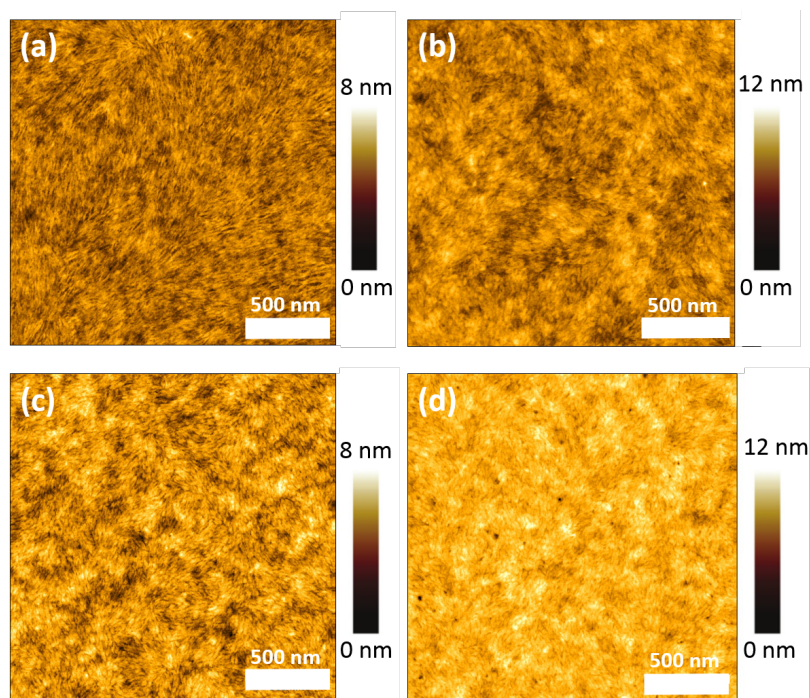


Figure 6.8: AFM images of PBDTTT-EFT:PNDIT2 (a), PBDTTT-EFT:2S-*trans*-PNDIT2-85% (b), PBDTTT-EFT:2S-*trans*-PNDIT2-93% (c), and PBDTTT-EFT:2S-*trans*-PNDIT2-95% (d). RMS roughness values are 0.67 nm, 1.06 nm, 0.93 nm, and 1.00 nm, respectively.

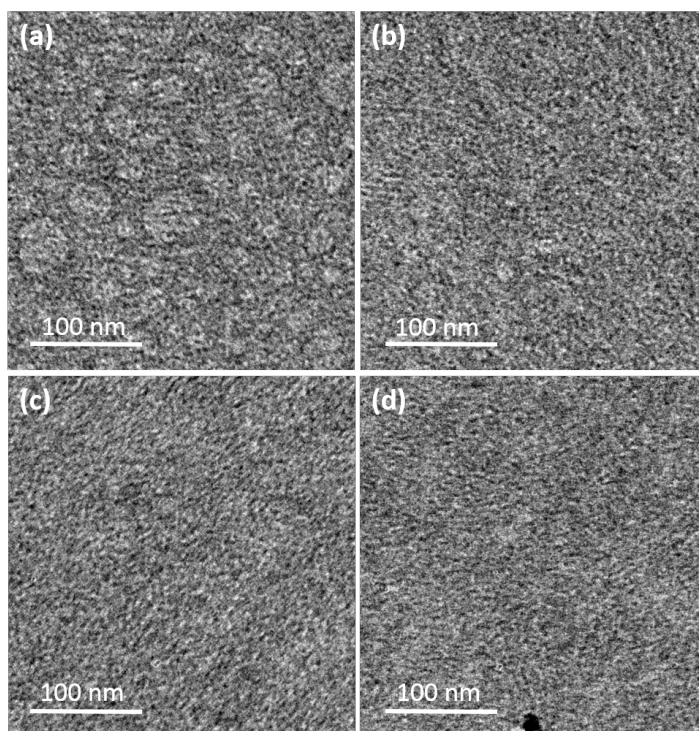


Figure 6.9: TEM images of PBDTTT-EFT:PNDIT2 (a), PBDTTT-EFT:2S-*trans*-PNDIT2-85% (b), PBDTTT-EFT:2S-*trans*-PNDIT2-93% (c), and PBDTTT-EFT:2S-*trans*-PNDIT2-95% (d).

93%, and 2S-*trans*-PNDIT2-95% blends, respectively. In any case, the AFM images of the thionated blends show a lack of coarse phase segregation with the thionated blends appearing to be relatively intermixed.

Surface-sensitive NEXAFS spectroscopy was performed to determine the surface chemical composition of the blends, see Figures C.3 and C.4. Analysis of the blend films indicates that there are differences in the surface composition of the PNDIT2 blend and its thionated analogs. The analysis shown in Figure C.4, which is based on the NEXAFS spectra for the neat materials shown in Figure C.3, indicates that the surface chemical composition of the blend PBDTTT-EFT:PNDIT2 films is comprised of 81 weight% PNDIT2, consistent with previous studies and AFM image analysis.<sup>19</sup> However, similar analysis for the blends containing thionated polymers shows a reduction in acceptor content at the blend surface. With thionation, the acceptor content is found to decrease to 67 weight% for PBDTTT-EFT:2S-*trans*-PNDIT2-85%, 67 weight% for PBDTTT-EFT:2S-*trans*-PNDIT2-93%, and 64 weight% for PBDTTT-EFT:2S-*trans*-PNDIT2-95%. The reduced surface segregation of the thionated polymers suggests a weaker driving force for phase separation between the PBDTTT-EFT and 2S-*trans*-PNDIT2, compared to blends with PNDIT2. Since a certain degree of vertical phase separation can be favorable for charge collection at the electrodes, the reduced weight% concentration of the 2S-*trans*-PNDIT2 at the surface of the blend films could have a negative impact on charge extraction in a the device.

The morphology of the blends is next investigated with TEM (Figure 6.9). The PBDTTT-EFT:PNDIT2 blend exhibits circular domains with a diameter of  $\sim 40 - 50$  nm. The thionated polymers, on the other hand, do not display such circular structures, but instead show a fibrillar morphology consistent with that observed in AFM images. The TEM images of the thionated samples also suggest a finer intermixing of donor and acceptor. Photoluminescence (PL) quenching measurements (Figure 6.10) show that all blends are efficient at quenching PL from the donor polymer consistent with nanoscale intermixing. (Note that while PL from the acceptor is weak and the quenching of excitons via hole transfer was not able to be quantified, there is little change in the HOMO values with thionation, at most 0.1 eV. Given the large offset in HOMO values between PBDTTT-EFT and PNDIT2, inefficient hole transfer is not likely to be an issue.) Some residual PL from PBDTTT-EFT is evident in the PBDTTT-EFT:PNDIT2 blend (PL quenching of  $\sim 98\%$ ), while PL appears to be completely quenched in the thionated blends (PL quenching  $> 99\%$ ). These differences in PL quenching are consistent with the TEM measurements which indicate a fine nanoscale morphology but with slightly larger phase separation for the PBDTTT-EFT:PNDIT2 blend. This morphology analysis suggests that upon thionation, the acceptor polymer becomes more miscible with the donor polymer. The finer intermixing in the thionated samples could be problematic for the charge separation and collection of charges from the donor/acceptor interface which is explored further below.

Grazing incidence wide-angle x-ray scattering (GIWAXS) was used in order to quantify the degree and orientation of molecular packing and aggregation in neat and blend films for the series of thionated polymers. These 2D images, as well as those for neat films of PNDIT2, are shown in Figure 6.11. PNDIT2 is a well-studied, high-mobility polymer used both in OPV and OFET research, and the GIWAXS patterns of neat films and in blends with different polymeric donor systems have been studied in depth.<sup>18, 20, 21</sup> For example, the high mobility observed in PNDIT2 has been attributed

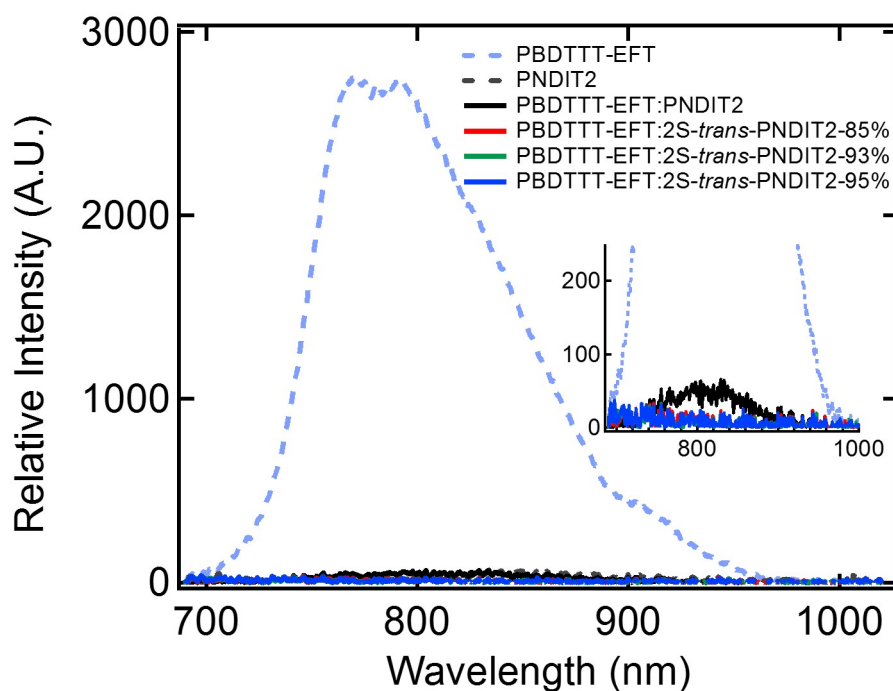


Figure 6.10: Photoluminescence spectra for neat PBDTTT-EFT and PNDIT2 films, as well as PBDTTT-EFT blended with PNDIT2, 2S-*trans*-PNDIT2-85%, 2S-*trans*-PNDIT2-93%, and 2S-*trans*-PNDIT2-95%. All four acceptor materials effectively quench the photoluminescence from PBDTTT-EFT, however the thionated PNDIT2 analogs do so to a larger degree. A 525 nm LED was used as the excitation wavelength.

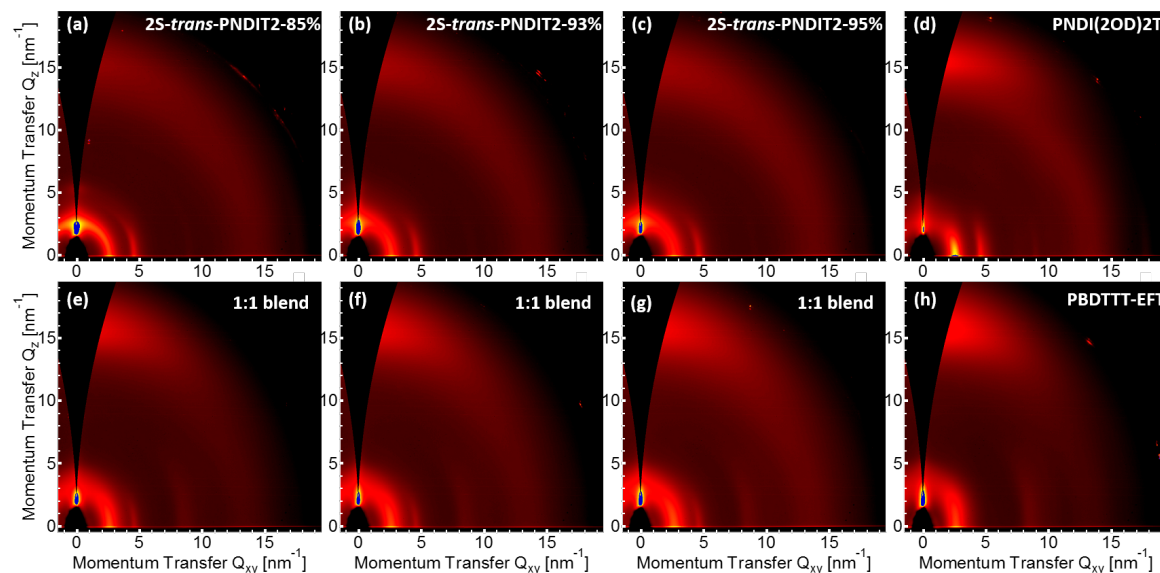


Figure 6.11: 2D GIWAXS images of neat acceptor films (a-d) are shown in the top row, while the corresponding blend films of PBDTTT-EFT with the thionated acceptors (e-h) are shown in the bottom row. The 2D image for neat PBDTTT-EFT is given in Appendix C. The reduced  $\pi - \pi$  stacking intensity in the  $Q_z$  direction between PNDIT2 and the thionated analogs is clearly visible.

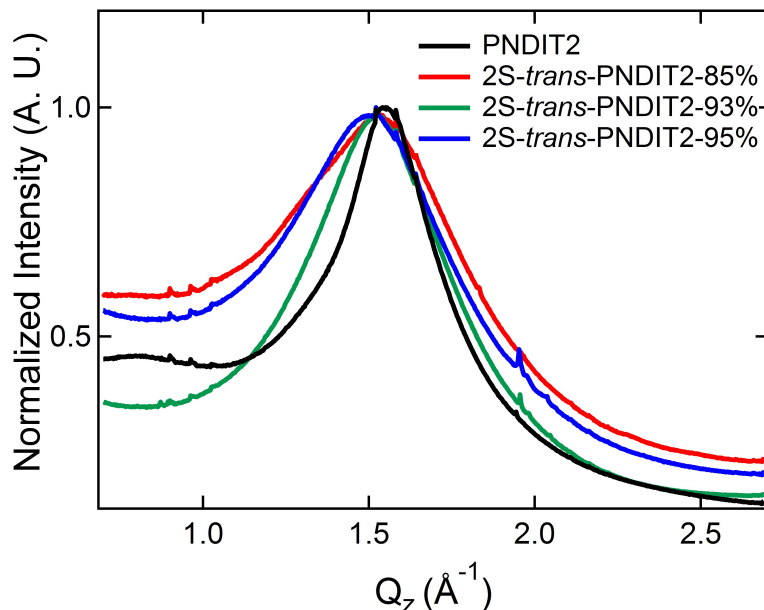


Figure 6.12: GIWAXS scattering profiles along the  $Q_z$  direction. A broadening of the (010) peak is clearly seen after thionation. The y-axis has been normalized to the (010) peak intensity to correct for variances in film thickness between samples deposited from different solution concentrations. The artifacts present at  $\sim 0.8 \text{ \AA}^{-1}$  and  $\sim 1.8 \text{ \AA}^{-1}$  are a due to imperfections in the stitching of the 2D images.

to strong aggregation in the  $\pi - \pi$  stacking direction, coupled with a face-on orientation, which is ideal for vertical charge transport in a diode configuration.<sup>21</sup> PNDIT2 films also exhibit a thin, edge-on skin layer facilitating transport in OFET devices.<sup>22</sup> This dominant bulk face-on stacking behavior is indicated by the appearance of a (010)  $\pi - \pi$  stacking peak along the  $Q_z$  direction and a (100) lamellar stacking peak along the  $Q_{xy}$  direction in the 2D GIWAXS image.<sup>20</sup> In contrast to neat PNDIT2, the GIWAXS images of the thionated series of polymers shows a significant reduction in the (010) peak intensity, reflecting less pronounced  $\pi - \pi$  stacking order in these polymers. A reduction in  $\pi - \pi$  stacking order is also clearly seen in the neat 1D out-of-plane GIWAXS line cuts displayed in Figure 6.12, which have been normalized to the (010) peak. From the figure, it is clear that the (010) peaks for the thionation polymers are significantly broader. Calculation of a coherence length based on the full-width at half maximum of these peaks give coherence lengths of 2.4 nm (PNDIT2), 1.6 nm (2S-*trans*-PNDIT2- 85%), 1.6 nm (2S-*trans*-PNDIT2-93%), and 1.5 nm (2S-*trans*-PNDIT2-95%). The narrower (010) peak measured in PNDIT2 films indicates that the  $\pi - \pi$  stacking order extends over more repeat units compared to the thionated materials, alluding to a higher degree of crystalline order in the PNDIT2 material. The neat films of the thionated polymers also show reduced texture, with less of a presence of face-on *versus* edge-on stacking. The GIWAXS images of the blend films with PBDTTT-EFT reflect a linear combination of the neat donor and acceptor polymers for all three thionated derivatives. This indicates that blending the polymers does not significantly prohibit the crystallization of either the donor, or the acceptor. The significant reduction in the  $\pi - \pi$  stacking order observed in the thionated samples may be responsible for differences in the morphology observed by



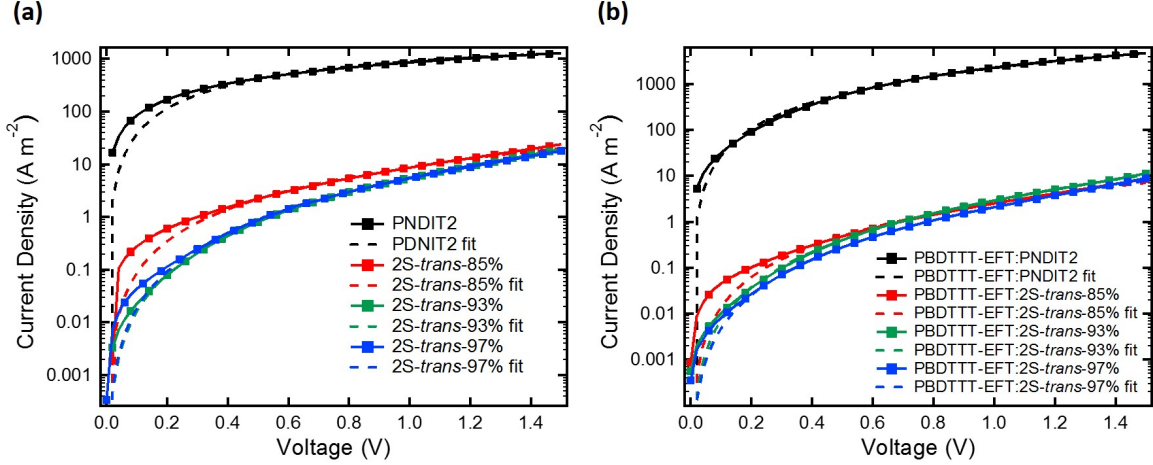


Figure 6.13: Current-voltage curves for neat SCLC devices (a) and for blend SCLC devices with PBDTTT-EFT (b). Squares are representative of the data while dashed lines represent the best fit for the Murgatroyd equation.

TEM, with stronger aggregation of the non-thionated polymer promoting a slightly coarser nanoscale morphology. Poor  $\pi - \pi$  stacking order is associated with lower electron mobility, causing an imbalance in electron and hole mobilities through the solar cell.<sup>14</sup> This can cause charge build-up in the active layer, which is responsible for increased recombination. In fact, OFETs of the thionated polymers displayed a systematic reduction in electron mobility with increasing degree of thionation, over PNDIT2, by an order of magnitude, from 0.16 cm<sup>2</sup>/Vs in PNDIT2 to 0.041 cm<sup>2</sup>/Vs, 0.024 cm<sup>2</sup>/Vs, and 0.018 cm<sup>2</sup>/Vs for 2S-*trans*-PNDIT2- 85%, 2S-*trans*-PNDIT2-93%, and 2S-*trans*-PNDIT2-95%, respectively.<sup>14</sup>

In the context of organic solar cells, space-charge limited current (SCLC) devices were fabricated to quantify the blend and neat mobility for PNDIT2 and its thionated analogs. The resulting current density-voltage curves are provided Figure 6.13. Mobility values, presented in Table 6.4, were calculated using the Murgatroyd equation, shown below:

$$J = \frac{9}{8} \epsilon_0 \epsilon_r \mu_0 \exp(0.89\beta \sqrt{V - V_{bi}/d}) \frac{V^2}{d^3} \quad (6.1)$$

where  $\epsilon_r$  is the relative dielectric permittivity of the material (assumed to be 3.5 for all films),  $\mu_0$  is the zero-field carrier mobility (shown in Table 6.4),  $d$  is the sample thickness, and  $\beta$  is the field activation factor.  $V - V_{bi}$  is taken to be 0 for all samples.  $\mu_0$  and  $\beta$  are the fitting parameters. SCLC measurements confirm the significantly lower electron mobility exhibited by the thionated PNDIT2 analogs, with neat films of 2S-*trans*-PNDIT2-85%, 2S-*trans*-PNDIT2-93%, and 2S-*trans*-PNDIT2-97% exhibiting electron mobility values of  $7.5 \times 10^{-6}$  cm<sup>2</sup>/Vs,  $1.2 \times 10^{-6}$  cm<sup>2</sup>/Vs, and  $8.3 \times 10^{-7}$  cm<sup>2</sup>/Vs, respectively, compared to an electron mobility of  $1.0 \times 10^{-2}$  cm<sup>2</sup>/Vs for PNDIT2. Blend films show similar trends, with the PBDTTT-EFT:PNDIT2 blend exhibiting an electron mobility of  $1.4 \times 10^{-3}$  cm<sup>2</sup>/Vs, compared to  $\sim 1 \times 10^{-7}$  cm<sup>2</sup>/Vs for the thionated samples. (Note that a batch with slightly higher conversion was used for the mobility measurements due to a shortage of the 2S-*trans*-PNDIT2-95% batch.)

In order to further confirm that the poor electron mobility of the thionated samples adversely affects charge extraction, transient short-circuit photocurrent measurements were performed. Measurements utilized a 200  $\mu$ s pulse of 525 nm at various

LED intensities. Figure 6.14 presents the transient photocurrent curves for the PNDIT2 and 2S-*trans*-PNDIT2-95%-based devices, with data for the two other thionated polymers presented in Appendix C. Figure 6.14 (a, b) show the response to increasing light intensity with Figure 6.14 (c, d) showing traces that have been normalized to the current measured at 200  $\mu\text{s}$ . For comparison with solar intensities, the steady-state  $I_{SC}$  under 100  $\text{mW}/\text{cm}^2$  AM 1.5G illumination is 0.153 mA and corresponds to a monochromatic intensity of  $\sim 2$  mW. On the microsecond timescales investigated, the processes of exciton generation, diffusion and dissociation are much faster than can be probed with this technique. However the extraction of charges subsequent to charge generation can be probed. For trap-free charge carrier transport, the transient turn-on dynamics are primarily determined by the charge-carrier mobility, and are largely intensity-independent.<sup>23</sup> This is exhibited in the normalized curves for PBDTTT-EFT:PNDIT2 devices, with a square response to light excitation that does not vary greatly with increasing LED intensity. However, the PBDTTT-EFT:2S-*trans*-PNDIT2-95% device strongly deviates from this behavior (shown clearly in Figure 6.14(d)). Strong intensity-dependent changes in the photocurrent traces are seen. At high intensities, an over-shoot in the turn-on for the photocurrent is observed, while at low intensities, the device turn-on is exceedingly slow, up to nearly 200  $\mu\text{s}$ . This behavior has been previously seen in all-polymer and polymer/nanocrystal solar cells and explained (and modeled) in terms of trap-limited transport.<sup>17,24</sup> Due to the presence of deep traps, charge carriers must first fill up these trap states resulting in dispersive current transients. An overshoot in photocurrent can be observed at high intensity due to build of space-charge that can lead to a redistribution in the internal electric field, increasing bimolecular and/or geminate recombination.<sup>23</sup> Looking at the turn-off dynamics, after an initial fast decay, there is a long-lived tail in the traces of the 2S-*trans*-PNDIT2-95% device that increases in prominence with decreasing light intensities. This long-lived photocurrent tail results from the slow detrapping of charges after turn-off and is absent in the efficient PBDTTT-EFT:PNDIT2 device. Similar behavior is observed for all three thionated acceptor polymers, with the current transients becoming more dispersive with increasing degree of thionation. This data is provided in Appendix C.

To confirm that there is intensity-dependent recombination at short-circuit, the short-circuit current as a function of light intensity from a high brightness white LED was measured, Figure 6.15. In this figure, current *versus* intensity is plotted on a log-log scale with the data fitted by a power law dependence of  $I_{SC} \propto I^\alpha$ , where

| SCLC Device                      | Film Thickness<br>(nm) | $\beta$              | Mobility<br>( $\text{cm}^2/\text{Vs}$ ) |
|----------------------------------|------------------------|----------------------|---|
| PBDTTT-EFT:PNDIT2                | 118                    | $1.2 \times 10^{-4}$ | $1.4 \times 10^{-3}$                    |
| PBDTTT-EFT:2S- <i>trans</i> -85% | 102                    | $6.4 \times 10^{-4}$ | $1.3 \times 10^{-7}$                    |
| PBDTTT-EFT:2S- <i>trans</i> -93% | 105                    | $7.9 \times 10^{-4}$ | $1.7 \times 10^{-7}$                    |
| PBDTTT-EFT:2S- <i>trans</i> -97% | 106                    | $7.6 \times 10^{-4}$ | $1.1 \times 10^{-7}$                    |
| PNDIT2                           | 108                    | $8.8 \times 10^{-4}$ | $1.0 \times 10^{-2}$                    |
| 2S- <i>trans</i> -PNDIT2-85%     | 138                    | $1.7 \times 10^{-5}$ | $7.5 \times 10^{-6}$                    |
| 2S- <i>trans</i> -PNDIT2-93%     | 157                    | $7.9 \times 10^{-4}$ | $1.2 \times 10^{-6}$                    |
| 2S- <i>trans</i> -PNDIT2-97%     | 130                    | $6.5 \times 10^{-4}$ | $8.3 \times 10^{-7}$                    |

Table 6.4: Extracted mobility values for the SCLC devices for blend and neat films.

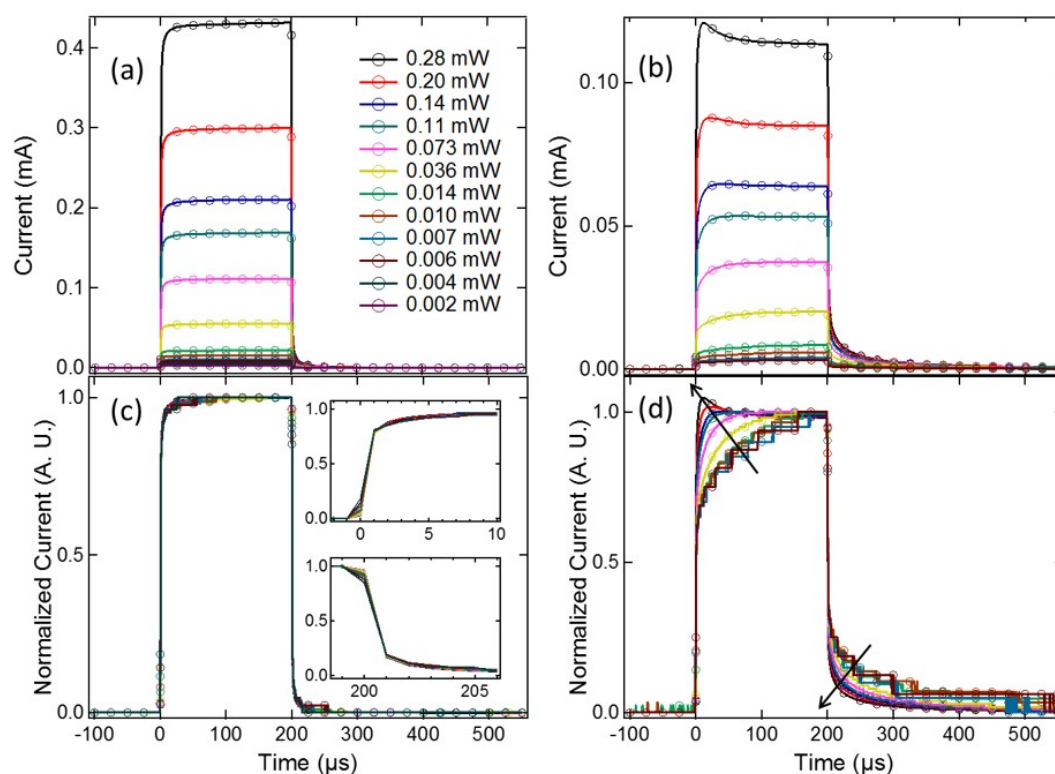


Figure 6.14: Current-voltage curves for neat SCLC devices (a) and for blend SCLC devices with PBDTTT-EFT (b). Squares are representative of the data while dashed lines represent the best fit for the Murgatroyd equation.

$I_{SC}$  is the short-circuit current and  $I$  is the LED intensity. The intensity dependence for PBDTTT-EFT:PNDIT2 devices is well fitted by the power law, with  $\alpha = 0.99$ . However, for the thionated polymers,  $\alpha$  is reduced to 0.90, 0.89 and 0.85 for 2S-*trans*-PNDIT2-85%, 2S-*trans*-PNDIT2-93%, and 2S-*trans*-PNDIT2-95%-based devices, respectively. Thus even at short-circuit current, the slow extraction of charges in the thionated cells results in intensity-dependent recombination.

## 6.4 Conclusions

The first part of this chapter explored the effect of systematic thionation on the solar cell performance of naphthalene diimide molecules. It was shown that, although each subsequent sulfur substituent further reduces the  $V_{OC}$  for devices fabricated with PBDTTT-EFT, the additional gain in  $J_{SC}$  and fill factor are sufficient to increase the overall OPV performance over devices made with the parent molecule, when thionation is used in a 2S-*trans* configuration. Although the overall power conversion efficiency of thionated NDI molecules remained low, this initial study motivated study of a higher performing polymeric NDI system, namely PNDIT2.

The effect of thionation of PNDIT2 on solar cell performance and bulk heterojunction morphology was next investigated. While thionation results in a lower band gap and deeper LUMO, solar cells based on the thionated polymers exhibited not only a systematic reduction in the  $V_{OC}$ , but also in  $J_{SC}$ , with thionation. This unexpected deterioration in  $J_{SC}$  is attributed to the lower mobility of the thionated polymers and

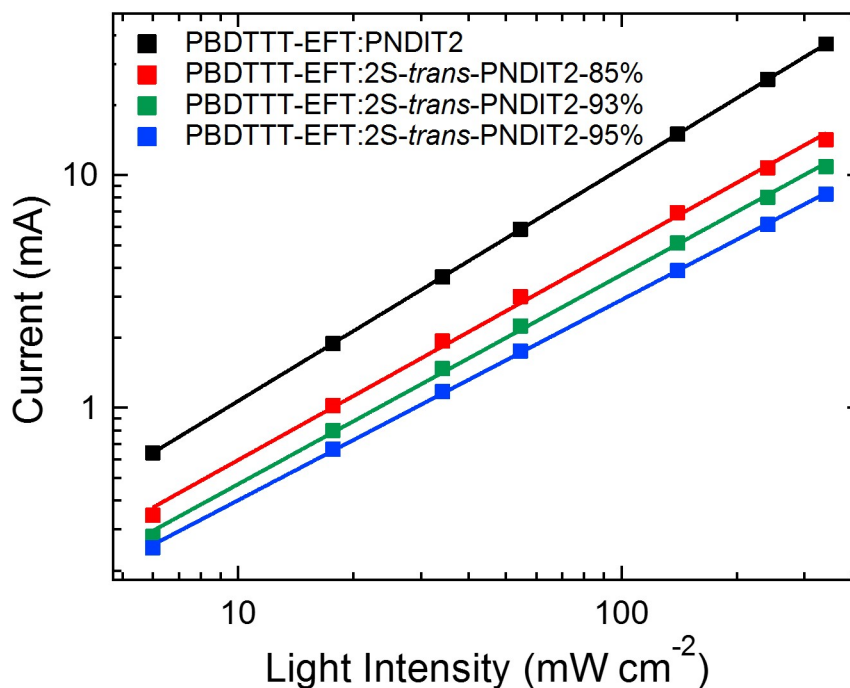


Figure 6.15: Current-voltage curves for neat SCLC devices (a) and for blend SCLC devices with PBDTTT-EFT (b). Squares are representative of the data while dashed lines represent the best fit for the Murgatroyd equation.

differences in morphology and molecular packing as revealed by AFM, TEM, NEXAFS spectroscopy and GIWAXS. In particular the thionated polymers appear to be more miscible with the donor polymer PBDTTT-EFT, resulting in a finer scale morphology compared to the PBDTTT-EFT:PNDIT2 blend. Thionation also disrupts  $\pi - \pi$  stacking, with the thionated blends showing reduced crystalline order of the acceptor phase. This reduced molecular order is linked to the significant lower electron mobilities observed with SCLC measurements. Transient short-circuit photocurrent measurements confirmed strongly trap-limited extraction dynamics, which result in intensity-dependent recombination at short circuit. While thionation has been a successful strategy to increase electron mobility in NDI-based small molecule materials,<sup>5</sup> the reduction in the electron mobility of the thionated NDI-based polymers hinders its effectiveness as a strategy to improve the performance of all-polymer solar cells. Other NDI-based polymers whose electron mobility is not so sensitive to molecular packing may result in better results upon thionation. This chapter therefore serves to highlight the complicated nature of organic semiconductors where seemingly simple changes in chemical structure can lead to pronounced unanticipated negative consequences.





# References

- [1] S. Dai, F. Zhao, Q. Zhang, T.-K. Lau, T. Li, K. Liu, Q. Ling, C. Wang, X. Lu, W. You, and X. Zhan, “Fused nonacyclic electron acceptors for efficient polymer solar cells,” *Journal of the American Chemical Society*, vol. 139, no. 3, pp. 1336–1343, 2017.
- [2] N. B. Kolhe, H. Lee, D. Kuzuhara, N. Yoshimoto, T. Koganezawa, and S. A. Jenekhe, “All-polymer solar cells with 9.4% efficiency from naphthalene diimide-biselenophene copolymer acceptor,” *Chemistry of Materials*, vol. 30, no. 18, pp. 6540–6548, 2018.
- [3] A. J. Tilley, R. D. Pensack, T. S. Lee, B. Djukic, G. D. Scholes, and D. S. Seferos, “Ultrafast triplet formation in thionated perylene diimides,” *Journal of Physical Chemistry Letters*, vol. 118, pp. 9996–10004, 2014.
- [4] F. S. Etheridge, R. Fernando, J. A. Golen, A. L. Rheingold, and G. Sauve, “Tuning the optoelectronic properties of core-substituted naphthalene diimides by the selective conversion of imides to monothioimides,” *RSC Advances*, vol. 5, no. 58, pp. 46534–46539, 2015.
- [5] A. Welford, S. Maniam, E. Gann, L. Thomsen, S. J. Langford, and C. R. McNeill, “Thionation of naphthalene diimide molecules: Thin-film microstructure and transistor performance,” *Organic Electronics*, vol. 53, pp. 287–295, 2018.
- [6] W. Chen, J. Zhang, G. Long, Y. Liu, Q. Zhang, M. Porsch, J. Daub, M. F. Toney, J. Huang, Z. Bao, Y. H. Kim, R. J. Kline, M. D. McGehee, and M. F. Toney, “From non-detectable to decent: Replacement of oxygen with sulfur in naphthalene diimide boosts electron transport in organic thin-film transistors (OTFT),” *Journal of Materials Chemistry C*, vol. 3, no. 31, pp. 8219–8224, 2015.
- [7] L. M. Kozycz, C. Guo, J. G. Manion, A. J. Tilley, A. J. Lough, Y. Li, and D. S. Seferos, “Enhanced electron mobility in crystalline thionated naphthalene diimides,” *Journal of Materials Chemistry C*, vol. 3, no. 43, pp. 11505–11515, 2015.
- [8] N. Pearce, E. S. Davies, R. Horvath, C. R. Pfeiffer, X.-Z. Sun, W. Lewis, J. McMaster, M. W. George, and N. R. Champness, “Thionated naphthalene diimides: Tuneable chromophores for applications in photoactive dyads,” *Physical Chemistry Chemical Physics*, vol. 20, pp. 752–764, 2018.
- [9] A. Facchetti, “Polymer donor-polymer acceptor (all-polymer) solar cells,” *Materials Today*, vol. 16, no. 4, pp. 123–132, 2013.

- [10] J. Roncali, "Synthetic principles for bandgap control in linear  $\pi$ -conjugated systems," *Chemical Reviews*, vol. 97, no. 1, pp. 173–206, 1997.
- [11] K. D. Deshmukh, R. Matsidik, S. K. Prasad, N. Chandrasekaran, A. Welford, L. A. Connal, A. C. Liu, E. Gann, L. Thomsen, D. Kabra, J. M. Hodgkiss, M. Sommer, and C. R. McNeill, "Impact of acceptor fluorination on the performance of all-polymer solar cells," *ACS Applied Materials and Interfaces*, vol. 10, no. 1, pp. 955–969, 2018.
- [12] H. Yan, Z. Chen, Y. Zheng, C. Newman, J. R. Quinn, F. Dötz, M. Kastler, and A. Facchetti, "A high-mobility electron-transporting polymer for printed transistors," *Nature*, vol. 457, no. 7230, pp. 679–686, 2009.
- [13] L. Gao, Z. G. Zhang, L. Xue, J. Min, J. Zhang, Z. Wei, and Y. Li, "All-polymer solar cells based on absorption-complementary polymer donor and acceptor with high power conversion efficiency of 8.27%," *Advanced Materials*, vol. 28, no. 9, pp. 1884–1890, 2016.
- [14] Y. H. Shin, A. Welford, H. Komber, R. Matsidik, T. Thurn-Albrecht, C. R. McNeill, and M. Sommer, "Regioregular polymer analogous thionation of naphthalene diimide–bithiophene copolymers," *Macromolecules*, vol. 51, no. 3, pp. 984–991, 2018.
- [15] R. Steyrleuthner, S. Bange, and D. Neher, "Reliable electron-only devices and electron transport in n-type polymers," *Journal of Applied Physics*, vol. 105, no. 6, p. 064509, 2009.
- [16] D. Nava, Y. Shin, M. Massetti, X. Jiao, T. Biskup, M. S. Jagadeesh, A. Calloni, L. Duò, G. Lanzani, C. R. McNeill, M. Sommer, and M. Caironi, "Drastic improvement of air stability in an n-type doped naphthalene-diimide polymer by thionation," *ACS Applied Energy Materials*, vol. 1, no. 9, pp. 4626–4634, 2018.
- [17] S. H. Liao, H. J. Jhuo, Y. S. Cheng, and S. A. Chen, "Fullerene derivative-doped zinc oxide nanofilm as the cathode of inverted polymer solar cells with low-bandgap polymer (PTB7-Th) for high performance," *Advanced Materials*, vol. 25, no. 34, pp. 4766–4771, 2013.
- [18] C. Mu, P. Liu, W. Ma, K. Jiang, J. Zhao, K. Zhang, Z. Chen, Z. Wei, Y. Yi, J. Wang, S. Yang, F. Huang, A. Facchetti, H. Ade, and H. Yan, "High-efficiency all-polymer solar cells based on a pair of crystalline low-bandgap polymers," *Advanced Materials*, vol. 26, no. 42, pp. 7224–7230, 2014.
- [19] K. D. Deshmukh, S. K. K. Prasad, N. Chandrasekaran, A. C. Y. Liu, E. Gann, L. Thomsen, D. Kabra, J. M. Hodgkiss, and C. R. McNeill, "Critical role of pendant group substitution on the performance of efficient all-polymer solar cells," *Chemistry of Materials*, vol. 29, no. 2, pp. 804–816, 2017.
- [20] Y. Tang and C. R. McNeill, "All-polymer solar cells utilizing low band gap polymers as donor and acceptor," *Journal of Polymer Science Part B: Polymer Physics*, vol. 51, no. 6, pp. 403–409, 2013.

- [21] R. Steyrleuthner, M. Schubert, F. Jaiser, J. C. Blakesley, Z. Chen, A. Facchetti, and D. Neher, “Bulk electron transport and charge injection in a high mobility n-type semiconducting polymer,” *Advanced Materials*, vol. 22, pp. 2799–2803, 2010.
- [22] T. Schuettfort, L. Thomsen, and C. R. McNeill, “Observation of a distinct surface molecular orientation in films of a high mobility conjugated polymer,” *Journal of the American Chemical Society*, vol. 135, no. 3, pp. 1092–1101, 2013.
- [23] I. Hwang and N. C. Greenham, “Modeling photocurrent transients in organic solar cells,” *Nanotechnology*, vol. 19, no. 42, p. 424012, 2008.
- [24] Z. Li, F. Gao, N. C. Greenham, and C. R. McNeill, “Comparison of the operation of polymer/fullerene, polymer/polymer, and polymer/nanocrystal solar cells: A transient photocurrent and photovoltage study,” *Advanced Functional Materials*, vol. 21, no. 8, pp. 1419–1431, 2011.



## Chapter 7

# NEXAFS calculations of thionated naphthalene diimide

Thionation has previously been shown to significantly and systematically alter the electronic structure of NDI-based molecules, which has implications for the performance of these materials in both OFET and OPV devices. In order to better understand the mechanism behind the systematic changes that occur in the electronic structure of NDI with thionation, a DFT-based approach has been used to calculate the NEXAFS spectra of a set of 7 thionated NDI molecules with varying nature and degree of thionation. It is found that the systematic broadening and intensity reduction in the peaks observed in the  $\pi^*$  manifold with increasing thionation are the result of distinct changes in the chemical environment of the outer carbon atoms that are bonded directly to either oxygen or sulfur. Specifically, the C 1s  $\rightarrow$  LUMO transition energy dramatically decreases with thionation, as the valence electron density of these carbon atoms is increased when highly electronegative oxygen atoms are replaced by less-oxidizing sulfur atoms. It is also shown that the significant core level shifts present in naphthalene diimide-based molecule results in a mixing of LUMO and LUMO + 1 character in the C 1s  $\rightarrow \pi^*$  manifold, meaning that experimentally observed peaks cannot be uniquely associated with the LUMO, LUMO + 1, etc. transitions.

## 7.1 Introduction and Context

The electronic structure of organic semiconductors plays a critical role in the optical and electronic properties of these materials that are paramount to efficient solar cell operation. For example, previous results chapters have shown the impact that substitutional and substituent atoms can have on the HOMO and LUMO energy levels of NDI molecules, which influence not only the optical properties of these materials, but also the electron mobility, free carrier lifetime, and the presence of charge traps, all of which influence device efficiency. It is therefore important to fully characterize the electronic structure of the NDI moiety, and also to better understand what role, specifically, substitutional atoms play in influencing the electronic structure of the material. This chapter explores the effect that systematic thionation has on the near-edge X-ray absorption fine structure (NEXAFS) spectra of the series of molecules shown in Figure 2.21. However, due to limitations afforded by NEXAFS spectroscopy, systematic changes in the  $\pi^*$  manifold with increasing thionation cannot easily be explained by experimental methods alone, and therefore a complimentary, theoretical approach is required to fully characterize the  $\pi^*$  character of these materials at the carbon K-edge.

Density functional theory (DFT) is commonly used to quantum mechanically predict the electronic structure of atoms and complex molecules in the ground state.<sup>1</sup> However, modifications to DFT-based approaches also enable the prediction of a material's electronic structure in the excited state.<sup>2-4</sup> First introduced in the Chapter 3, this chapter relies on the DFT-based eXcited electron and Core Hole approach to calculate the X-ray absorption spectra of the series of NDI-based molecules explored in the previous chapter. Although the experimental NEXAFS spectra of these materials has been previously reported,<sup>5</sup> this chapter aims to build upon these experimental findings by enabling the explanation of systematic trends observed in experiments. This chapter includes the main text of the journal article pertaining to these calculations, published in the Journal of Chemical Physics, with the published supporting information available in Appendix D.

*Understanding the effect of thionation on  
naphthalene diimide using first-principles  
predictions of near-edge X-ray absorption fine  
structure spectra*

**Kira Rundel**, Yufeng Liang, Adam Welford, David Prendergast, and Christopher  
R. McNeill

*The Journal of Chemical Physics*, 2019, **150**, 104302.

American Institute of Physics | DIO: 10.1063/1.5084754



## 7.2 Article

The Journal  
of Chemical Physics

ARTICLE

[scitation.org/journal/jcp](https://scitation.org/journal/jcp)

# Understanding the effect of thionation on naphthalene diimide using first-principles predictions of near-edge x-ray absorption fine structure spectra

Cite as: J. Chem. Phys. 150, 104302 (2019); doi: 10.1063/1.5084754

Submitted: 6 December 2018 • Accepted: 14 February 2019 •

Published Online: 11 March 2019



View Online



Export Citation



CrossMark

Kira Rundel,<sup>1</sup> Yufeng Liang,<sup>2</sup> Adam Welford,<sup>1</sup> David Prendergast,<sup>2</sup> and Christopher R. McNeill<sup>1,a)</sup>

### AFFILIATIONS

<sup>1</sup>Department of Materials Science and Engineering, Monash University, Wellington Road, Clayton, VIC 3800, Australia

<sup>2</sup>The Molecular Foundry, Lawrence Berkeley National Laboratory, Berkeley, California 94720, USA

<sup>a)</sup>E-mail: [christopher.mcneill@monash.edu](mailto:christopher.mcneill@monash.edu)

### ABSTRACT

The near edge X-ray absorption fine structure (NEXAFS) spectra of naphthalene diimide molecules with increasing degrees of thionation show distinct and systematic changes in the C 1s  $\rightarrow \pi^*$  manifold. However, interpretation of such spectra is difficult using experimental data alone, due to the limitation in experimental NEXAFS resolution. In this work, we have calculated the NEXAFS spectra of naphthalene diimide molecules with increasing degrees of thionation using the density functional theory-based eXcited electron and Core Hole approach. We find that the systematic broadening and intensity reduction in the peaks observed in the  $\pi^*$  manifold with increasing thionation are the result of distinct changes in the chemical environment of the outer carbon atoms that are bonded directly to either oxygen or sulfur. Specifically, the C 1s  $\rightarrow$  lowest unoccupied molecular orbital (LUMO) transition energy dramatically decreases with thionation, as the valence electron density of these carbon atoms is increased when highly electronegative oxygen atoms are replaced by less-oxidizing sulfur atoms. It is also shown that significant core level shifts present in naphthalene diimide-based molecule result in a mixing of the LUMO and LUMO + 1 character in the C 1s  $\rightarrow \pi^*$  manifold, meaning that experimentally observed peaks cannot be uniquely associated with the transitions of LUMO, LUMO + 1, etc.

Published under license by AIP Publishing. <https://doi.org/10.1063/1.5084754>

### INTRODUCTION

Semiconducting organic materials, such as conjugated polymers and small molecules, have shown great potential for electronic applications boasting favorable properties such as mechanical flexibility and solution processability.<sup>1–4</sup> In such materials, semiconducting behavior arises from a conjugated core, defined as having alternating single and double bonds, which extensively delocalizes  $\pi$  molecular orbitals along the backbone of the material, giving rise to interesting electronic and optical properties.<sup>5</sup> Such characteristics make organic semiconductors suitable for applications in field-effect transistors,<sup>2</sup> solar cells,<sup>6</sup> and light emitting diodes.<sup>7</sup>

Importantly, the electronic properties of conjugated semiconductors are anisotropic because the delocalized electron density is

only present along the backbone of the material, rendering molecular orientation extremely important for efficient charge transport through the material. Near Edge X-ray Absorption Fine Structure (NEXAFS) spectroscopy is a useful characterization method commonly used to determine the surface and bulk molecular orientation by probing electronic transitions of core level electrons to unoccupied molecular orbitals (for example, from carbon 1s orbitals to  $\pi^*$  orbitals; see Fig. 1 for schematic).<sup>8</sup> In addition, useful information regarding the oxidation state and chemical environment of the core-excited atoms can also be extracted from the measured spectrum because different conjugated polymers and molecules exhibit dissimilar NEXAFS spectra, a reflection of their unique chemical structures.<sup>8</sup> Indeed, the distinct NEXAFS spectra of different materials are used as the basis for chemical contrast in soft X-ray microscopy.<sup>9</sup>

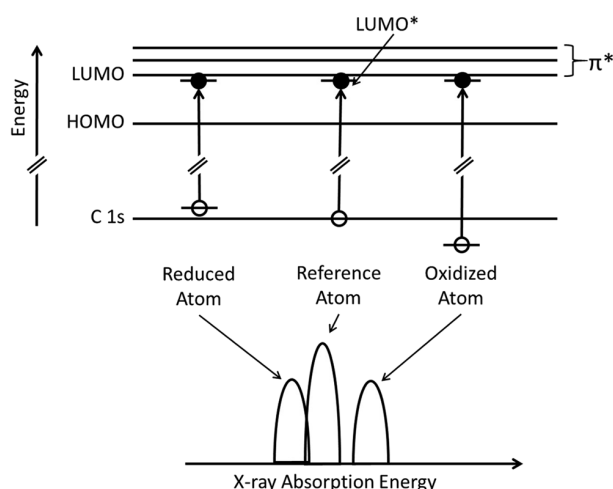


**FIG. 1.** Schematic illustrating the shift in core and excited energy levels in the ground state, compared to two inequivalent excited atoms in the same molecule. These shifts are reflected in the energy differences of the LUMO transition peak in the atomically resolved NEXAFS spectra calculated using the XCH approach. Note that the excited electron does not occupy (ground state) LUMO, but rather an orbital shifted in energy due to localization caused by interaction with the core hole; hence, the final state is labelled LUMO\* in this figure.

However, the assignment of spectral features measured by NEXAFS spectroscopy is difficult due to the lack of reference spectra and the complex nature of NEXAFS transitions.<sup>8</sup> In order to interpret and assign spectral features to atomic-site-specific core-electronic transitions in an organic semiconductor, first-principles calculations, such as the eXcited electron and Core Hole (XCH) approach<sup>10</sup> used in this work, are useful tools that can be employed to unpack the atom-specific contributions to a resonant transition.<sup>11–14</sup>

The lowest energy near-edge spectral features of conjugated organic systems reflect transitions from a core orbital (the carbon 1s in our case) to the lowest unoccupied molecular orbital (LUMO), and conjugation would typically lead to a LUMO with  $\pi^*$  character. These features appear in NEXAFS spectra at  $\sim 284$  eV.<sup>15</sup> Therefore, this energy range is of particular importance for studying functional conjugated materials because its spectral features reflect the details of the electron acceptor energy levels in the material. Furthermore, these  $\pi^*$  spectral features are commonly used in polarization dependent NEXAFS measurements to determine the orientation of semiconducting organic molecules, due to the perpendicular orientation of the atomic  $p$  orbital character in these orbitals relative to the planar conjugated backbone of organic semiconductors. At higher energies, above  $\sim 290$  eV, broad shape resonances are observed, which are attributed to transitions to  $\sigma^*$  orbitals, oriented along the C–C bond axes. Resonant  $\sigma^*$  transitions are dominated by contributions from saturated hydrocarbon chains that are commonly attached as side chains to promote the solubility of organic semiconductors in common organic solvents.<sup>16</sup> These side-chain atoms can also influence the peaks in the  $\pi^*$  region depending on whether they are bonded directly to a carbon atom in the conjugated part of the material or not, in which case the hydrocarbon

chain may affect the local bonding environment of the carbon atom in the structure.<sup>11</sup>  $\sigma^*$  resonances are generally less useful for probing the molecular orientation of organic semiconductors due to the flexibility of the side chains, which promotes disordered side chain conformations, and a larger distribution of bond lengths (both static and thermally activated) which leads to broadening of  $\sigma^*$  peaks.

In this paper, we aim to interpret the effect that systematic thionation (the replacement of oxygen atoms with sulfur atoms) has on the NEXAFS spectra of a series of naphthalene diimide (NDI) molecules. Naphthalene diimide is a common building block that is widely exploited by the organic electronics community due to its high electron affinity that results from the substitution of its aromatic core with two sets of electron withdrawing carboxylic imide rings.<sup>5</sup> The NDI moiety has been used as the basis for both small molecule and polymeric semiconductors, with NDI-based materials achieving excellent mobilities in n-channel field-effect transistors<sup>17</sup> and good efficiencies in all polymer solar cells.<sup>18</sup> NDI is also a versatile molecule whose chemical structure can be tuned by adding solubilizing alkyl side chains at the nitrogen positions of the imide groups, with the nature of the side chains varied to tune processing and molecular packing. Furthermore, side groups can be added to the core positions enabling either functionalization of the core, core expansion, or the linking of NDI molecules to other molecules to form larger molecular structures such as polymers. Recently, thionation has been shown to be an attractive strategy for tuning the LUMO of NDI-based materials.<sup>19–21</sup> Thionation has also been shown to significantly increase the transistor mobilities of NDI-based small molecules, most likely due to improved intermolecular interactions.<sup>19</sup> Previously, we have shown that the systematic thionation of the NDI core results in systematic changes to the material's electronic structure, which is determined by measuring the NEXAFS spectrum at the carbon K-edge.<sup>22</sup> While the changes are systematic, it is difficult to interpret such spectral changes using experimental data alone, as the results of a NEXAFS experiment encompass the entire molecule and the technique is unable, without theoretical insight, to resolve atomic contributions to the overall absorption spectrum.<sup>16</sup> Here, we use the XCH approach in order to calculate the C 1s core absorption spectra for the series of systematically thionated NDI molecules shown in Fig. 2(a). We focus on the  $\pi^*$  region, from 283.5 to 286.5 eV (see Fig. S1 for the full energy range, up to 300 eV), which encompasses transitions to  $\pi^*$  orbitals located along the conjugated core of the molecule, which is of particular importance for charge transport in organic semiconductors.<sup>16</sup> (The higher energy region of the spectra is dominated by transitions in the side-chains which are of less interest and more challenging to model due to the disorder.) From theoretical calculations, we are able to successfully reproduce the major features seen in the NEXAFS spectra of the molecules shown in Fig. 2(a) and understand the evolution in near-edge structure with increasing degrees of thionation in terms of changes in core state energies that significantly shift the energy of the C 1s to  $\pi^*$  transitions. Importantly, for NDI-based molecules, we show that, due to large shifts in core level energies of over 2 eV, there is a mixing of LUMO character across the  $\pi^*$ -manifold, meaning that the different peaks in the  $\pi^*$ -manifold of these materials cannot be identified exclusively with a particular unoccupied molecular orbital such as the LUMO and LUMO + 1. These theoretical calculations also reveal

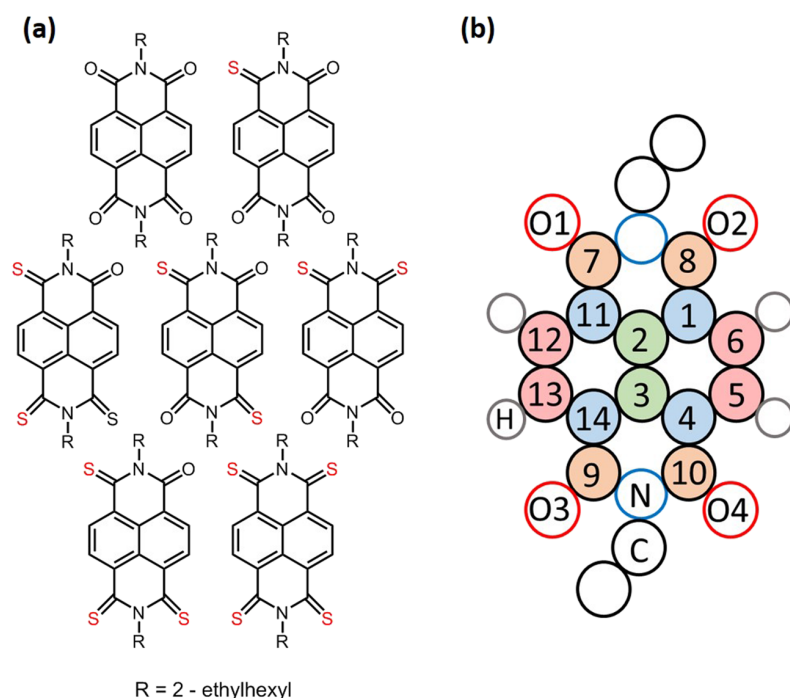


**FIG. 2.** (a) Molecular structures of the seven materials studied in this work: parent, 1S, 2S-*cis* (middle row, left), 2S-*trans* (middle row, center), 2S-*cis imide* (middle row, right), 3S, and 4S. (b) Sketch of the NDI molecular structure used for simulations, including labeling of carbon and oxygen atoms. For simplicity, the hydrogen atoms bonded to the ethyl end groups are not shown in the sketch. The colors are coordinated with Figs. 3 and 4 and Table II.

the effect of the breaking of symmetry on the molecular orbitals and NEXAFS spectra of these materials, an important step in understanding the effect of thionation on the electronic properties of these molecules.<sup>19</sup>

## BACKGROUND ON NEXAFS INTERPRETATION

Figure 1 shows a schematic diagram for a resonant transition from a 1s core orbital in the carbon K-shell to the lowest unoccupied molecular orbital (LUMO), ignoring core-hole effects (center). However, due to the complex interaction between the core hole that is created and the excited electron, calculations of the actual resonant transition for an excited atom must take into account the changes in the initial-state core-orbital energy as well as in the final excited-state energy, as is done within the energy alignment scheme applied using the XCH approach.<sup>23,24</sup> Furthermore, since complex molecules such as organic semiconductors typically feature heteroatoms, differences in chemical environment lead to differences in the initial and final-state energies for every inequivalent atom in the material. This heterogeneity in the chemistry manifests as multiple contributions to the measured NEXAFS at varying energies and intensities, adding to the complexity of the spectrum and the difficulty in its interpretation. An example of a core-level excitation to the lowest unoccupied molecular orbital (LUMO) for inequivalent carbon atoms in the same molecule is also shown in Fig. 1, which demonstrates that the, potentially, dramatic influence an atom's chemical environment has on a resonant transition energy. In the schematic, the reference atom can be considered as a benchmark for comparison. As in all cases, the creation of a core-hole on this atomic site, following the X-ray excitation, induces changes in the electronic

structure of the system as a whole, but especially so around the excited atom. Generally, we expect ground state orbitals that originally overlapped the atomic site of the excitation to become more localized on that site and for their energies to shift accordingly—typically to lower energies than their ground state equivalents. We will label these excited-atom specific orbitals as LUMO<sup>\*</sup>(*i*), where atom *i* was excited. Figure 1 also indicates excitations of two other atoms which, by reference, are oxidized (reduced) with respect to the first (right and left sides of the schematic, respectively). For example, if the reference atom was a C atom bound to another C atom, then a relatively oxidized (reduced) atom might be bound to a N (B) atom (anything with a significantly different electronegativity). In cases where an available, unoccupied molecular orbital (such as the LUMO) overlaps the core orbitals of each of these atoms with the correct local symmetry (as required by the dipole selection rule)—even in their core-excited states—then transitions to the “same” orbital from these different atoms will appear at different photon energies. This is akin to the so-called chemical shift observable in X-ray photoemission spectra (XPS), with more oxidized (reduced) atoms of the same element evident as absorption peaks at higher (lower) photoabsorption energies, albeit typically with smaller shifts than their XPS equivalents.

## COMPUTATIONAL METHODS

To reduce the computational overhead of our simulations, the molecular geometries of the series of NDI-based small molecules studied in this work contained ethyl groups, replacing the 2-ethylhexyl groups used for experimental measurements. These molecular geometries were optimized using the density functional

theory (DFT) within the Quantum-ESPRESSO suite.<sup>25</sup> The electronic structure of these systems was computed using the Perdew-Burke-Ernzerhof form<sup>26</sup> of the generalized-gradient approximation to the exchange-correlation energy within DFT. Calculations were performed under periodic boundary conditions in supercells of sufficient size to prevent spurious interactions between neighboring periodic images. Valence electron-ion interactions were approximated using Vanderbilt's ultrasoft pseudopotentials.<sup>27</sup> A plane-wave basis was employed to represent the Kohn-Sham orbitals and the associated electron density, with plane-wave kinetic energy cutoffs, consistent with the pseudopotentials, of 25 and 225 Ry, respectively.

X-ray absorption calculations employed the eXcited electron and Core-Hole (XCH) approach, which models the first core-excited state using an occupancy constraint on the Kohn-Sham orbitals. The core-excited atom is represented using a modified pseudopotential, and the electron excited from this atom is placed in the first available valence orbital (analogous to the LUMO of the ground state), labeled LUMO\* in Fig. 1. Under this constraint, the electronic structure is generated self-consistently as an effective "ground state" for this core-excited system. The resulting Kohn-Sham spectrum is used to construct the X-ray absorption spectrum according to Fermi's Golden Rule, with core transition matrix elements to available empty orbitals computed using the projector augmented wave approach.<sup>28</sup> The excited state electronic structure is sampled across the Brillouin zone of the supercell, an approach which leads to a continuous spectral intensity at energies high above the absorption edge and has been shown to approximately reproduce the electronic structure of the continuum above the ionization potential (IP).<sup>29,30</sup> Efficient sampling of the Brillouin zone is enabled through the Shirley interpolation scheme.<sup>31,32</sup> The combination of a delocalized plane wave basis and Brillouin zone sampling has been shown to reliably reproduce the X-ray absorption spectra (XAS) of molecules and molecular phases across broad energy ranges (not just the near-edge region). Relative alignment of excitations from different atoms (i.e., the same element in different chemical contexts) is achieved through relative formation energies, as described in previous work,<sup>23,24</sup> and can reproduce the so-called "chemical shifts" in XAS peaks to an accuracy of ~0.1 eV. Actual core-level shifts can be estimated by comparing core-excited total energies for different atoms in the same molecule. Calculated spectral features are broadened uniformly by convolution with a Gaussian of 0.2 eV standard deviation.

We note that the use of local or semi-local functionals (such as the generalized gradient approximation (GGA) used here) is known to underestimate both bandgaps and bandwidths in the electronic density of states. These issues can be addressed to some degree using the first-order perturbation theory, as in the GW approximation,<sup>33,34</sup> or through the use of hybrid exact exchange functionals.<sup>35</sup> However, the need for a self-consistent description of the core-excited state (beyond perturbation theory) and the expense of current hybrid implementations render such efforts intractable for this study. Where possible, we highlight the shortcomings of our calculations based on these limitations of GGA; however, the interpretation of the spectra that we provide should remain valid.

X-ray absorption spectra can be modeled using various approaches with varying degrees of accuracy. Beyond core-hole approaches, the use of linear-response time-dependent density

functional theory (TDDFT)<sup>36</sup> is typically limited to localized orbital implementations, which can reliably describe bound excitations at the near-edge only, while solutions to the Bethe-Salpeter equation<sup>37</sup> are computationally more demanding and, similar to TDDFT, lack the added advantage of using DFT total energy estimates for the relative alignment of excitations on different atoms.

## RESULTS AND DISCUSSIONS

The series of systematically thionated NDI molecules explored in this work is shown in Fig. 2(a) and includes the parent NDI molecule, with all four flanking oxygen atoms, through to the 4S molecule, which is fully thionated and contains no oxygen atoms. The molecules used for experimental NEXAFS measurements utilized 2-ethylhexyl side chains to aid in solubility; however, for calculations, these side chains were replaced by ethyl end-groups. The incorporation of side-chain atoms was determined to have a minimal effect on the calculated spectra in the  $\pi^*$  energy region, which may be expected since they are bonded to nitrogen atoms and do not alter the bonding environment of the carbons probed during excitation of the molecule; see Fig. S2. Figure 2(b) shows a sketch of the parent NDI molecule with relevant atomic labels and shading corresponding to atoms that are considered equivalent and contribute equally to the total simulated XAS spectrum in symmetric molecules. For simplicity, hydrogen atoms bonded to carbon atoms in the ethyl end-groups are omitted from the sketch. The atomic labelling used in Fig. 2(b) is applied to all molecules studied in the series.

Figure 3 provides a side-by-side comparison between the experimental carbon K edge NEXAFS spectra in the  $\pi^*$  region in (a) and simulated C 1s core excitation spectra obtained using the XCH approach in (b). Note that the experimental NEXAFS spectra were acquired of thin films (~20 nm thick) spin-coated on silicon. Data are shown for an X-ray angle of incidence of 55° to exclude orientation effects.<sup>16</sup> While the films studied were semicrystalline in nature, the spot size of the experimental beam (~0.1 mm) was much larger than the grain size observed with atomic force microscopy (<10  $\mu$ m).<sup>22</sup> Due to the thickness of these films and the limited electron mean free path, effects due to electronic interactions with the substrate are also excluded. The calculated spectra, which show contributions from all carbon atoms in the molecules, are in good agreement with experimental results. The experimental results of the parent molecule comprise two distinct peaks in the  $\pi^*$  region, the first at 284.1 eV (which will be referred to as P1) and the second at 285.6 eV (which will be referred to as P2). The complete series exhibits clear differences between molecules with differing sulfur content. Two key systematic changes to the NEXAFS spectra in the  $\pi^*$  region are observed: (1) P1, at ~284 eV, demonstrates a lowering in intensity and subsequently shows broadening with increasing sulfur content and (2) there is a shoulder that emerges on the lower-energy side of P2, which gains intensity with each subsequent sulfur addition. For example, the first peak in the parent spectrum exhibits a full width at half maximum (FWHM) of ~0.4 eV in the first peak, while the first peak of the 4S molecule has a FWHM of ~0.7 eV—a broadening of over 57%. There is also a notable inverse correlation between the P1 intensity and sulfur content. Looking at P2 of the parent molecule, there is a slight asymmetry with a shoulder on



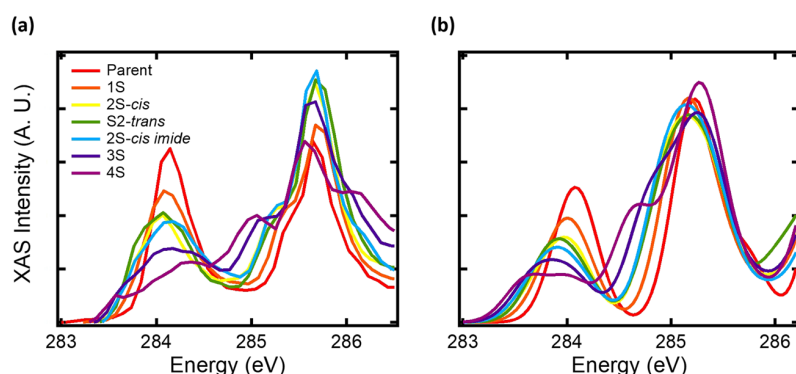


**FIG. 3.** (a) Experimental and (b) simulated carbon K-edge NEXAFS spectra, in the  $\pi^*$  region, of the thionated NDI series. Experimental data were measured with an X-ray angle of incidence of  $55^\circ$  and were normalized to the step-edge at 320 eV.

the low energy side, which shifts to lower energies with thionation. [As thionation does cause subtle changes in molecular packing,<sup>22</sup> a concern is that such changes may also be responsible for, or contribute to, the changes seen in the  $\pi^*$  region. Examining a series of NDI molecules where the side chains are varied (which also leads to subtle changes in molecular packing<sup>38</sup>), we find that the experimentally measured structure in the  $\pi^*$  region is rather robust and does not change with small shifts in molecular packing (see Fig. S3 of the [supplementary material](#)).] Because experimental NEXAFS measurements simultaneously probe all carbon atoms in a material, it is difficult to easily interpret these spectral changes relying on experimental data alone. Theoretical spectral calculations coupled with a detailed analysis of the final state orbitals aid in the understanding of these spectral differences while enabling an interpretation of the effect thionation has on the electronic structure of the NDI molecule.

Figure 4 shows the total calculated C 1s core excited spectra (black lines) for the parent (top) and 4S (bottom) molecules from Fig. 3, as well as the individual atomic contributions (dashed lines) for equivalent atoms following the labelling and color scheme of Fig. 2(b). For the parent molecule, the calculated peak centered at 284.1 eV (denoted  $P1_{\text{parent}}$ ) comprises contributions from transitions to LUMO states in atoms C1, C5, and their equivalents (blue and red dashed lines). The excitation energies for C1 and C5 are 284.2 eV and 284.0 eV, respectively, the result of a slight change in the ionization potential (IP) between atoms with differing bonding environments. These IP changes were calculated with respect to the C3 atom as follows:

$$IP_{C3} = E_{\text{FCH}_{C3}} - E_{\text{GS}}, \quad (1)$$

where the total energy difference reflects the cost of creating the C3 core-excited state  $E_{\text{FCH}_{C3}}$  with respect to the original ground-state total energy,  $E_{\text{GS}}$ . Then, for the C7 atom, a change in the ionization potential (IP) relative to the C3 atom is calculated as follows (with cancellation of the ground-state energy):

$$\Delta IP = IP_{C7} - IP_{C3} = E_{\text{FCH}_{C7}} - E_{\text{FCH}_{C3}}. \quad (2)$$

The 1s to LUMO transition energy for carbon atoms bonded to oxygen atoms, C8 and similar atoms (orange dashed lines), is so high that this excitation does not contribute to  $P1_{\text{parent}}$ , with the corresponding peak having an energy of 286.6 eV, well outside the window generally considered to correspond to  $\pi^*$  transitions. The inner carbon atoms (C2 and C3, green dashed lines) lie along the long

molecular axis of NDI, a nodal plane for the LUMO, rendering the  $1s \rightarrow \text{LUMO}$  transition dipole-forbidden. Thus, the contributions to the first peak in the parent molecule,  $P1_{\text{parent}}$ , are from 1s to LUMO transitions associated with atoms C1, C5, and equivalents only. A similar situation is observed for the lowest-energy peak in the 4S spectrum,  $P1_{4S}$ , with contributions mainly from C1, C5, and their equivalents; however, the process of thionation results in a larger  $\Delta IP$  for C5 and equivalent atoms from 284.0 to 283.6 eV (red dashed

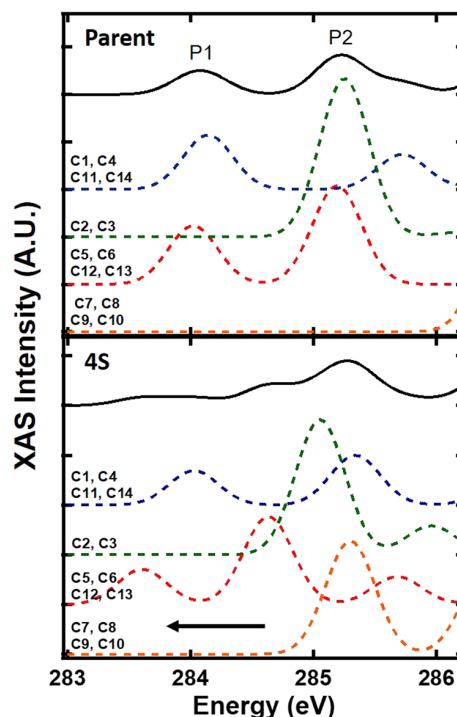


**FIG. 4.** (a) Atomically resolved contributions for all non-equivalent carbon atoms, compared to the overall (solid black line) calculated C 1s core excitation spectra for the parent (top) and 4S (bottom) molecules between 283 and 286 eV.

**TABLE I.** Energy (in eV) corresponding to the LUMO and LUMO + 1 transitions of select atoms in the  $\pi^*$  region. P1 denotes the first peak at  $\sim 284$  eV and P2 denotes the second peak at  $\sim 285.2$  eV in the total calculated spectra for each molecule. The table includes LUMO energies for C2, although this transition is dipole forbidden and therefore “silent” on the plot.

| Molecule             | Total |       | C1    |          | C2    |          | C5    |          | C7    |          |
|----------------------|-------|-------|-------|----------|-------|----------|-------|----------|-------|----------|
|                      | P1    | P2    | LUMO  | LUMO + 1 | LUMO  | LUMO + 1 | LUMO  | LUMO + 1 | LUMO  | LUMO + 1 |
| Parent               | 284.1 | 285.2 | 284.2 | 285.7    | 284.7 | 285.3    | 284.0 | 285.2    | 286.6 | 287.9    |
| 1S                   | 284.0 | 285.2 | 284.1 | 285.5    | 284.6 | 285.2    | 284.0 | 285.0    | 285.4 | 286.8    |
| 2S- <i>cis</i>       | 284.0 | 285.1 | 284.1 | 285.4    | 284.5 | 285.2    | 283.9 | 285.0    | 285.4 | 286.7    |
| 2S- <i>trans</i>     | 284.0 | 285.2 | 284.0 | 285.3    | 284.5 | 285.2    | 283.8 | 284.9    | 285.4 | 286.6    |
| 2S- <i>cis imide</i> | 284.0 | 285.1 | 284.2 | 285.6    | 284.5 | 285.1    | ...   | 284.9    | 285.3 | 286.7    |
| 3S                   | 283.8 | 285.2 | 283.9 | 285.2    | 284.4 | 285.1    | 283.7 | 284.8    | 285.4 | 286.5    |
| 4S                   | 283.6 | 285.6 | 284.0 | 285.3    | 284.3 | 285.1    | 283.6 | 284.6    | 285.3 | 286.4    |

lines), explaining the broadening of the first peak. A summary of peak positions for the composite P1 and P2 peaks and of a selection of atomic contributions for the full series of molecules is given in Table I. It is important to note that the spectral composition of the other molecules, apart from the parent and 4S molecules, in the series becomes complicated by the breaking of symmetry, as shown in Fig. 5, to be further discussed below. Any disruptions in symmetry, most prevalently in the 1S and 3S molecules but also, to some degree, in all three 2S configurations, result in inequivalent atomic contributions to the total calculated spectra, dependent on a carbon atom's proximity to a sulfur atom. The atomic contributions shown in Table I, therefore, provide only an overview of changing peak positions as the degree of thionation is increased and do not fully account for the deviations arising from asymmetry in the molecular structure.

The second main peak in the parent molecule centered at  $\sim 285.5$  eV in Fig. 4(a),  $P2_{\text{parent}}$ , has contributions from  $1s \rightarrow \text{LUMO} + 1$  resonances in the parent molecule, specifically from C2 and C5 atoms. (As discussed above, the lowest energy peak for C2 and C3 atoms is the  $1s \rightarrow \text{LUMO} + 1$  transition since the  $1s \rightarrow \text{LUMO}$  transition is dipole forbidden.) For the 4S molecule,  $P2_{4S}$  has contributions from  $1s \rightarrow \text{LUMO} + 1$  transitions in excited atoms C1 and C2 as well as from  $1s \rightarrow \text{LUMO}$  transitions associated with excitation of carbon atoms directly bonded to sulfur atoms (i.e., C8). The substitution of oxygen for sulfur atoms results in a smaller  $\Delta\text{IP}$  for C8 and equivalent atoms, bringing the  $1s \rightarrow \text{LUMO}$  transition back within the energy window of Fig. 4. However, the  $\Delta\text{IP}$  of C8 and equivalent atoms is still significant enough such that the  $1s \rightarrow \text{LUMO}$  is mixed in with the  $1s \rightarrow \text{LUMO} + 1$  transitions for C2 and C5 atoms. This results in a mixture of both the LUMO and LUMO + 1 character in

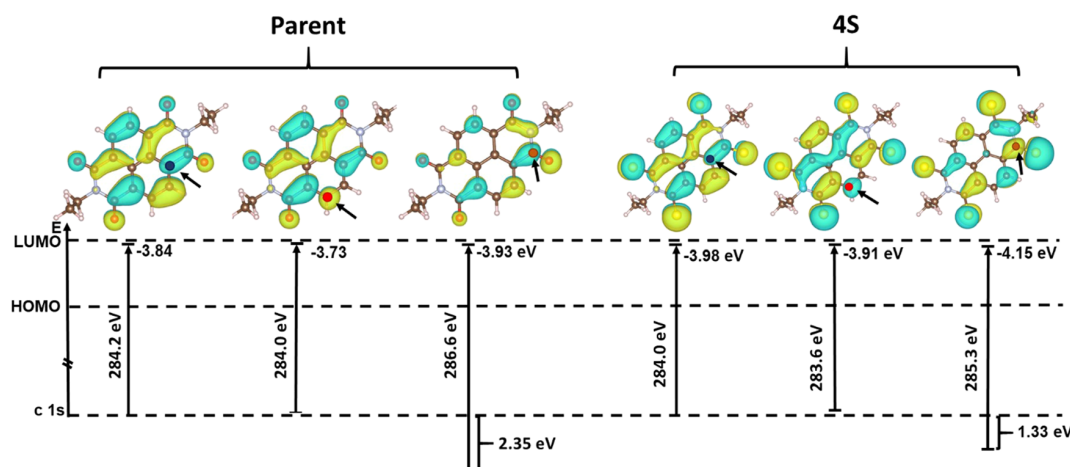


**FIG. 5.** Density distributions of the electronic component of different core-excited LUMO orbitals for the parent and 4S molecules. Below each final-state orbital is a sketch of the excitation from the C 1s energy to the corresponding LUMO energy. The excitation for C8 for both the parent and 4S molecules shows a dramatic increase in excitation energy, as well as the relative change in ionization potential that accounts for this increase. As a reference, the LUMO energy dashed line is relative to the parent molecule's ground state LUMO of 3.50 eV. The 4S molecule has a ground-state LUMO of 4.11 eV. Isosurface values are chosen in each case to reflect volumes that contain 80% of the norm of these orbital densities.

**TABLE II.** Calculated shifts in the ionization potential (in eV) of core orbitals, compared to the C3 core orbital. Atoms listed in the first column are grouped by equivalent atoms in symmetric molecules, see Fig. 1. For clarity, equivalent atoms are grouped and distinguished by either bold or italicized font.

| Atom       | Parent        | 1S           | 2S- <i>cis</i> | 2S- <i>trans</i> | 2S- <i>cis imide</i> | 3S             | 4S              |
|------------|---------------|--------------|----------------|------------------|----------------------|----------------|-----------------|
| <b>C2</b>  | <b>0.0002</b> | <b>0.02</b>  | <b>0.0007</b>  | <b>0.000008</b>  | <b>0.0184</b>        | <b>-0.0095</b> | <b>0.000021</b> |
| <i>C1</i>  | -0.20         | -0.14        | -0.18          | -0.25            | 0.01                 | -0.28          | -0.11           |
| <i>C4</i>  | -0.20         | -0.21        | -0.18          | -0.06            | -0.27                | -0.04          | -0.10           |
| <i>C11</i> | -0.20         | -0.03        | -0.12          | -0.06            | -0.002               | -0.14          | -0.10           |
| <i>C14</i> | -0.20         | -0.28        | -0.13          | -0.25            | -0.30                | -0.09          | -0.11           |
| <b>C5</b>  | <b>-0.42</b>  | <b>-0.40</b> | <b>-0.44</b>   | <b>-0.55</b>     | <b>-0.44</b>         | <b>-0.59</b>   | <b>-0.61</b>    |
| <b>C6</b>  | <b>-0.42</b>  | <b>-0.43</b> | <b>-0.44</b>   | <b>-0.49</b>     | <b>-0.58</b>         | <b>-0.50</b>   | <b>-0.61</b>    |
| <b>C12</b> | <b>-0.42</b>  | <b>-0.55</b> | <b>-0.60</b>   | <b>-0.55</b>     | <b>-0.59</b>         | <b>-0.59</b>   | <b>-0.61</b>    |
| <b>C13</b> | <b>-0.42</b>  | <b>-0.46</b> | <b>-0.61</b>   | <b>-0.49</b>     | <b>-0.46</b>         | <b>-0.62</b>   | <b>-0.61</b>    |
| <i>C7</i>  | 2.36          | 1.44         | 1.37           | 1.38             | 1.45                 | 1.34           | 1.35            |
| <i>C8</i>  | 2.35          | 2.37         | 2.30           | 2.28             | 1.45                 | 2.25           | 1.33            |
| <i>C9</i>  | 2.35          | 2.23         | 1.37           | 2.28             | 2.27                 | 1.37           | 1.33            |
| <i>C10</i> | 2.36          | 2.31         | 2.30           | 1.38             | 2.32                 | 1.37           | 1.34            |

P2<sub>4S</sub>, which is contrary to the conventional labelling system used to distinguish between peak character in the  $\pi^*$  region.

The shoulder observed emerging at ~285.1 eV in molecules with a higher degree of thionation is also pertinent to the C5 atom and is attributed to the down-shift in excitation energy for the LUMO + 1 state for C5. The relative intensity increase of P2<sub>4S</sub> compared to P2<sub>parent</sub> in the calculated spectra is attributed to an emerging contribution to P2<sub>4S</sub> by the atoms bonded directly to the substituted sulfur atoms: C7-C10 (orange dashed lines). Figure 4 illustrates that, for the parent molecule, these atoms are involved in neither the first nor the second excitation peak in the  $\pi^*$  region due to the large  $\Delta$ IP in the parent molecule. However, the C 1s core excited spectra of the fully thionated molecule, 4S, in the lower panel of Fig. 4, demonstrate a clear contribution by these atoms to the total intensity of the

second excitation peak, further illustrating the down-shift in excitation energy with thionation.

Figure 5 provides final state orbital projections for the excited state LUMO of the parent and 4S molecules, following excitation of various atoms, denoted by colored dots corresponding to the color scheme in Fig. 2(b) and also pointed out by arrows. Focusing first on the parent molecule, the final state orbitals for all three excited atoms exhibit  $\pi$  character, identified by the distribution above and below the plane of the molecule, in the P<sub>z</sub> direction. The final state orbitals resulting from C1 and C5 excitations are similar, extending largely across the entirety of the conjugated part of the molecule. Distinctly, the orbital corresponding to the C8 excitation, while also exhibiting

**TABLE III.** Excited LUMO orbital energies (in eV).

| Atom       | Parent       | 1S           | 2S- <i>cis</i> | 2S- <i>trans</i> | 2S- <i>cis imide</i> | 3S           | 4S           |
|------------|--------------|--------------|----------------|------------------|----------------------|--------------|--------------|
| GS         | -3.50        | -3.61        | -3.66          | -3.66            | -3.69                | -3.72        | -4.11        |
| <b>C2</b>  | <b>-3.59</b> | <b>-3.69</b> | <b>-3.74</b>   | <b>-3.74</b>     | <b>-3.75</b>         | <b>-3.78</b> | <b>-3.82</b> |
| <b>C3</b>  | <b>-3.59</b> | <b>-3.68</b> | <b>-3.74</b>   | <b>-3.74</b>     | <b>-3.74</b>         | <b>-3.79</b> | <b>-3.82</b> |
| <i>C1</i>  | -3.84        | -3.91        | -3.93          | -3.93            | -3.97                | -3.95        | -3.98        |
| <i>C4</i>  | -3.84        | -3.90        | -3.93          | -3.96            | -3.93                | -3.98        | -3.98        |
| <i>C11</i> | -3.84        | -3.93        | -3.95          | -3.96            | -3.96                | -3.97        | -3.98        |
| <i>C14</i> | -3.84        | -3.90        | -3.95          | -3.93            | -3.93                | -3.98        | -3.98        |
| <b>C5</b>  | <b>-3.74</b> | <b>-3.78</b> | <b>-3.83</b>   | <b>-3.87</b>     | <b>-3.82</b>         | <b>-3.90</b> | <b>-3.91</b> |
| <b>C6</b>  | <b>-3.74</b> | <b>-3.82</b> | <b>-3.83</b>   | <b>-3.84</b>     | <b>-3.90</b>         | <b>-3.85</b> | <b>-3.91</b> |
| <b>C12</b> | <b>-3.74</b> | <b>-3.86</b> | <b>-3.88</b>   | <b>-3.87</b>     | <b>-3.90</b>         | <b>-3.89</b> | <b>-3.91</b> |
| <b>C13</b> | <b>-3.74</b> | <b>-3.80</b> | <b>-3.88</b>   | <b>-3.84</b>     | <b>-3.82</b>         | <b>-3.91</b> | <b>-3.91</b> |
| <i>C7</i>  | -3.93        | -4.14        | -4.12          | -4.12            | -4.19                | -4.12        | -4.15        |
| <i>C8</i>  | -3.93        | -4.04        | -4.04          | -4.04            | -4.20                | -4.03        | -4.15        |
| <i>C9</i>  | -3.93        | -3.98        | -4.12          | -4.04            | -3.99                | -4.17        | -4.15        |
| <i>C10</i> | -3.93        | -3.98        | -4.04          | -4.12            | -3.99                | -4.17        | -4.15        |

**TABLE IV.** Bader charge analysis (in units of *e*, the number of electrons). Small differences in symmetry equivalent atoms are not significant, reflecting numerical errors resulting from the finite supercell volume and the density of grid points defined by the plane-wave energy cutoff.

| Atom       | Parent       | 1S           | 2S- <i>cis</i> | 2S- <i>trans</i> | 2S- <i>cis imide</i> | 3S           | 4S          |
|------------|--------------|--------------|----------------|------------------|----------------------|--------------|-------------|
| <b>C2</b>  | <b>0.02</b>  | <b>0.19</b>  | <b>0.18</b>    | <b>0.15</b>      | <b>0.08</b>          | <b>0.01</b>  | <b>0.19</b> |
| <b>C3</b>  | <b>-0.01</b> | <b>0.08</b>  | <b>0.13</b>    | <b>0.13</b>      | <b>-0.02</b>         | <b>0.02</b>  | <b>0.23</b> |
| <i>C1</i>  | 0.14         | -0.08        | -0.06          | -0.04            | 0.07                 | 0.42         | 0.10        |
| <i>C4</i>  | 0.11         | 0.14         | -0.01          | 0.06             | -0.02                | 0.12         | 0.15        |
| <i>C11</i> | -0.02        | -0.03        | 0.06           | 0.08             | 0.05                 | -0.07        | -0.11       |
| <i>C14</i> | 0.07         | 0.06         | 0.05           | -0.02            | -0.06                | -0.21        | -0.13       |
| <b>C5</b>  | <b>-0.06</b> | <b>0.04</b>  | <b>0.10</b>    | <b>-0.12</b>     | <b>-0.05</b>         | <b>-0.12</b> | <b>0.23</b> |
| <b>C6</b>  | <b>-0.04</b> | <b>-0.01</b> | <b>-0.13</b>   | <b>-0.08</b>     | <b>-0.17</b>         | <b>-0.22</b> | <b>0.15</b> |
| <b>C12</b> | <b>-0.19</b> | <b>-0.10</b> | <b>-0.10</b>   | <b>-0.10</b>     | <b>-0.10</b>         | <b>-0.08</b> | <b>0.27</b> |
| <b>C13</b> | <b>0.17</b>  | <b>-0.08</b> | <b>-0.18</b>   | <b>-0.13</b>     | <b>0.01</b>          | <b>0.12</b>  | <b>0.19</b> |
| <i>C7</i>  | -2.65        | 0.27         | 0.43           | 0.35             | 0.40                 | 0.39         | 0.29        |
| <i>C8</i>  | -2.67        | -2.69        | -2.68          | -2.71            | 0.35                 | -2.72        | 0.37        |
| <i>C9</i>  | -2.70        | -2.63        | 0.33           | -2.69            | -2.66                | 0.36         | 0.33        |
| <i>C10</i> | -2.74        | -2.77        | -2.76          | 0.41             | -2.72                | 0.23         | 0.35        |

$\pi$  character, is more localized over the excitation center, although still exhibiting sizeable admixtures from carbon atoms located on the other side of the molecule. Although there is a slight change in the character of the excited state between C1 and C5, compared to C8, the much more drastic change is in the excitation energy difference between the resulting excited-state orbitals (indicated below each orbital in the figure). The  $1s \rightarrow$  LUMO transition energies of C1, C5, and C8 are 284.0 eV, 284.2 eV, and 286.6 eV, respectively. The 2.6 eV difference between the  $1s \rightarrow$  LUMO transition of the C1 atom compared to that of C8 is mainly due to the core level shift (CLS) of the C8 atom, 2.35 eV, highlighting the important role local chemistry plays in the excitation process.

Similar observations can be made for the 4S molecule: The LUMO orbitals exhibit  $\pi$  character that extends across the entire molecule for C1 and C5 excitations. However, the LUMO density distribution resulting from exciting the C8 atom is much more delocalized across the molecule compared to that of the parent molecule. The excitation energy difference between C1 and C8 in the 4S molecule is also reduced to 1.3 eV, compared to the 2.6 eV shift

mentioned earlier for the parent molecule. This is attributed to the 1.33 eV CLS calculated for the 4S molecule. Table II summarizes the calculated IP relative to atom C3 for all carbon atoms and for all molecules. The calculated excited LUMO orbital energies are also tabulated in Table III.

Additionally, Bader charge analysis<sup>39</sup> has been employed to quantify the number of electrons associated with each carbon center in the molecules (Table IV). Because the analysis is performed for the electron density, with subtraction of the nuclear charge, the net negative values in Table IV correspond to positively charged atomic volumes. Therefore, it is observed that the carbon atoms bonded directly to oxygen atoms (C7-C10) in the parent molecule have a net-positive charge, implying a relative oxidized state. Conversely, atoms C7-C10 in the 4S molecule have a net-negative charge, implying a relatively reduced state when compared to C7-C10 in the parent molecule. These differences can be explained chemically: Oxygen has a higher electronegativity than sulfur, resulting in carbon atoms bonded directly to oxygen atoms sharing electrons with the neighboring oxygen atoms. These carbon atoms (C7-C10) then become

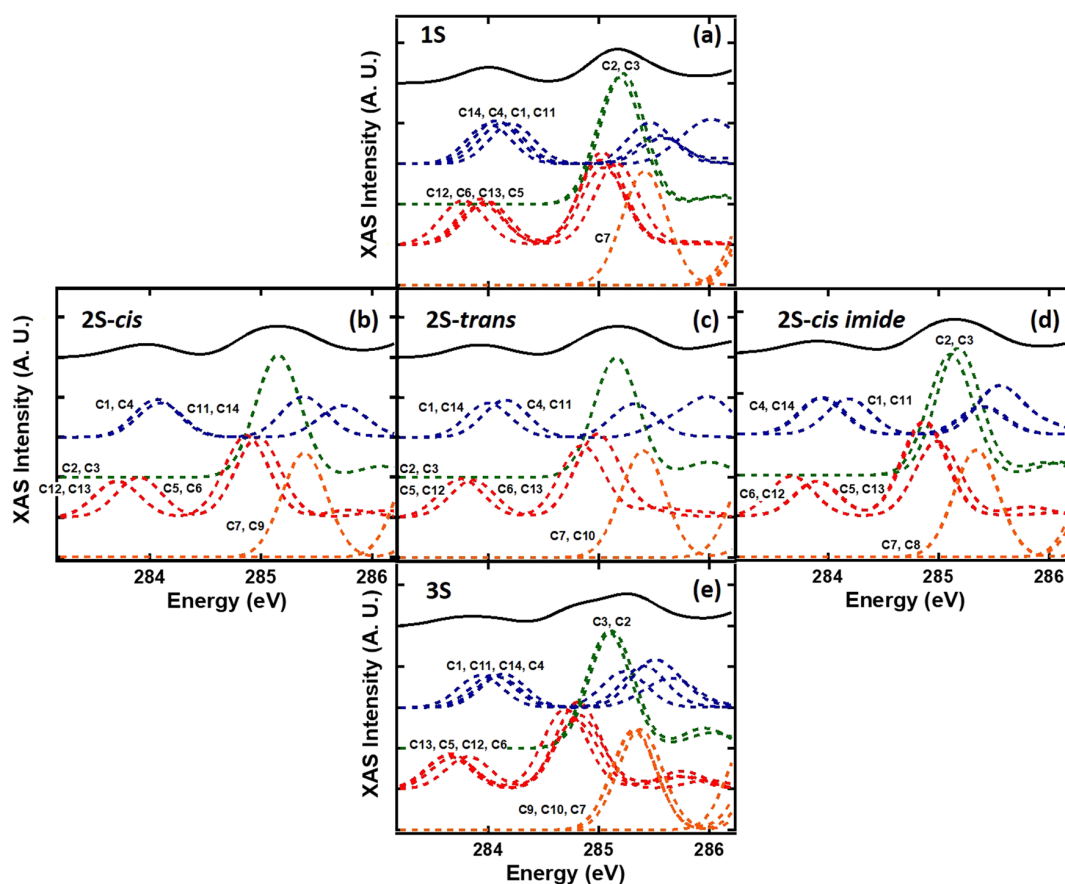


**FIG. 6.** Atomically resolved spectral contributions of the remaining molecules in the series: 1S (a), 2S-cis (b), 2S-trans (c), 2S-cis imide (d), and 3S (e). A break in molecular symmetry results in a noticeable shift in the orbital energies for excited atoms, reflected in a convolution of peak locations.



oxidized and exhibit a large down-shift in the C 1s energy, reflected in the 2.35 eV  $\Delta$ IP listed in Table II. The lower electronegativity associated with sulfur reduces  $\Delta$ IP for the C7-C10 atoms bonded directly to sulfur atoms (compared to when these same atoms are bonded to oxygen atoms as in the parent molecule), resulting in a net-negative charge on these atoms. The IP is therefore significantly reduced at 1.33 eV. This ultimately leads to the lower energy required to excite core electrons to the molecule's LUMO, observed in the experimental NEXAFS spectrum of the 4S molecule, compared to the parent.

Considering the other molecules in the series reveals the effect of an increased degree of thionation and the breaking of symmetry. The 1S and 3S molecules are not symmetric and therefore have no equivalent atoms, reflected in the peak splitting shown in Fig. 6. The C7 atom in the 1S molecule, for example, is the only atom directly bonded to a sulfur atom, with the C7 atom exhibiting a distinct change in IP to the other carbon atoms at the equivalent geometric positions (i.e., that are bonded to oxygen atoms) and with distinct chemical environments. Hence, the C7 atom has an IP of 1.44 eV compared to  $\sim$ 2.3 eV for C8, C9, and C10. Thus, only the 1s  $\rightarrow$  LUMO peak for C7 appears in the energy window of Fig. 6(a) with the 1s  $\rightarrow$  LUMO peaks for C8, C9, and C10 remaining at higher energies. The breaking of symmetry also has a subtle effect on the other atoms in 1S. The atoms nearby C7, namely, C11 and C12, have distinct core energies compared to their equivalents. Interestingly, C11 experiences a positive relative change in IP, while C12 experiences a negative relative change in IP. The other nearest carbon atoms, C8 and C1, are not affected as much likely due to the nitrogen atom in between C7 and C8, C1. The two-fold symmetry of the 2S derivatives restores some symmetry with pairs of equivalent atoms, indicated in the central panel in Fig. 6. Similar to the case for 1S, in these 2S derivatives, the proximity of the excited carbon atom to a sulfur atom is also reflected in the change in IP: Carbon atoms closer to sulfur atoms exhibit a smaller IP compared to carbon atoms located closer to oxygen atoms (see Table II). HOMO, LUMO, and LUMO + 1 orbitals for all molecules studied in this series are available in the supplementary material, as well as excited-state orbitals for each non-equivalent atomic excitation. Calculations of LUMO energies (Table III) and Bader analysis (Table IV) are also reported for all atoms. It is noted that thionation also produces changes in the LUMO energy levels; however, these changes are subtle compared to the changes in IP. Thus, while changes in the optical properties of the materials are dominated by changes in the HOMO and LUMO levels with thionation, it is the changes in the energies of the ionization potential that are responsible for the major changes in the NEXAFS spectra.

## CONCLUSIONS

Using first-principles calculations based on the density functional theory, we have calculated the NEXAFS spectra of a series of NDI molecules with systematically increasing degrees of thionation. Good agreement between experimental and calculated spectra was found, with the evolution of near-edge structure understandable in terms of changes in the core-level shifts of the constituent atoms. Due to the large  $\Delta$ IP of the atoms bonded to oxygen atoms, the C 1s  $\rightarrow$  LUMO transitions associated with these atoms in the parent NDI molecule are shifted to higher energies and do not appear

within the 284 eV to 286 eV range generally associated with 1s  $\rightarrow$  LUMO transitions. The vastly different chemical environments in NDI-based molecules thus result in a mixing of character in the experimentally measured 1s  $\rightarrow$   $\pi^*$  manifold. This means that even for the parent NDI molecule, the different peaks in the 1s  $\rightarrow$   $\pi^*$  manifold cannot be exclusively associated with the transitions of 1s  $\rightarrow$  LUMO, 1s  $\rightarrow$  LUMO + 1, etc. Thionation results in shifting of the peaks associated with the C 1s  $\rightarrow$  LUMO transitions of carbon atoms previously bonded to oxygen atoms. The ionization potentials of other atoms are also changed by thionation to a lesser degree, dependent upon proximity to the substituted atom and symmetry, resulting in further splitting and shifting of peaks. This analysis is particularly useful for the interpretation of NEXAFS spectra, with the knowledge of the atom-specific origins of peaks and associated molecular orbitals important for the use of NEXAFS spectroscopy and related techniques to probe molecular orientation. Understanding the molecular and chemical origins of peaks is also key for techniques that use NEXAFS-based contrast for probing the structure of organic semiconductor blends.

## SUPPLEMENTARY MATERIAL

See supplementary material for the comparison of experimental and calculated NEXAFS spectra out to 300 eV, effect of changing side chain on the calculated spectra, effect of side chain on experimental spectra, and molecular orbital projections of HOMO, LUMO, and LUMO + 1 for neutral molecules.

## ACKNOWLEDGMENTS

X-ray absorption theory and simulations were performed as part of a user project with DP at The Molecular Foundry (TMF), Lawrence Berkeley National Laboratory (LBNL). Computing resources were provided in part by TMF, managed by the High Performance Computing Services Group at LBNL, and by the National Energy Research Scientific Computing center (NERSC). TMF and NERSC are U.S. Department of Energy Office of Science User Facilities at LBNL operated under Contract No. DE-AC02-05CH11231. The authors would like to thank Artem Baskin for helpful discussions.

## REFERENCES

- H. Dong, X. Fu, J. Liu, Z. Wang, and W. Hu, *Adv. Mater.* **25**, 6158 (2013).
- H. Sirringhaus, *Adv. Mater.* **26**, 1319 (2014).
- Y. Zhao, Y. Guo, and Y. Liu, *Adv. Mater.* **25**, 5372 (2013).
- L. Dou, J. You, Z. Hong, Z. Xu, G. Li, R. A. Street, and Y. Yang, *Adv. Mater.* **25**, 6642 (2013).
- A. J. Heeger, *Synth. Met.* **125**, 23 (2001).
- C. W. Tang, *Appl. Phys. Lett.* **48**, 183 (1986).
- J. H. Burroughes, D. D. C. Bradley, A. R. Brown, R. N. Marks, K. Mackay, R. H. Friend, P. L. Burns, and A. B. Holmes, *Nature* **347**, 539 (1990).
- J. Stöhr, *NEXAFS Spectroscopy* (Springer, Berlin, 1992).
- H. Ade and A. P. Hitchcock, *Polymer* **49**, 643 (2008).
- D. Prendergast and G. Galli, *Phys. Rev. Lett.* **96**, 215502 (2006).
- G. M. Su, S. N. Patel, C. D. Pemmaraju, D. Prendergast, and M. L. Chabiny, *J. Phys. Chem. C* **121**, 9142 (2017).
- G. Fratesi, V. Lanzilotto, S. Stranges, M. Alagia, G. P. Brivio, and L. Floreano, *Phys. Chem. Chem. Phys.* **16**, 14834 (2014).

- <sup>13</sup>R. Püttner, P. Schmidt-Weber, T. Kampen, C. Kolczewski, K. Hermann, and K. Horn, *J. Electron Spectrosc. Relat. Phenom.* **215**, 16 (2017).
- <sup>14</sup>C. Ehlert, M. Holzweber, A. Lippitz, W. E. S. Unger, and P. Saalfrank, *Phys. Chem. Chem. Phys.* **18**, 8654 (2016).
- <sup>15</sup>H. Ade and S. Urquhart, in *Chemical Applications of Synchrotron Radiation*, edited by T.-K. Sham (World Scientific, 2002), pp. 285–355.
- <sup>16</sup>M. M. Nahid, E. Gann, L. Thomsen, and C. R. McNeill, *Eur. Polym. J.* **81**, 532 (2016).
- <sup>17</sup>Z. Chen, Y. Zheng, H. Yan, and A. Facchetti, *J. Am. Chem. Soc.* **131**, 8 (2009).
- <sup>18</sup>L. Gao, Z. G. Zhang, L. Xue, J. Min, J. Zhang, Z. Wei, and Y. Li, *Adv. Mater.* **28**, 1884 (2016).
- <sup>19</sup>L. M. Kozycz, C. Guo, J. G. Manion, A. J. Tilley, A. J. Lough, Y. Li, and D. S. Seferos, *J. Mater. Chem. C* **3**, 11505 (2015).
- <sup>20</sup>F. S. Etheridge, R. Fernando, J. A. Golen, A. L. Rheingold, and G. Sauve, *RSC Adv.* **5**, 46534 (2015).
- <sup>21</sup>N. Pearce, E. S. Davies, R. Horvath, C. R. Pfeiffer, X.-Z. Sun, W. Lewis, J. McMaster, M. W. George, and N. R. Champness, *Phys. Chem. Chem. Phys.* **20**, 752 (2018).
- <sup>22</sup>A. Welford, S. Maniam, E. Gann, L. Thomsen, S. J. Langford, and C. R. McNeill, *Org. Electron.* **53**, 287 (2018).
- <sup>23</sup>P. Jiang, D. Prendergast, F. Borondics, S. Porsgaard, L. Giovanetti, E. Pach, J. Newberg, H. Bluhm, F. Besenbacher, and M. Salmeron, *J. Chem. Phys.* **138**, 024704 (2013).
- <sup>24</sup>A. H. England, A. M. Duffin, C. P. Schwartz, J. S. Uejio, D. Prendergast, and R. J. Saykally, *Chem. Phys. Lett.* **514**, 187 (2011).
- <sup>25</sup>P. Giannozzi, S. Baroni, N. Bonini, M. Calandra, R. Car, C. Cavazzoni, D. Ceresoli, G. L. Chiarotti, M. Cococcioni, I. Dabo, A. Dal Corso, S. De Gironcoli, S. Fabris, G. Fratesi, R. Gebauer, U. Gerstmann, C. Gougoussis, A. Kokalj, M. Lazzeri, L. Martin-Samos, N. Marzari, F. Mauri, R. Mazzarello, S. Paolini, A. Pasquarello, L. Paulatto, C. Sbraccia, S. Scandolo, G. Sclauzero, A. P. Seitsonen, A. Smogunov, P. Umari, and R. M. Wentzcovitch, *J. Phys.: Condens. Matter* **21**, 395502 (2009).
- <sup>26</sup>J. P. Perdew, K. Burke, and M. Ernzerhof, *Phys. Rev. Lett.* **77**, 3865 (1996).
- <sup>27</sup>D. Vanderbilt, *Phys. Rev. B* **41**, 7892 (1990).
- <sup>28</sup>M. Taillefumier, D. Cabaret, A. M. Flank, and F. Mauri, *Phys. Rev. B: Condens. Matter Mater. Phys.* **66**, 1 (2002).
- <sup>29</sup>O. Shih, A. H. England, G. C. Dallinger, J. W. Smith, K. C. Duffey, R. C. Cohen, D. Prendergast, and R. J. Saykally, *J. Chem. Phys.* **139**, 135104 (2013).
- <sup>30</sup>J. S. Uejio, C. P. Schwartz, R. J. Saykally, and D. Prendergast, *Chem. Phys. Lett.* **467**, 195 (2008).
- <sup>31</sup>D. Prendergast and S. G. Louie, *Phys. Rev. B: Condens. Matter Mater. Phys.* **80**, 235126 (2009).
- <sup>32</sup>E. L. Shirley, *Phys. Rev. B: Condens. Matter Mater. Phys.* **54**, 16464 (1996).
- <sup>33</sup>F. Aryasetiawan and O. Gunnarsson, *Rep. Prog. Phys.* **61**, 237 (1998).
- <sup>34</sup>L. Hedin, *Phys. Rev.* **139**, A796 (1965).
- <sup>35</sup>A. D. Becke, *J. Chem. Phys.* **98**, 1372 (1993).
- <sup>36</sup>M. E. Casida, in *Recent Advances in Density Functional Methods, Part 1*, edited by D. P. Chong (World Scientific, Singapore, 1995), p. 155.
- <sup>37</sup>E. E. Salpeter and H. A. Bethe, *Phys. Rev.* **84**, 1232 (1951).
- <sup>38</sup>Z. Ma, H. Geng, D. Wang, and Z. Shuai, *J. Mater. Chem. C* **4**, 4546 (2016).
- <sup>39</sup>W. Tang, E. Sanville, and G. Henkelman, *J. Phys.: Condens. Matter* **21**, 84204 (2009).

## 7.3 Conclusions

This chapter successfully employed the XCH approach to predict the NEXAFS spectra for the series of thionated NDI molecules shown in Figure 2.21. Additional analysis shows the strong impact that sulfur substitutional atoms have on the electron distribution over the entire molecule, which is more delocalized over the whole molecule, compared to the parent molecule, whose four, highly electronegative, oxygen atoms pull the electron density to the outer edges of the molecule. The calculations also highlight the mixing of character for peaks calculated in the  $\pi^*$  region, which is in contradiction to the conventional peak labeling system that refers to the first peak as the LUMO peak, the second as the LUMO + 1, *etc.* This understanding helps to explain why transitions from certain sites are possible at a given energy, while at other sites, at that same energy, they are not. Ultimately, this chapter provides a detailed explanation of why seemingly simple changes in chemical structure can lead to drastic variations in the electronic properties of organic semiconductors.

# References

- [1] R. G. Parr, “Density Functional Theory of Atoms and Molecules,” in *Horizons of Quantum Chemistry*, pp. 5–15, 1980.
- [2] C. Ehlert, M. Holzweber, A. Lippitz, W. E. S. Unger, and P. Saalfrank, “A detailed assignment of NEXAFS resonances of imidazolium based ionic liquids,” *Physical Chemistry Chemical Physics*, vol. 18, no. 12, pp. 8654–8661, 2016.
- [3] G. M. Su, S. N. Patel, C. D. Pemmaraju, D. Prendergast, and M. L. Chabinyc, “First-principles predictions of near-edge X-ray absorption fine structure spectra of semiconducting polymers,” *The Journal of Physical Chemistry C*, vol. 121, no. 17, pp. 9142–9152, 2017.
- [4] D. Prendergast and G. Galli, “X-Ray absorption spectra of water from first principles calculations,” *Physical Review Letters*, vol. 96, p. 215502, 2006.
- [5] A. Welford, S. Maniam, E. Gann, L. Thomsen, S. J. Langford, and C. R. Mcneill, “Thionation of naphthalene diimide molecules: Thin-film microstructure and transistor performance,” *Organic Electronics*, vol. 53, pp. 287–295, 2018.



# Chapter 8

## Conclusions and outlook

### 8.1 Conclusions

The aim of this thesis was to determine the effect that substituent and substitutional atoms, along with molecular structure, have on the optoelectronic and morphological properties of naphthalene diimide-based small molecule and polymeric acceptors in organic solar cells, and how these properties influence solar cell performance. This required a large range of techniques that encompassed both experimental and theoretical approaches. Although this thesis did not survey all possible substituent and substitutional atoms that can be used to modify the properties of the NDI moiety, it has evaluated oxygen, sulfur, and nitrogen as possible core substituents, and increasing degrees of thionation of the imide oxygens as substitutional modifications. A significant theme of this work is to demonstrate that, while all substituents and substitutional atoms do influence the optical and electronic properties of NDI, they do so to varying degrees and with a broad range of implications to solar cell performance, and that it is not possible to definitively say that one substituent (i.e. sulfur) is necessarily the best to use for any situation. These conclusions are summarized in more detail below.

Chapter 4 explored the effect that core oxygen, sulfur, and nitrogen substituents have on the properties of the NDI moiety. Although it was not expected that these molecules would exhibit high solar cell performance (due to the strong aggregation of the NDI moiety), distinctions in the optical, electronic, and physical properties of the molecules strongly influenced OPV efficiency. For example, it was shown that the additional core substituents reduce the optical band gap of NDI significantly, changing the color of the molecule from white (parent) to red for oxygen, yellow for sulfur, and blue for nitrogen. The reduced band gap allowed for additional photon absorption by the acceptor material in solar cells, giving the devices' short-circuit current and external quantum efficiency a noticeable boost for NDI-O and NDI-S-based devices. However, for NDI-N, it was shown that the LUMO was raised sufficiently to be above that of the donor material, resulting in a dramatic decrease in efficiency with almost no EQE response from the donor, indicating extremely inefficient charge separation. Substituent atoms were further shown to disrupt the 3D crystalline packing order of the parent molecule, which can also have implications for efficient solar cell performance. However, it was ultimately found that the small size of the NDI moiety was not ideal for both active layer morphology and charge transport, and intelligent molecular design modifications were necessary to improve the performance of core-substituted NDI-based small molecule acceptors.

In order to expand upon the findings of Chapter 4, Chapter 5 utilized the same three substituents (oxygen, sulfur, and nitrogen) but with added changes to molecular structure, which intended to increase the conjugation length in order to realize efficient solar cell operation. Two molecular structures were used: one incorporating a triarylamine core with three flanking NDI moieties, and the other linking two NDIs via a bithiophene bridge (analogous to the well-known polymer, PNDIT2). The resulting solar cells fabricated with these materials showed enhanced power conversion efficiencies over their smaller NDI constituents. In particular, the Star NDI-S material exhibited a PCE of 2.4%, which was amongst the highest power conversion efficiencies for any NDI-based small molecule acceptor at the time of publication in 2017. Further analysis into the active layer morphology of the star shaped materials revealed that the addition of the triarylamine linker did indeed suppress the aggregation of the acceptor molecules, resulting in favorable active layer morphologies. However, as with the molecules explored in Chapter 4, it was shown that the electronic properties of the material were largely influenced by the substituent atom, with the Star NDI-N material exhibiting poor solar cell performance due to its low exciton dissociation ability with the donor material. Ultimately, these two chapters highlight the importance of not only selecting appropriate substituent atoms, but also incorporating strategic molecular design that enables optimum active layer morphologies.

After establishing the significant influence that both molecular structure and substituent atoms have on the optoelectronic properties of NDI-based materials, Chapter 6 explored the effect of thionation on NDI-based materials incorporating both small molecule as well as polymeric structures. Although thionated NDI molecules were explored, emphasis was placed on how thionation affects PNDIT2 – one of the most efficient polymeric acceptor materials to-date, exhibiting over 11% PCE as of early 2019.<sup>1</sup> This was based on thionation being demonstrated as a successful strategy in improving electron mobility of the NDI moiety in organic field-effect transistors,<sup>2,3</sup> with the goal being to further enhance the efficiency of solar cells incorporating a thionated acceptor polymer. However, Chapter 6 illustrated that thionation dramatically reduces the performance of PBDTTT-EFT:PNDIT2 solar cells, due primarily to the reduced  $\pi - \pi$  stacking behavior of the acceptor polymer, ensuing from increased levels of thionation. The sharp decrease in electron mobility of these materials is also to blame for the large drop in efficiency. Further, the incorporation of sulfur atoms in the NDI moiety resulted in a narrowing of the band gap of PNDIT2, reducing the  $\text{HOMO}_{\text{donor}} - \text{LUMO}_{\text{acceptor}}$  offset, which caused a significant reduction in device  $V_{OC}$  values. It was thus concluded that thionation is not an effective strategy in improving the performance of PNDIT2 as an acceptor in all-polymer solar cells.

Following the dramatic revelations of Chapter 6, in which it was demonstrated that seemingly subtle chemical modifications of NDI-based acceptors not only drastically alter their physical, but also their electronic structure, Chapter 7 aimed to better understand these changes through theoretical modeling. This was achieved by utilizing DFT-based calculations to predict the near-edge X-ray absorption fine structure spectra for a series of NDI molecules with increasing degrees of thionation. This series had previously been shown to exhibit systematic changes in the  $\pi^*$  region of the carbon K-edge NEXAFS spectrum,<sup>3</sup> however limitations in the resolution of NEXAFS experiments hinder the full interpretation of these systematic changes. The eXcited electron and Core Hole approach was used to calculate NEXAFS spectra, with the added advantage of being able to break the average X-ray absorption spectra into contributions

of each carbon atom, excited individually. This revealed that oxygen substitutional atoms result in strong core level shifts within the molecule, pulling the electron density from the center of the molecule towards the outer oxygen atoms. However, the reduced electronegativity of sulfur substitutional atoms resulted in the electron density being more localized over the center of the molecule. It was also demonstrated that the peaks in the  $\pi^*$  region of the NEXAFS spectra are a result of excitations to a mixture of final-state orbitals as opposed to just one, contradicting conventional peak labeling protocol in this energy region. Such a thorough characterization of the  $\pi^*$  region of NDI is vital for proper interpretation of NEXAFS results, and this chapter serves to provide examples for one series of modified molecules, which can be extrapolated and applied to similar systems.

## 8.2 Outlook

Following the work presented in this thesis, there is great potential to further explore the effect that various other substituent atoms have on not only naphthalene diimide, but also additional building blocks commonly used in OPV research. For example, the oxygen, sulfur and nitrogen atoms used as substituents in Chapter 4 could also be used to modify the properties of perylene diimide (PDI), which has historically exhibited higher OPV efficiencies due to the extended electron delocalization offered by the larger backbone of PDI compared to NDI.<sup>4</sup> Additionally, core fluorination has been shown to improve the electron mobility in NDI-based molecules used in organic field effect transistors,<sup>5</sup> which could also have positive implications for solar cell operation.

Chapter 5 utilized two molecular structures that served to increase the conjugation length of NDI-based molecular acceptors, including a bithiophene bridge as well as a triarylamine core to realize a star-shaped molecule. Despite both of these structures exhibiting higher OPV device performance compared to the core-substituted molecules presented in Chapter 4, they are not nearly an exhaustive list of the potential molecular structures that could be used to improve the conjugation length of an NDI-based molecular acceptor. Future work in this area could include a nearly infinite number of molecular structures, however there is a smaller number of structures that have been used to successfully improve the performance of PDI-based molecular acceptors, which have, historically, received more attention than their smaller, NDI-based counterparts. For example, Zhang and coworkers<sup>6</sup> first introduced a PDI-based small molecule acceptor that utilized a selenophenyl bridge to link two PDI units together, coupled with oxygen core substituents. This material, paired with the donor material, PBDTTT-C-T, exhibited a power conversion efficiency of over 4% in OPV devices. Conversely, Wu et al.<sup>7</sup> showed that four PDI units linked via a 4,8-bis(5-alkyl-2-thienyl)-benzo[1,2-b:4,5-b']dithiophene (BDT-Th) unit could demonstrate power conversion efficiencies above 8%. It would therefore be warranted to further explore the potential of alternative molecular structures to continue to improve upon the record efficiencies of NDI-based molecular acceptors.

The conclusions that were drawn from Chapter 6 are somewhat contradictory: 2*S-trans* thionation of an NDI molecule improved the solar cell efficiency in a molecular structure, but significantly reduced efficiency when a polymeric structure was used. It would therefore be interesting and warranted to further explore additional potential



molecular and polymeric structures in order to better optimize thionation as a strategy to improve solar cell performance.

Finally, the calculations pertaining to Chapter 7 can be applied to investigate the X-ray absorption spectra of any organic semiconductor, beyond those explored in this thesis. For example, calculating XAS spectra for the molecules presented in Chapter 4 would be of great interest, to further understand how oxygen, sulfur, and nitrogen individually impact the structure observed in the  $\pi^*$  region of the carbon K-edge. However, the XCH approach could also be used to calculate the fine structure of extremely high-performing materials, in order to better understand their electronic structure and how it leads to high solar cell efficiencies.

Although not pertaining directly to NDI-based small molecules, the past three years has seen significant improvements in organic solar cell efficiency, made possible by the discovery and subsequent intelligent modifications of small molecule acceptors for organic solar cells. Just recently (January 2019), a new article was published in *Joule*, featuring a polymeric donor:small molecule acceptor active layer blend that exhibits power conversion efficiencies as high as 15.7%.<sup>8</sup> Further, this publication demonstrates that only minimal losses in efficiency occur when the active layer is deposited at thicknesses up to 300 nm - a key criteria for commercialization due to limitations in the accuracy of film deposition when organic cells are fabricated on a roll-to-roll process.<sup>9</sup>

Additional exploration into the viability of commercialization for organic solar cells has demonstrated compelling predictions for the financial outlook of solar energy derived from organic photovoltaics.<sup>10</sup> In November of 2018, Guo *et al.*<sup>10</sup> published a cost analysis for solution processed organic solar cells, produced on a mass scale. They found that, for regions with an ample solar resource, as in Australia, the levelized cost of energy (LCOE) for printed organic photovoltaic modules with 10% efficiency and a 20 year lifetime with 0.05% annual degradation, could be as low as \$0.02 AUD/kWh - substantially lower than the \$0.10 – \$0.17 AUD/kWh for energy derived from solar cells in Australia today.<sup>11</sup> Findings over the past several months have proven that the first assumption, of 10% efficiency, is already feasible with today's technology, however performance, with minimal annual degradation, is still of concern. One study, from 2015, in which an atmosphere-controlled chamber with less than 0.1 ppm water and oxygen was used to house encapsulated solar cells, demonstrated an extrapolated lifetime as high as 20 years for a polymer:fullerene system.<sup>12</sup> This degradation is predominantly caused by an initial "burn-in," which is a fast degradation of almost 40% initially, which slows over time, giving way to a more gradual period of linear degradation. This is therefore not consistent with the stable 0.05% annual degradation assumed by Guo *et al.*, and it is essential to design materials that are not susceptible to such drastic burn-in degradation, and exhibit only limited, gradual reductions in performance over time. Eliminating fullerenes from the active layer blend is one key strategy to reducing the degradation, discussed in more detail in the Introduction Chapter. However a similar study for a polymer:small molecule system is lacking from the existing literature.

Overall, the outlook for commercialization of organic solar cells appears positive, particularly with the recent advancements that have been made with alternative small molecule electron acceptor materials. As such, there has already been an increase in the number of companies that sell organic solar cells, although these are still only being used in niche applications, and on a small scale. Expansion of such products to grow the OPV market will further promote the mainstream adoption of organic solar

---

cells on a mass scale.



# References

- [1] Z. Li, L. Ying, P. Zhu, W. Zhong, N. Li, F. Liu, F. Huang, and Y. Cao, “A generic green solvent concept boosting the power conversion efficiency of all-polymer solar cells to 11%,” *Energy and Environmental Science*, vol. 12, no. 1, pp. 157–163, 2019.
- [2] N. Pearce, E. S. Davies, R. Horvath, C. R. Pfeiffer, X.-Z. Sun, W. Lewis, J. McMaster, M. W. George, and N. R. Champness, “Thionated naphthalene diimides: Tuneable chromophores for applications in photoactive dyads,” *Physical Chemistry Chemical Physics*, vol. 20, pp. 752–764, 2018.
- [3] A. Welford, S. Maniam, E. Gann, L. Thomsen, S. J. Langford, and C. R. Mcneill, “Thionation of naphthalene diimide molecules: Thin-film microstructure and transistor performance,” *Organic Electronics*, vol. 53, pp. 287–295, 2018.
- [4] H.-W. Luo and Z.-T. Liu, “Recent developments of di-amide/imide-containing small molecular non-fullerene acceptors for organic solar cells,” *Chinese Chemical Letters*, vol. 27, no. 8, pp. 1283–1292, 2016.
- [5] Z. Yuan, Y. Ma, T. Gessner, M. Li, L. Chen, M. Eustachi, T. R. Weitz, C. Li, and K. Muellen, “Core-fluorinated naphthalene diimides: synthesis, characterization, and application in n-type organic field-effect transistors,” *Organic Letters*, vol. 18, no. 3, pp. 456–459, 2016.
- [6] X. Zhang, J. Yao, and C. Zhan, “A selenophenyl bridged perylene diimide dimer as an efficient solution-processable small molecule acceptor,” *Chemical Communications*, vol. 51, no. 6, pp. 1058–61, 2014.
- [7] Q. Wu, D. Zhao, A. M. Schneider, W. Chen, and L. Yu, “Covalently Bound Clusters of Alpha-Substituted PDI—Rival Electron Acceptors to Fullerene for Organic Solar Cells,” *Journal of the American Chemical Society*, vol. 138, no. 23, pp. 7248–7251, 2016.
- [8] J. Yuan, Y. Zhang, L. Zhou, G. Zhang, H.-L. Yip, T.-K. Lau, X. Lu, C. Zhu, H. Peng, P. A. Johnson, M. Leclerc, Y. Cao, J. Ulanski, Y. Li, and Y. Zou, “Single-Junction Organic Solar Cell with over 15% Efficiency Using Fused-Ring Acceptor with Electron-Deficient Core,” *Joule*, 2019.
- [9] R. Xue, J. Zhang, Y. Li, and Y. Li, “Organic Solar Cell Materials toward Commercialization,” *Small*, vol. 14, no. 41, 2018.
- [10] J. Guo and J. Min, “A Cost Analysis of Fully Solution-Processed ITO-Free Organic Solar Modules,” *Advanced Energy Materials*, vol. 9, no. 3, 2019.

- [11] “Solar Report,” *Australian Energy Council*, 2018.
- [12] W. R. Mateker, I. T. Sachs-Quintana, G. F. Burkhard, R. Cheacharoen, and M. D. McGehee, “Minimal long-term intrinsic degradation observed in a polymer solar cell illuminated in an oxygen-free environment,” *Chemistry of Materials*, vol. 27, no. 2, pp. 404–407, 2015.

# Appendix A

## Supplementary material for Chapter 4

The appendix for Chapter 4 contains the following data:

- Cyclic voltammograms and corresponding opto-electronic properties for NDI-P, NDI-O, NDI-S, and NDI-N
- 2D GIWAXS image for a neat PBDTTT-EFT film

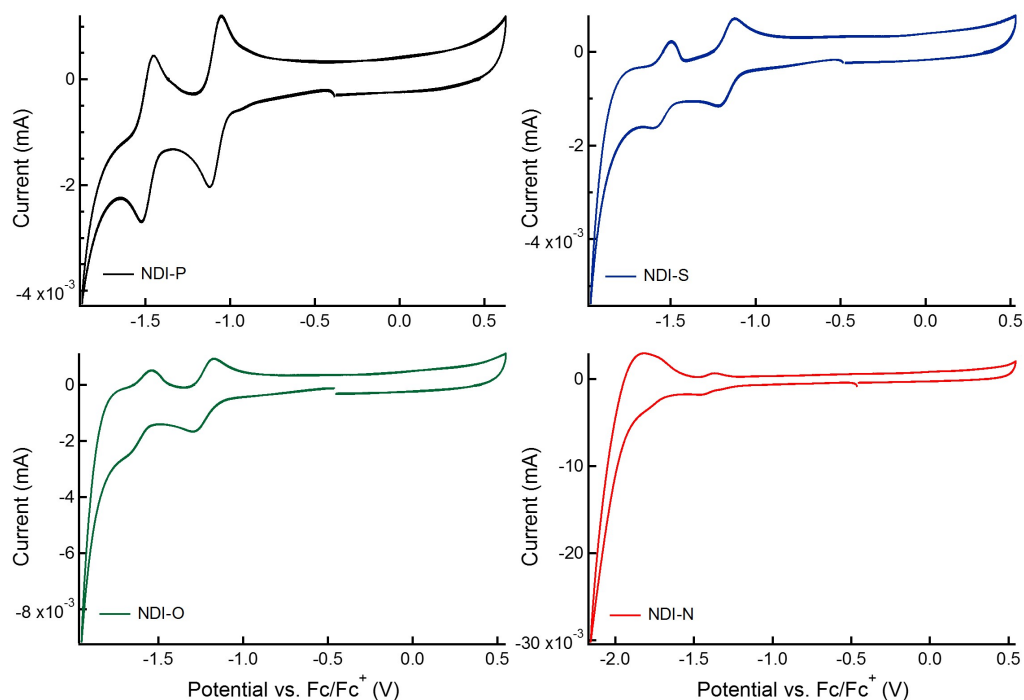


Figure A.1: Cyclic voltammograms for the NDI-based small molecule acceptors versus ferrocene.

| Mat.  | $E_{1/2, Fc/Fc^+}$ (V) | $E_{1/2}^{red}$ (V) | $\lambda_{abs, onset}$ (eV) | $E_{LUMO}$ (eV) | $E_{HOMO}$ (eV) |
|-------|------------------------|---------------------|-----------------------------|-----------------|-----------------|
| NDI-P | 0.37                   | -1.07               | 3.08                        | -3.73           | -6.81           |
| NDI-O | 0.45                   | -1.24               | 2.52                        | -3.56           | -6.08           |
| NDI-S | 0.47                   | -1.17               | 2.18                        | -3.63           | -5.81           |
| NDI-N | 0.46                   | -1.42               | 1.87                        | -3.38           | -5.25           |

Table A.1: Opto-electronic properties for the NDI-based small molecules. The HOMO energy level was determined from the difference between the electrochemically determined LUMO energy and the optical absorption onset from solution UV-visible measurements.

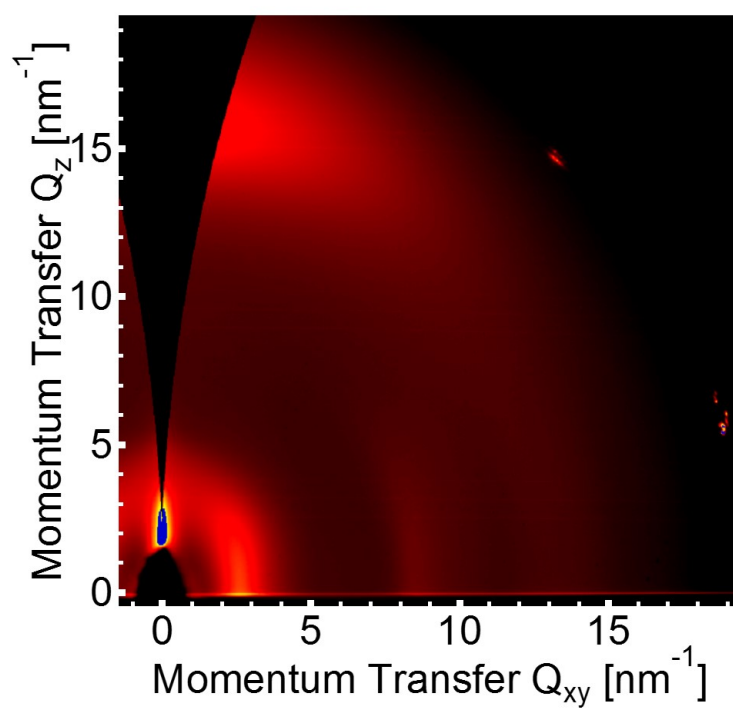


Figure A.2: 2D GIWAXS image for a neat PBDTTT-EFT film.





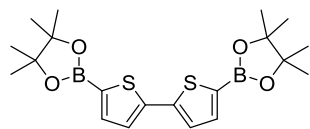
# Appendix B

## Supplementary material for Chapter 5

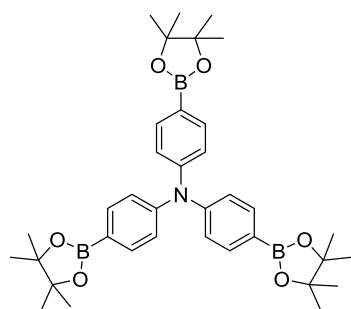
The appendix for Chapter 5 contains the electronic supplementary information for *Naphthalene diimide-based small molecule acceptors for organic solar cells*, which includes the following data:

- Additional synthesis for the six materials
- Cyclic voltammograms and experimental information
- Solution and thin film absorption data
- Device Optimization
- 1D GIWAXS profiles
- Photoluminescence quenching data
- SCLC data for Star NDI-O

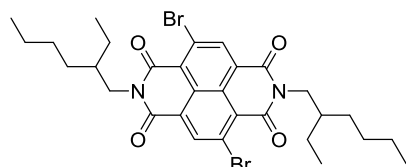
## Additional Synthesis

**5,5'-bis(4,4,5,5-tetramethyl-1,3,2-dioxaborolan-2-yl)-2,2'-bithiophene**

Off white solid (2.85 g, 56%). M.p. 210-211 °C.  $^1\text{H}$  NMR (400 MHz,  $\text{CDCl}_3$ )  $\delta$  7.52 (d,  $J$  = 3.6, 2H, ArH), 7.28 (d,  $J$  = 3.6, 2H, ArH), 1.35 (s, 24H,  $\text{CH}_3$ ).  $^{13}\text{C}$  NMR (100 MHz,  $\text{CDCl}_3$ )  $\delta$  144.0, 138.1, 125.8, 84.4, 24.9. LRMS (ESI)  $m/z$  obsd  $[\text{M}+\text{Na}]^+$  441.1, calcd  $\text{C}_{20}\text{H}_{28}\text{B}_2\text{NaO}_4\text{S}_2$   $[\text{M}+\text{Na}]^+$  441.2.

**tris(4-(4,4,5,5-tetramethyl-1,3,2-dioxaborolan-2-yl)phenyl)amine**

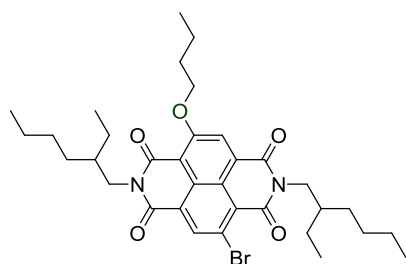
White solid (4.20 g, 83%). M.p. >300 °C.  $^1\text{H}$  NMR (400 MHz,  $\text{CDCl}_3$ )  $\delta$  7.69-7.67 (m, 6H, ArH), 7.09-7.06 (m, 6H, ArH), 1.34 (s, 36H,  $\text{CH}_3$ ).  $^{13}\text{C}$  NMR (100 MHz,  $\text{CDCl}_3$ )  $\delta$  149.9, 136.1, 123.6, 83.8, 25.0. LRMS (ESI)  $m/z$  obsd  $[\text{M}+\text{Na}]^+$  646.3, calcd  $\text{C}_{36}\text{H}_{48}\text{B}_3\text{NNaO}_6$   $[\text{M}+\text{Na}]^+$  646.2.

**4,9-dibromo-2,7-bis(2-ethylhexyl)benzo[lmn][3,8]phenanthroline-1,3,6,8(2H,7H)-tetraone**

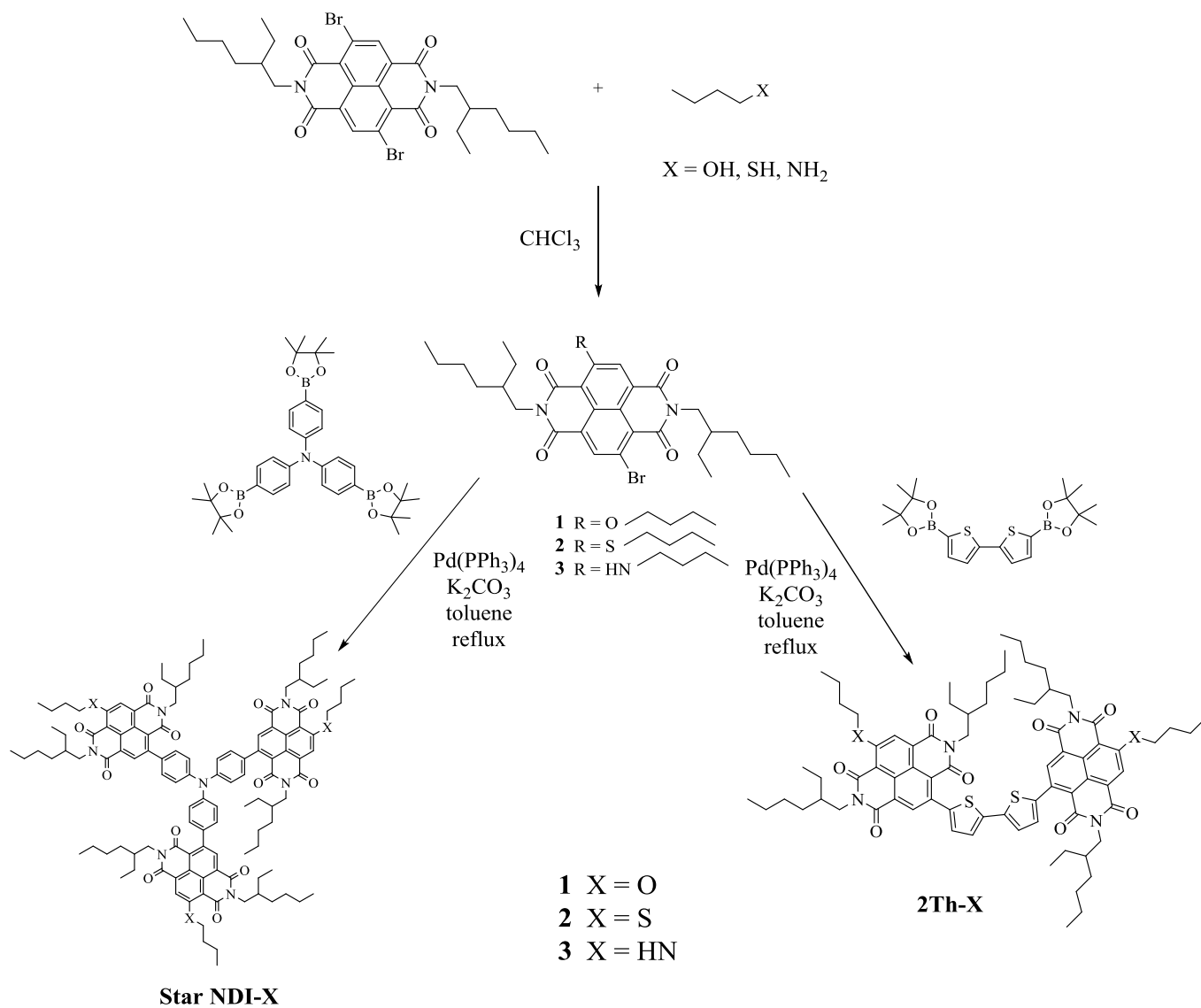
Yellow solid (600 mg, 30%). M.p. 246-248 °C.  $^1\text{H}$  NMR (400 MHz,  $\text{CDCl}_3$ )  $\delta$  9.00 (s, 2H, NDI), 4.20-4.11 (m, 4H,  $\text{CH}_2$ ), 1.97-1.91 (m, 2H, CH), 1.41-1.25 (m, 16H,  $\text{CH}_2$ ), 0.95-0.87 (m, 12,  $\text{CH}_3$ ).  $^{13}\text{C}$  NMR (100 MHz,  $\text{CDCl}_3$ )  $\delta$  161.4, 161.2, 139.3, 128.5, 127.9, 125.5, 124.3, 45.3, 37.9, 30.8, 28.7, 24.1, 23.2, 14.2, 10.7. LRMS (ESI)  $m/z$  obsd  $[\text{M}+\text{H}]^+$  649.1, calcd  $\text{C}_{30}\text{H}_{37}\text{Br}_2\text{N}_2\text{O}_4$   $[\text{M}+\text{H}]^+$  649.1.

**4-bromo-9-butoxy-2,7-bis(2-ethylhexyl)benzo[lmn][3,8]phenanthroline-1,3,6,8(2H,7H)-tetraone (Compound 1)**

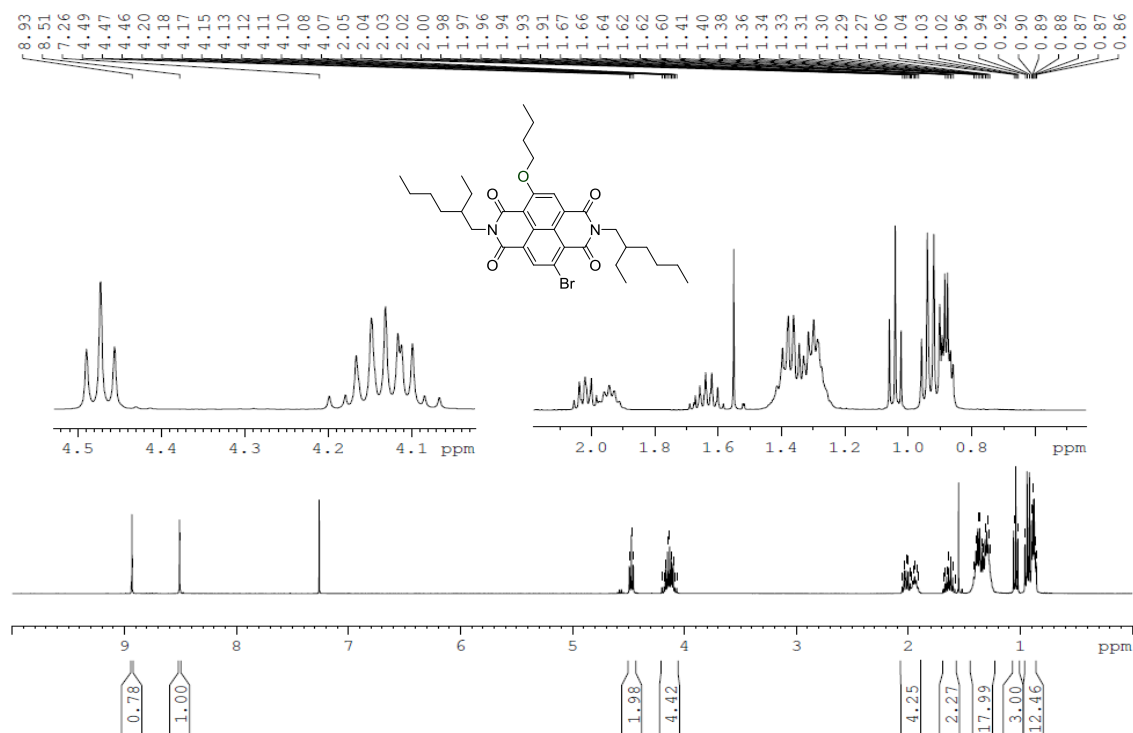
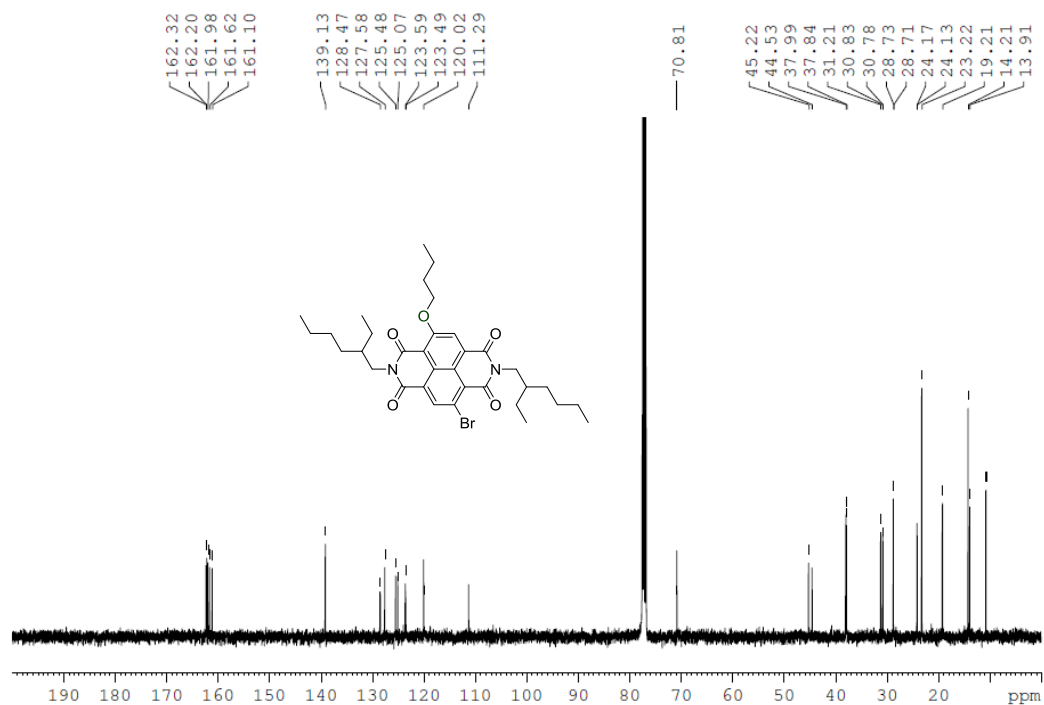
4,9-dibromo-2,7-bis(2-ethylhexyl)benzo[lmn][3,8]phenanthroline-1,3,6,8(2H,7H)-tetraone



(0.20 g, 0.31 mmol) was dissolved in chloroform (40 mL). Then,  $\text{K}_2\text{CO}_3$  (0.43 g, 3.1 mmol) and butyl alcohol (0.11 mL, 1.2 mmol) were added to the solution and heated under reflux for 24 h. Dichloromethane (30 mL) was added to the reaction mixture and the solution was washed with water (3  $\times$  30 mL). The organic phase was collected, dried over anhydrous  $\text{MgSO}_4$  and the solvent removed under vacuum. The crude product was purified by column chromatography with using 30% *n*-hexane in dichloromethane to give title compound as a bright yellow solid (150 mg, yield 76%). M.p. 131-132 °C.  $^1\text{H}$  NMR (400 MHz,  $\text{CDCl}_3$ )  $\delta$  8.93 (s, 1H, NDI), 8.51

**Figure ES1.** Reaction scheme for the molecular acceptors.

## NMR Spectra

**Figure ES2.** 400 MHz  $^1\text{H}$  NMR (300 K,  $\text{CDCl}_3$ ) spectrum of compound **1**.**Figure ES3.** 100 MHz  $^{13}\text{C}$  NMR (300 K,  $\text{CDCl}_3$ ) spectrum of compound **1**.

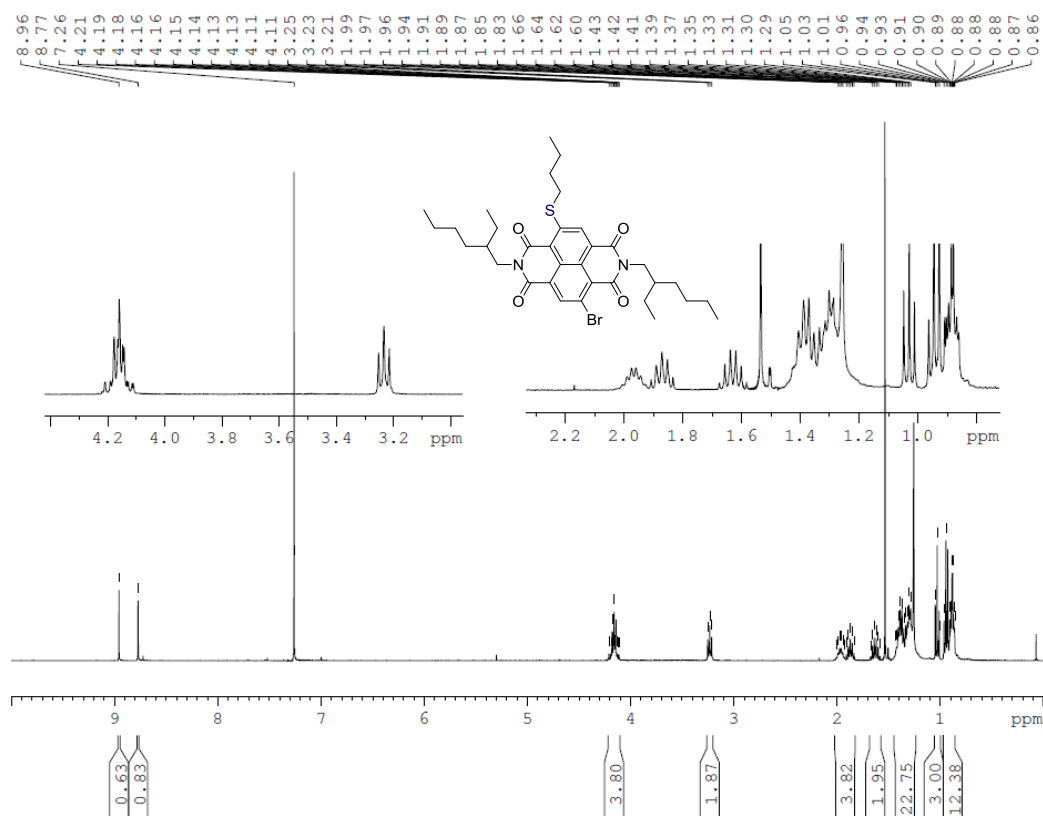


**Figure ES4.** 400 MHz <sup>1</sup>H NMR (300 K, CDCl<sub>3</sub>) spectrum of compound 2.

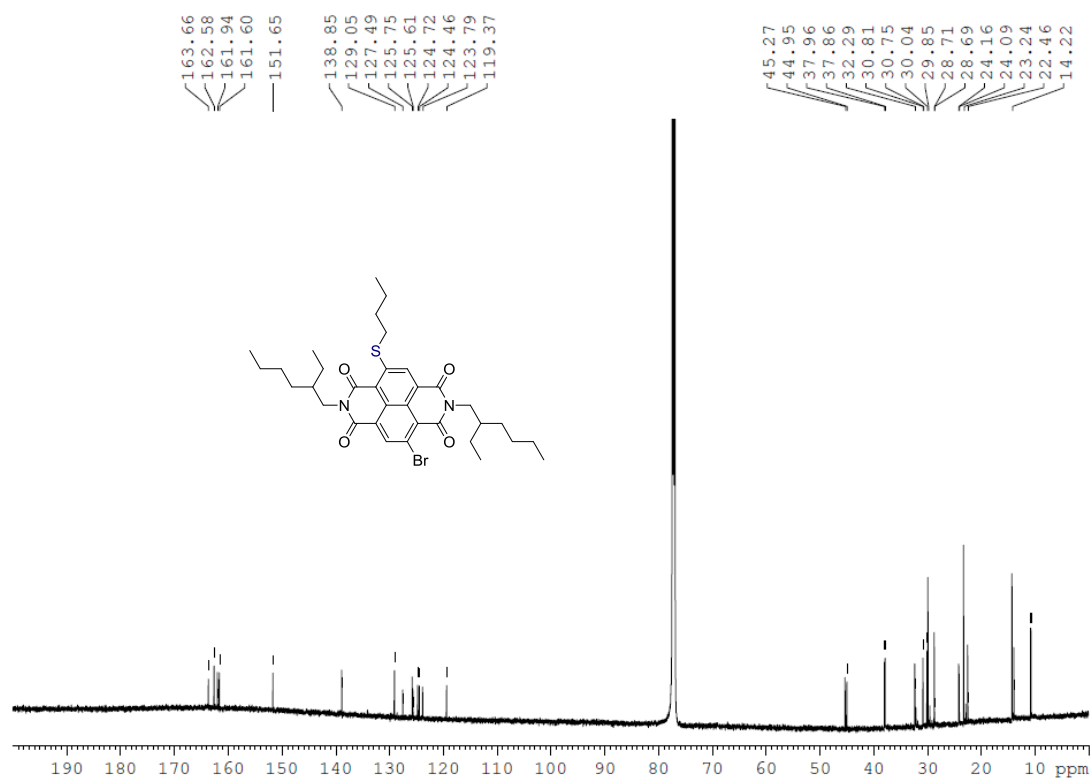


**Figure ES5.** 100 MHz <sup>13</sup>C NMR (300 K, CDCl<sub>3</sub>) spectrum of compound 2.

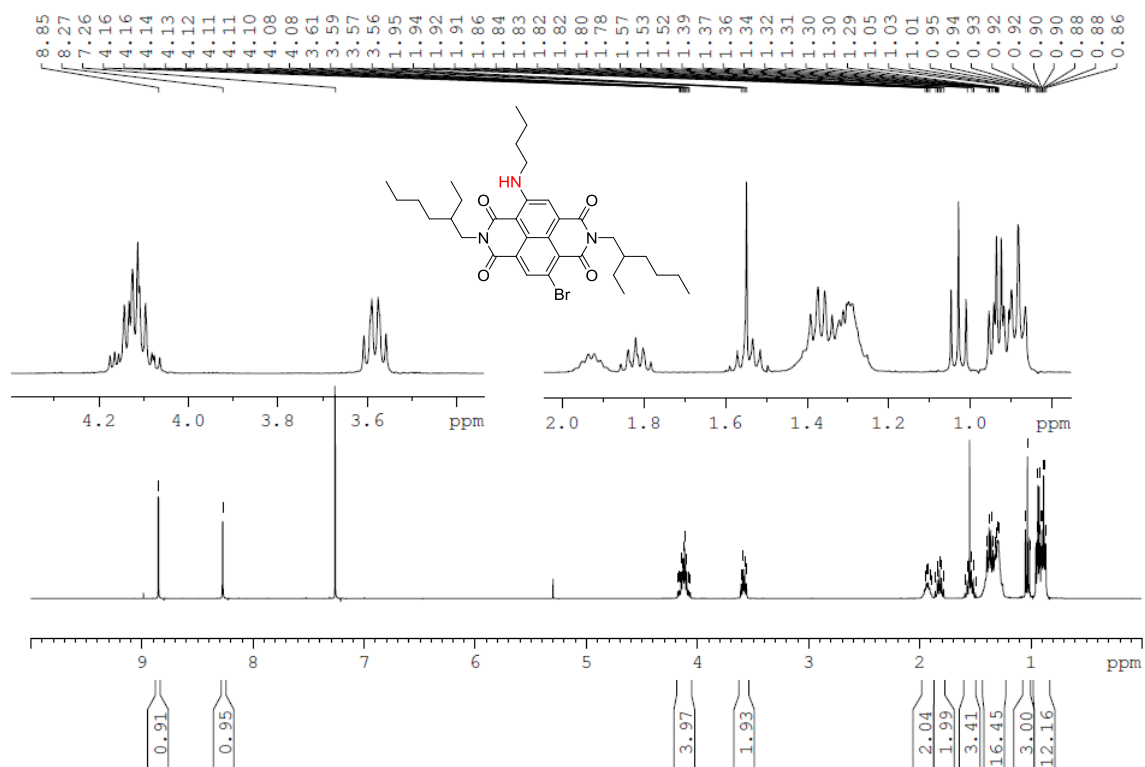


**Figure ES6.** 400 MHz <sup>1</sup>H NMR (300 K, CDCl<sub>3</sub>) spectrum of compound **3**.

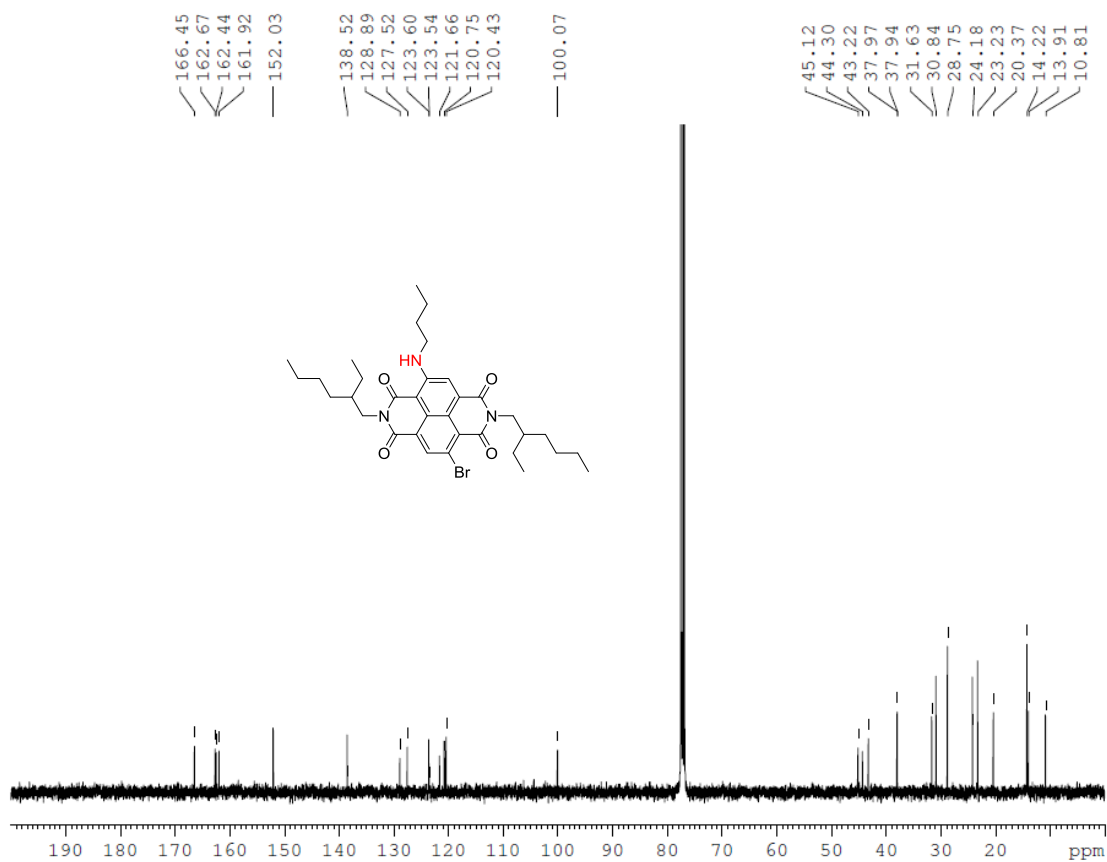


**Figure ES7.** 100 MHz <sup>13</sup>C NMR (300 K, CDCl<sub>3</sub>) spectrum of compound **3**.

Chemical structure of compound 10 is shown above the spectrum. The structure is a complex polycyclic molecule with multiple carbonyl groups, ether linkages, and alkyl chains. The <sup>13</sup>C NMR spectrum displays peaks from 13.94 to 163.29 ppm. A solvent peak is present at 70.70 ppm.

<sup>13</sup>C NMR peaks (ppm): 163.29, 163.15, 162.99, 161.86, 161.64, 147.21, 145.00, 136.75, 129.93, 128.67, 128.46, 124.65, 124.22, 122.83, 122.59, 119.59, 111.21, 70.70, 44.40, 37.99, 37.87, 31.27, 30.83, 28.77, 28.68, 24.15, 23.24, 23.21, 19.24, 14.24, 13.94.

**Figure ES9.** 100 MHz  $^{13}\text{C}$  NMR (300 K,  $\text{CDCl}_3$ ) spectrum of compound *Star NDI-O*.



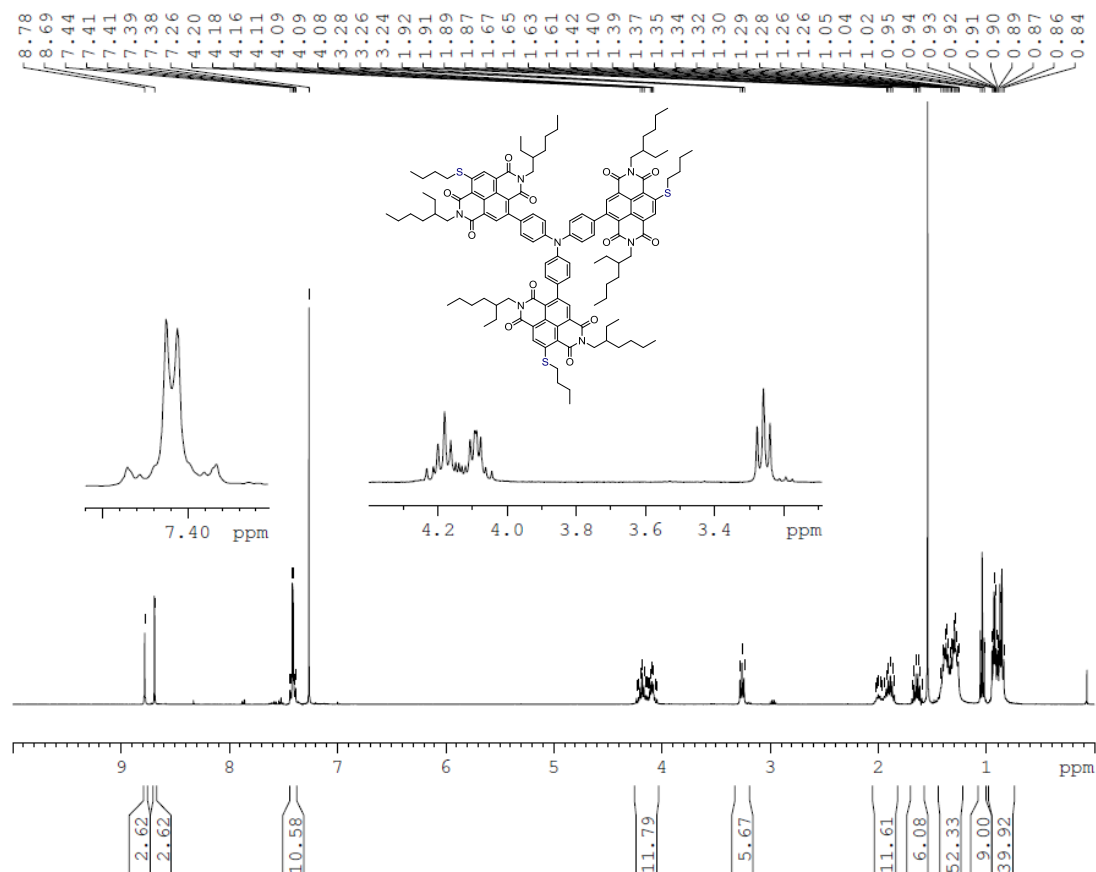


**Figure ES10.** 400 MHz  $^1\text{H}$  NMR (300 K,  $\text{CDCl}_3$ ) spectrum of compound *Star NDI-S*.

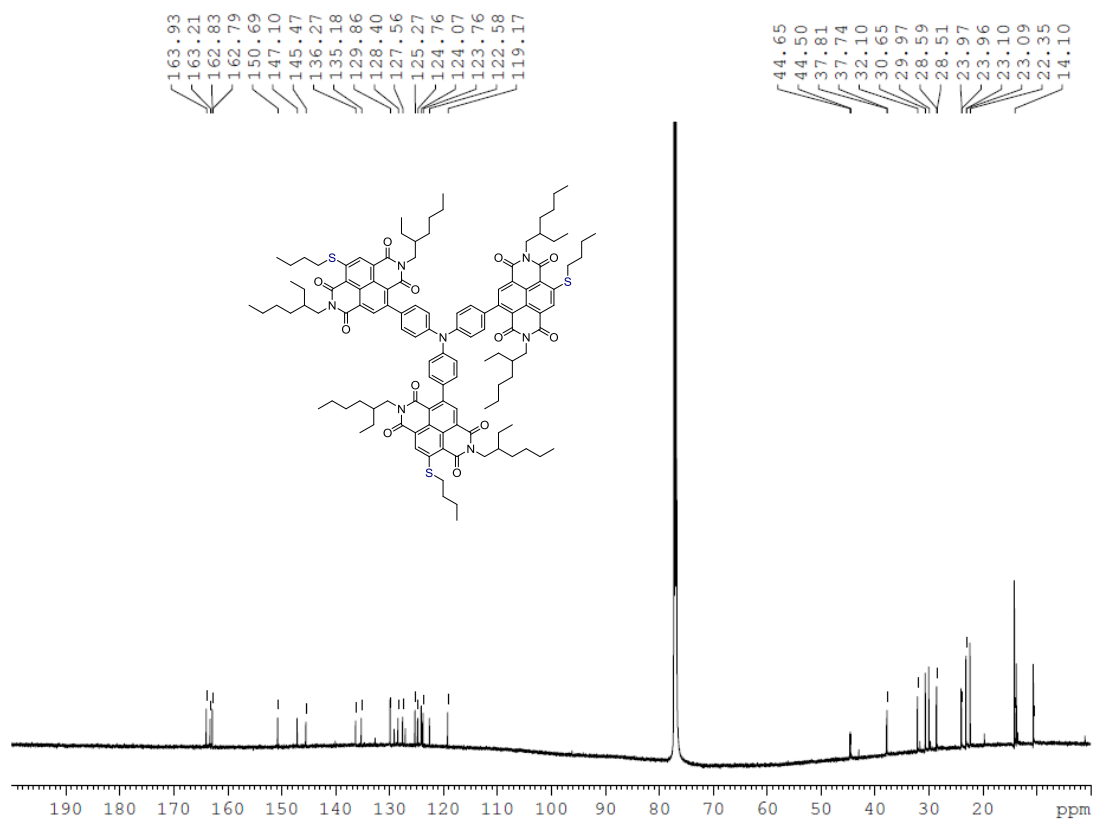


**Figure ES11.** 150 MHz  $^{13}\text{C}$  NMR (300 K,  $\text{CDCl}_3$ ) spectrum of compound *Star NDI-S*.

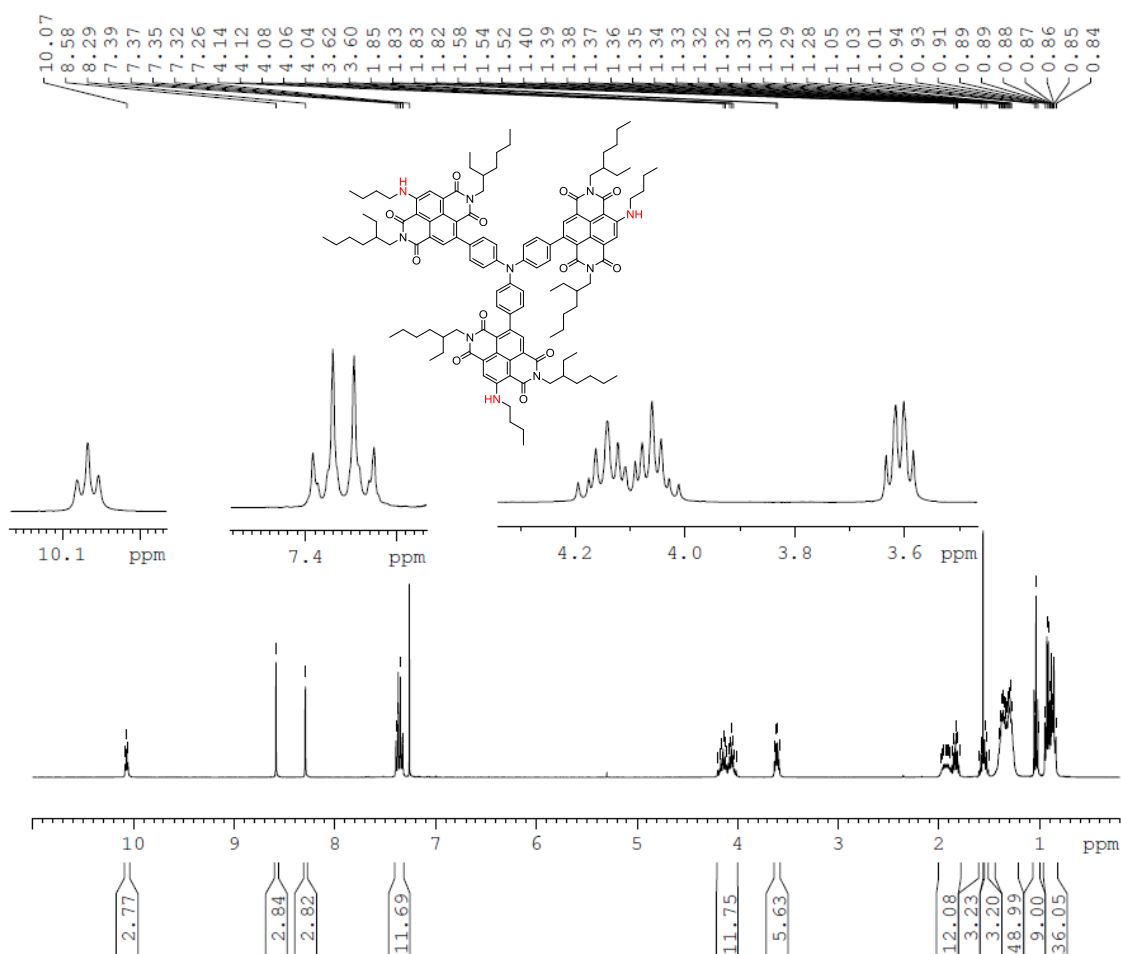


**Figure ES12.** 400 MHz  $^1\text{H}$  NMR (300 K,  $\text{CDCl}_3$ ) spectrum of compound *Star NDI-N*.

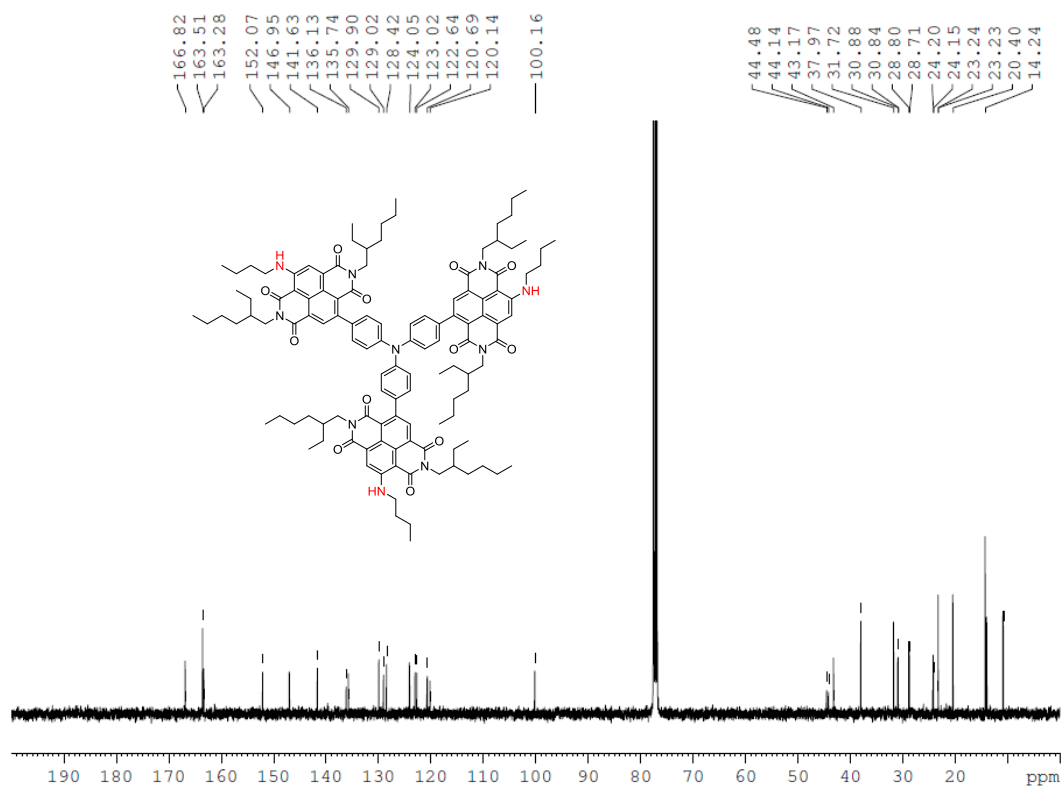


**Figure ES13.** 100 MHz  $^{13}\text{C}$  NMR (300 K,  $\text{CDCl}_3$ ) spectrum of compound *Star NDI-N*.

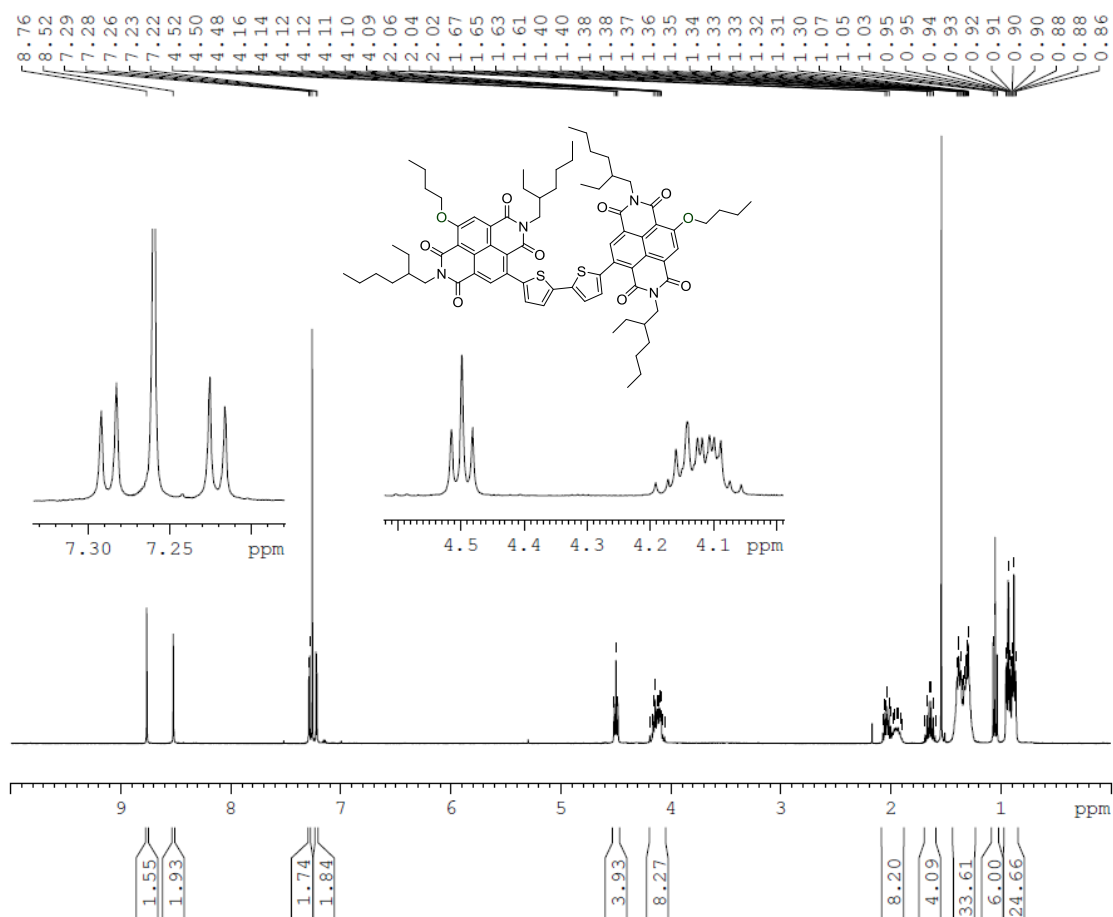


**Figure ES14.** 400 MHz  $^1\text{H}$  NMR (300 K,  $\text{CDCl}_3$ ) spectrum of compound **2Th-O**.

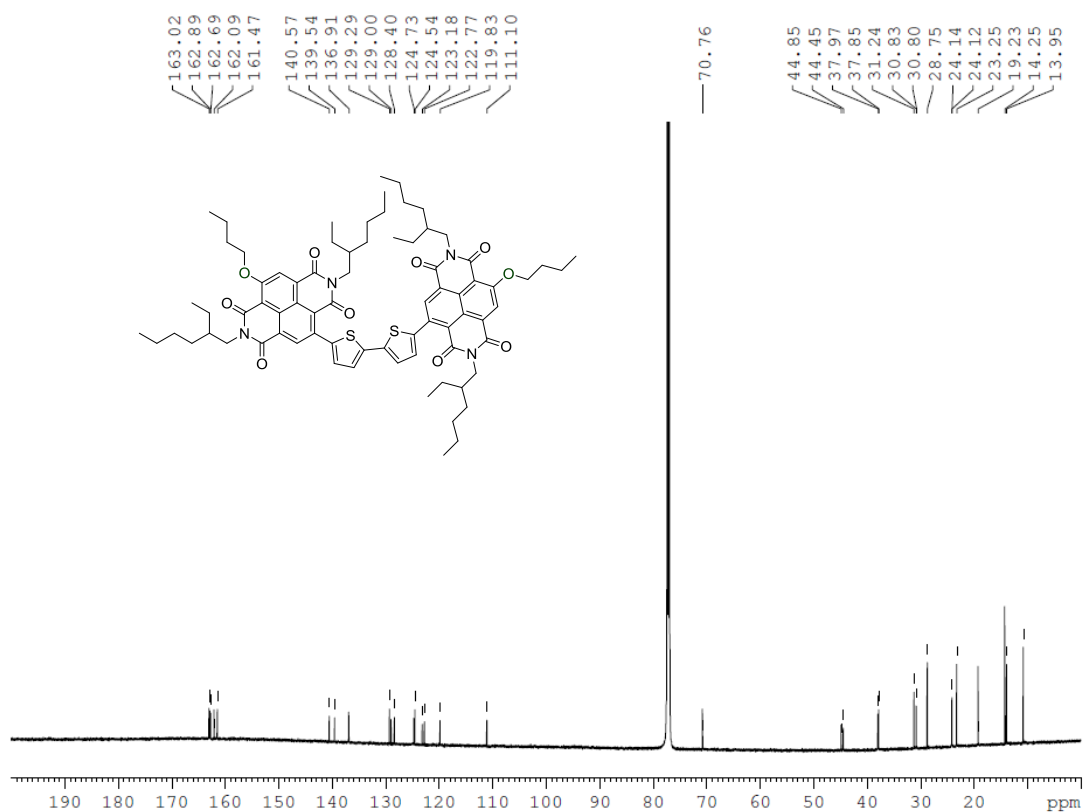


**Figure ES15.** 150 MHz  $^{13}\text{C}$  NMR (300 K,  $\text{CDCl}_3$ ) spectrum of compound **2Th-O**.

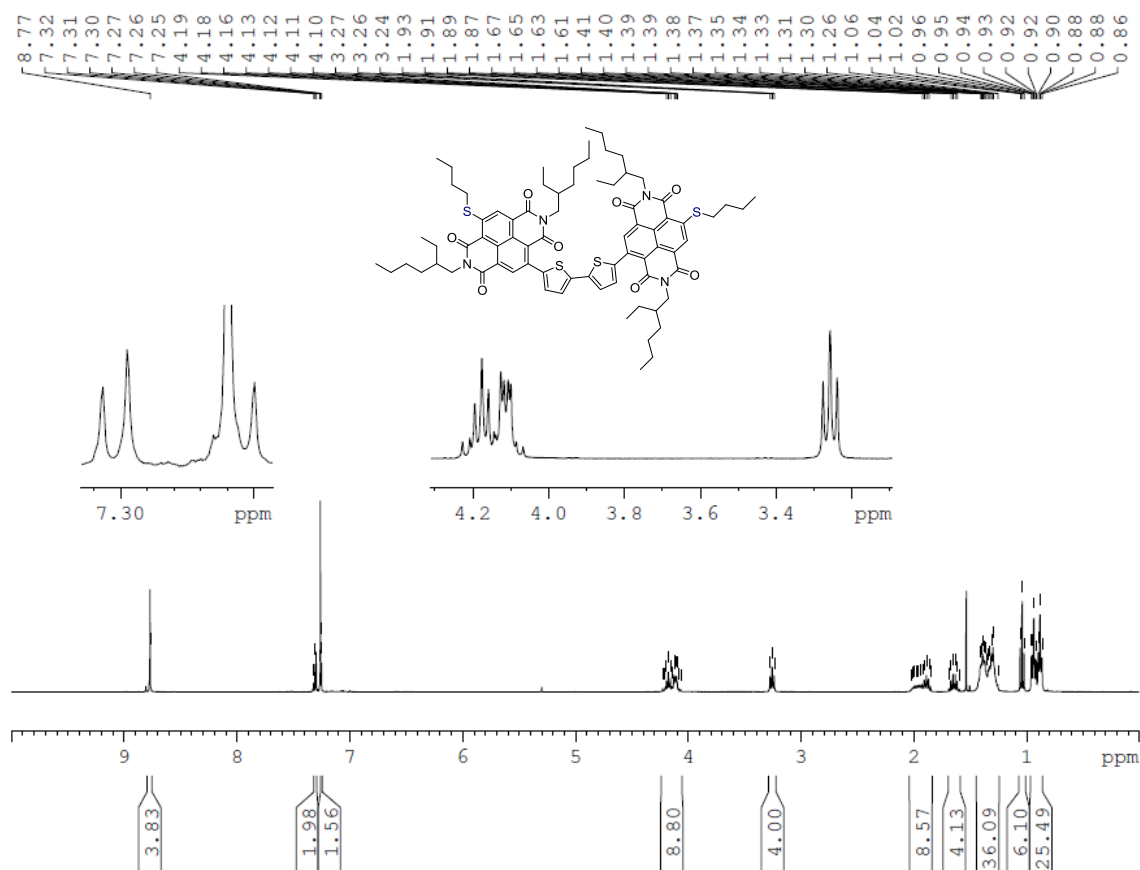


**Figure ES16.** 400 MHz <sup>1</sup>H NMR (300 K, CDCl<sub>3</sub>) spectrum of compound **2Th-S**.

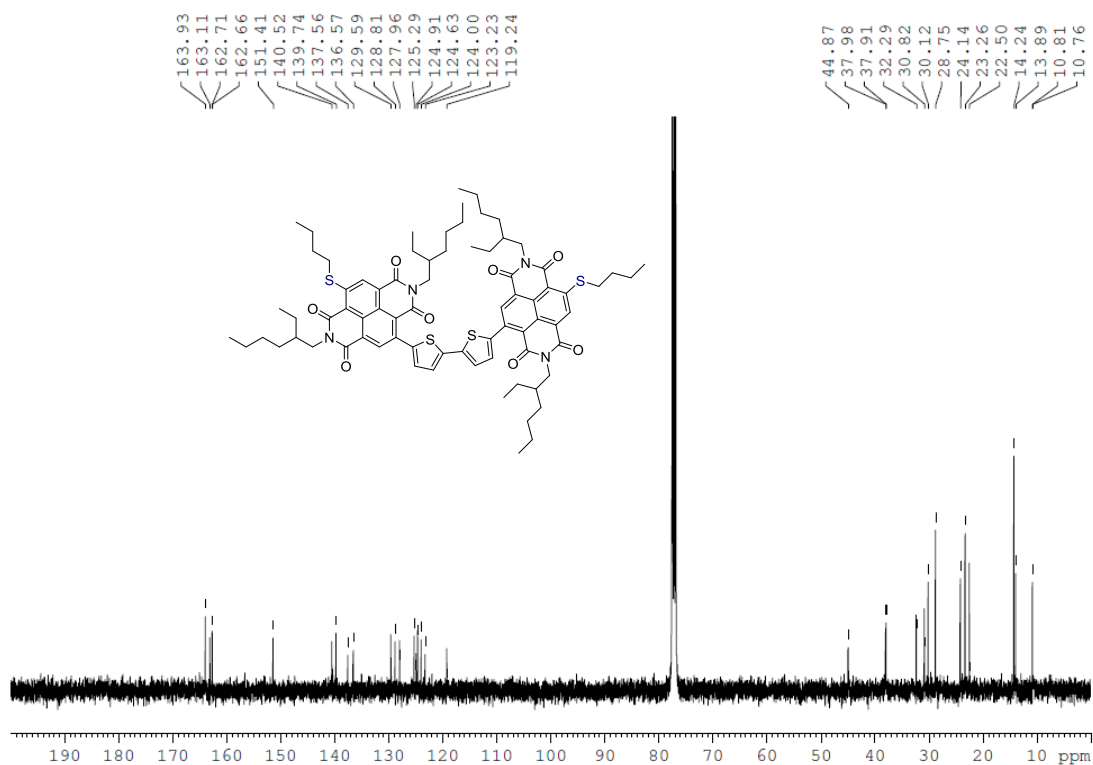


**Figure ES17.** 150 MHz <sup>13</sup>C NMR (300 K, CDCl<sub>3</sub>) spectrum of compound **2Th-S**.

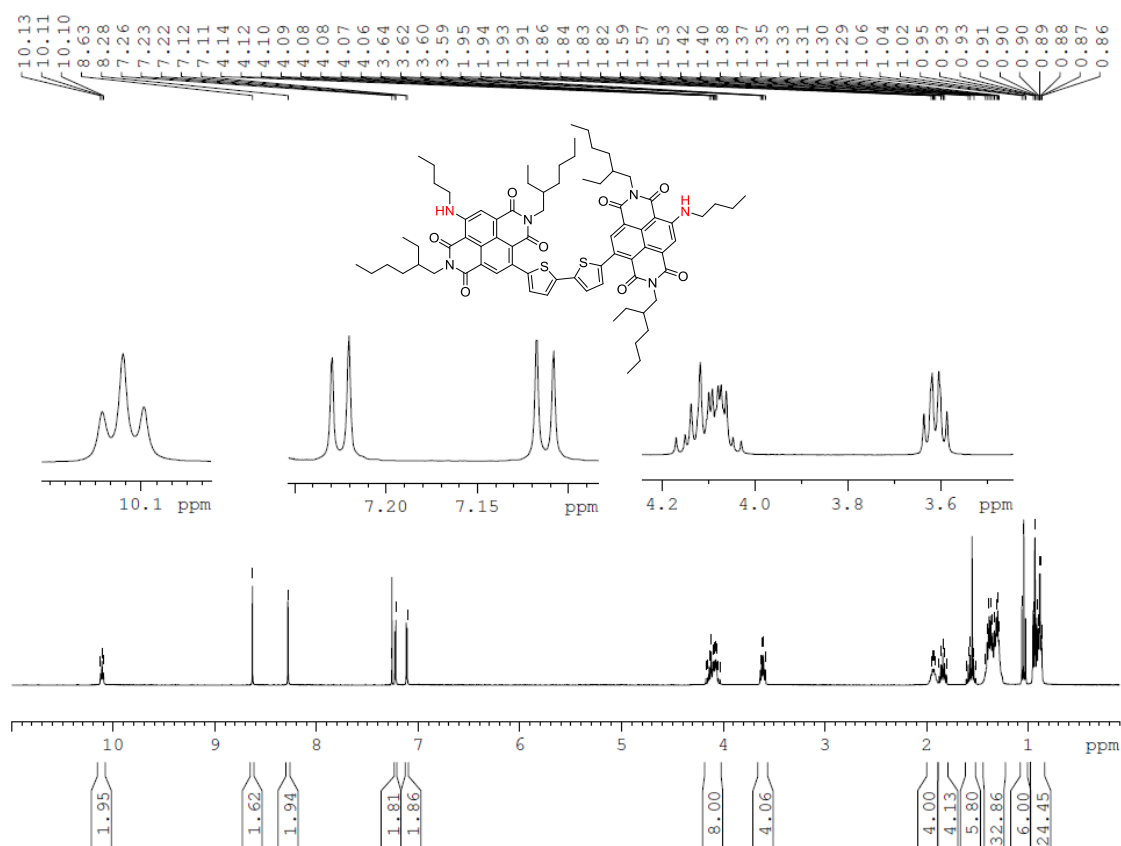


**Figure ES18.** 400 MHz  $^1\text{H}$  NMR (300 K,  $\text{CDCl}_3$ ) spectrum of compound **2Th-N**.

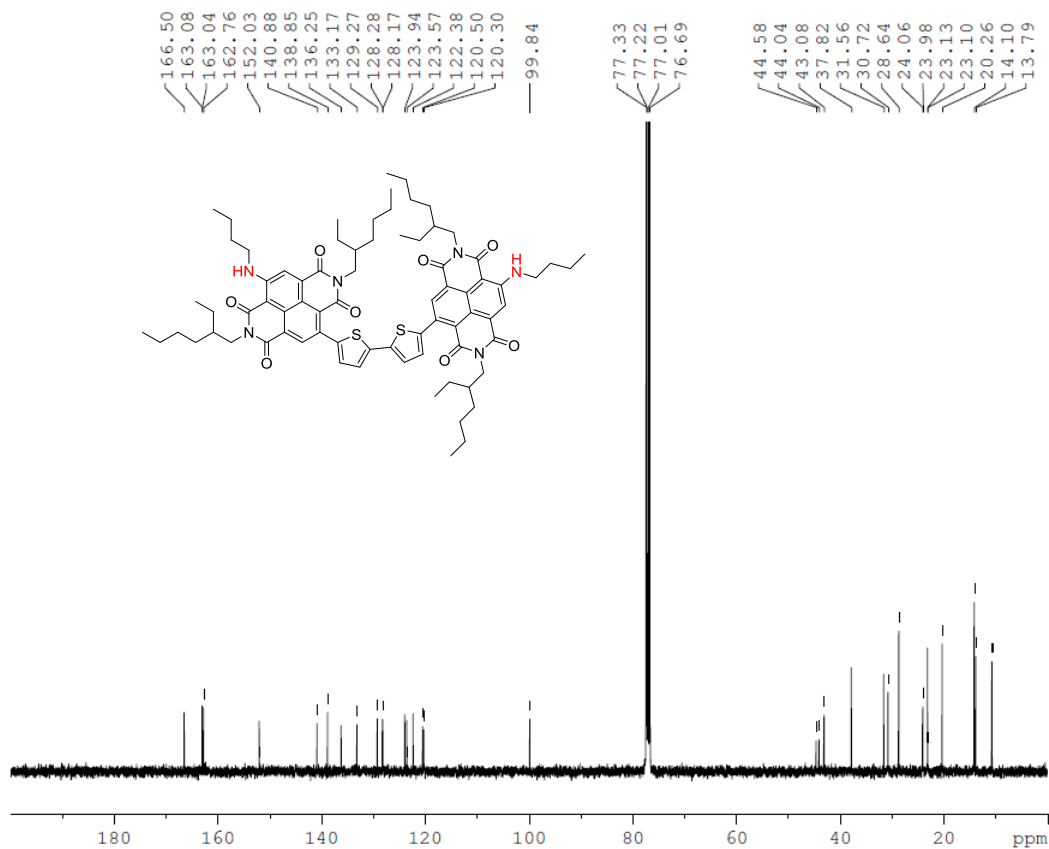


**Figure ES19.** 100 MHz  $^{13}\text{C}$  NMR (300 K,  $\text{CDCl}_3$ ) spectrum of compound **2Th-N**.

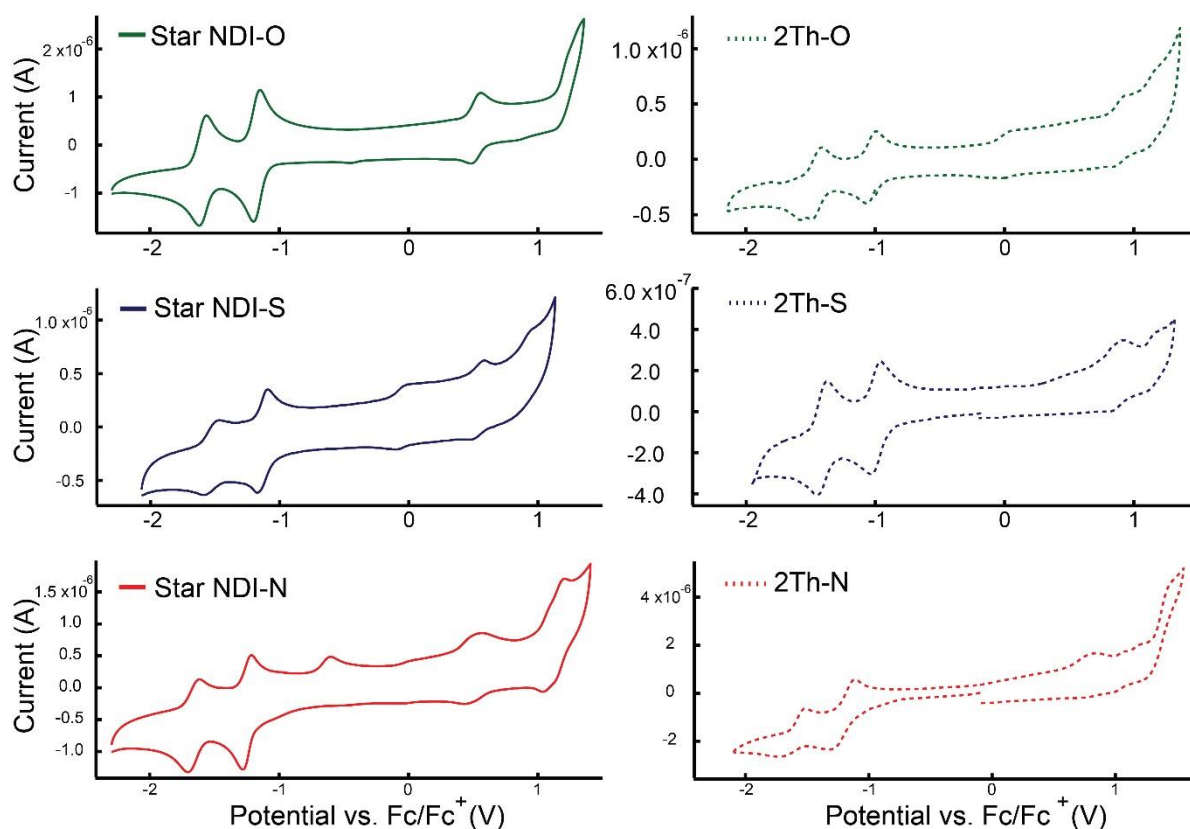
## Cyclic Voltammetry

A Powerlab ML160 potentiostat interfaced via a Powerlab 4/20 controller to a PC running Echem for Windows was used for the solution-based cyclic voltammetry measurements. Argon-purified dichloromethane was used as the solvent for tetrabutylammonium hexafluorophosphate ( $\text{Bu}_4\text{NPF}_6$ ) (0.1 M), the supporting electrolyte. 0.05M of each acceptor material was then added to this solution prior to measurements. All CV measurements were made at room temperature using a glassy carbon working electrode (2.0 mm diameter), a platinum wire counter electrode and a second platinum wire as a quasi-reference electrode, separated from the bulk of the solution by a frit. This system was internally calibrated with ferrocene/ferrocenium ( $\text{Fc}/\text{Fc}^+$ ). A scan rate of 100 mV/s was used for all measurements, with voltammograms recorded within a range from -2000 to 1500 mV. LUMO values were extracted from the first reduction peak using the following equations, assuming the  $\text{Fc}/\text{Fc}^+$  redox reaction takes place at 4.8 eV with respect to vacuum:

$$E_{1/2} = \frac{E_{p1,\text{red}} + E_{p1,\text{ox}}}{2} - E_{1/2 \text{ Fc/Fc}^+}$$

$$E_{\text{LUMO}} = -(E_{1/2} + 4.8)$$

A similar procedure involving the oxidation peak was used to calculate the HOMO value. Oxidation and reduction potentials are given in Table ESI1.

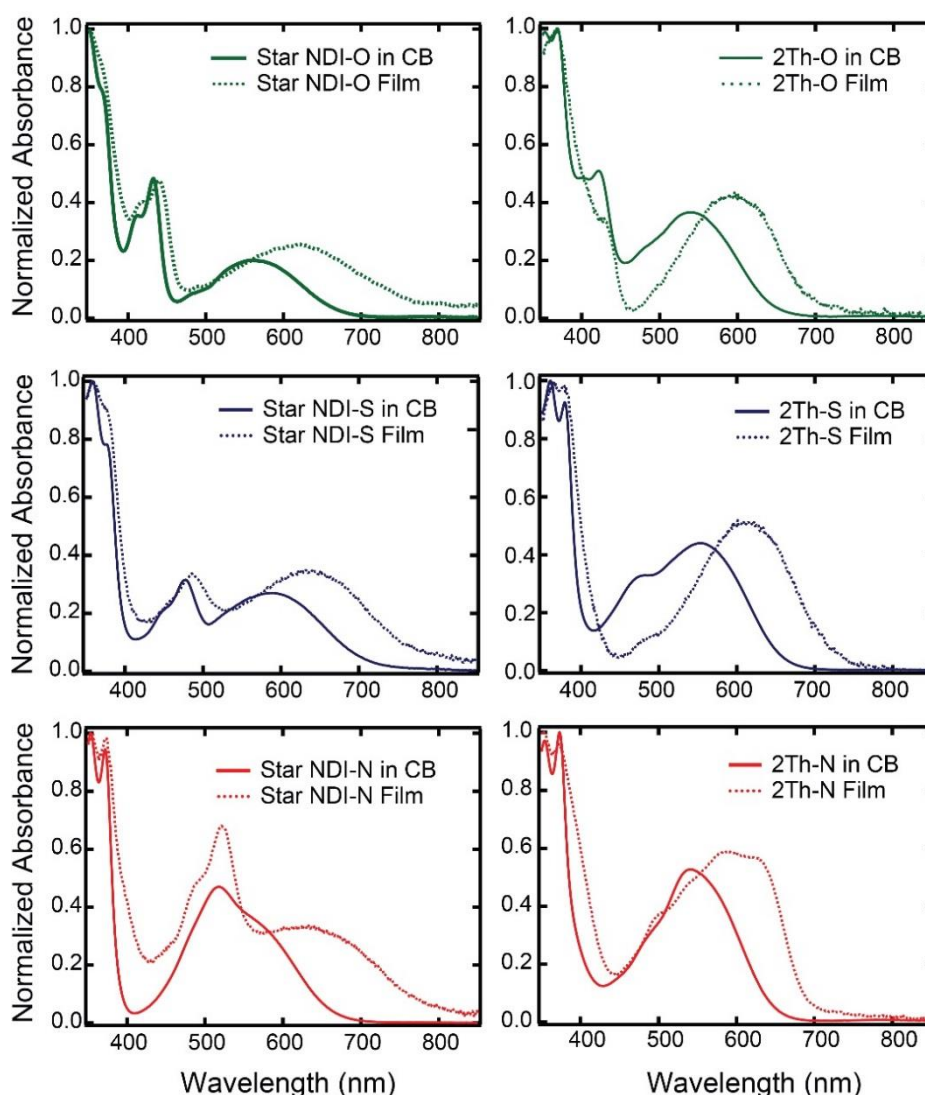


**Figure ES20.** Cyclic voltammograms for all six molecular acceptors.

**Table ES1.** Half-peak reduction and oxidation potentials as well as solution absorption onset values for each molecular acceptor.

| <b>Material</b> | <b><math>E_{1/2 \text{ FC/FC}^+}</math> (V)</b> | <b><math>E_{1/2}^{\text{red}}</math> (V)</b> | <b><math>E_{1/2}^{\text{ox}}</math> (V)</b> | <b><math>\lambda_{\text{abs, onset}}</math> (nm)</b> |
|-----------------|---|--|---|--|
| Star NDI-O      | 0.26  | -1.14  | 0.60  | 676  |
| Star NDI-S      | 0.17  | -1.13  | 0.52  | 709  |
| Star NDI-N      | 0.09  | -1.23  | 0.56  | 665  |
| 2Th-O           | 0.14  | -1.03  | 0.88  | 648  |
| 2Th-S           | 0.19  | -1.00  | 0.90  | 659  |
| 2Th-N           | 0.10  | -1.21  | 0.71  | 647  |

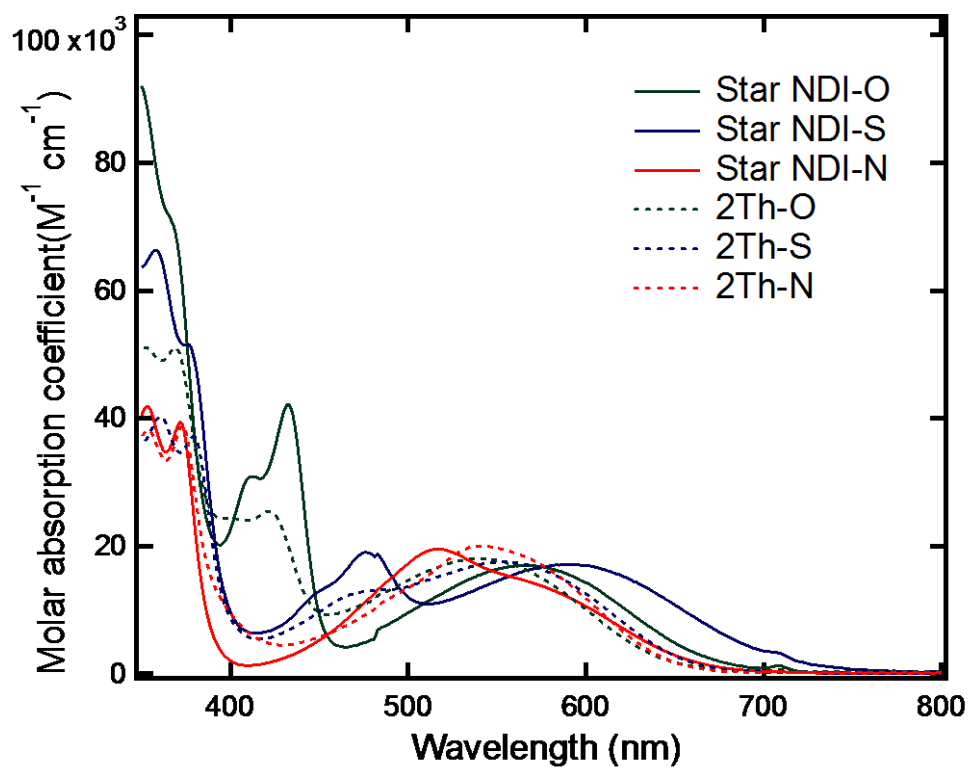
A 0.1 g/l solution of each acceptor in chlorobenzene was used for all solution-based UV-Vis measurements. The solution absorption-onset wavelength was used to calculate the optical band gap in order to draw comparisons between the optical and electrochemically-based computed band gaps.

**Absorbance**

**Figure ES21.** Normalized solution and thin-film absorbance spectra for the acceptors.

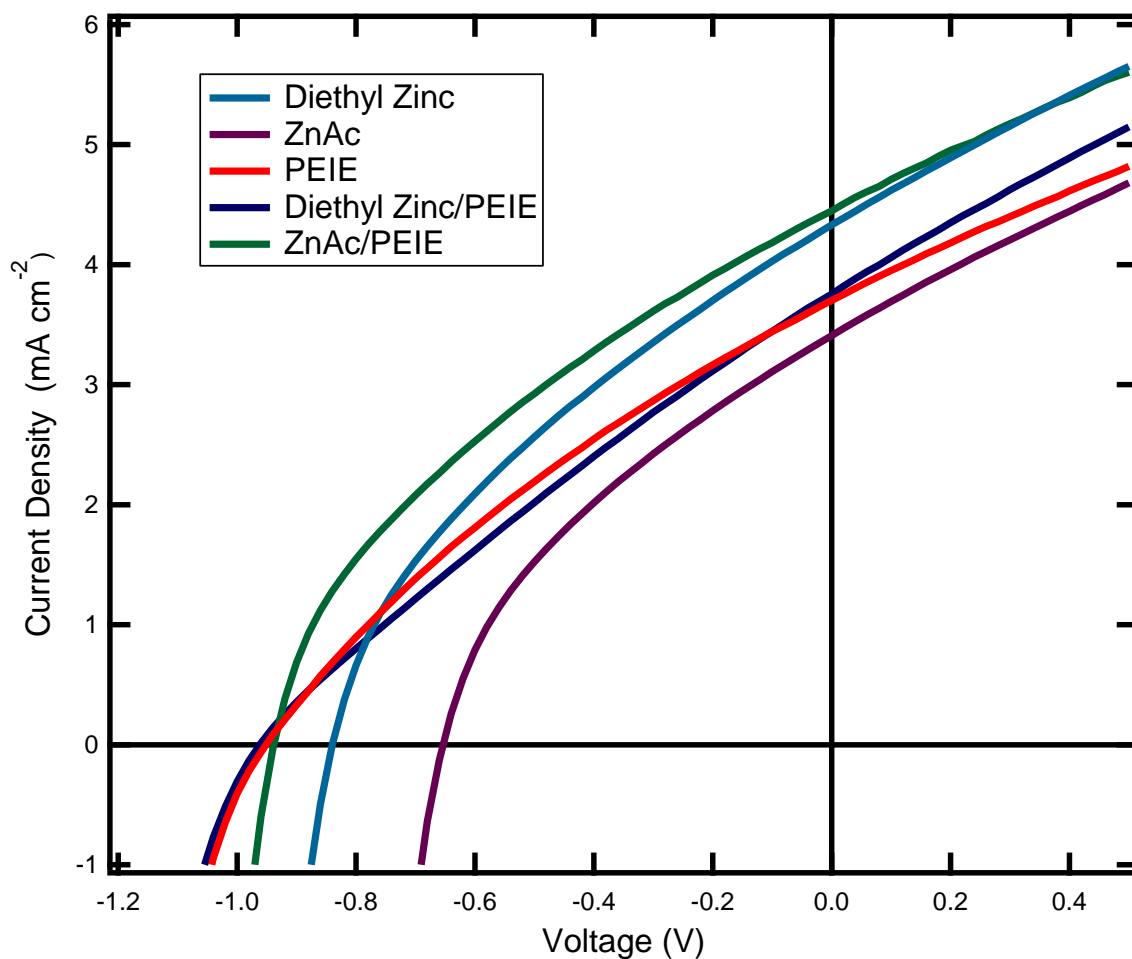
A quartz vial was used for all solution and fused silica substrates with minimal reflectance were used for all solid-state UV-visible absorption measurements. These were both cleaned sequentially via sonication in acetone and 2-propanol for ten minutes. The molecules in solution were measured with a concentration of 0.1 g/l in chlorobenzene while films were spin cast at 6000 RPM from a 30 g/l solution in chlorobenzene. A Perkin Elmer Lambda 950 UV-Vis spectrometer was used for all measurements which were taken in the range from 350 nm to 900 nm. All films were normalized to the largest absorption peak, near or above 350 nm.



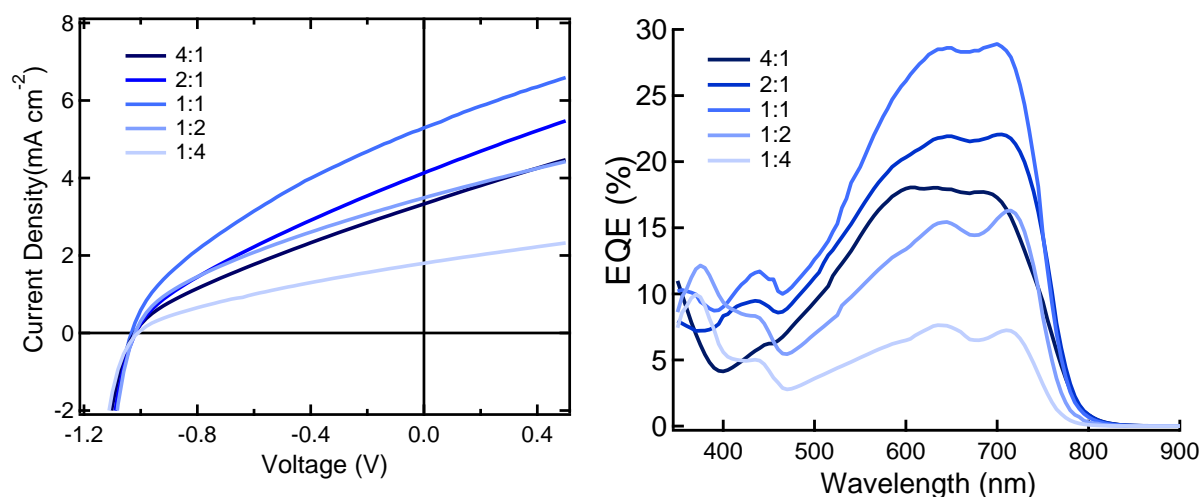


**Figure ES22.** Absorption spectra for all six molecular acceptors at room temperature in chlorobenzene.

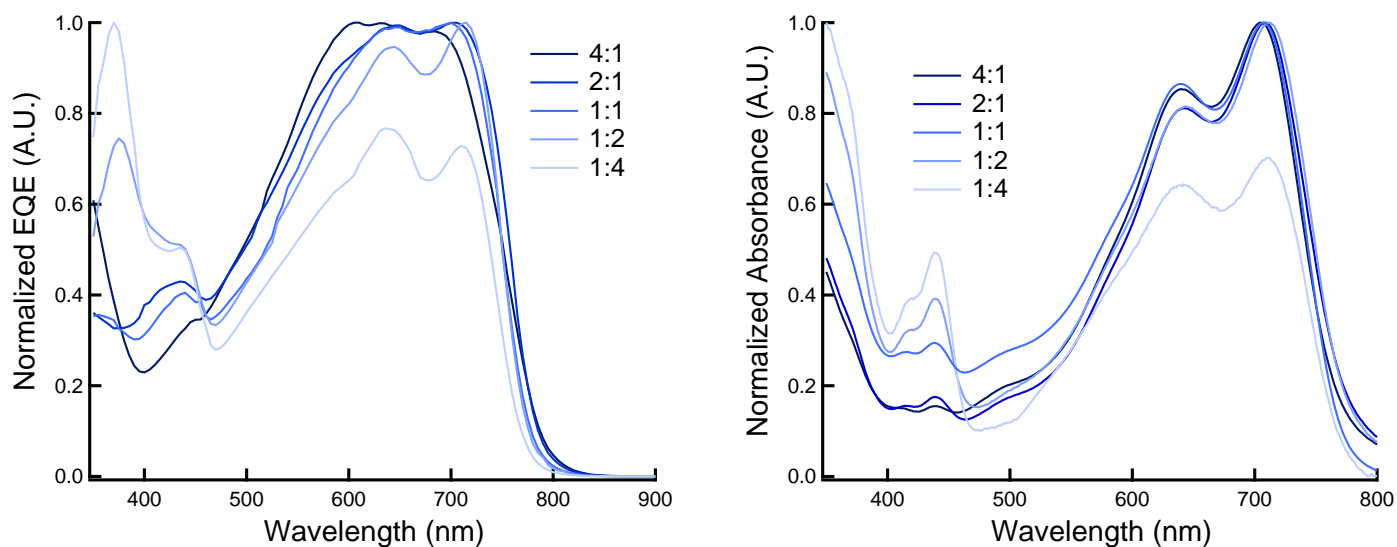
## Device Optimization



**Figure ES23.** J-V curves showing the electron transport layer comparison for devices made with Star NDI-O. Two different zinc oxide precursors were chosen: diethyl zinc solution (1:3 volume ratio in tetrahydrofuran) and zinc acetate. The double layer of ZnAc and PEIE was shown to increase the  $V_{OC}$  and  $J_{SC}$  over devices without the PEIE layer.



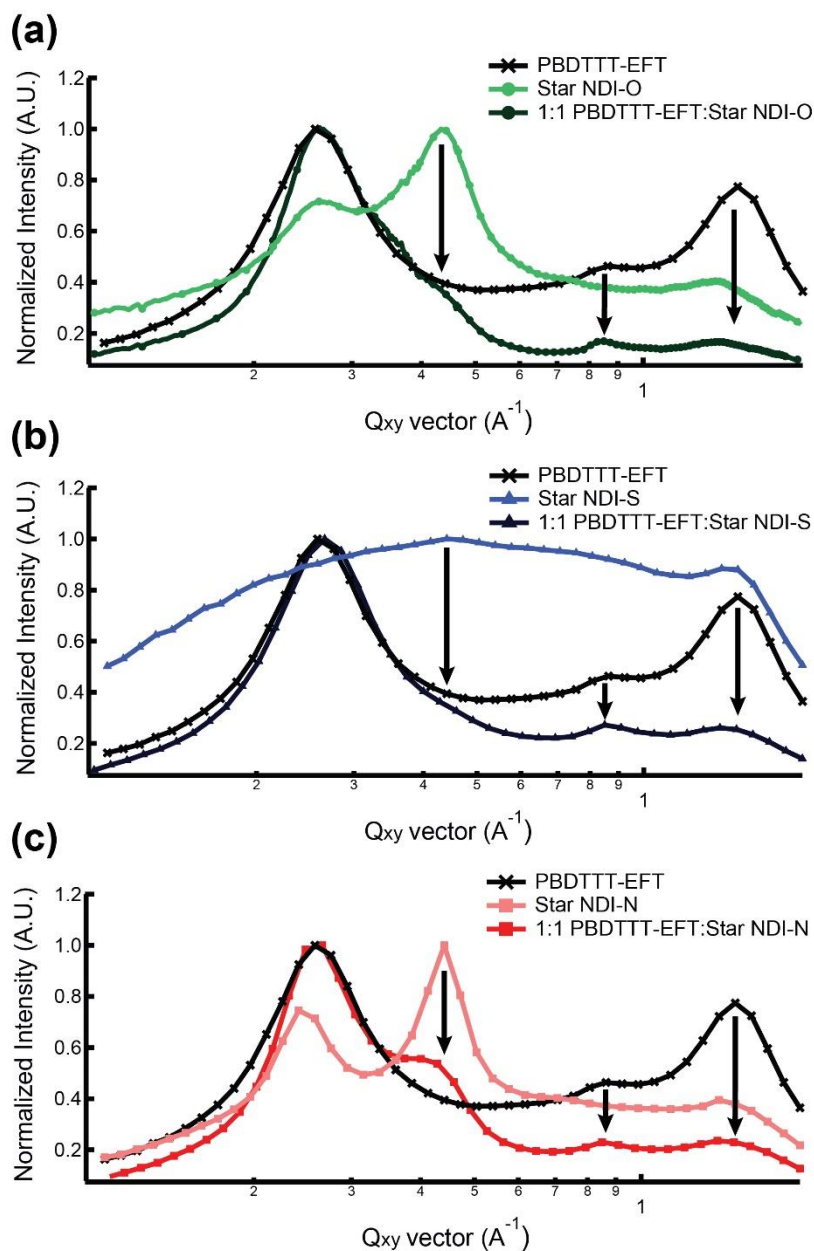
**Figure ES24.** J-V curves (left) and EQE spectra (right) of various donor:acceptor wt. ratios for PBDTTT-EFT:Star NDI-O devices. The optimal device performance was achieved at a 1:1 wt. ratio. Additional optimization includes experimentation with adding DIO as a solvent additive and film thickness.



**Figure ES25.** Normalized EQE and Absorbance spectra for various donor:acceptor wt. ratios for PBDTTT-EFT:Star NDI-O devices. Analysis shows the donor material only modestly contributes to the devices' observed photocurrent.

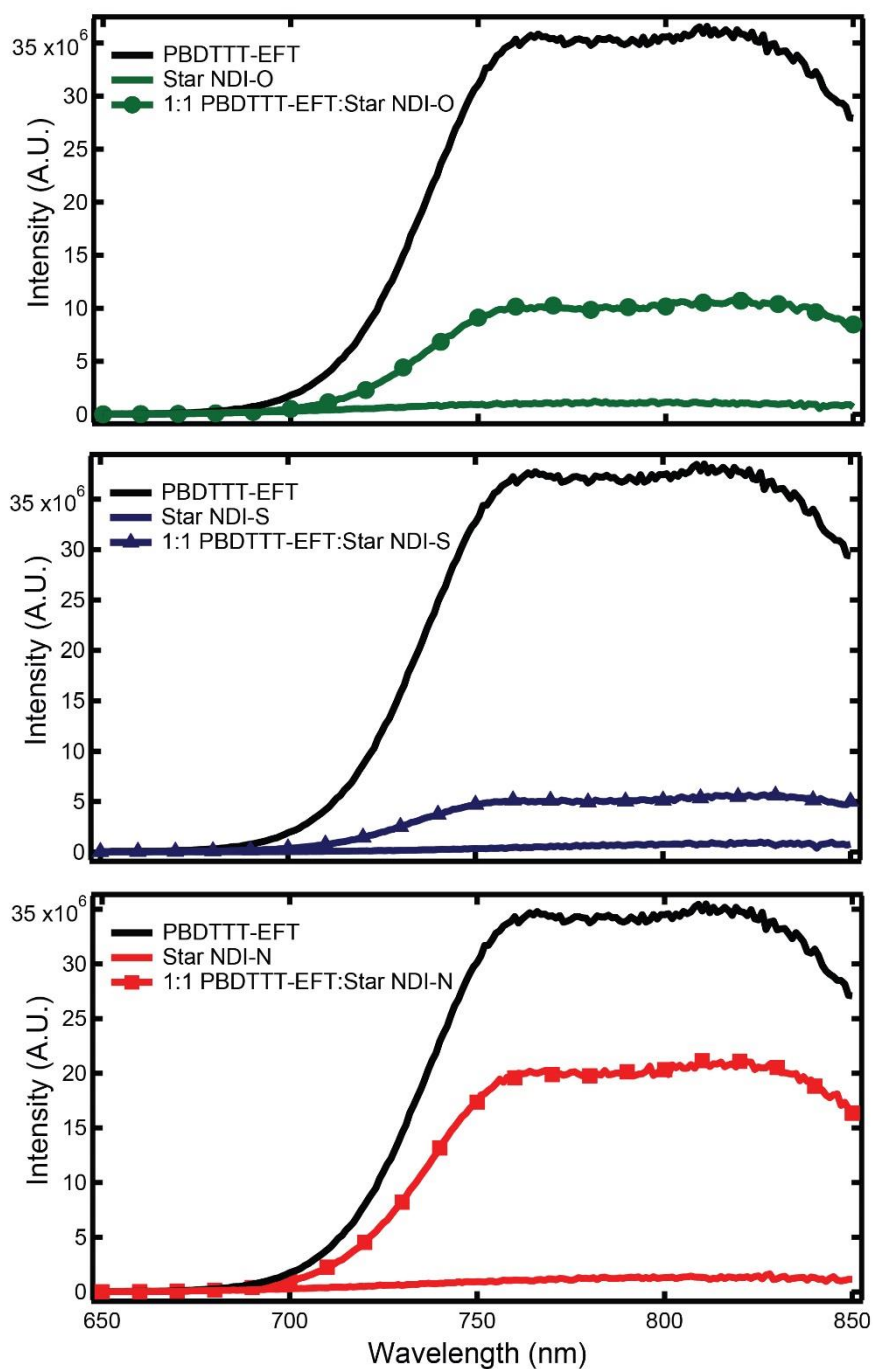
**Table ES2.** *J-V* characteristics for Star NDI-O during optimization. Similar optimization was carried out for the other acceptors, and it was found the same processing conditions were optimal for each acceptor with PBDTTT-EFT.

| Solvent | D:A ratio | % DIO | Spin Speed (RPM) | $J_{sc}$ (mA cm <sup>-2</sup> ) | $V_{oc}$ (V) | FF (%) | PCE (%) |
|---------|-----------|-------|------------------|---------------------------------|--------------|--------|---------|
| CB      | 4:1       | 0     | 6000             | 2.75                            | 1.01         | 30.1   | 0.84    |
| CB      | 2:1       | 0     | 6000             | 4.12                            | 1.02         | 31.7   | 1.34    |
| CB      | 1:2       | 0     | 6000             | 3.49                            | 1.02         | 35.4   | 1.26    |
| CB      | 1:4       | 0     | 6000             | 1.80                            | 1.01         | 33.3   | 0.60    |
| DCB     | 2:1       | 0     | 6000             | 4.16                            | 0.93         | 37.0   | 1.43    |
| DCB     | 1:1       | 0     | 6000             | 3.78                            | 0.99         | 37.8   | 1.41    |
| DCB     | 1:2       | 0     | 6000             | 1.56                            | 0.80         | 36.0   | 0.45    |
| DCB     | 1:1       | 0.5   | 6000             | 2.91                            | 0.78         | 37.3   | 0.85    |
| DCB     | 1:1       | 1.0   | 6000             | 2.85                            | 0.96         | 33.3   | 0.91    |
| CB      | 1:1       | 0     | 3000             | 4.79                            | 1.00         | 35.6   | 1.71    |
| CB      | 1:1       | 0.2   | 6000             | 4.70                            | 1.01         | 34.5   | 1.63    |
| CB      | 1:1       | 0.5   | 6000             | 4.41                            | 0.98         | 33.3   | 1.45    |

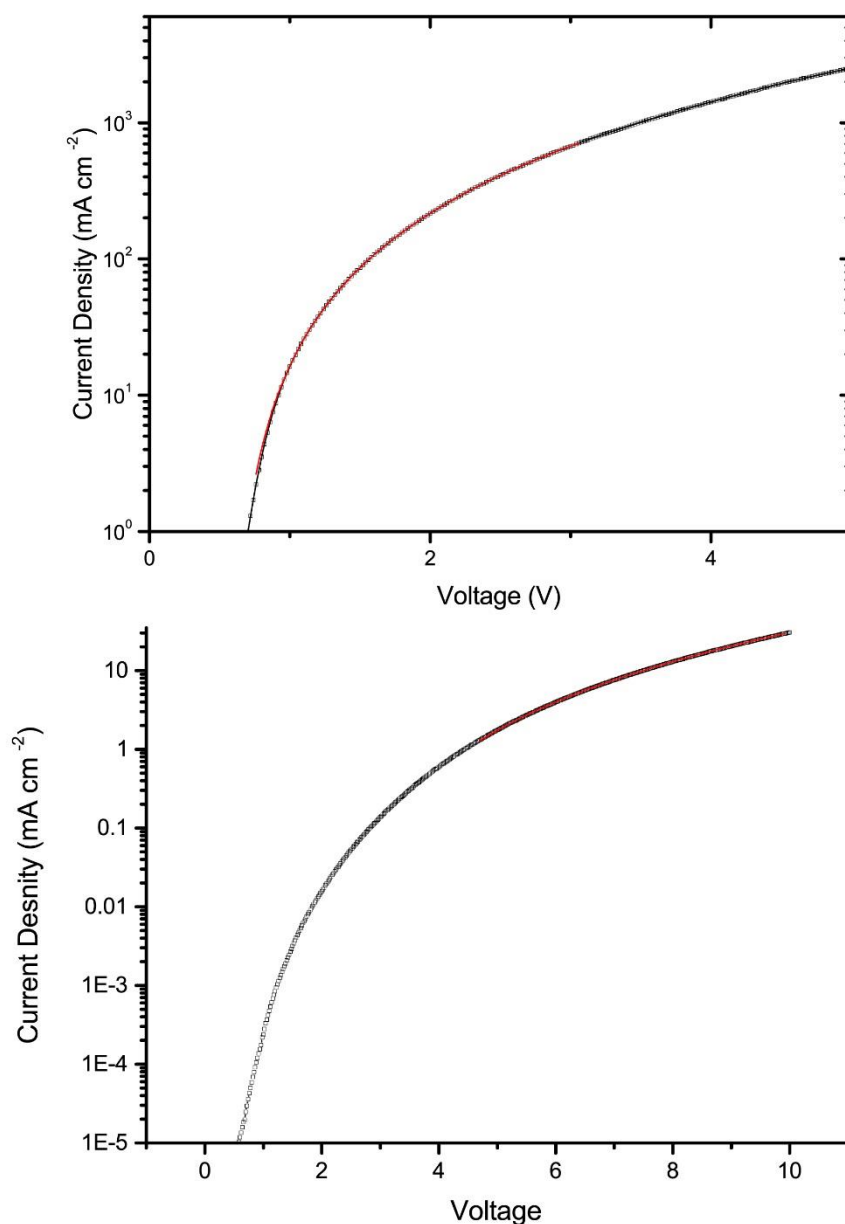
**1D GIWAXS Line Cut Profiles**

**Figure ES26.** Normalized 1D GIWAXS line cut profiles show the GIWAXS patterns for the blend films are a linear combination of the donor and acceptor materials, with the donor material largely dominating the film's overall crystallinity. Neat and blend line cuts for PBDTTT-EFT with Star NDI-O (a), Star NDI-S (b) and Star NDI-N (c) are shown.

## Photoluminescence Quenching



**Figure ES27.** Steady-state photoluminescence spectra for the three neat Star acceptors and neat PBDTTT-EFT as well as 1:1 blend films, which indicate varying PL quenching efficiencies. Excitation was at 600 nm and the photoluminescence intensity has been corrected.

**SCLC Mobility for Star NDI-O**

**Figure ES28.** J-V curves for SCLC devices made PBDTTT-EFT:Star NDI-O devices. Hole-only devices (top) were composed as follows: ITO/MoOx/Active Layer/Ag. Electron-only devices (bottom) had an ITO/ZnO/Active Layer/Ca/Al configuration. Mobility values of  $4.6 \times 10^{-4} \text{ cm}^2 \text{ Vs}$  for holes and  $1.7 \times 10^{-7} \text{ cm}^2 \text{ Vs}$  for electrons were computed.

# Appendix C

## Supplementary material for Chapter 6

The appendix for Chapter 6 contains the following data:

- Low  $M_n$  PNDIT2  $J - V$  curves
- Neat AFM images for polymeric acceptors
- Neat NEXAFS data
- Blend NEXAFS analysis
- Neat GIWAXS image of PBDTTT-EFT
- Transient short-circuit photocurrent data



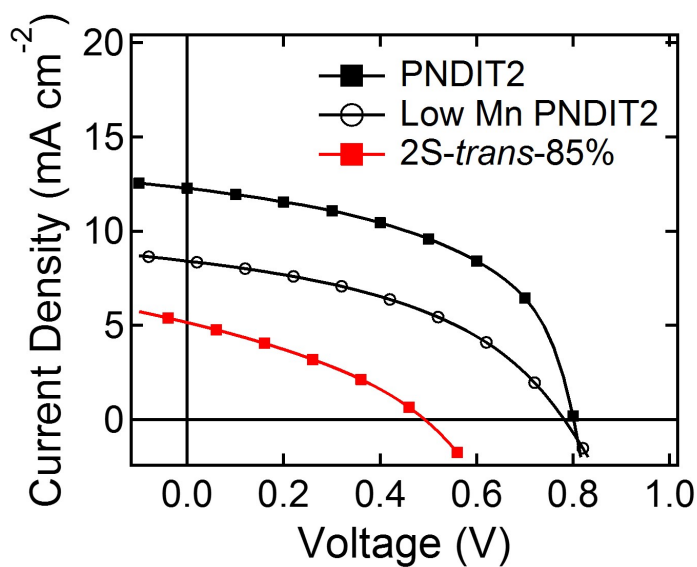


Figure C.1:  $J - V$  curves for the reference PNDIT2 acceptor (squares) and the low molecular weight sample of PNDIT2 (circles). For reference, the  $J - V$  curve for PBDTTT-EFT:2S-trans-PNDIT2-85% systems is also shown.

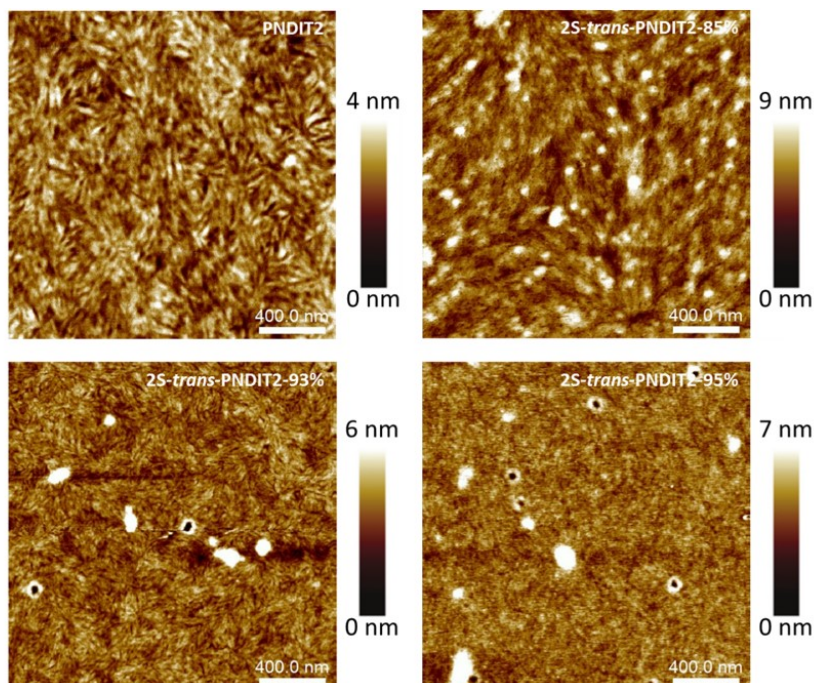


Figure C.2: Neat AFM images. The thionated polymers retain the fibrillar features of the PNDIT2, however surface roughness increases and an increasing number of pinholes emerges with increasing thionation.

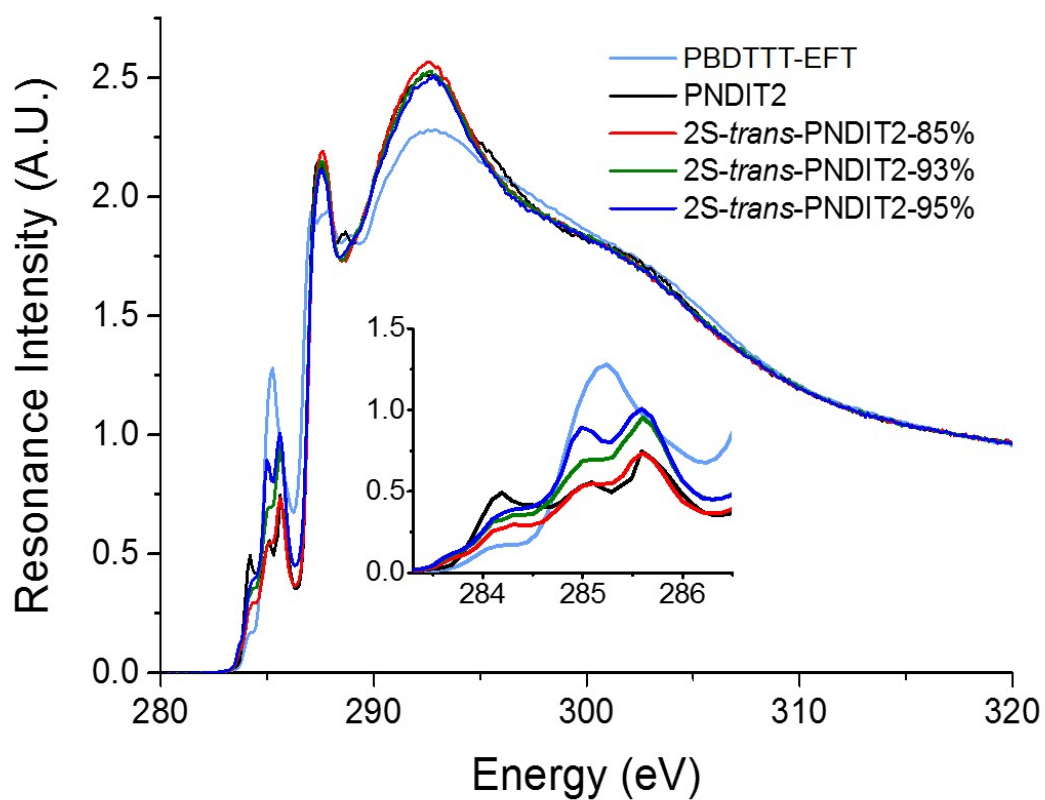


Figure C.3: NEXAFS data (collected in partial electron yield mode) for neat PBDTTT-EFT, PNDIT2, 2S-*trans*-PNDIT2-85%, 2S-*trans*-PNDIT2-93%, and 2S-*trans*-PNDIT2-95% films spin cast at 3000 RPM from chlorobenzene.

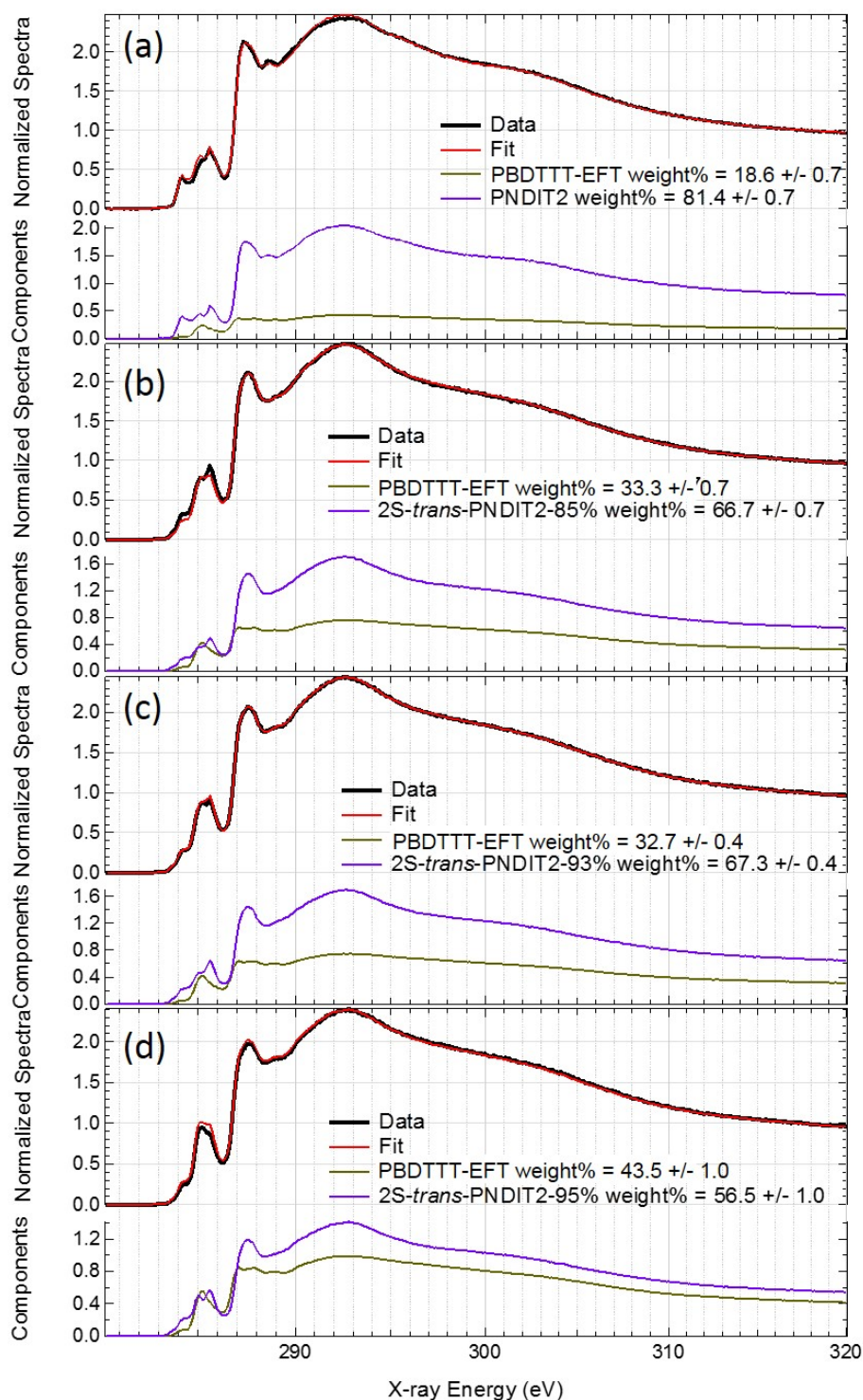


Figure C.4: Blend NEXAFS data for (a) PBDTTT-EFT:PNDIT2, (b) PBDTTT-EFT:2S-*trans*-PNDIT2-85%, (c) PBDTTT-EFT:2S-*trans*-PNDIT2-93%, and (d) PBDTTT-EFT:2S-*trans*-PNDIT2-95% blend films using optimized device conditions. The black lines represent the experimental data, collected in partial electron yield mode while the red lines provide a fit of the data using the neat NEXAFS spectra for each component. The weight% surface composition for each component of the blend films is also given.

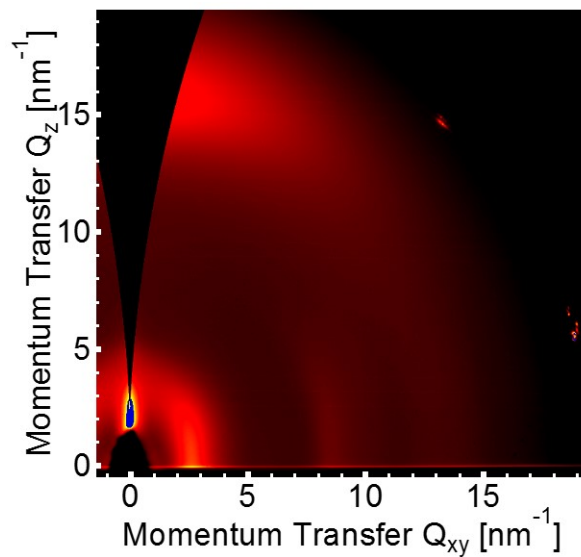


Figure C.5: 2D GIWAXS image of neat PBDTTT-EFT.

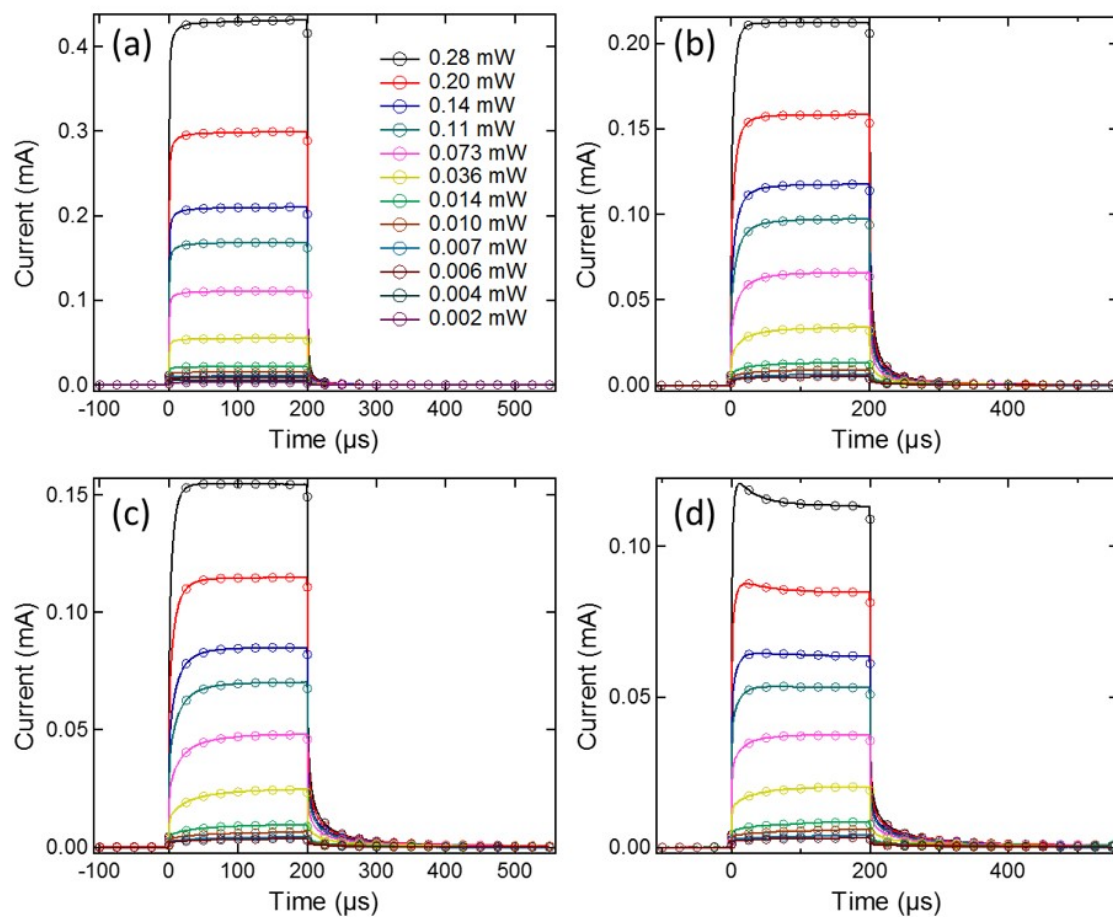


Figure C.6: Transient short-circuit photocurrent measurements for devices employing PBDTTT-EFT:PNDIT2 (a), PBDTTT-EFT:2S-trans-PNDIT2-85% (b), PBDTTT-EFT:2S-trans-PNDIT2-93% (c) and PBDTTT-EFT:2S-trans-PNDIT2-95% (d), in response to a 200  $\mu$ s pulse with wavelength 525 nm, for various intensities. All figure parts share the legend given in (a).



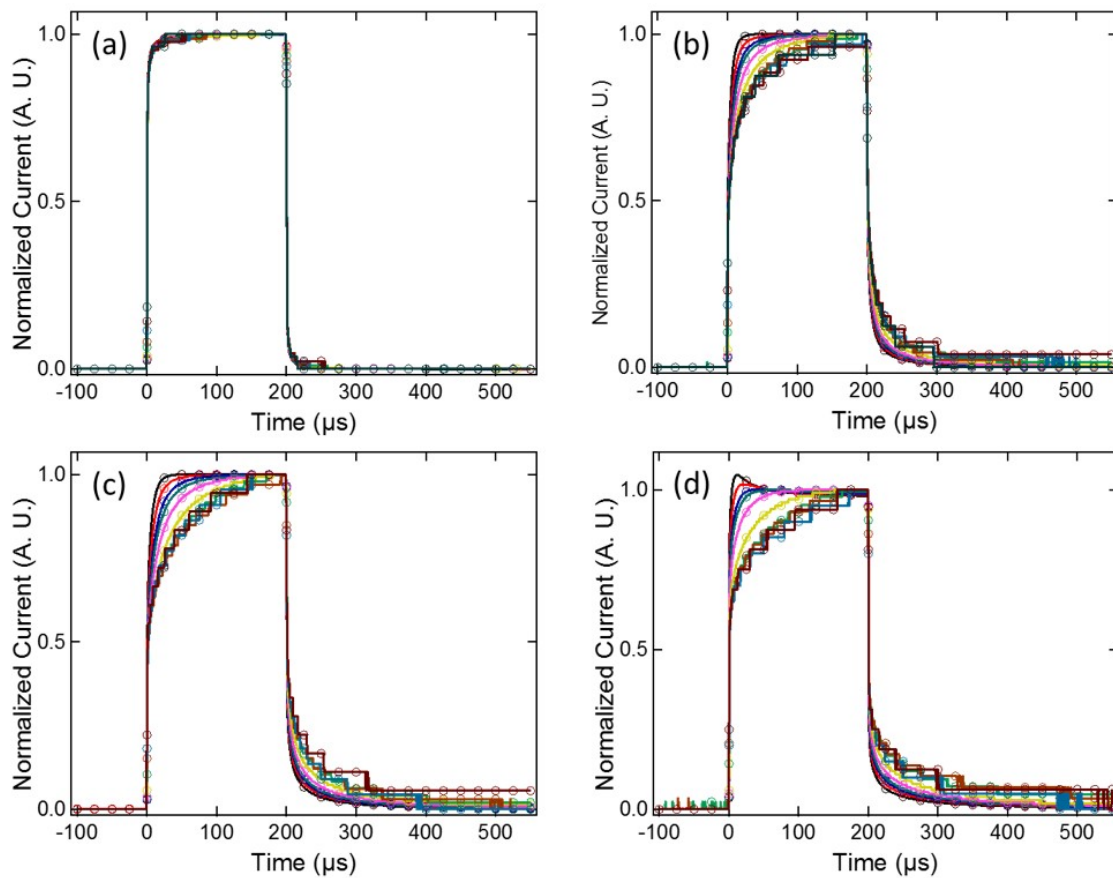


Figure C.7: Transient short-circuit photocurrent measurements for devices employing PBDTTT-EFT:PNDIT2 (a), PBDTTT-EFT:2S-trans-PNDIT2-85% (b), PBDTTT-EFT:2S-trans-PNDIT2-93% (c) and PBDTTT-EFT:2S-trans-PNDIT2-95% (d), in response to a 200  $\mu\text{s}$  pulse with wavelength 525 nm, for various intensities. Curves have been normalized to the value at 200  $\mu\text{s}$ . All figure parts share the legend given in Figure C.6(a).

# Appendix D

## Supplementary material for Chapter 7

The appendix for Chapter 7 contains the supplementary material for *Understanding the effect of thionation on naphthalene diimide using first-principles predictions of near-edge x-ray absorption fine structure spectra*, which includes the following data:

- Comparison of experimental and calculated NEXAFS spectra to 300 eV
- Effect of changing side chain on the calculated spectra
- Effect of changing side chain on experimental spectra
- Molecular orbital projections of HOMO, LUMO and LUMO + 1 for neutral molecules

\*Supplemental Material for

## Understanding the effect of thionation on naphthalene diimide using first-principles predictions of near-edge x-ray absorption fine structure spectra

Kira Rundel<sup>1</sup>, Yufeng Liang<sup>2</sup>, Adam Welford<sup>1</sup>, David Prendergast<sup>2</sup>, and Christopher R. McNeill<sup>1\*</sup>

<sup>1</sup>Department of Materials Science and Engineering, Monash University, Wellington Road, Clayton, VIC 3800, Australia. E-mail: [christopher.mcneill@monash.edu](mailto:christopher.mcneill@monash.edu)

<sup>2</sup>The Molecular Foundry, Lawrence Berkeley National Laboratory, Berkeley, California 94720, United States

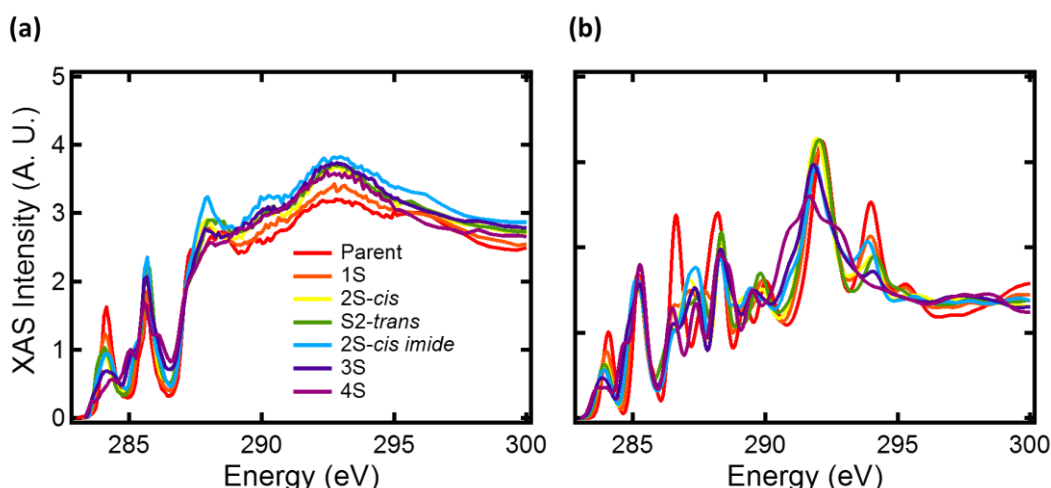


Figure S1. Comparison of experimental (a) and calculated (b) NEXAFS spectra for the series of thionated molecules, up to 300 eV. Experimental data were measured with an X-ray angle of incidence of 55° and were normalized to a step-edge at 320 eV. Note that the disagreement between experiment and theory above 286 eV is due to the fact that the sides

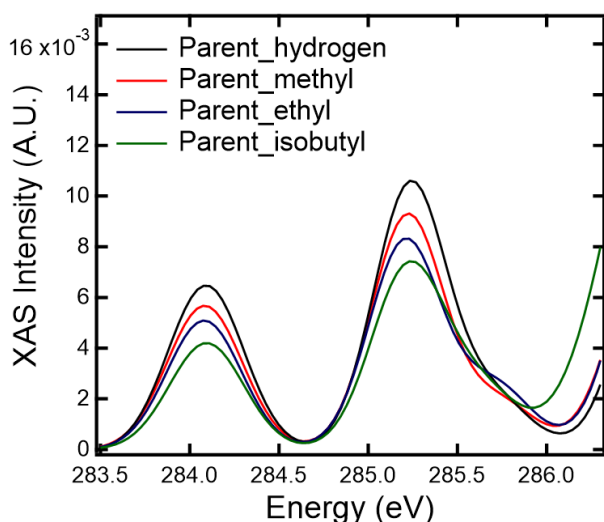


Figure S2. Comparison of NEXAFS spectra in the  $\pi^*$  region, calculated using various end-groups for the parent molecule.

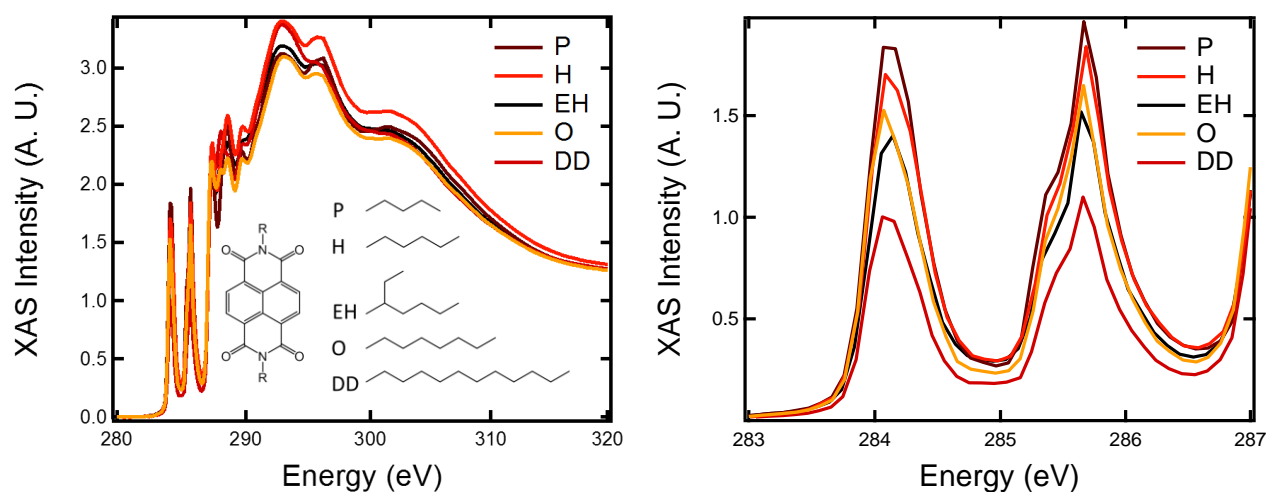
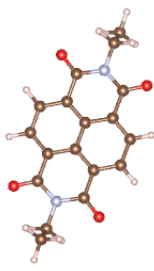
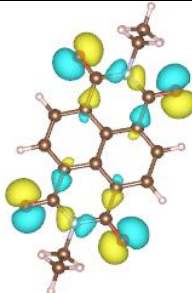
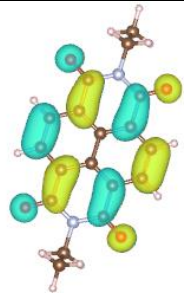
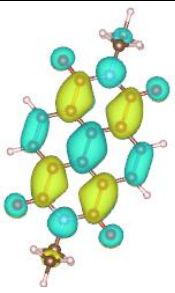
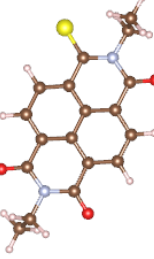
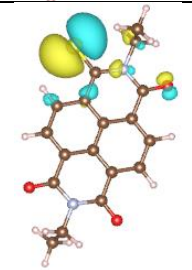
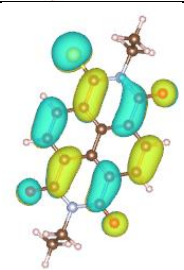
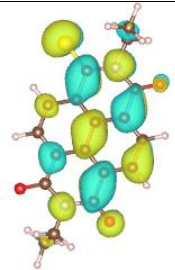
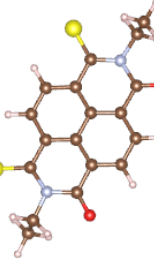
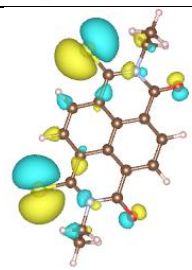
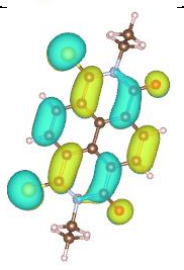
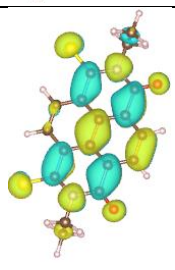
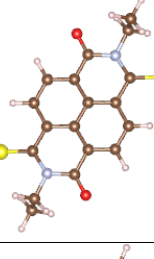
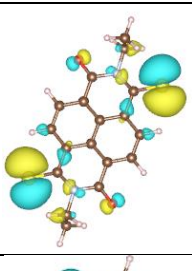
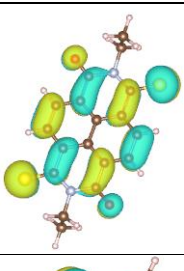
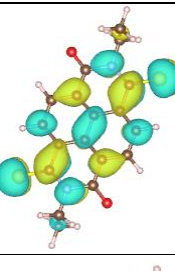
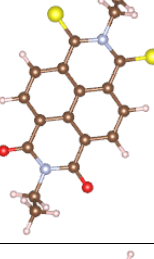
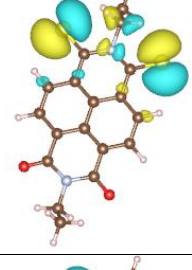
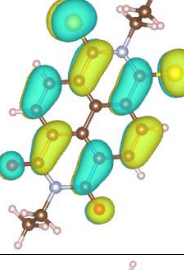
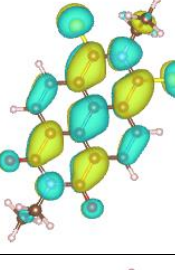
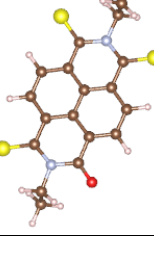
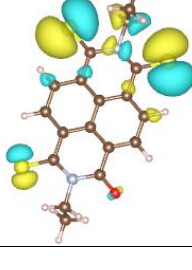
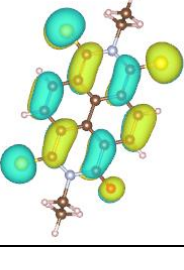
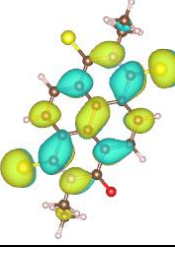


Figure S3. Comparison of the NEXAFS spectra of NDI derivatives with different sidechains demonstrating an insensitivity of the  $\pi^*$  manifold to subtle changes in molecular packing.



Molecular orbital projections of HOMO, LUMO and LUMO + 1 for neutral molecules.

|              | Molecule  | HOMO  | LUMO   | LUMO + 1  |
|--------------|---|---|--|---|
| Parent       |    |    |    |    |
| 1S           |    |    |    |    |
| 2S-cis       |   |   |   |   |
| 2S-trans     |  |  |  |  |
| 2S-cis imide |  |  |  |  |
| 3S           |  |  |  |  |

